16 Apr 1992

1992 OURE report, including the 2nd Annual UMR Undergraduate Research Symposium -- Entire Proceedings

University of Missouri--Rolla

OPPORTUNITIES

FOR THE

UNDERGRADUATE

RESEARCH EXPERIENCE

(OURE)

University of Missouri-Rolla
1992

ACKNOWLEDGMENT

The Opportunities for Undergraduate Research Experiences program began in 1990. This volume represents the proceedings of the second annual OURE program. The aims of the program are to enrich the learning process and make it more active, encourage interaction between students and faculty members, raise the level of research on the campus, help recruit superior students to the graduate program, and support the notion that teaching and research are compatible and mutually reinforcing.

As the papers herein attest, the OURE program continues to achieve its goals -- UMR students have performed research on an enormous variety of topics, have worked closely with faculty members, and have experienced deeply both the pleasures and frustrations of research. Several of the undergraduates whose papers are included are now graduate students at UMR or elsewhere.

The first section of this volume is made up of papers presented at the second annual UMR Undergraduate Research Symposium held on April 16, 1992.

We thank all who contributed.

Harry J. Sauer, Jr.
Dean of Graduate Study

CONTENTS

UNDERGRADUATE RESEARCH

SYMPOSIUM PAPERS

PHYSICAL AND NUMERICAL EXPERIMENTS ON FLAT PLATE BOUNDARY LAYERS

Scott A. Atterberry
Department of Mechanical and Aerospace
Engineering and Engineering Mechanics

ABSTRACT

The results of an interactive computer program developed to predict the boundary layer flow over a flat plate with suction or injection are presented. The results include the solutions for the Blasius function and its derivatives, the velocity profiles, the shear stress distribution, and the temperature distribution. The program can be used for predicting steady, two-dimensional, laminar, viscous flow fields with temperature gradients.

A wind tunnel setup that can be used in addition to the computer program is described. The setup description includes a description of the flat plate, the wind tunnel test section, and the suction/injection unit. The experimental setup allows for boundary layer measurements over the plate at an angle of attack other than zero.

INTRODUCTION

Interactive computer programs can be very effective learning aides/tools especially when used in conjunction with similar physical experiments. One area in which an interactive computer program can enhance learning is in studying boundary layer flow fields. Reducing the problem to a steady, two-dimensional, laminar, incompressible, viscous flow over a flat plate allows the use of a personal computer and, therefore, increases the accessibility to the program. With current personal computer technology, user interactive programs with extensive graphics capabilities are not out of the question. The goal of this paper is to present results from an interactive computer program and to show that the user interactive computer program developed can be used as an effective tool for studying boundary layer flows over flat plates including those with suction and injection.

In addition to the computer program, an experimental model was developed which can be used along with the computer program to provide hands on experience for those studying boundary layer flows. The experimental setup also allows for boundary layer measurements at angles of attack, where the computer code is limited to a zero degree angle of attack.

PROBLEM FORMULATION

Consider a steady, two-dimensional, incompressible, viscous flow over a flat plate at zero degrees angle of attack as shown in Figure 1. For a flat plate in this type of flow, the pressure gradient in the x-direction ($\partial p/\partial x$) is zero, and the pressure gradient in the y-direction ($\partial p/\partial y$) is very small. At low flow velocities, the density, ρ, can be considered constant (i.e. incompressible flow), as can the absolute viscosity, μ, and the thermal conductivity, k.

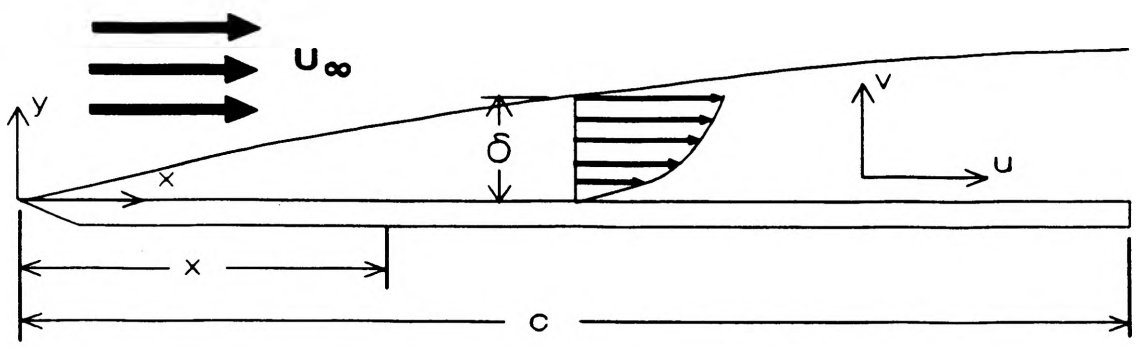

Figure 1: Boundary Layer Over a Flat Plate

Using these assumptions the momentum, continuity, and energy equations can be reduced to equations (1), (2) and (3).

$$u\frac{\partial u}{\partial x} + v\frac{\partial u}{\partial y} = \nu\frac{\partial^2 u}{\partial y^2} \tag{1}$$

$$\frac{\partial u}{\partial x} + \frac{\partial v}{\partial y} = 0 \tag{2}$$

$$\rho c_p\left(u\frac{\partial T}{\partial x} + v\frac{\partial T}{\partial y}\right) = k\frac{\partial^2 T}{\partial y^2} + \mu\left(\frac{\partial u}{\partial y}\right)^2 \tag{3}$$

The reduced equations lead to a solution for investigating the velocity and shear force distributions in the boundary layer. The boundary conditions used to solve the differential equations are simply

$$\begin{aligned} &at\ y = 0: && u = v = 0; && \frac{\partial T}{\partial y} = 0 \\ &at\ y = \infty: && u = u_\infty; && T = T_\infty \end{aligned} \tag{4}$$

To avoid solving the partial differential equations given in Equations (1), (2), and (3), the independent variables (x,y) can be transformed to (ξ,η) where

$$\xi = x \tag{5}$$

$$\eta = y\sqrt{\frac{U_\infty}{\nu x}} \tag{6}$$

Also a dimensionless temperature variable (7), θ, and a stream function (8), ψ, can be defined such that

$$T = T_\infty + \frac{U_\infty^2}{2c_p}\theta(\eta) \tag{7}$$

$$\psi = f(\eta)\sqrt{\nu U_\infty x} \tag{8}$$

Performing the transformations leads to an ordinary differential equation for f(η) known as the Blasius equation (9), and equations for u (10), v (11), and τ (12) in terms of f(η) and its derivatives. In addition, the energy equation (3) can be rewritten as Equation (13) in terms of θ and f, their derivatives, and Prandtl's number, Pr.

$$2f''' + ff'' = 0 \tag{9}$$

$$u = U_\infty f' \tag{10}$$

$$v = \tfrac{1}{2}(\eta f' - f)\sqrt{\frac{\nu U_\infty}{x}} \tag{11}$$

$$\tau = \mu\frac{\partial u}{\partial y} = U_\infty f''\sqrt{\frac{U_\infty}{\nu x}} \tag{12}$$

$$\theta'' + Pr f\theta' + 0.5 Pr f'^2 = 0$$
$$\text{where } Pr = \frac{c_p\mu}{k} \tag{13}$$

The boundary conditions for the transformed system are:

$$\begin{array}{lll} at\ \eta = 0: & f = f' = 0 & \theta' = 0 \\ at\ \eta = \infty: & f' = 1 & \theta = 0 \end{array} \tag{14}$$

For a more details on of the transformation processes, the reader may refer to Kuethe and Chow [Ref. 1].)

While the ordinary differential equations (9) and (13) are simpler to solve than the original boundary layer equations, they are still nonlinear, and must be solved numerically. Upon knowing the values of f and its derivatives, the solution of the energy equation (13) will provide us with the temperature distribution inside the boundary layer. The numerical approach taken in solving the problem is described in the following section.

COMPUTATIONAL APPROACH

Recall the Blasius equation given in Equation (6). This equation can be written as a system of three first order differential equations. This system can then be integrated using a Runge Kutta numerical scheme. Two of the initial boundary conditions f(0)=0 and f'(0)=0 are known. However, boundary condition of f"(0) is unknown.

An initial guess for f"(0) is assigned so that integration using 4th order Runge Kutta calculations can be used to find solutions for f and its derivatives for $0 \leq \eta \leq 10$. If the absolute value of $f'(\eta = 10) - 1.0$ is not less than or equal to 10^{-6}, the initial guess for f"(0) is altered, and the values for f and its derivatives are recalculated using the new value for f"(0). This iterative process continues until the solution converges or until a maximum number of iterations is exceeded.

When the solution converges the boundary layer thickness is taken to be the point where the horizontal velocity inside the boundary layer is equal to 99.4 % of the freestream velocity. The displacement and momentum thicknesses were found by integration using the trapezoidal rule. The local skin friction coefficient was found from the shear stress value at the surface of the plate.

The values of f and its derivatives are also used in calculating the temperature distribution. With f and its derivatives known, the only unknowns in the energy equation (13) are θ'' and θ' (note that Pr is known from the properties of the fluid). By applying a central difference formula developed from a first order Taylor's Series expansion, the energy equation can be written at every point where the values for f and its derivatives are known. The resulting system of equations can then be solved using Gaussian elimination.

The theoretical values for the boundary layer thickness, displacement thickness, local skin friction coefficient, and the momentum thickness can be calculated by noting that Rex = $U_\infty x/\nu$ and using Equations (15), (16), (17), and (18) respectively, as taken from Kuethe and Chow [Ref. 1] :

$$\delta = 5.2\sqrt{\frac{\nu x}{U_\infty}} = \frac{5.2x}{\sqrt{Re_x}} \qquad (15)$$

$$\delta^* = \frac{1.7208x}{\sqrt{Re_x}} \qquad (16)$$

$$c_f = \frac{0.664}{\sqrt{Re_x}} \qquad (17)$$

$$\theta_m = 0.664\sqrt{\frac{\nu x}{U_\infty}} \qquad (18)$$

The variable for the momentum thickness, θ_m, should not be confused with the dimensionless temperature which was defined as θ.

COMPUTER PROGRAM ARRANGEMENT

An interactive program was written to facilitate the use of the program as a learning aide. C computer language was chosen because of its enhanced screen graphics capabilities and because user interactive programs can be written effectively using the language. An overview of the program arrangement is given in Figure 2.

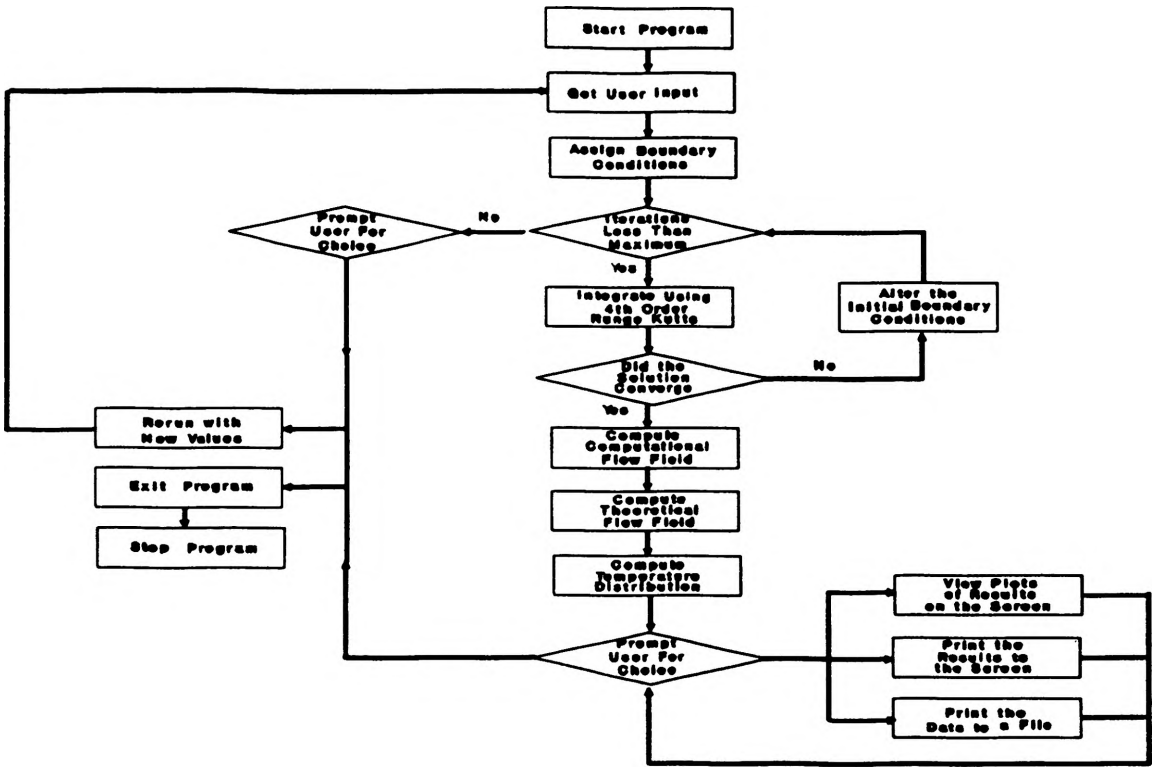

Figure 2: Program Flow Chart

The user is asked to enter the free stream velocity, the distance from the leading edge of the plate to the point of interest, and the suction/injection velocity at that station. The user is also given the option of using fluid properties of air at sea level standard temperature and pressure, or defining different fluid properties.

As indicated by the flow chart in Figure 2, after getting the user input and assigning boundary conditions, the program enters a loop in which the system of first order differential equations discussed earlier are integrated using 4th order Runge Kutta calculations. If the solution does not converge, the initial guess for $f''(0)$ is altered, and the differential equations are again integrated using Runge Kutta calculations. This iterative process continues until the solution converges or until the maximum number of allowed iterations is exceeded.

When the solution converges, the flow field values are calculated, and the user has three output options available: (1) The results can be viewed graphically on the screen, (2) The results can be viewed in a tabular format on the screen, and (3) The data can be printed to a file for later use. The user also has the options of rerunning the program with new values, or exiting the program.

The user can view plots of the Blasius functions and its derivatives, the horizontal and vertical velocity distributions, shear stress distribution, and temperature distribution. Examples of these plots are given in Figures 3(a,b,c) for the Blasius function and Figures 4(a,b,c,d,e) for the horizontal and vertical velocity profiles, the shear stress distribution, and the temperature distributions, respectively. These examples were obtained from the results for air at 20 degrees C.

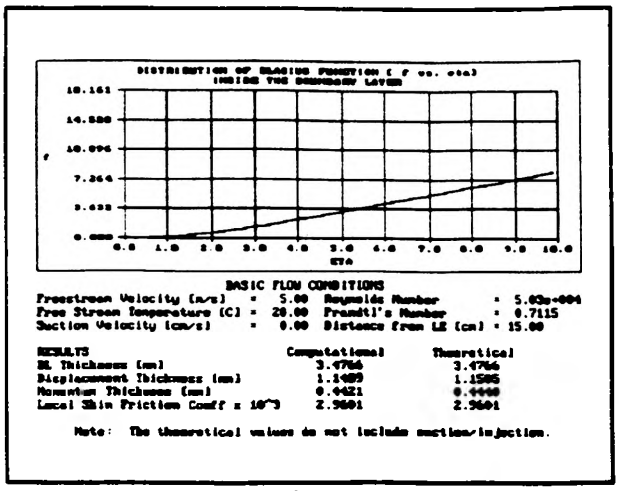

Figure 3(a): f vs η

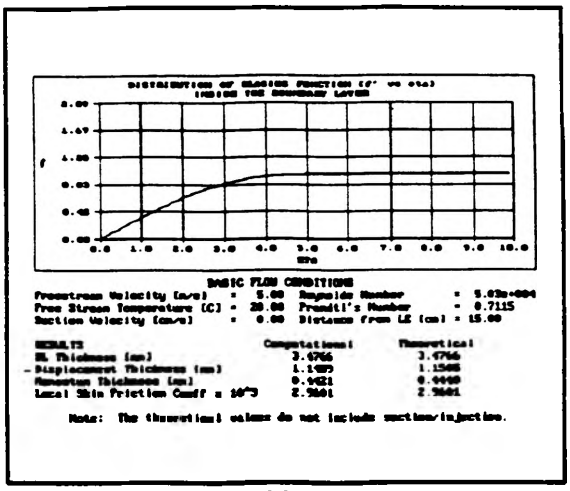

Figure 4(b): f' vs η

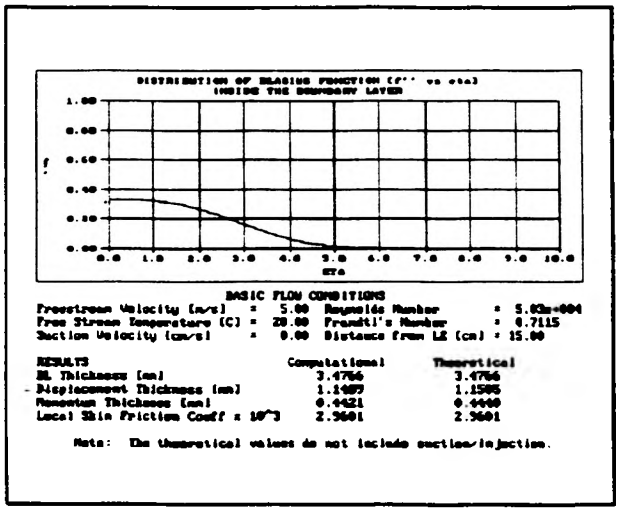

Figure 5(c): f" vs η

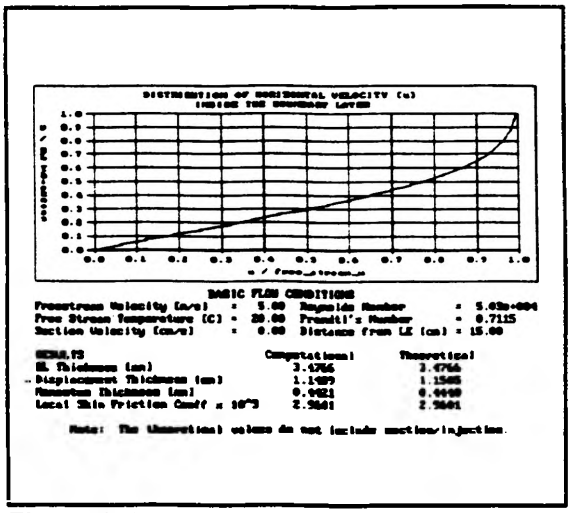

Figure 4(a): y/δ vs u/U_∞

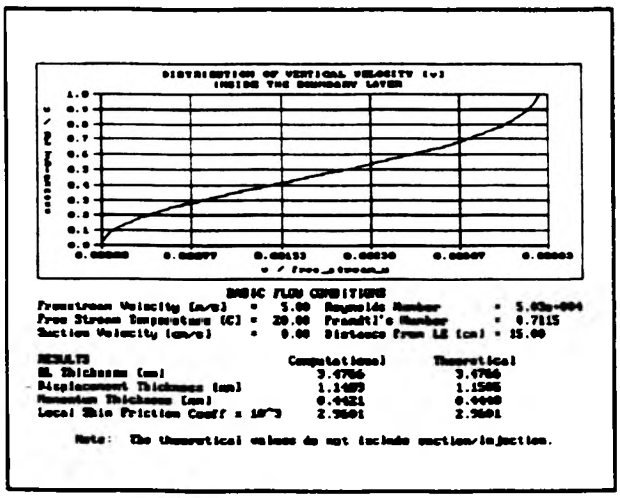

Figure 5(b): y/δ vs v/U_∞

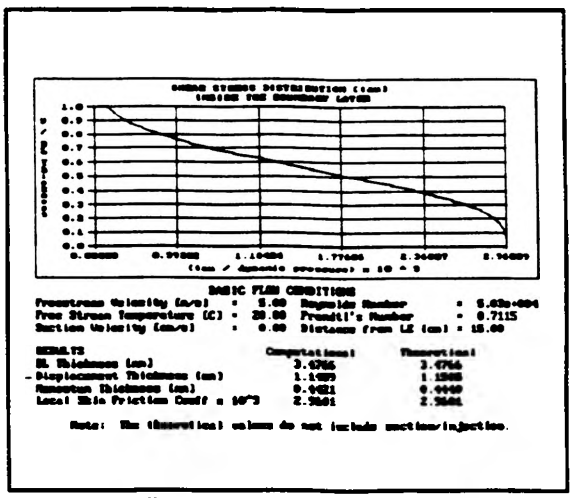

Figure 6(c): y/δ vs τ/q_∞

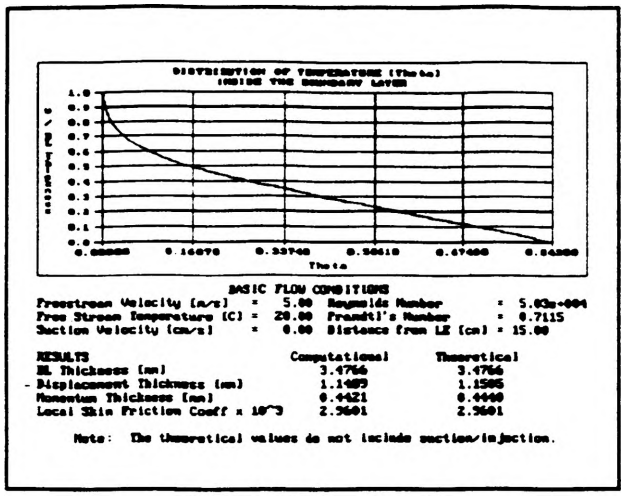

Figure 7(d): y/δ vs θ

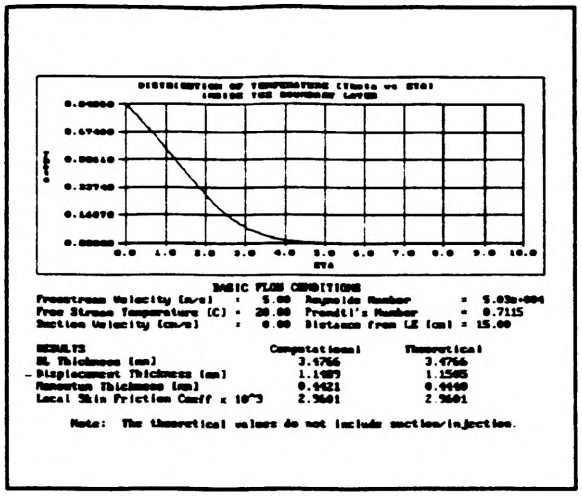

Figure 8(e): θ vs η

When viewing the tabular results on the screen, the first screen to appear will be similar to the example shown in Figure 5. As can be seen from the figure, the upper portion of the screen is used to echo

```
          Flat Plate Boundary Layer Program--Output
      Numerical experiments on flat plate boundary layer flow:

                        ECHO OF USER INPUT

  Distance from the plate leading edge [cm]                    :   15.0000
  Freestream velocity [m/sec]                                  :    5.0000
  Suction(-) or injection(+) velocity at this station [cm/s]   :    0.0000
  Freestream temperature [ degrees C ]                         :   20.0000
  Specific heat with constant pressure [ J/(kg-deg C) ]        : 1004.0000
  Kinematic viscosity [m^2/s]                                  : 1.4900e-005
  Absolute viscosity [ kg/(m-s) ]                              : 1.8000e-005
  Fluid density [kg/m^3]                                       :    1.2100
  Thermal conductivity [ W/(m - deg C) ]                       :    0.0254

                        BASIC FLOW CONDITIONS
  Freestream Velocity [m/s]    =   5.00   Reynolds Number       =  5.03e+004
  Free Stream Temperature [C]  =  20.00   Prandtl's Number      =  0.7115
  Suction Velocity [cm/s]      =   0.00   Distance from LE [cm] = 15.00

  RESULTS                              Computational      Theoretical
  BL Thickness [mm]                       3.4766             3.4766
  Displacement Thickness [mm]             1.1489             1.1505
  Momentum Thickness [mm]                 0.4421             0.4440
  Local Skin Friction Coeff x 10^3        2.9601             2.9601

       Note:  The theoretical values do not include suction/injection.
```

Figure 9: The Initial Output Screen

the user input parameters, followed by a basic flow conditions section which repeats some of the values from the user input and presents the calculated values of Reynold's number and Prandtl's number. The final section of the screen is used for the main results of the program. The computational and theoretical values are tabulated for the boundary layer thickness, the displacement thickness, the momentum thickness, and the local skin friction coefficient. Then, on the following screens, the resulting data for the Blasius function and its derivatives, followed by the dimensionless values of the horizontal and vertical velocities, shear stress, and temperatures, are shown in a tabular format.

PROGRAM RESULTS

A closer look at the example results presented in the previous sections will allow a relatively easy comparison of the computational results to the theoretical results. For air at 20 degrees C, with a freestream

velocity of 5 m/s, and at a station 15 cm from the leading edge of a flat plate, and no suction or injection, the computer program predicts the boundary layer thickness, δ, to be 3.4766 mm, which is exactly the same as that predicted by theory. The program predicted values slightly lower than the theoretical values for the displacement thickness and the momentum thickness. Theory predicted $\delta^* = 1.1505$ mm and $\theta m = 0.4440$ mm. The values predicted by the program were $\delta^* = 1.1489$ mm and $\theta m = 0.4421$ mm, with percent errors of -0.139% and -0.428% respectively. The local skin friction coefficient was found to be 2.9601 x 10^{-3} from both the program and from theory. Other cases studied have the same general trends as those shown here. However, the greatest advantage of this code is not in its ability to predict the theoretical values for flat plate boundary layer flows without suction or injection.

The program can be easily be used as an effective tool for studying flat plate boundary layer flow including the effects of suction and injection. The results from three cases, one without suction or injection, one with suction, and one with injection, will be investigated by looking at the output screens generated by the program. Due to space limitations, only two plots for each case will be included in the discussion. The plots in the first column will be y/δ vs u/U_∞. The plots in the second column will be y/δ vs τ/q_∞, where q_∞ is the free stream dynamic pressure, $\rho U_\infty/2$.

The suction/injection velocity was 0, -5, and +5 cm/s for each case, respectively. For all three cases: $U_\infty = 15$ m/s, x = 10 cm, and the fluid is air at sea level standard temperature and pressure. Figures 6, 7, and 8 represent the three cases respectively.

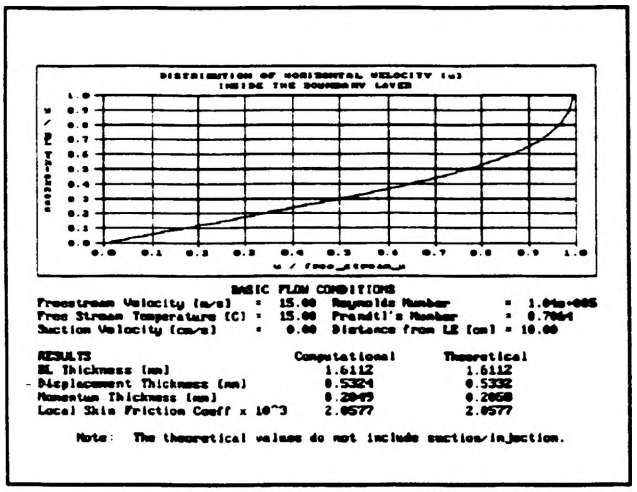

Figure 7(a): y/δ vs u/U_∞

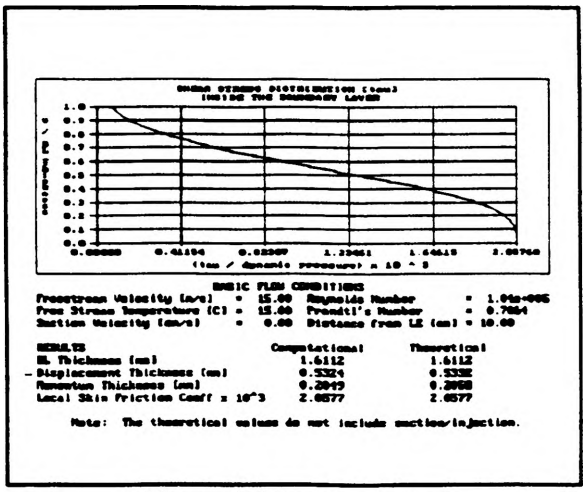

Figure 7(b): y/δ vs τ/q_∞

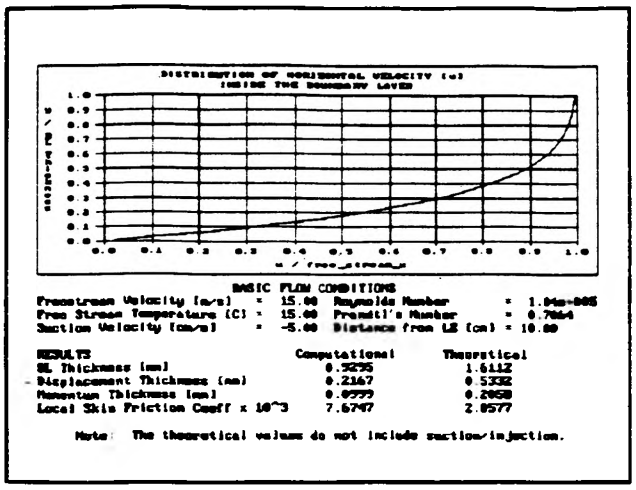

Figure 8(a): With Suction

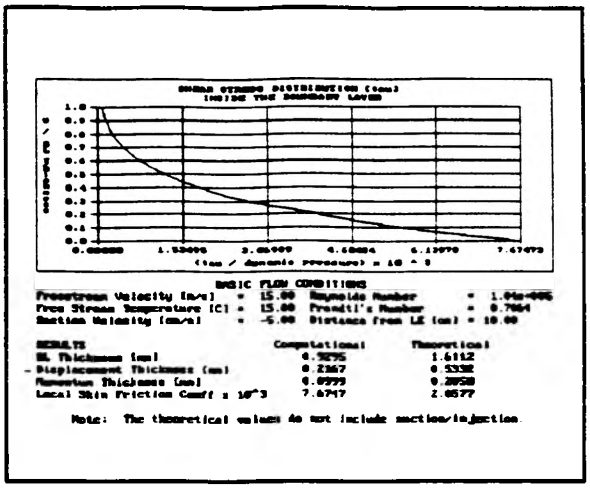

Figure 8(b): With Suction

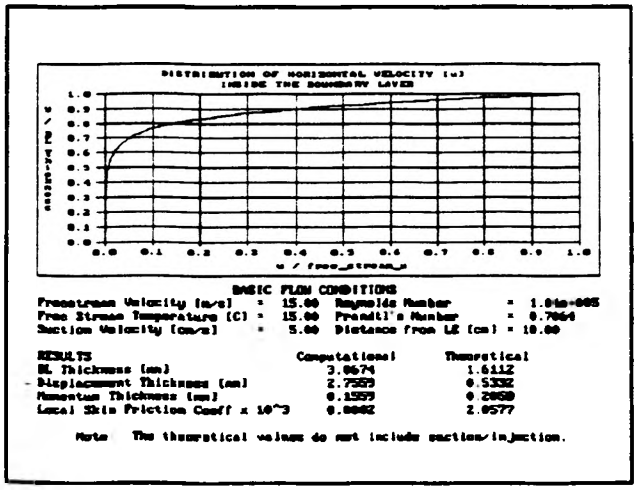

Figure 9(a): With Injection

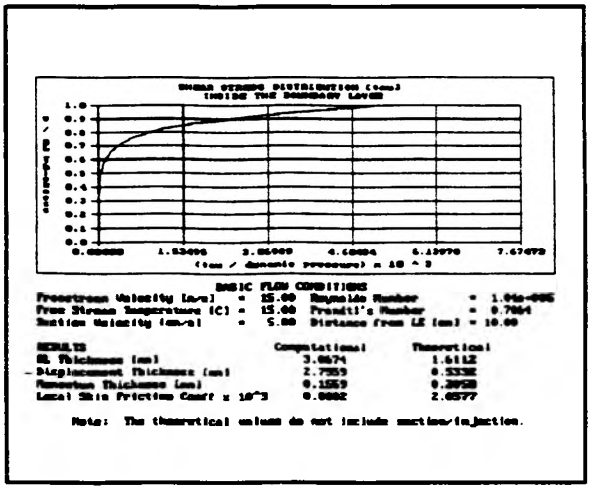

Figure 9(b): With Injection

In all cases shown, the theoretical results given below each plot will be the same because the theoretical results do not contain suction or injection. This allows for easy checking to see the change from an initial no suction or injection flow. It is also easy to see the change in any of the plotted parameters, u/U_∞, v/U_∞, τ/q_∞, or θ by merely inspecting the plots of two different runs. Thus, the effects of suction and injection can be investigated relatively easily by using this program.

EXPERIMENTAL SETUP

The experimental setup developed can be used along with the computer code to enhance the learning process. The experimental work will provide hands on experience, while the computer code can be used for quick results and lengthy parameter studies. A sketch of the experimental setup is shown in Figure 9.

The experimental setup consists of a wind tunnel test section, a hollow aluminum plate, and a suction/injection unit. The wind tunnel test section is 4 feet long with an 18" by 18" cross section.The plate is constructed of 3 individual aluminum plates fastened together to form a suction chamber. Tapped holes on the bottom of the plate allow for the hook up of a suction/injection unit. Suction or injection into the flow is achieved through holes in the top plate. The suction/injection unit purchased has a maximum pump

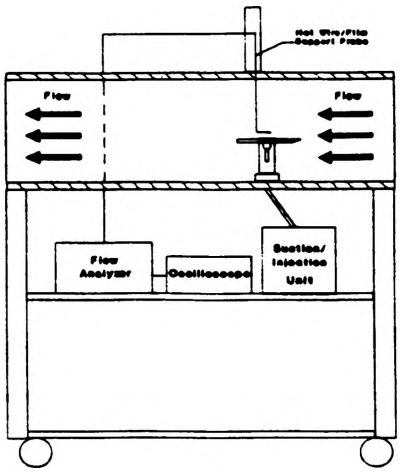

Figure 10: Wind Tunnel Test Section

revolutions per minute of around 600 rpm, allows for multiple pump heads (up to 4 total) to be used. The maximum flow rate attainable is 2280 ml/min.

CONCLUDING REMARKS

The interactive computer program developed will hopefully prove to be a useful tool and learning aide. The computational results match almost exactly with theoretical predictions for flat plate boundary layer flow. In addition, the computer code can be used to investigate the effects of suction and injection on the flow field values.

The experimental setup described is still being tested. However, it is hoped that the combination of the interactive computer code and the wind tunnel experiments will heighten the interest and improve learning about boundary layers. Many possibilities exist for expanding the capabilities of the computer code such as:

* Include the effects of heat transfer
* Add the capability to handle turbulent flow
* Allow for non-zero angles of attack

ACKNOWLEDGEMENTS

The author wishes to acknowledge the contributions of Dr. Fathi Finaish who suggested the article, helped to formulate the problem, and assisted in editing the article.

REFERENCES

1. Chow, Chuen-Yen and Kuethe, Arnold M. *Foundations of Aerodynamics*. New York: John Wiley & Sons, 1986.

2. Anderson, John D, Jr. *Fundamentals of Aerodynamics*.

3. DeVaney, et al. "Boundary Layer Control Experiment." AE 282 Lab Design Report, University of Missouri-Rolla, 1990.

A PARAMETRIC INVESTIGATION ON AEROELASTIC BEHAVIOR OF AN AIRFOIL IN STEADY FLOW

EDWARD J. FELTROP
Department of Mechanical and Aerospace Engineering
and Engineering Mechanics
University of Missouri-Rolla

ABSTRACT

A parametric study is performed to investigate the influence of a number of aerodynamic, inertia and damping parameters upon the dynamic response of an elastically-supported rigid wing in steady flow. The dimensionless equations governing the vertical and angular motion of this wing are solved by an interactive computer program which facilitates the systematic analysis of the effects of changes in these parameters upon the dynamic response of the system. This investigation demonstrates the coupling of the vertical and angular motion of the wing, and illustrates the strong influence of damping, spring stiffness, initial spring deflection, and initial angular velocity upon the behavior of the system.

INTRODUCTION

Birds and insects fly by means of a complex combination of pitching and plunging of their wings. Similarly, fish propel themselves through water by pitching their tails. In both cases complex motions are performed to develop controlled, separated flow structures which produce propulsive aerodynamic or hydrodynamic forces[1][2]. In recent years numerous researchers have studied various unsteady separated flow configurations, most of which have been generated by either pitching or plunging an airfoil subjected to steady flow[3][4][5]. The generation and control of such flow structures could have a dramatic impact on the performance of aerodynamic and hydrodynamic vehicles.

This paper attempts to expand upon the previous research by studying the dynamic response of an elastically-supported airfoil in steady flow. An understanding of the system's aeroelastic behavior is an essential precursor to the practical investigation of the vortex structures which it generates. A computer program utilizing a simplified numerical model was developed to estimate the rotational and translational motion of this airfoil. Through this program it is possible to investigate the influence of damping, spring stiffness, initial spring deflection, and initial angular velocity upon the aeroelastic behavior of the system.

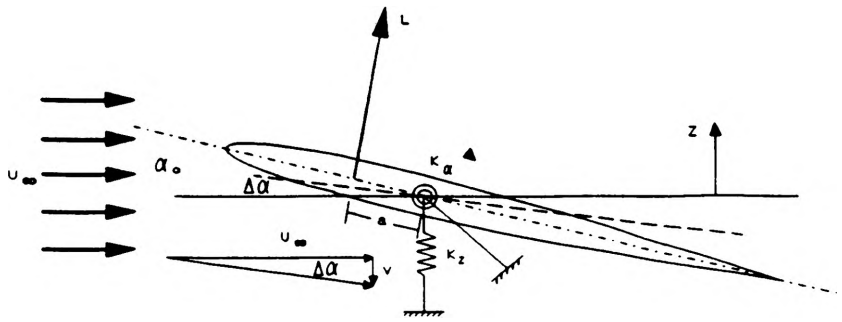

Fig. 1 An Airfoil mounted on translational and rotational supports

GOVERNING EQUATIONS

The wing model depicted in Figure (1) is supported by translational and rotational springs with stiffness coefficients of k_z and k_α, respectively, and is subjected to a flow velocity of U_∞. Damping for the translational and rotational motion is expressed in terms of the damping coefficients c_z and c_α. The length a denotes the rearward distance from the aerodynamic center to the axis of rotation of the model. In static conditions, the model rests at an angle of α_o from the horizontal, with its rotational axis located at a height of z = 0.0. With the assumption that the wing model is a flat plate airfoil with infinite aspect ratio, the equations governing the vertical and angular motions of this model may be written as[6]

$$m\, d^2z/dt^2 = -c_z dz/dt - k_z z + 1/2\rho c_l S U_\infty \sqrt{U_\infty^2 + (dz/dt)^2} \qquad (1)$$

$$I\, d^2\alpha/dt^2 = -c_\alpha d\alpha/dt - k_\alpha \alpha + 1/2 a\rho c_l S U_\infty \sqrt{U_\infty^2 + (dz/dt)^2} \qquad (2)$$

Since the parameter space of this problem is large, the analysis is simplified by combining the numerous parameters into groups of flow, geometry, time, stiffness, damping, and inertia parameters. With this, the second order governing equations (1) and (2) may be rewritten as four first order ordinary differential equations. This will lead to the following dimensionless equations:

$$DZ/DT = V \qquad (3)$$

$$DV/DT = -(2\pi)^2 Z - C_Z V + A c_l U\sqrt{U^2+V^2} \qquad (4)$$

$$Da/DT = \Omega \tag{5}$$

$$D\Omega/DT = -(2\pi)K_{\alpha}\alpha - C_{\alpha}\Omega + AMC_1 U\sqrt{U^2+V^2} \tag{6}$$

where A and M are the dimensionless aerodynamics and inertia parameters, C_z and C_α are the translational and rotational damping parameters and K_α is the rotational stiffness parameter. Equations (3) through (6) were numerically integrated using the fourth order Runge-Kutta Method. For a complete derivation of these equations, the reader is referred to the study by Finaish, et al[6].

NUMERICAL RESULTS AND DISCUSSION

This section presents examples of the influence of several physical parameters upon the general behavior of the system. Although the treatment of these motions is essentially qualitative, the following default parameters clarify the relative scope of this investigation:

U_∞	=	8.00 m/s
k_z	=	1000.00 N/m
k_α	=	2.00 N m/rad
c_z	=	1.00 N/m s
c_α	=	0.05 N m/rad s
a	=	0.05 m
S	=	0.07 m^2
m	=	2.00 kg
I	=	0.30 N m

α_o is given in each of the following charts as *STATIC ALPHA*.

Influence of Initially Deflected Translational Springs:

Figure 2 depicts the response of the system to an initial translational spring deflection of z_o/c, with a neutral angle of attack of zero. The rapid decay of translational amplitude shown in Figure 2 (a), (c), and (e) is the result of both the high translational spring stiffness and the differences in frequency and phase of the vertical and angular motions. The only apparent effect of the vertical motion upon the rotational motion is the small degree of instability shown on the curves in Figures 2 (b), (d), and (e) during the first two seconds of the time interval. These small perturbations are also the product of the phase and frequency differences between the translational and rotational motion of the model.

Influence of Initial Angular Velocity:

The initial angular velocities considered in Figure 3 produce large rotational deflections, but the translational deflections are relatively moderate. The vertical and rotational oscillations have

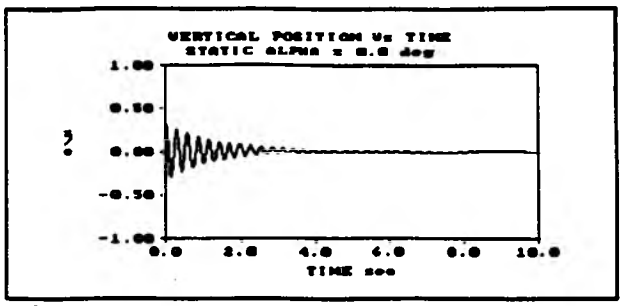

Fig. 2 (a) $z_0/c = 0.328$

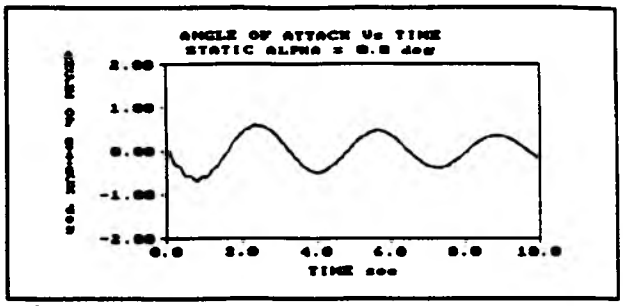

Fig. 2 (b) $z_0/c = 0.328$

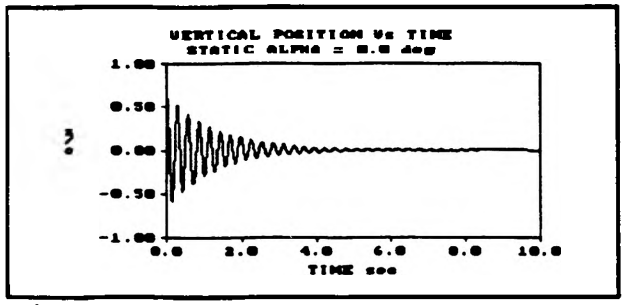

Fig. 2 (c) $z_0/c = 0.656$

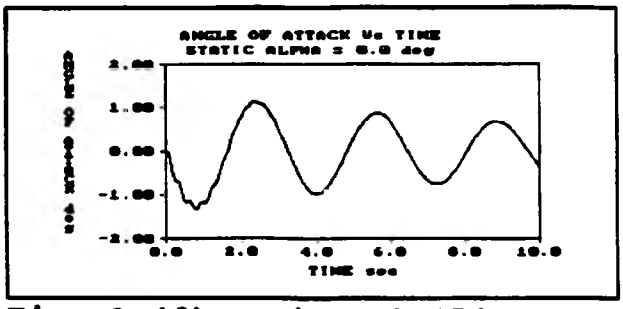

Fig. 2 (d) $z_0/c = 0.656$

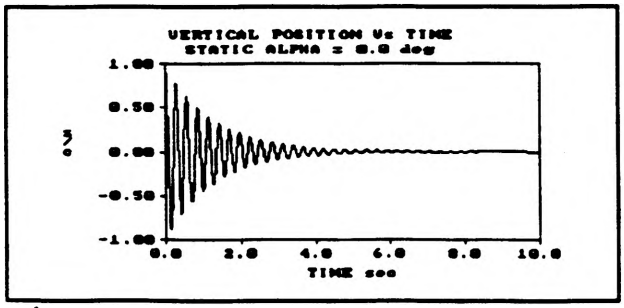

Fig. 2 (e) $z_0/c = 0.984$

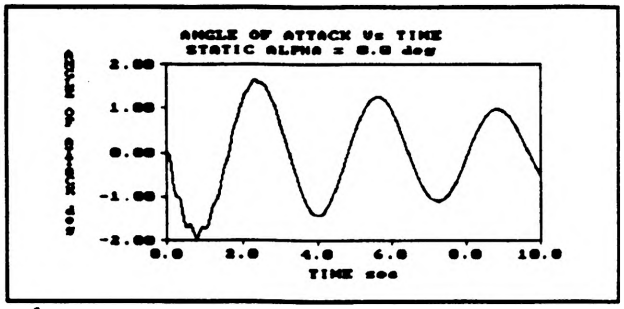

Fig. 2 (f) $z_0/c = 0.984$

the same frequency, and are essentially in phase, although the change in effective angle of attack due to the model's vertical velocity may result in a small shift in the phase of the angular oscillations. This phase shift and the assumption that the model stalls at an angle of 12° are the main sources of the secondary vibrations shown in Figure 3 (a), (c), and (e). The decay of vertical and rotational amplitude are due primarily to vertical and angular damping.

Influence of Angular Damping:

Figure 4 illustrates the manner in which an increase in the angular damping causes the amplitudes of the vertical and rotational oscillations to decay, along with a very gradual decay in vibrational frequency. Vertical and rotational oscillations

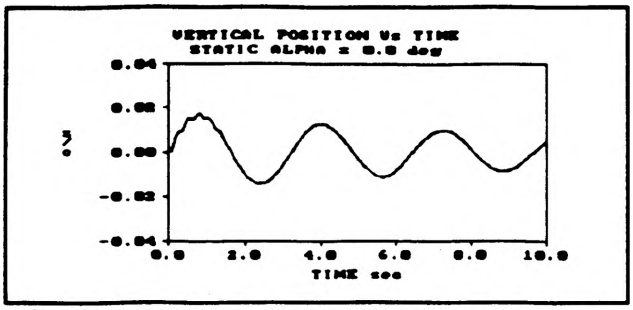

Fig. 3 (a) ω_0 = 0.3 rad/sec

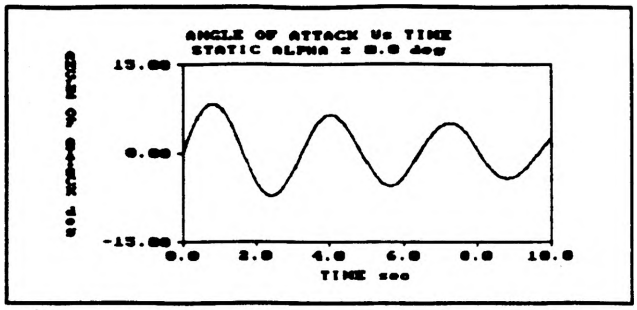

Fig. 3 (b) ω_0 = 0.3 rad/sec

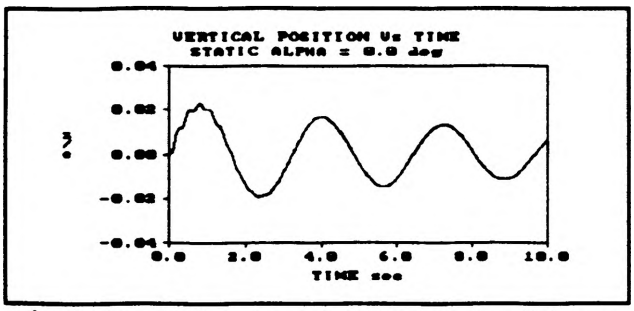

Fig. 3 (c) ω_0 = 0.4 rad/sec

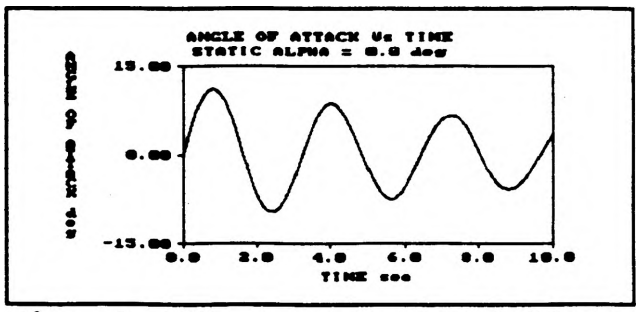

Fig. 3 (d) ω_0 = 0.4 rad/sec

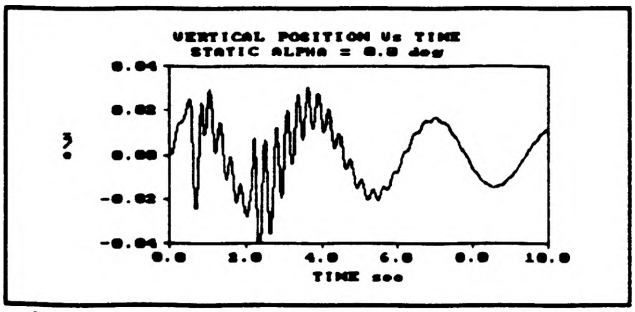

Fig. 3 (e) ω_0 = 0.5 rad/sec

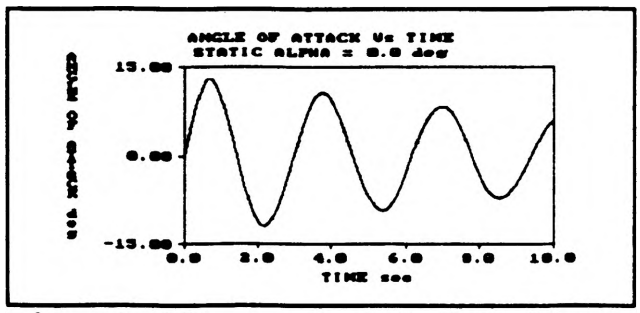

Fig. 3 (f) ω_0 = 0.5 rad/sec

maintain the same frequency and phase throughout this sequence. The early translational instability is related to the relatively high translational spring stiffness.

An Example of Regulated Harmonic Motion:

The time sequence shown in Figure 5 (a) and (b) depicts a wing which begins to flutter as its angle of attack converges upon the wing's stall angle of 12° (after approximately 12 seconds). In Figure 5 (c) and (d), the tendency to flutter is forestalled by increasing the rotational spring stiffness. As a result, the vibrations in Figure 5 (c) begin to show a periodic beat structure. In addition, the frequency of rotational oscillations in Figure 5 (d) is reduced slightly.

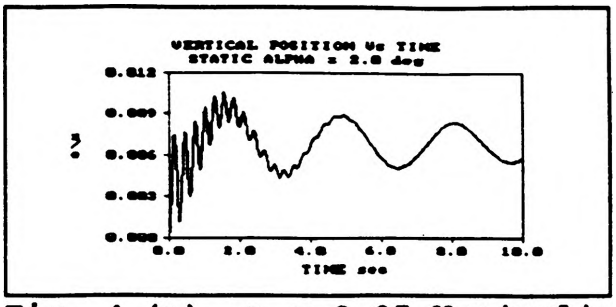

Fig. 4 (a) c_α = 0.05 N m/rad/s

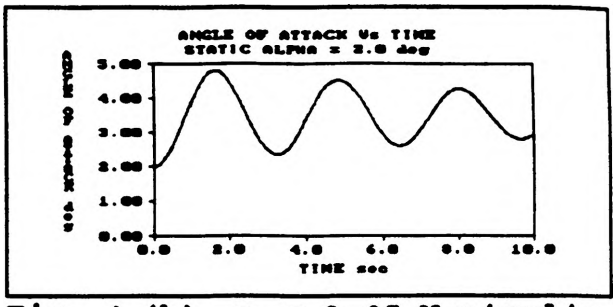

Fig. 4 (b) c_α = 0.05 N m/rad/s

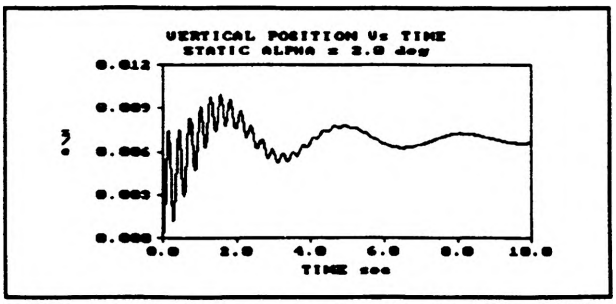

Fig. 4 (c) c_α = 0.15 N m/rad/s

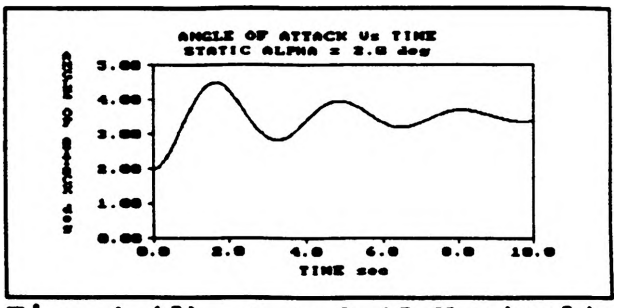

Fig. 4 (d) c_α = 0.15 N m/rad/s

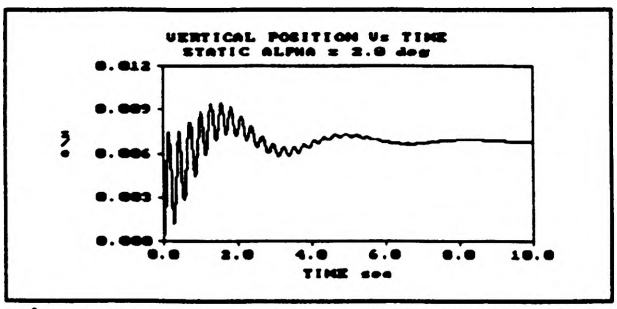

Fig. 4 (e) c_α = 0.25 N m/rad/s

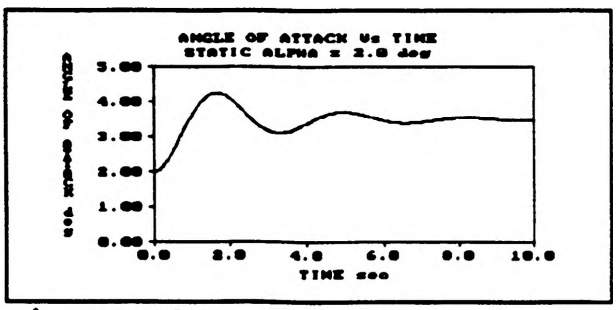

Fig. 4 (f) c_α = 0.25 N m/rad/s

For Figure 5 (e) and (f) both the rotational spring stiffness and the rotational damping have been increased, producing a very clear beat in the translational oscillations. The frequency of the angular oscillations in Figure 5 (f) has been further reduced to that of the translational oscillations in Figure 5 (e), and both are in phase. Consequently, the maximum vertical and angular deflections occur simultaneously. It is interesting to note that the number of vertical oscillations per rotational oscillation in Figure 5 (e) and (f) corresponds to those of Figure 2 (e) and (f).

Although the calculated dynamic response visualized in Figure 5 (e) and (f) is dependent upon the assumption that the wing's lift varies linearly, and that it stalls abruptly at α = 12.0°, the predicted response agrees qualitatively with results obtained with the experimental setup described by Finaish, et al[1].

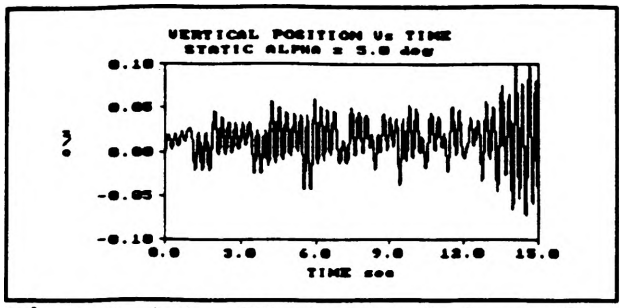

Fig. 5 (a) Flutter at t = 15 s

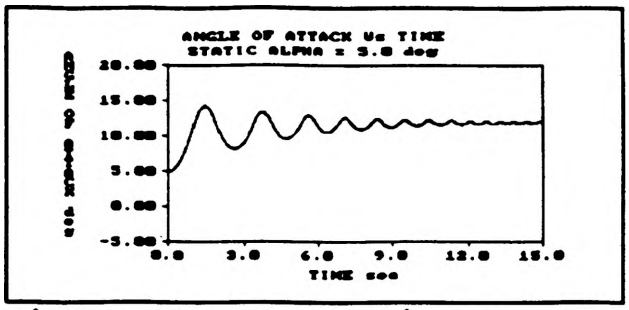

Fig. 5 (b) Converging α

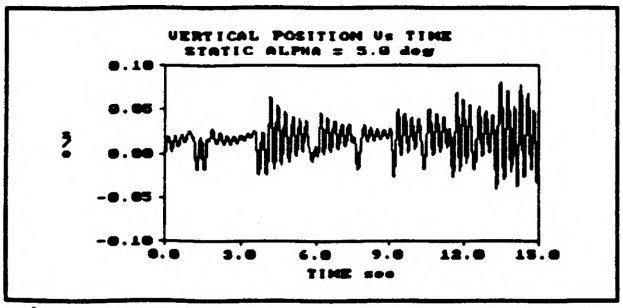

Fig. 5 (c) Emergence of beats

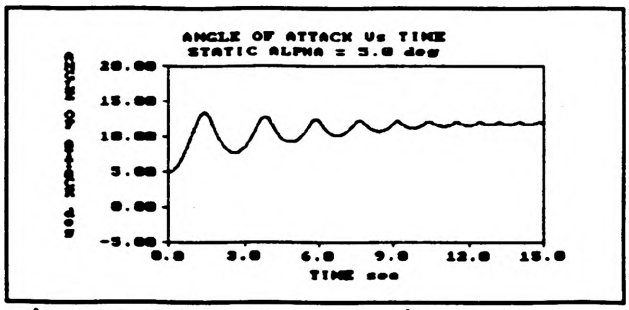

Fig. 5 (d) Converging α

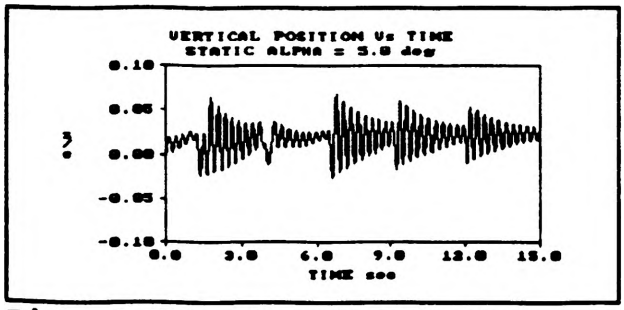

Fig. 5 (e) Regular Beats

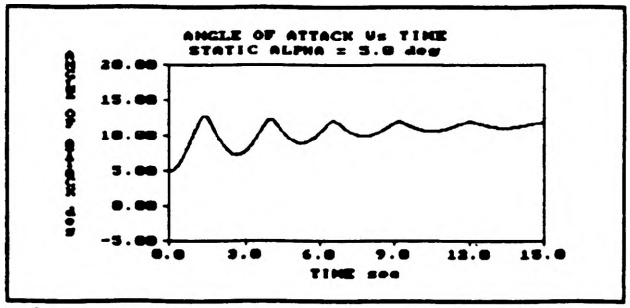

Fig. 5 (f) Converging α

Influence of Translational and Rotational Spring Stiffness

The primary results of an increase in translational spring stiffness are a small increase in vertical oscillation frequency, smaller vertical deflections, and a reduction in the time needed for the vertical oscillations to diminish. Angular motion is essentially unaffected by the increasing translational spring stiffness, with the exception of a very slight damping due to differing phase and frequency between the vertical and angular oscillations.

In the case of the rotational spring stiffness, an increase in stiffness leads to an increase in the frequency of angular deflections, a decrease in their magnitudes, a decrease in the difference between the neutral angle α_0 and the angle of attack to

which the system eventually converges, and a decrease in the magnitude of the translational deflections. In addition, the instability shown in Figure 4 (a), (c), and (e) is present in the early translational oscillations.

CONCLUDING REMARKS

In general, the effects of the wing model's translational motion have only a small impact upon its angular motion, with the exception of the case in which the model is released from an initially deflected position of the translational springs. On the other hand, the model's angular motion is quite important in determining the dynamic response of the system. This is due to the fact that the forcing functions of the equations governing this system are the aerodynamic lift and pitching moment, which are strongly dependent upon the model's angle of attack. Subsequently, the parameters to which the system is particularly sensitive are those which regulate its rotational motion, such as angular damping and spring stiffness. In addition, numerous parameters affecting the manner in which the model's motion originates have a strong initial impact upon the system's behavior.

The results obtained with the formulation utilized in this paper are somewhat limited by the simplified numerical model used to calculate the wing's lift. For this reason, most of the parametric studies were restricted to small angles of attack. However, the aeroelastic response depicted in Figure 5 (e) and (f) shows reasonable qualitative agreement with experimental results.

In order to understand how propulsive unsteady separated flow structures may be generated and controlled, it is first necessary to develop an understanding of a given system's dynamic response. The interactive program developed for this investigation provides a convenient and inexpensive means of rapidly approximating the effects of a parameter change upon the aeroelastic behavior of the system. This then allows the wind tunnel investigations to be limited to configurations which are predicted to generate the desired dynamic response. A wide variety of response modes are obtainable through the appropriate selection of physical parameters regulating the system's behavior. The next logical step in the refinement of this investigation would involve the development of a numerical routine to calculate the nonlinear unsteady lift. By removing the assumption of linearly-varying lift, the numerical results should become even more indicative of actual system response, making this program a valuable tool in the investigation of aeroelastic behavior.

NOMENCLATURE

A = Dimensionless aerodynamic parameter = $\rho l_c S/(2m)$

a = Rearward distance from aerodynamic center to elastic axis

α = Wing angle of attack

α_o = Static (neutral) angle of attack

c = Wing chord length

C_z = Dimensionless translational damping constant = $c_z/(m/t_c)$

C_α = Dimensionless rotational damping constant = $c_\alpha/(I/t_c)$

C_l = Wing lift coefficient

c_z = Translational damping constant

c_α = Rotational damping constant

$d\alpha$ = Induced angle of attack

d/dt = First derivative with respect to time

d^2/dt^2 = Second derivative with respect to time

D/DT = Dimensionless first derivative with respect to time

g = Gravitational acceleration

I = Wing mass moment of inertia

K_z = Dimensionless translational stiffness constant = $k_z/(m/t_c^2)$

K_α = Dimensionless rotational stiffness constant = $k_\alpha/(ml_c^2/t_c^2)$

k_z = Translational stiffness constant

k_α = Rotational stiffness constant

l_c = Characteristic length = mg/k_z

M = Dimensionless inertia parameter = mal_c/I

m = Wing mass

ρ = Air density

S = Wing area

t = Time

t_c = Characteristic time = $2\pi\sqrt{m/k_z}$

T = Dimensionless time = t/t_c

U_∞ = Free stream velocity

U = Dimensionless velocity in x-direction = U_∞/w_c

V = Dimensionless velocity in z-direction = v/w_c

v = Vertical flow (wing) velocity = dz/dt

w_c = Characteristic velocity = g / $2\pi\sqrt{m/k_z}$

Z = Dimensionless vertical position

z = Vertical position

z_o = Initial vertical position with displaced spring

ω = Angular velocity of wing = $d\alpha/dt$

ω_o = Initial angular velocity wing = $d\alpha/dt$

Ω = Dimensionless wing angular velocity = $\omega/(1/t_c)$

ACKNOWLEDGMENTS

This study was supported by the "Opportunities for Undergraduate Research Experience" program at the University of Missouri-Rolla. The guidance, support, and advice of Dr. F. Finaish during the course of this project are deeply appreciated.

REFERENCES

[1] Finaish, F., and Feltrop, E., "An Experimental System to Investigate Subsonic Aeroelastic Behavior of Lifting Surfaces", AIAA 30th Aerospace Sciences Meeting and Exhibit, January, 1992, Reno, Nevada.

[2] Lighthill, J., Aerodynamic Aspects of Animal Flight. In: Swimming and Flying in Nature. (eds. Wu, Y; Brokaw, C.; Brennan, C.), Vol. II, pp. 423-491. New York; Plenum Press.

[3] Freymuth, P., "The Vortex Patterns of Dynamic Separation: A Parametric and Comparative Study., Prog. Aerospace Sci., Vol. 22, pp. 161, 1985.

[4] Gad-el-Hak, M., "Unsteady Separation on Lifting Surfaces", Appl. Mech. Rev., Vol. 40, No. 4, 1987.

[5] Freymuth, Pl, "Propulsive Vortical Signature of Plunging and Pitching Airfoils", AIAA Journal, Vol. 26, pp. 881, 1988.

[6] Finaish, F., and Johnston, A., "Dynamic Response of an Elastically-Supported Wing Model in Steady Flow: Numerical Experiment for Undergraduates", to appear in International Journal of Mechanical Engineering Education

Development of an Experimental System for Steady and Unsteady Aerodynamic Testing

Jacopo Frigerio

Department of Mechanical and Aerospace Engineering
and Engineering Mechanics
University of Missouri-Rolla
Rolla, Missouri 65401

Abstract

This paper discusses the design and development of a new experimental system designed to produce a variety of steady and unsteady flows. Accelerating, decelerating and oscillating flows over lifting surfaces are primary examples of the unsteady flow configurations that can be generated. Also this report presents details of preliminary tests performed to determine the performance of this system. These include quantitative and qualitative testing on two-dimensional and three-dimensional flow configurations.

1. Introduction

Wind tunnel testing is an essential tool in aerospace engineering as well as in performing basic scientific research. The recent developments in Computational Fluid Dynamics (CFD) and the use of this technology in engineering and in research require a verification source and a reference guide to economize computational efforts. The wind tunnel is a primary tool that can provide such needs. Most wind tunnels are designed as open-circuit or closed circuit tunnels where the freestream flows are steady [1]. Very often the modification of these tunnels to produce unsteady flow proves to be difficult and costly.

Recenty, a research program on unsteady flow testing was initiated at the Depertment of Mechanical and Aerospace Engineering and Engineering Mechanics at UMR. There a new subsonic wind tunnel has been designed and developed. The tunnel has been designed primarily to conduct basic research on unsteady flow configurations were the flow and/or test model motion is time dependant. The main focus of these research efforts is exploring possibilities of utilizing unsteady flow effects that could have significant consequences on enhancing aerodynamic performance of lifting bodies [2].

This paper presents part of these efforts and focuses on the development of a new experimental system designed for conducting aerodynamic testing on unsteady flows.

2. System Design and Capabilities

To develop an experimental system that can be utilized for steady and unsteady flow testing, a test section and movable cart were designed and constructed. One of the design requirements of

the system was to incorporate it into an 18" X 18" subsonic wind tunnel. The cart was designed so it could be maneuvered inside the tunnel test section to generate accelerating and decelerating motions.

As shown in Figure 1, the test section is supported on a support frame which was constructed from wood and consists of four levels. The two lower levels were built into the system for use as shelves to accommodate data acquisition equipment and needed hardware.

An 18" X 18" X 96" plexiglass test section was constructed and mounted on the support frame. Clear 1/2" plexiglass was selected to allow for flow visualization experiments to be performed from both sides and the top. Each plexiglass wall is supported by 2" angle aluminum, which was screwed to the glass and bolted to the deck of the main frame.

To generate unsteady flows, a movable cart and test model carrier were also developed. As can be seen in Figure 1 (b), the cart rides on rails that span the length of the support frame on the third level. The cart was constructed from 1/2" aluminum and travels outside of the test section in between the third level and the deck. Two aluminum angles were mounted to the platform to be used as rails which guide the cart.

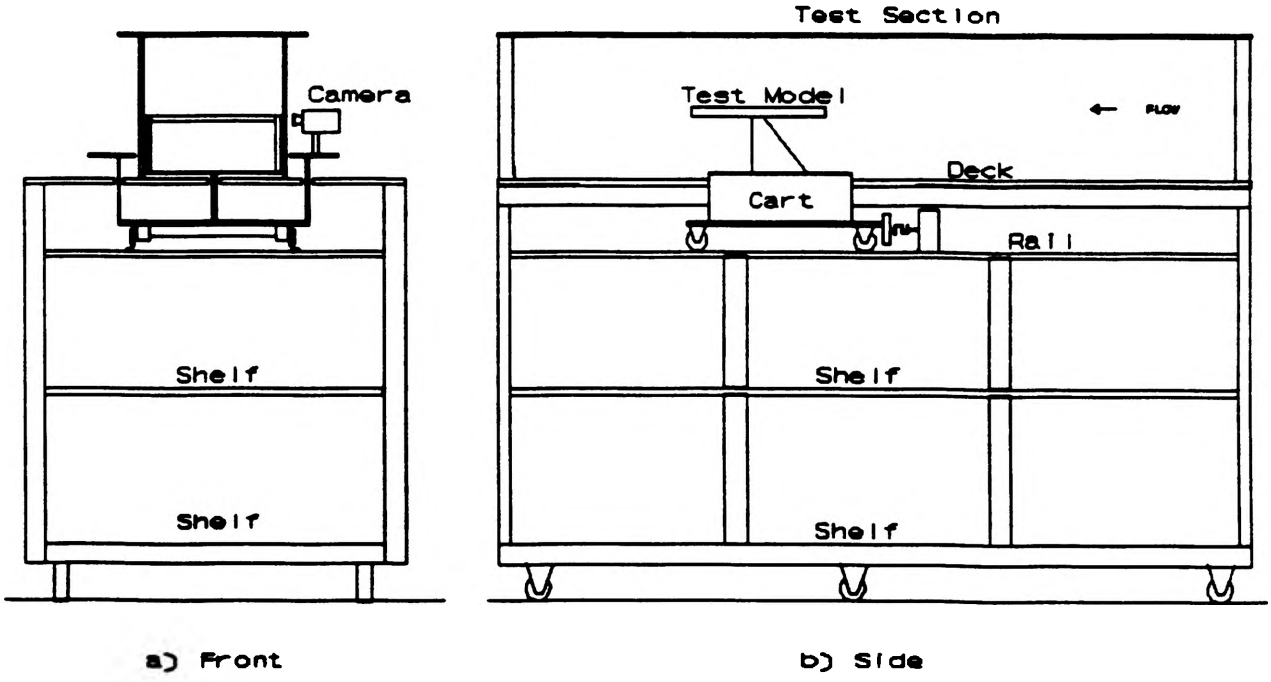

Figure 1 Front and Side Views of the Experimental System

A slot was left in the deck so that a test model carrier could be installed and maneuvered inside the test section. For steady flow testing, this slot is covered with linoleum to prevent air leakage into the test section. The carrier is constructed of 1/4" aluminum and mounted on a vertical plate on the cart. In addition to the test model carrier, the cart also carries two aluminum plates where a movie camera can be mounted outside the test section for flow visualization purposes. The various components of the cart-carrier set up are shown in Figure 2.

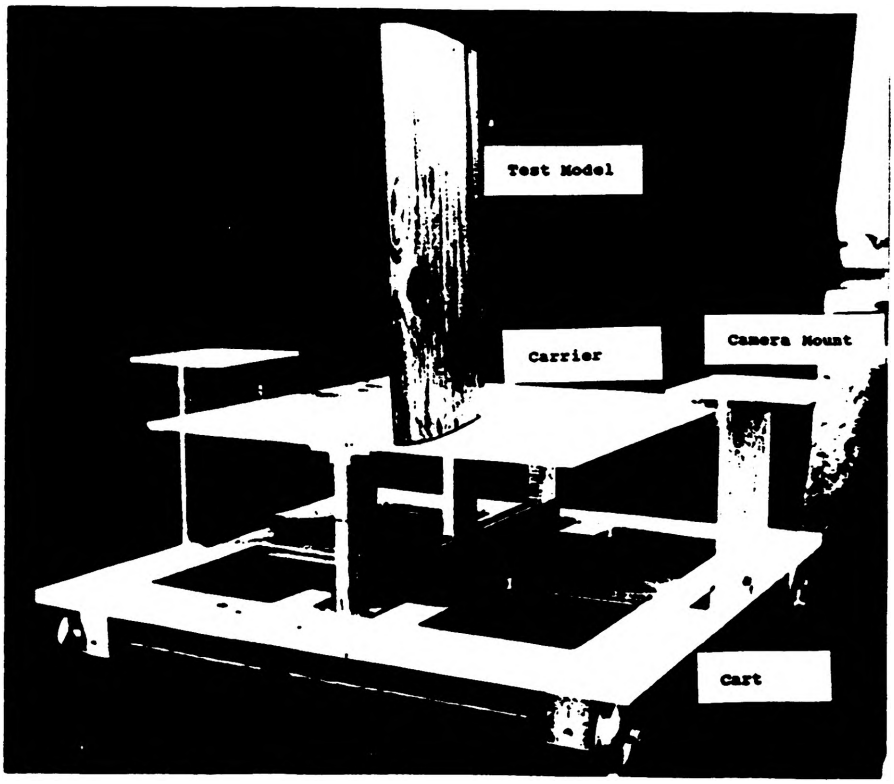

Figure 2 Photograph of the Cart-Carrier Set Up

For quantitative testing such as drag measurements, a load cell can be mounted between a fixed block and the cart. This load

cell is rated for 100 lbs and accurate to 1/100 lbs.

As mentioned earlier, the experimental system can be employed to generate a wide range of accelerating and decelerating motions. A spring set up is employed to produce rapid accelerations. In this arrangement the cart is attached to a set of springs at a distance of 4 ft from the mounting block by nylon string, shown in Figure 3. The distance allows for enough space in front of the cart to produce the required acceleration.

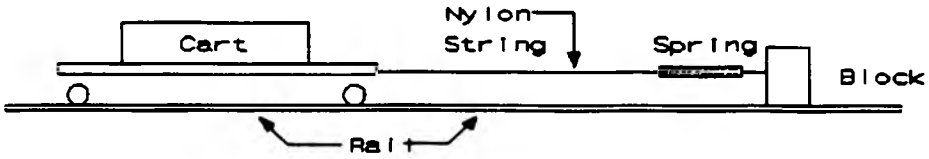

Figure 3 Experimental Set Up for Cart Acceleration

As can be seen in Figure 4, by using a large spring stiffness such as k1, a nearly impulsive motion can be generated. With decreasing spring stiffness, such as k2 or k3, and/or decreasing the initial spring deflection a wide range of acceleration rates can be obtained.

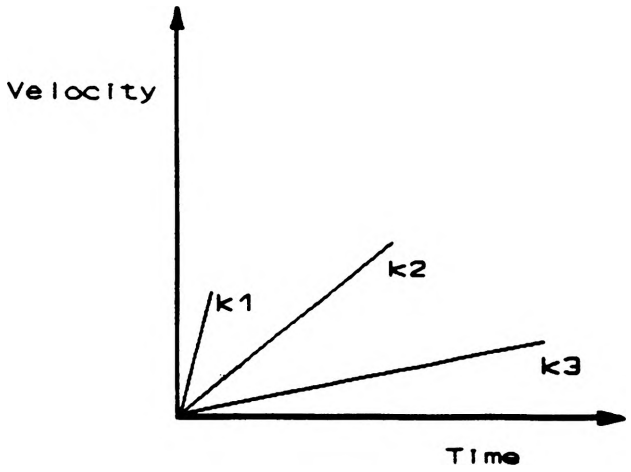

Figure 4 Examples of Acceleration Rates Using Springs

Once construction of the experimental system was completed, the flow quality within the tunnel was investigated. This was done by performing measurements of the velocity profile. Four stations were selected, starting at distance of 13" from the front of the test section and equally spaced through a distance of 68". The velocity profiles were measured at each station with a pitot-static tube traversed through a small opening in the top of the test section. The data from these measurements resulted in a reasonable representation of the boundary layer thickness over the tunnel ceiling. The boundary layer thickness was plotted vs.

the distance along the test section at a velocity of 44 ft/sec. As can be seen in Figure 5, the boundary layer thickness increased from 1 1/4" at a distance of 9", to 2 1/2" at a distance of 90". This is a reasonable value for this test section at this velocity.

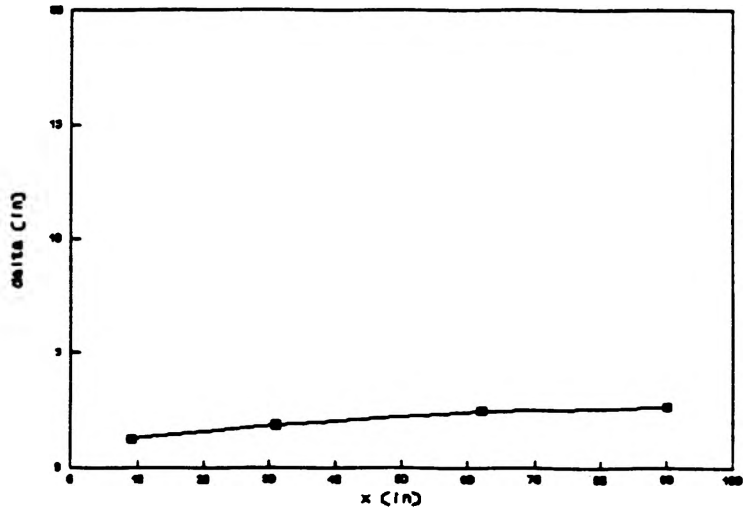

Figure 5 Boundary Layer Thickness Along Tunnel Ceiling at 44 ft/sec

3. Experiments in Steady Flow: A Quantitative Example

In addition to the unsteady testing capabilities, the system can be employed for steady flow testing. As an example, the set up shown in Figure 6 is utilized to measure the drag on a test model. The model was mounted on the carrier vertically with an angle of attack adjustment mechanism. The drag on the wing was sensed by a load cell and transmitted to a load cell digital meter. The test section flow velocity was measured by a pitot-static tube and a pressure transducer.

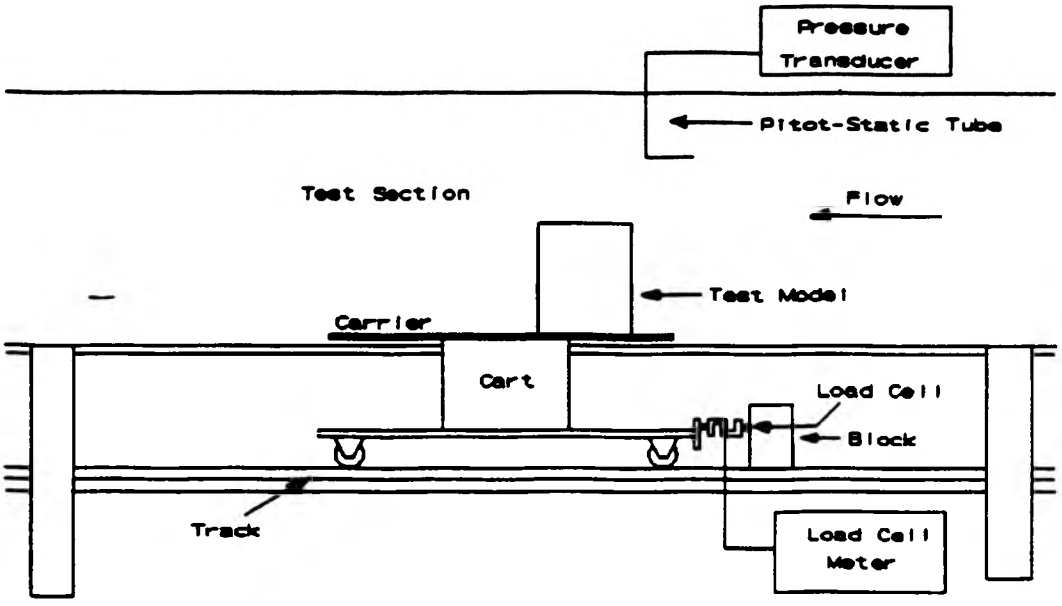

Figure 6 Drag Measurement Set Up

Figure 7 shows an example of the wing drag coefficient as a function of angle of attack. A 6" X 17" flat plate model was subjected to a flow velocity of 40.8 ft/sec. As expected the graph shows a sharp increase in drag coefficient at an angle of attack of 20 degrees.

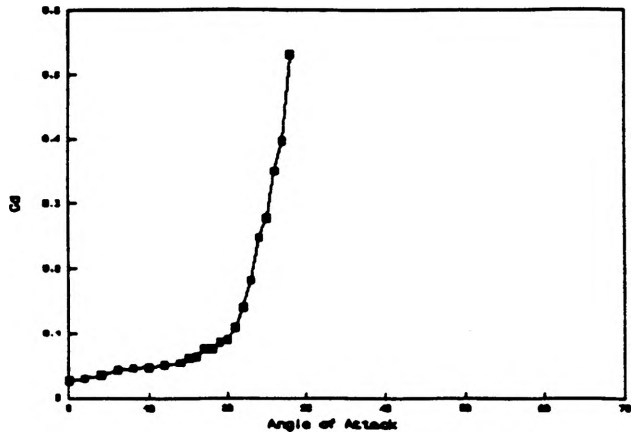

Figure 7 Example of Drag Coefficient vs. Angle of Attack for a Flat Plate Wing Model

4. Experiments in Unsteady Flow: A Qualitative Example

To present an example of the unsteady flow testing capabilities of the system, a few flow visualization experiments on accelerating flow starting from rest were performed. The vertical model was again mounted on the cart with the spring system described above. Prior to releasing the cart, liquid titanium tetrachloride ($TiCl_4$) was injected directly to the surface of the wing [3]. This liquid reacts with the moisture in the airflow and produces dense white smoke, which was photographed by a Bolex movie camara at a rate of 64 frames per second.

Figure 8 is an illustration which shows a typical vortex development near the wing tip. This development consists of a wing tip vortex and a leading edge vortex which converge at the upper right corner of the test model.

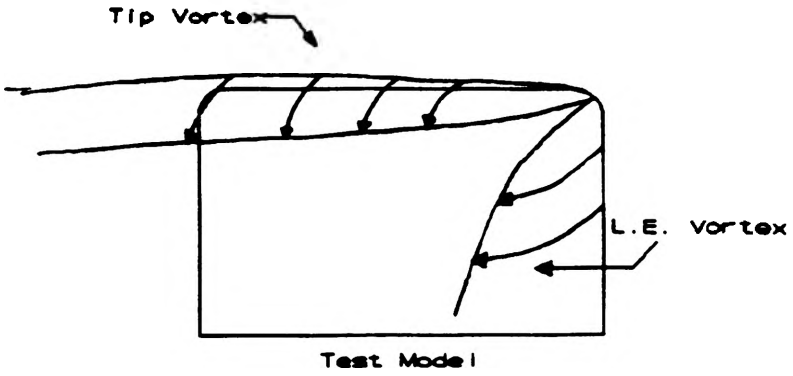

Figure 8 A Sketch of a Typical Wing Tip Vortex System

Figure 9 shows an example of a photographic sequence that visualizes the wing tip and leading edge vorticies over a flat plate model with an initial acceleration rate of 10 ft/sec^2. In this sequence, the flow is from right to left and the time increment is 1/32 seconds.

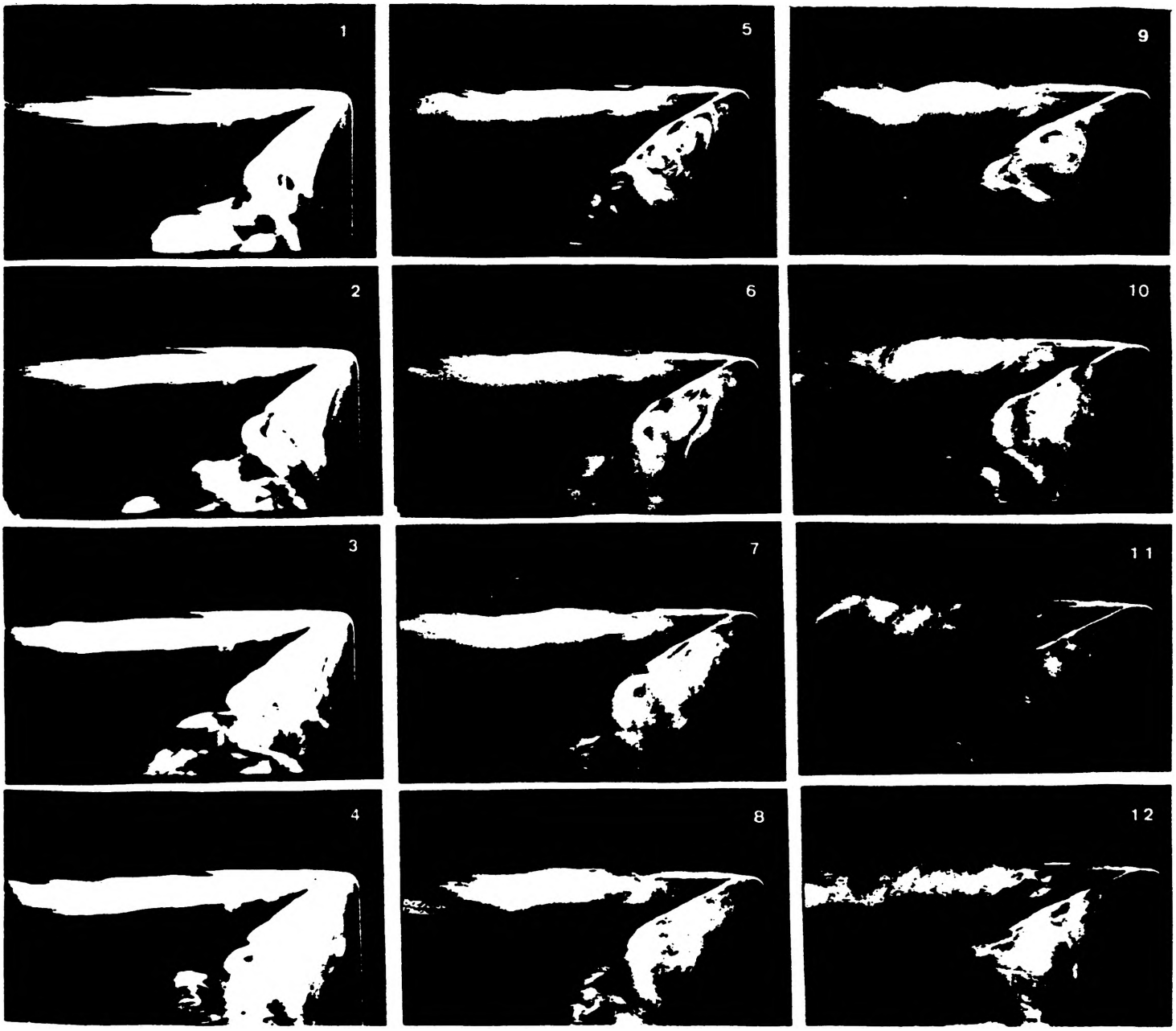

Figure 9 Photographic Sequence Visualizes Vortex Developments Near a Rectangular Wing Tip in Accelerating Flow

The initial acceleration for this experiment was determined by photographing a scale behind the model. The velocity of the cart can be determined by finding the distance the cart traveled per frame and knowing the frame rate of the movie camara. The acceleration can then be found by finding the differences in velocity for a series of frames. Figure 10 is a sample of a series for an initial acceleration of 10 ft/sec^2.

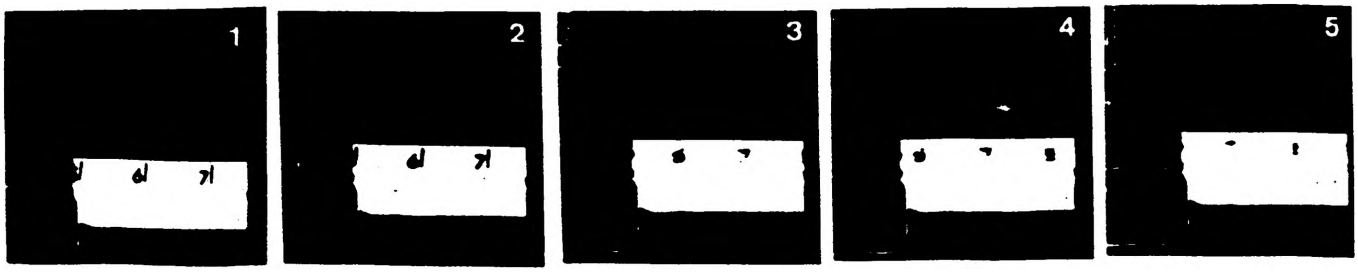

Figure 10 Photographic Sequence of a Scale Used for Determining Acceleration Rates

5. Concluding Remarks

This paper reports the development of an exprimental system incorporated into an 18" X 18" subsonic wind tunnel to add unsteady flow testing capabilities. This system can be employed for aerodynamic testing on accelerating flow, decelerating flow, and oscillating flow over lifting surfaces. This system is being utilized for quantitative and qualitative experiments on a variety of unsteady configurations. The main focus of these experiments is exploration into the possibilities of utilizing unsteady flow effects that could have significant consequences on enhancing aerodynamic performance of lifting surfaces.

Acknowledgements

The technical assistance by Mr. B. Hribar in fabricating several portions of the experimental system is appriciated. This project was supported in part by the OURE program at the University of Missouri-Rolla and by NASA-Missouri consortium. Dr. F. Finaish was the project advisor.

References

1) Pope, A. and Rea, Wm. ; Low Speed Wind Tunnel Testing; John Wiley & Sons; New York; 1984
2) Finaish, F., On vortex Structures and Processes Over Bluff Bodies In Impulsive Flow; Exp. in Fluids, 11, pp. 262-267, 1991
3) Finaish, F., Freymuth, P., and Bank, W., The Application Range of Titanium Tetrachloride for Flow Visualization in Aerodynamic Testing; Fourth International Symposium on Flow Visualization, Paris, France, August 26-29, 1986. Flow Visualization IV pp.197-202

STIMULATION OF AMORPHIZING REACTIONS IN CO-SI MULTI-LAYERS

Jeanne K. Jackson
Metallurgical Engineering

Abstract

Co-Si multi-layer specimens do not normally amorphize. To possibly stimulate amorphization, Ti was added by evaporation and the specimens were annealed at 300 and 400 degrees Celsius. The results showed that amorphization occurred at 400 degrees Celsius in the presence of Ti, but did not occur at 300 degrees Celsius. Further research would be necessary to conclude whether the amorphization was stimulated by the addition of Ti or the temperature increase.

INTRODUCTION

With the age of electronics upon us, there is a growing need for research into the area of multi-layer thin films. As dimensions of the film decrease, interfacial area begins to increase and volume decreases. Along with this increase in interfacial area is an increase in property dependency on the interfacial region.

Nano-scale multi-layers in crystalline and amorphous form are being studied for their electronic, magnetic, mechanical, and structural properties. Schwarz and Johnson discovered [1] that crystalline multi-layers on a nanometric scale would become amorphous upon annealing. However, the solid state amorphization reaction (SSAR) does not readily occur in all elemental pairs. Schwarz and Johnson hypothesized that there must be a large negative heat of mixing (approximately 10 kcal/mol). This aids in formation of an amorphous alloy with a lower free energy than that of the two-phase elemental structure or crystalline compound. It is also important that the size difference between the two elements must be large (molar volume ratio < .7). Large size difference correlate with fast diffusion and disordered interfaces. Negative heats of mixing promote intermixing and disordered interfaces provide nucleation sites for amorphization.

If more elemental pairs could be made to amorphize, the range of available materials could be broadened. Addition of a third element may enhance amorphization by increasing the negative heat of mixing or the disorder between interfaces. Another factor of amorphization is the thickness effect [2]. Intermixing may occur in systems that do not normally amorphize when the layers are below a critical thickness. Experiments on Mo-Ni superlattice samples determined that good crystallization perpendicular to the layers was present when layers were thicker than 8.3 angstroms. When the thickness was less than 8.3 angstroms, long-range crystalline order no longer existed.

A study of the effects of a third element diffused between layered heterostructures of two different thicknesses was performed. Co and Si were chosen as the pure, crystalline layers. The Co-Si system is a practical choice because of its similarities to the Ni-Si system, which does amorphize.

Therefore, small thermodynamic or kinetic changes brought on by the addition of a third element might prompt a SSAR to occur in the Co-Si system. Examination of candidate third elements suggested that the kinetic factor could be more easily altered than the thermodynamic factor and that Ti was most likely to produce the needed change. Results reported during the study of GaAs-Co thin films [3] support the concept that the kinetic effect is more influential in determining amorphization.

PROCEDURE

Preparing Co-Si Specimens:

Nine Co-Si samples were prepared in advance using a double-gun deposition apparatus at the National Nanofabrication Facility at Cornell University. Samples were prepared by sputtering twelve pairs of Co-Si layers onto a (100) Si substrate. Four samples had layers 100 angstroms thick and five had 50-angstrom layers. The thickness of the layers was estimated from the sputtering rate and the deposition time. An attempt to measure layer thicknesses using the scanning electron microscope (SEM) was unsuccessful, so the transmission electron microscope (TEM) was used to examine the specimen.

Initially, efforts were made to use a technique developed at the East Fishkill Laboratory of IBM for preparing TEM specimens [4]; but there was insufficient time during this project to develop the necessary skill. As an alternative, an acute corner formed by cleaving the specimen perpendicular to the deposited layers was examined. To view the edge of the specimen, an estimated 90 degree mount was hand-made. Accurate measurements could not be made because there was no way of assuring that the electron beam was parallel to the layer interfaces. Figure 1 is a micrograph of a sample having 100 angstroms per layer nominally. The layers can be counted; but because the beam orientation was not known precisely, no accurate measurement of thickness could be made.

The final attempt to check the accuracy of the layers was made by using grazing-incidence asymmetric Bragg diffraction. Dr. Mark Shumsky at the UMR-MRC was able to detect Co and Si presence, but was not able to actually measure layer thicknesses due to time constraints. Figure 2 and 3 show the Co and Si peaks for a specimen with 100 angstrom layers and no Ti deposition or annealing. The largest peak, which is present at 2-theta angle of 69.161 degrees, is Si (100). The cobalt peak is at 65.89 degrees. If the layers had been perfectly pure and thick, the peaks would have been very narrow. By the thickness of the peaks, it is apparent that the layers are either not perfectly pure or are too thin. These peaks can still be used, however, for qualitatively sensing the effectiveness of third elements in stimulating amorphization in multi-layer specimens of fixed thickness.

Ti Deposition:

Ti was deposited on one edge and diffused between the interfaces. The effect of the Ti addition can be examined by depositing the Ti on only one edge and annealing the specimen long enough to diffuse the Ti partially through the specimen. This technique was used anticipating that the effect of varying amounts of Ti in a single sample would be revealed. Figure 4 shows the specimen orientation and expected diffusion direction.

To prevent deposition on any other surface, a clamp was devised as depicted in figure 5. The spiral clamp held the sample on edge and a Si wafer

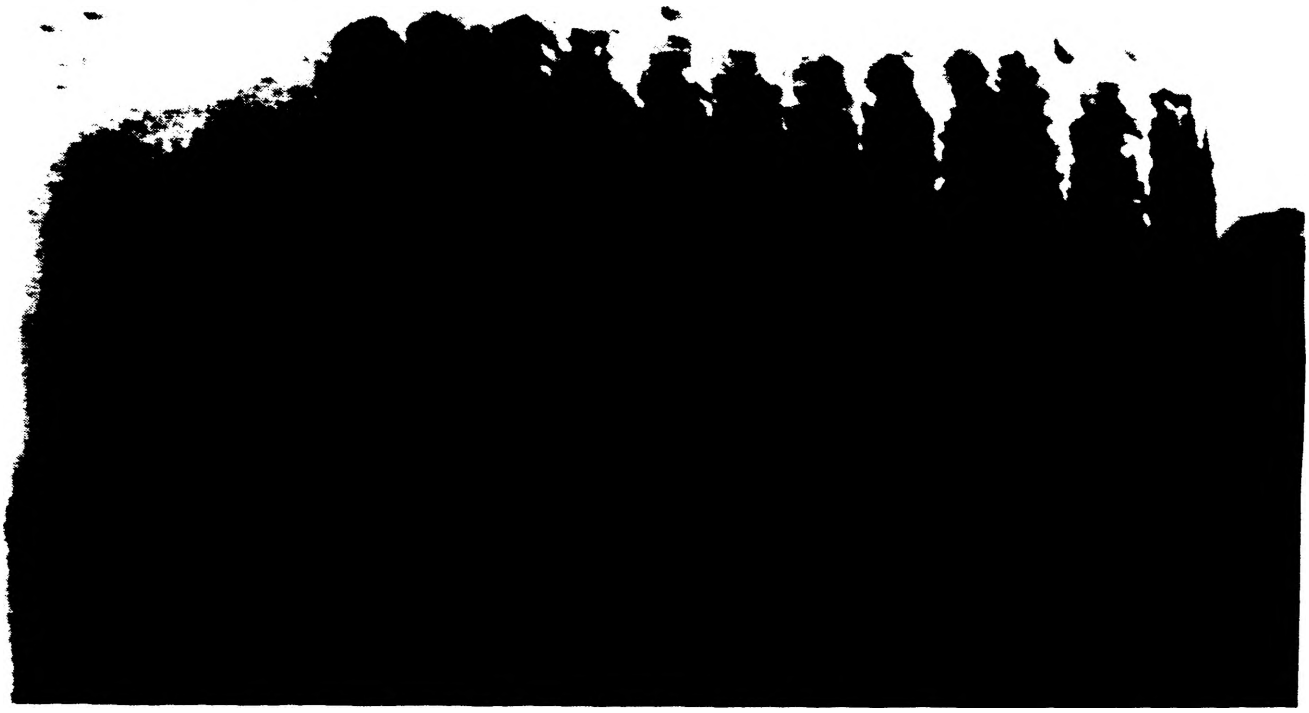

Figure 1 Co-Si multi-layers
(Note: angle of specimen prevents
accurate quantitative measurements)

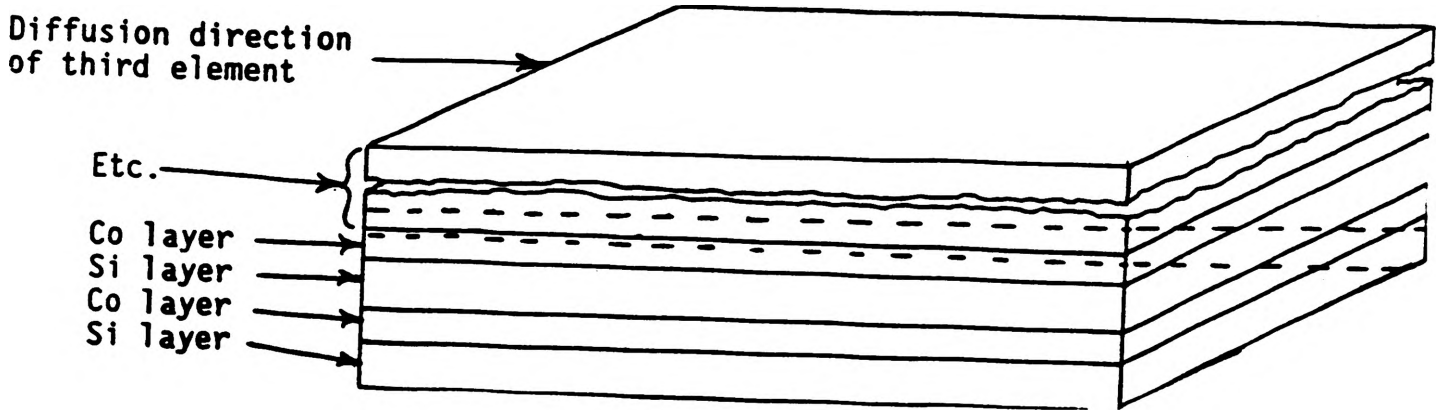

Figure 2 Co-Si multi-layers
with the diffusion direction of Ti

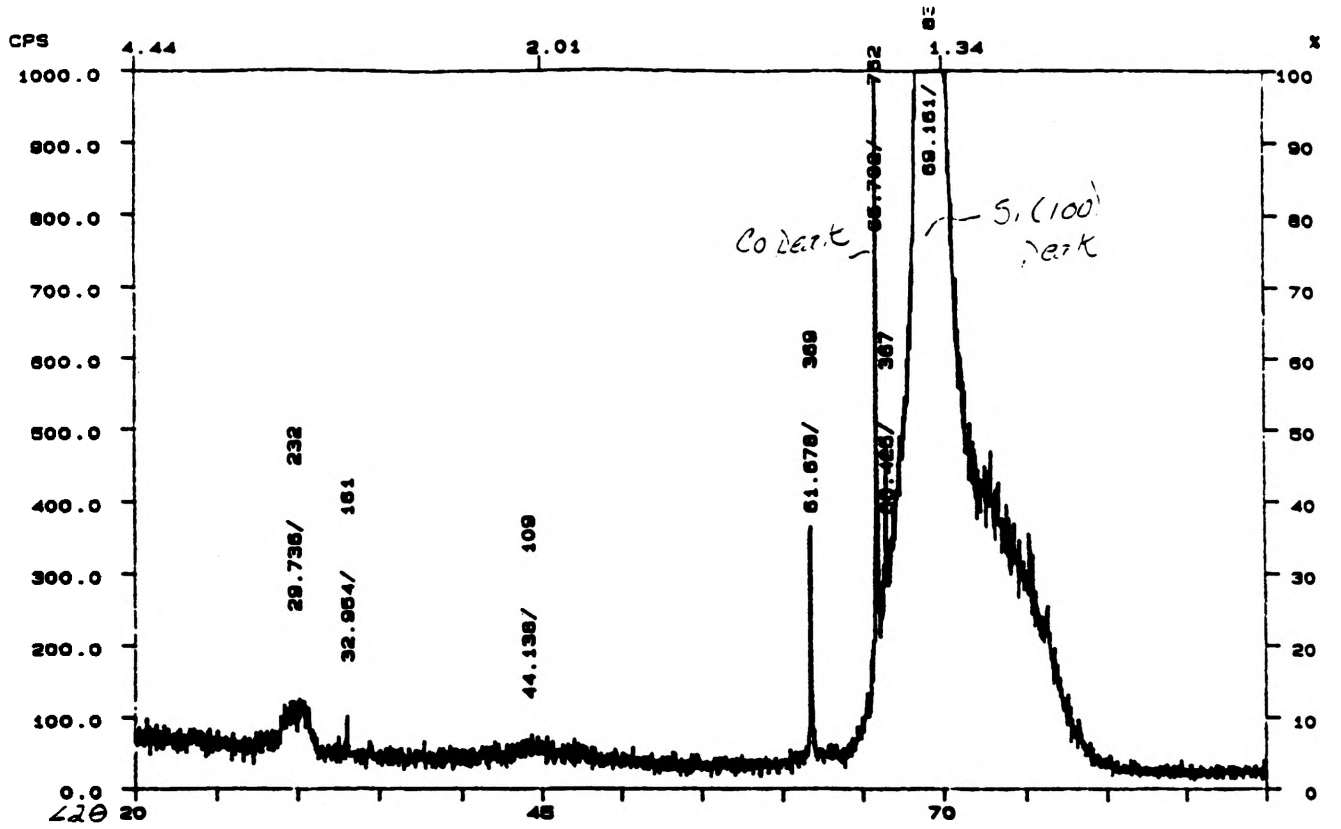

Figure 3 Co-Si sample
(Note Si (100) peak at 69.2
and Co peak at 65.8 degrees)

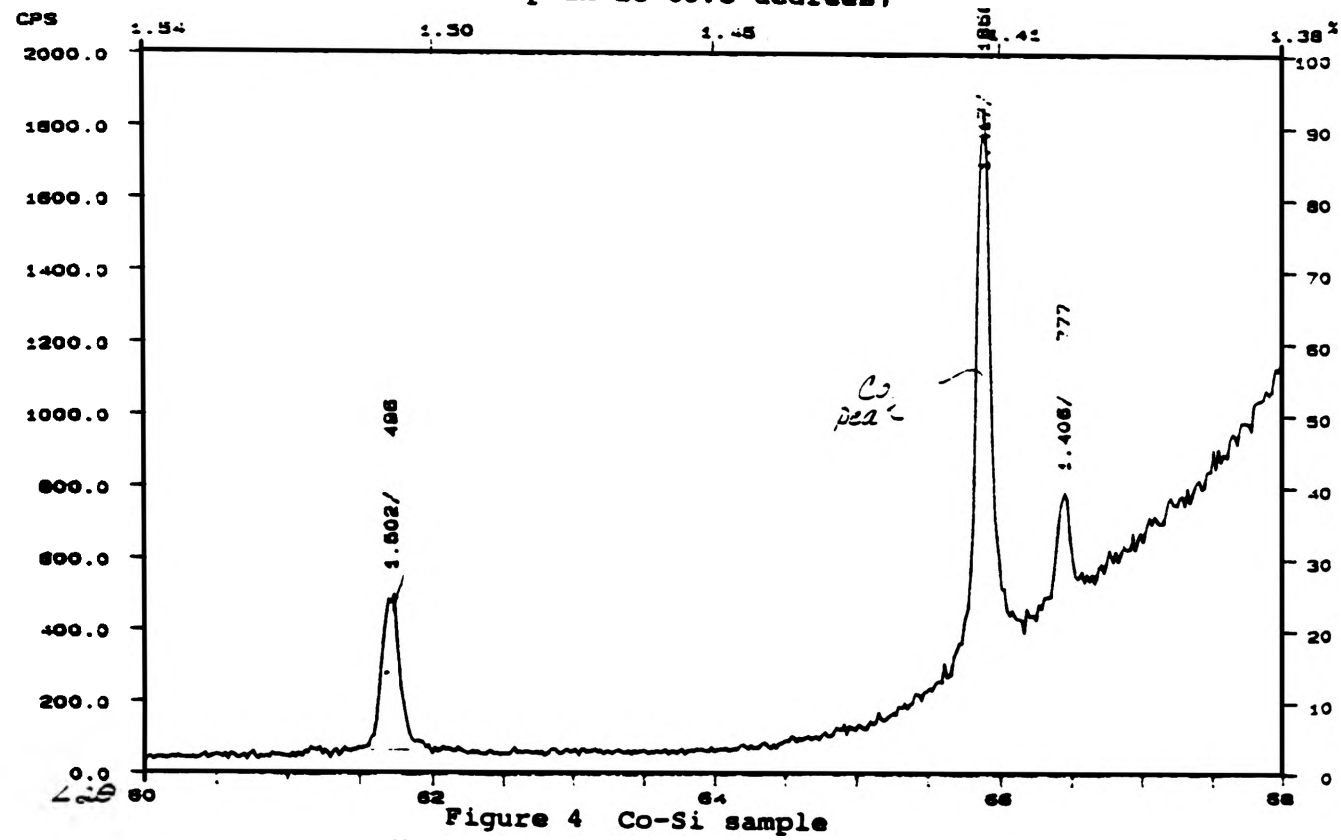

Figure 4 Co-Si sample
(Note Co peak at 65.8 degrees)

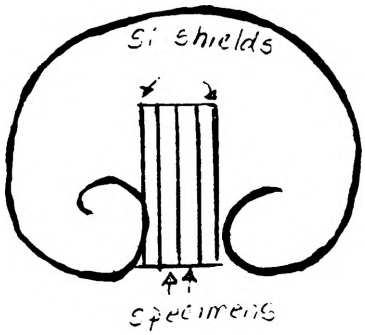

Figure 5 Clamp device to hold specimen during titanium deposition

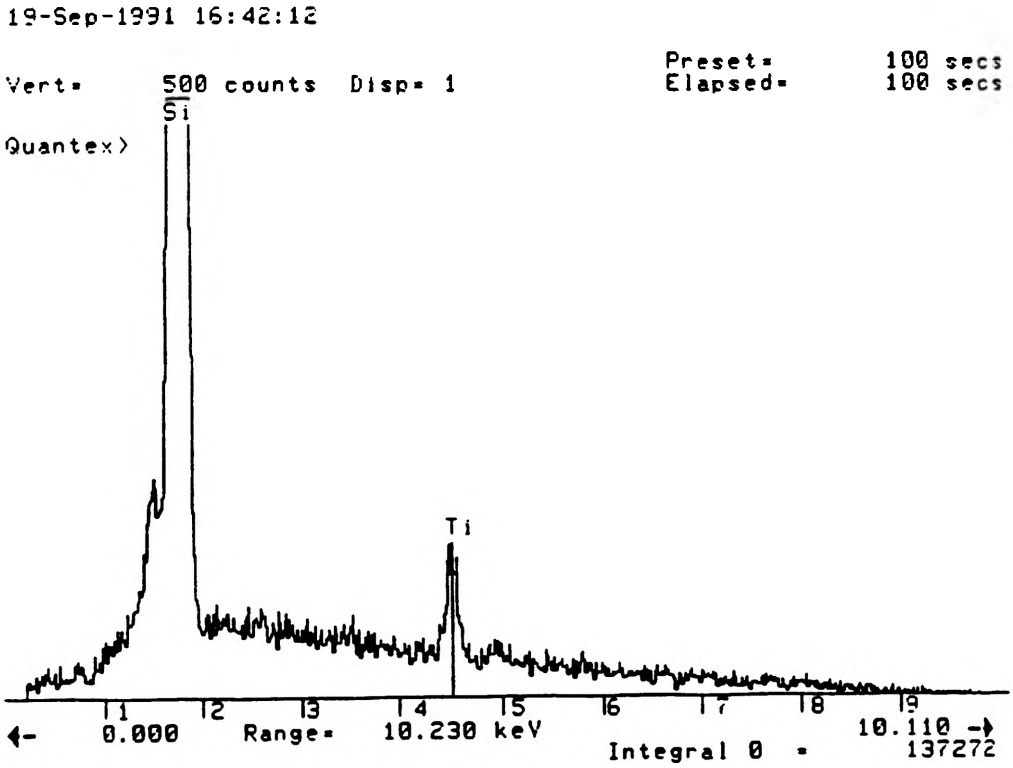

Figure 6 EDS chart of Co-Si sample with Ti evaporated on surface

with approximately the same dimensions was placed on each side of the sample to avoid Ti deposition on either surface. Using this clamp, from one to three samples could be coated at a time.

The first method of deposition to be tested was sputter coating. It is very important that the sputter coater be thoroughly cleaned with acetone before use to avoid contamination of the specimens by elements already present on the coater interior and ejected by secondary collision. A .025" thick Ti foil ring was cut out and adhered to the magnet with carbon paint, using care not to let impurities get on the foil. It is also important that Ti be kept in a desiccator whenever it is not being used due to its high oxidation potential. To test the procedure, Si wafers were sputter coated rather than an actual specimen. When the Si wafer was examined using energy dispersive spectroscopy (EDS), only Si was detected. Upon examination of these results and further research, it was concluded that it is nearly impossible to deposit Ti onto Si by sputter coating.

The second, and much more successful, method of Ti deposition was evaporation. The weight of Ti needed for evaporation was calculated from a standard nomogram. Using a desired thickness of 500 angstroms of Ti and a source-to-surface distance of 10 cm, 26 mg of Ti evaporant is needed. This converts to 2.89 cm of .5mm diameter Ti wire. To ensure a thorough coat and to allow for losses, which will be discussed later, five centimeters of Ti wire were used. The wire is bent into a tight ball using pliers cleaned with acetone and placed in a tungsten boat. The wire is bent into the ball to produce a smaller surface-to-volume ratio, so less oxidation can occur during evaporation. The evaporation was first tested on a Si chip placed in a clamp. Evaporation occurred at approximately 40 V and 21 amps. The presence of Ti was verified by EDS and SEM techniques (see figure 6).

Ti was evaporated onto the Co-Si multi-layer specimens in the same manner, but a movable shield was installed to protect the specimen until surface oxide on the molten Ti had been evaporated. The shield was kept over the specimen while the voltage was being raised and for 20 seconds thereafter. It was then rotated to the side and titanium deposited on the samples. The Ti that evaporated along with the oxide plus the small amount that remained in the tungsten boat were estimated to consume about half the starting amount.

Diffusing Ti into Co-Si Specimen:

A tube furnace was used for the annealing process. To maintain more uniformity in temperature, a copper tube was placed inside the tube furnace and ceramic wool insulation was inserted in each end to limit convectional effects. The temperature was monitored using a thermocouple that was separate from the one controlling the furnace. The specimen was contained inside a Vycor tube, which was evacuated and back-filled with argon to a slightly reduced atmosphere. Each specimen was annealed at a specified temperature for ten minutes. Specimens were annealed at 300 and 400 degrees Celsius. After each sample was annealed, its Vycor tube was cut open and the sample was analyzed by X-ray diffractometry.

RESULTS

Specimens A and B were used to compare the effect of different annealing temperatures for ten minute heat treatments. Both specimens had 100-angstrom layers of Co and Si and contained Ti. Sample A was annealed at 300 degrees Celsius, and Sample B was annealed at 400 degrees Celsius. As shown in figure 7, 300 degrees Celsius is not high enough to cause intermixing between the two

crystalline layers. The small, wide peak present at 2-theta of 42 is probably slight intermixing that occurred during deposition of the Co and Si. Upon examining sample B (illustrated in figure 8), it becomes evident that annealing a Co-Si sample at 400 degrees Celsius with Ti diffusing through the layers permits an intermixing of the layers.

The third sample tested, specimen D, was to confirm that amorphization occurred at 400 degrees Celsius in the presence of Ti. This can be seen by the increase in magnitude of the two peaks present at two-theta of approximately 42 and 46 from a specimen with no Ti addition or annealing (figure 9) to specimen D (figure 10). The short, wide peaks in figure 9 are due to slight intermixing that occurred during the deposition of Co and Si layers.

DISCUSSION

Co-Si multi-layer specimens were examined using grazing-incidence asymmetric Bragg diffraction. An increase in the magnitude of the peaks is observed in samples with Ti additions annealed at 400 degrees Celsius, whereas little change occurs at 300 degrees Celsius. This leads to the conclusion that there is an increase in amorphization at 400 degrees Celsius, but 300 degrees Celsius is not a high enough annealing temperature to affect the heterostructure significantly.

There was doubt raised by Dr. Shumsky about the legitimacy of these peaks. His concern was that the graph of the diffraction from the sample D surface with the Co film on top (figure 10) was almost identical to the graph of the diffraction from the Si substrate surface of sample D (figure 11). To see if the diffractometer was faulty or the Si substrate and the Co film surface truly have the same diffraction after annealing with Ti, a silicon (100) wafer was examined. The diffraction pattern showed no peaks in the range of forty to fifty for 2-theta. This leads to the conclusion that peaks in graphs five through eight represent intermixing.

Another problem often encountered was during the Ti evaporation. The Ti sample was too large for the tungsten boat. The Ti would begin to evaporate, and the melted titanium would cause a short circuit in the tungsten boat. When this occurred, some of the Ti was not deposited on the sample. A small amount of melted Ti would remain in the boat. If a slightly larger tungsten boat were available, it would help solve this problem.

Aside from these possible equipment errors, contamination is the next most likely error. Though the Ti was kept in a desiccator and never touched by hand, it was exposed to air for short periods of time. This was more likely to have an adverse effect after the specimen was coated. The specimens had to be transported to another building to be sealed in an argon-filled tube. During experimentation, all apparatuses were repeatedly cleaned with acetone or methanol to avoid further contamination.

There are several other investigations in the area of solid state amorphization of Co-Si multi-layer specimens with the addition of titanium which may be further explored. A comparison of a Co-Si sample annealed without the addition of Ti to a sample with the addition of Ti would reveal whether the addition of the Ti actually aided in intermixing, or the increase in temperature was enough to trigger it. According to past research, the temperature increase should not induce amorphization.

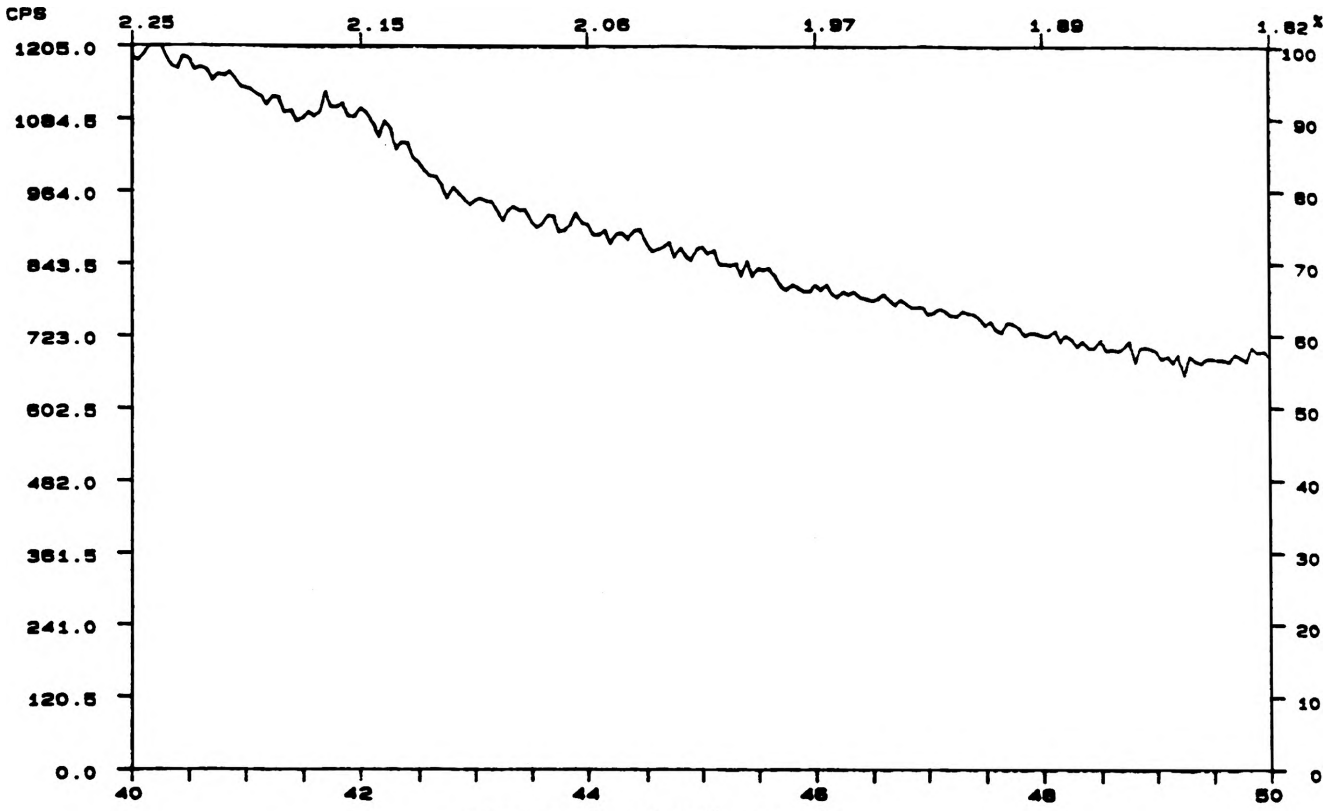

Figure 7 Co-Si sample
annealed at 300 C with Ti addition

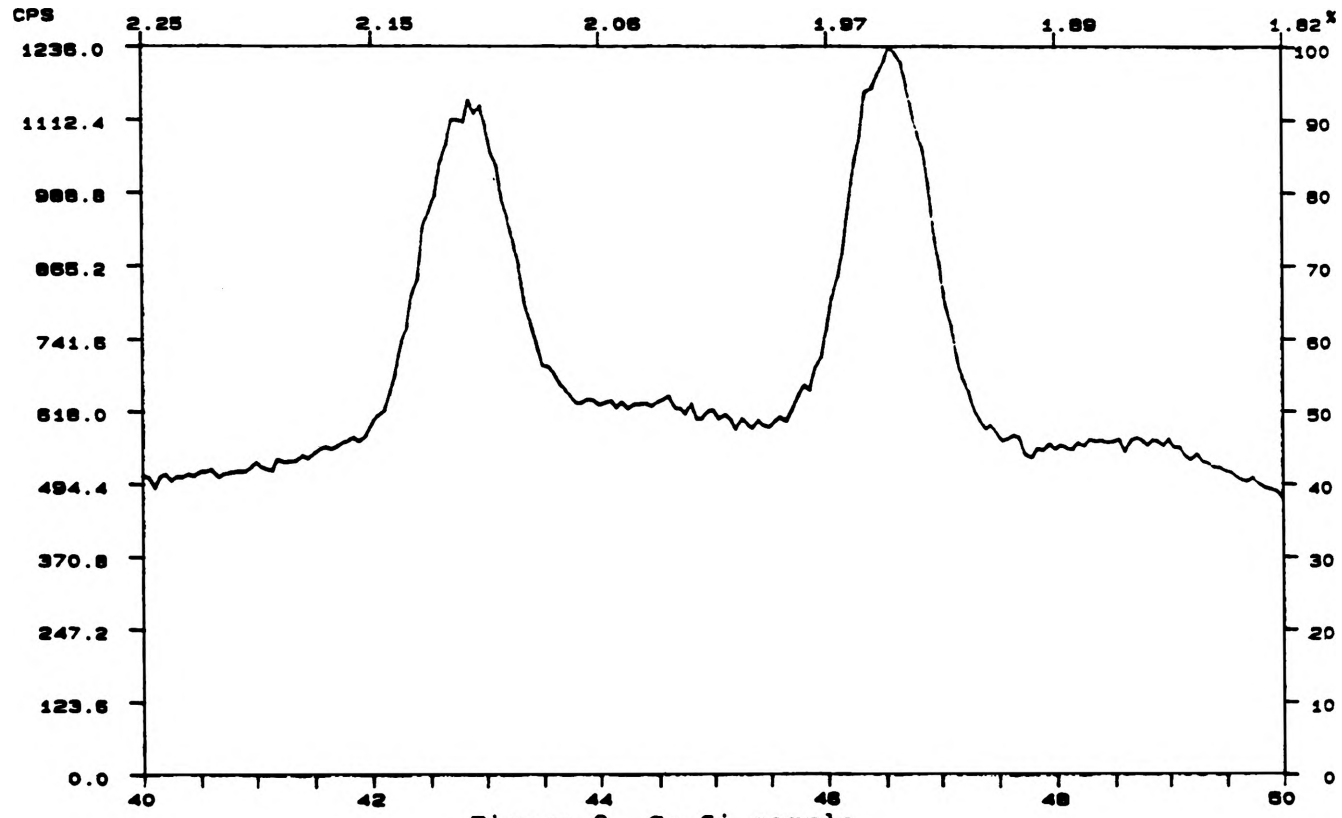

Figure 8 Co-Si sample
annealed at 400 C with Ti addition

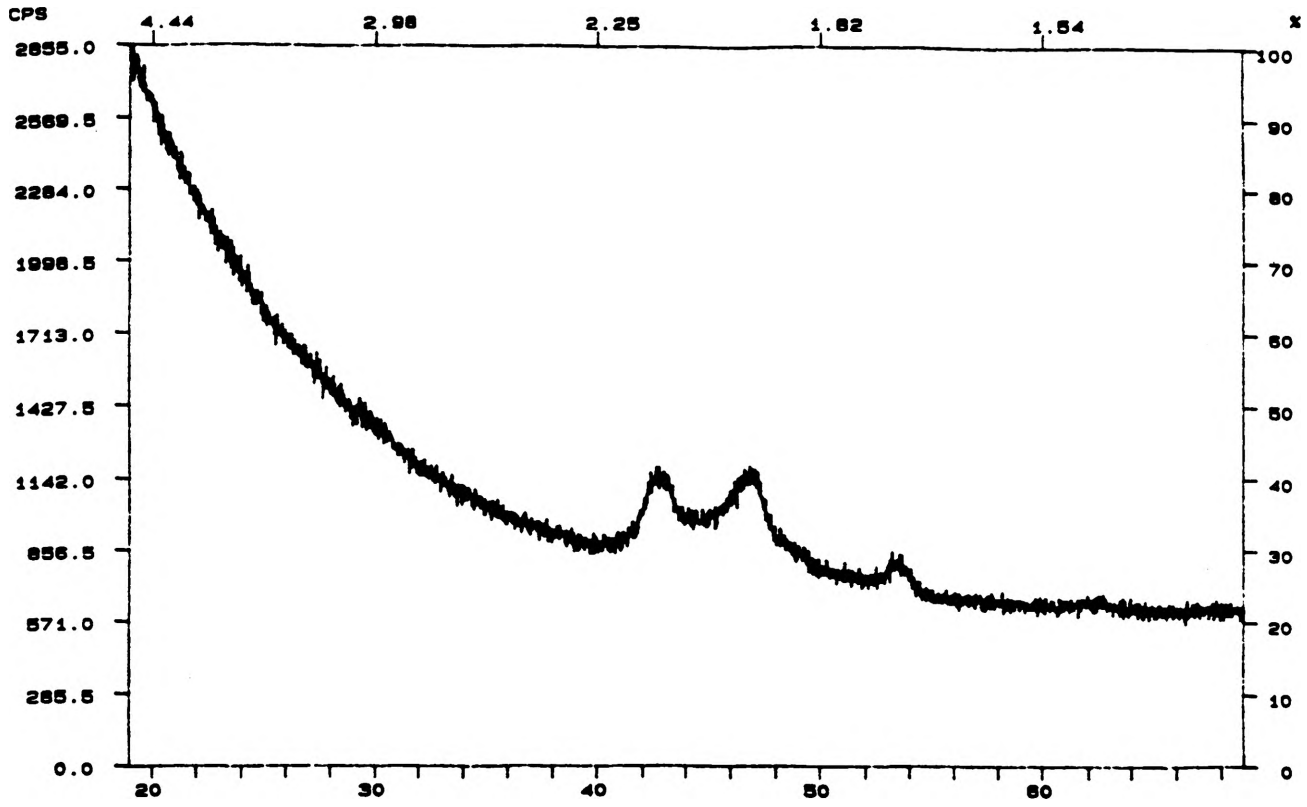

Figure 9 Co-Si sample
with no treatment

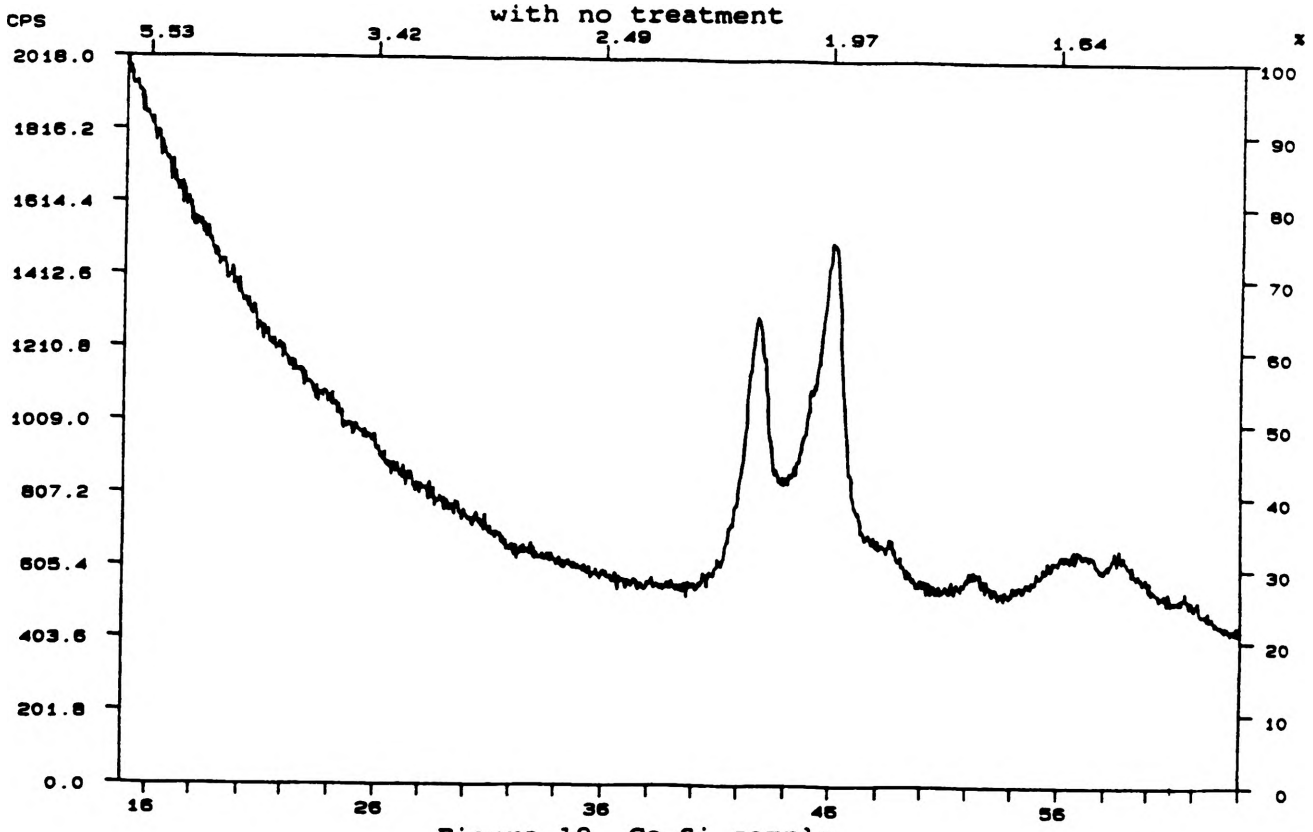

Figure 10 Co-Si sample
annealed at 400 C with Ti addition
(diffraction on Co film surface)

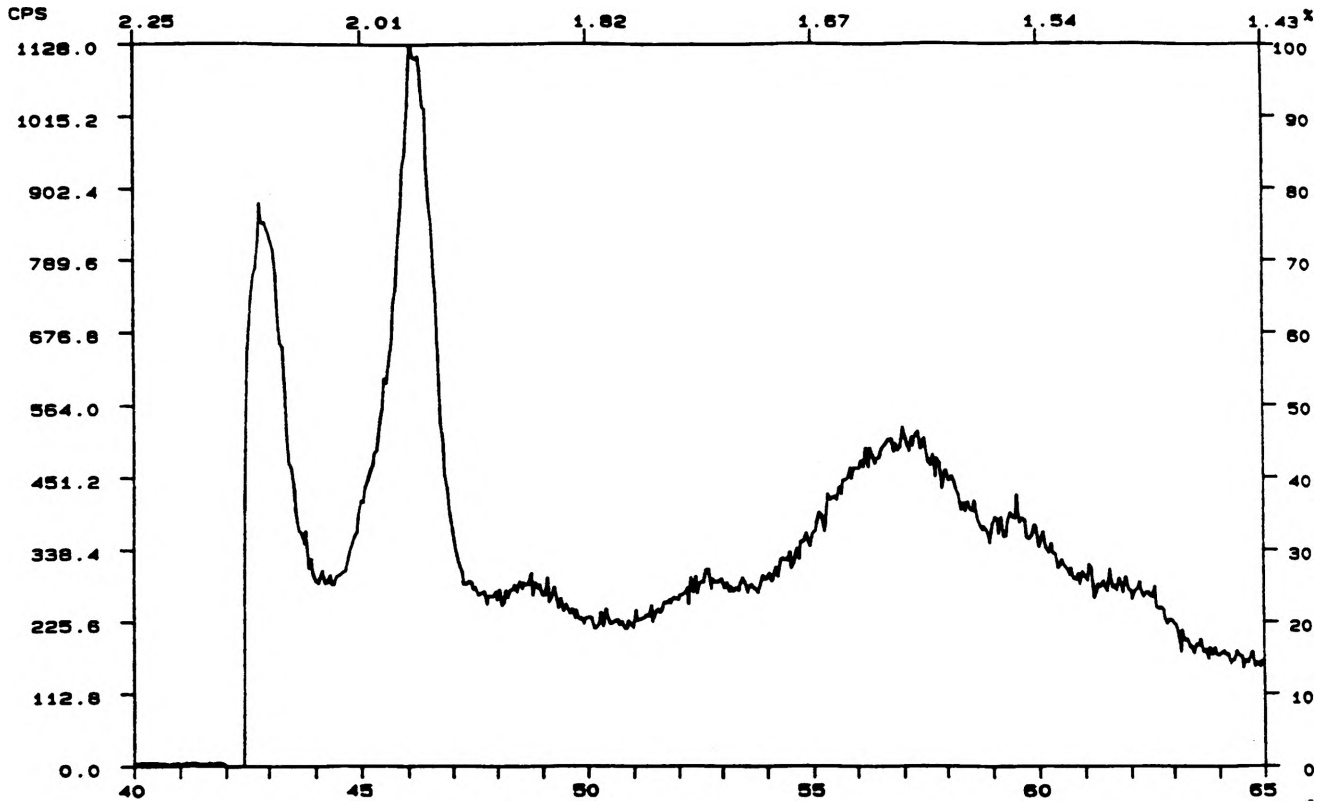

Figure 11 Co-Si sample
annealed at 400 C with Ti addition
(diffraction on substrate surface)

Other interesting experiments may be to attempt to cause intermixing by annealing under pressure or by the addition of a different third element than Ti. Once an amorphous structure has been produced, magnetic and mechanical properties such as tensile strength, toughness, and hardness can be tested and compared to the original Co-Si crystalline heterostructure.

CONCLUSION

There is sufficient evidence that a Co-Si system annealed for ten minutes at 400 degrees Celsius with the addition of Ti amorphizes. The fact that intermixing was not intensified when a specimen was annealed at 300 degrees Celsius under the same conditions illustrates the temperature dependency of amorphization. Further research is necessary to determine whether or not the addition of Ti is actually responsible for enhancing amorphization.

ACKNOWLEDGMENTS

I have learned far more working on this research project this past year than any in classes I have taken. I would like to thank Dr. Harry Weart for giving me this opportunity and for his advice, patience, and understanding (especially the latter two). Special thanks also goes to Scott Miller for his assistance in SEM and TEM analysis and Ti deposition and to Dr. Mark Shumsky for his assistance with the X-ray diffraction.

REFERENCES

1. Clemens, Bruce M.; Sinclair, Robert
"Metastable Phase Formation in Thin Films and Multilayers"
MRS Bullentin
February 1990 pp. 19 - 28

2. Khan, M.R.; Chun, C.S.L.; Felcher, G.P.; Grimsditch, M.; Kueny, A.; Falco, C.M.; Schuller, I.K.
"Structural, elastic, and transport anomalies in molybdenum/nickel superlattices"
Physical Review B Vol 27, No 12
June 15, 1983 pp. 7186 - 7193

3. Shiau, F.Y.; Chen, S.L.; Loomans, M.; Chang, Y.A.
"Formation and growth of an amorphous phase by solid-state reaction between GaAs and Co thin films"
Journal of Material Research
July 1991 pp. 1532 - 1540

4. Benedict, J.D.; Anderson, Ron; Klepeis, S.J.; Chaker, M.
"A Procedure for cross-sectioning specific semi-conductor devices for both SEM and TEM analysis"
MRS Procedings Vol 199
Copyright 1990 pp189

AUTOMATED SEEBECK MEASUREMENTS APPLIED TO CONDUCTING CERAMICS

J. S. Shapiro
Physics

ABSTRACT

The Seebeck coefficient (also known as thermopower) is important in the characterization of conducting ceramics because it is very sensitive to the electronic structure. An apparatus was built during the Fall of 1990 and Spring of 1991 which was designed to measure the Seebeck coefficient in small high-resistivity samples in the temperature range from 80 K to 450 K. A reproducible thermocouple-to-sample electrical and thermal contact technique was found to be important to data accuracy but difficult to achieve. The goals of this project were to improve the thermocouple block design to give better thermal and electrical contact with the sample and to make statistically significant and accurate measurements on several sets of samples.

INTRODUCTION

If a conducting sample is placed in a thermal gradient, a voltage across the sample equal to the temperature difference multiplied by the Seebeck coefficient, is produced. The Seebeck coefficient is accordingly defined to be:

$$S = \lim_{\Delta T \to 0} \frac{\Delta V}{\Delta T} \qquad (1)$$

The Seebeck coefficient represents the transport entropy per unit charge carrier. In certain types of ceramics known as hopping conductors (so named because the charges hop from site to site) the Seebeck coefficient represents the charge carrier concentration as given by Heikes' formula [1].

$$S = \frac{k}{q} \ln\left[\frac{1-c}{c}\right] \qquad (2)$$

where k is Boltzmann's constant; q is the charge carrier; and c is the fractional charge density.

The Seebeck coefficient is measured by applying various thermal gradients across the sample and then dynamically measuring several δT, δV pairs, as shown in Figure 1. The slope of the linear best fit for this data is the Seebeck coefficient at the average temperature.

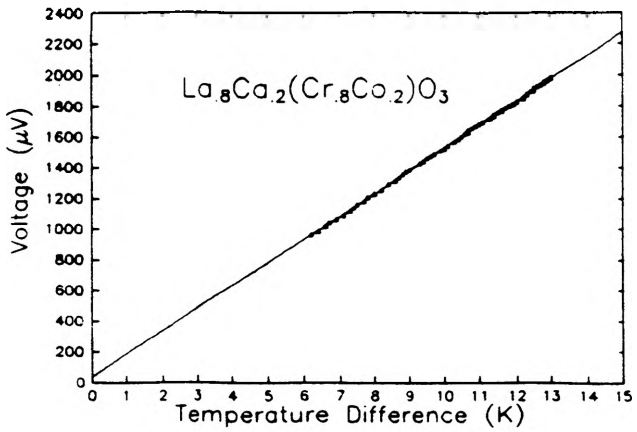

Figure 1 δV vs δT

Previous Work.

An apparatus was built during the Fall of 1990 and the spring of 1991 which was designed to measure high impedance samples from 450 K to 80 K. The use of thin, wide samples of high resistivity materials provides the smallest electrical impedance of the sample. Such a sample would also have a small thermal impedance and generate a small δT. The $La_{.9}Sr_{.1}(Mn,Cr)O_3$ series was measured. When the sample-remounted-reproducibility of the $La_{.9}Sr_{.1}MnO_3$ data was tested a variety of Seebeck coefficients were recorded. The trends were the same for the different sample remounts but the maximum Seebeck values were scaled. This indicates a problem with the thermal impedance between the sample and the thermocouple blocks, which will be discussed later.

EXPERIMENTAL SETUP

An IBM PC is used to control all the instruments through an Hewlett-Packard Interface Bus (HPIB) card. The PC also has an IBM Data Acquisition and Control Adapter (DACA) which is used to control the sample heater. All the software is written in QuickBasic and is usually run interpreted (non-compiled) to facilitate changes and or corrections.

An HP 3497A Data Acquisition/Control Adapter (with HPIB) with a room temperature compensation thermocouple board is used to measure the temperature at the ends of the sample. The copper leg of the T-type thermocouple (Special-Limit-of- Error grade) is used as the voltage lead.

The voltage across the sample is measured with a Keithley 197 Microvolt DMM. The meter has $1\mu V$ resolution and an input impedance of $> 1G\Omega$. The voltage measurement error is below 1% when the sample impedance is less than $10M\Omega$.

The temperature of the Janis SuperTran 2 cryostat head is controlled to within 0.1K using a Lakeshore Cryotronics Model DRC 81C Temperature Controller. The cryostat can reach

temperatures from 100K to 450K. The cryostat chamber is operated under a rough vacuum for thermal insulation.

The sample holder consists of two blocks of aluminum with embedded thermocouples. Because the thermocouple is not in direct contact with the sample it is possible that the measured temperature difference is larger than that of the sample. However, because the blocks are made of aluminum, which has a thermal conductivity of 2.86 W cm^{-1} K^{-1} [2] (70% as conductive as silver), and the thermocouples are mounted close to the surface of the blocks, the temperature of the thermocouples is very close to that at the surface of the aluminum block.

There have been three different sample holders built. The first was used from October, 1990 through January, 1991. It used a single alignment rod and small isothermal blocks. The second design was used from February to October, 1991. This design used two alignment rods to facilitate sample mounting. The isothermal blocks were still relatively small and thin. The third design was used from October, 1991 to present. This design uses four alignment rods which make sample mounting very easy. The isothermal blocks on this design are both much larger and thicker than previous designs. The third sample holder is shown in Figure 2.

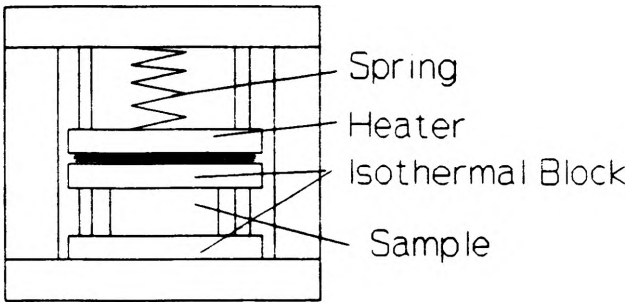

Figure 2 Sample Holder

Measurement Method

The measurements on this apparatus are taken while the temperature is decreasing. This means that the cryostat starts at the highest setpoint and decreases by some user defined amount until it reaches the lowest setpoint. If a setpoint is below room temperature an operator must turn on the flow of liquid nitrogen. When the lowest setpoint is reached the computer resets the setpoint to room temperature and the operator must then turn off the liquid nitrogen.

As the sample temperature approaches a setpoint the computer turns on the sample heater to create a range of temperature differences across the sample. The computer repeatedly reads the voltage and temperature difference across the sample. It fits these data with a straight line and saves the slope as the Seebeck coefficient at the average temperature of the data set. This process is repeated for each setpoint.

Error in the Measurements

A sample geometry which has a large area and small thickness is chosen to reduce the overall sample impedance for high resistivity samples. The problem with this geometry is that the temperature difference across the sample is less accurately known. Because the thermocouples are inside the isothermal block, and if the junction between the isothermal block and the sample has a high thermal impedance, then the temperature across the sample will be smaller than the measured temperature difference. This results in a Seebeck coefficient which is lower than the actual Seebeck coefficient.

By knowing the thermal impedances of the materials involved in Figure 2, the actual Seebeck coefficient can be shown to be:

$$S_s = S_m + \frac{2R_b(S_m - S_b) + 2R_j(S_m - S_j)}{R_s} \qquad (3)$$

where the subscripts s, m, b, and j correspond to: sample, measured, (isothermal) blocks, and junction. R is the thermal impedance. The isothermal block term is included because the thermocouple is not at the surface of the block. Generally this term would be very small given the low thermal resistivity of aluminum. If the junctions and the isothermal blocks have a very low thermal impedance compared to the sample then the measured Seebeck coefficient approaches the actual value.

A thermal paste is applied to both sides of the sample to minimize the thermal impedance of the junctions. However, if a different amount of thermal paste is applied, or a different thermal paste is used in successive runs, then the junction thermal impedance will be different and this will cause different measured Seebeck coefficients. Because there is no method in which the Seebeck coefficient can be artificially amplified, the highest value is the closest to the actual Seebeck coefficient. This can be seen in Figure 3 (note: the data in Figure 3 was taken using the second sample holder design.)

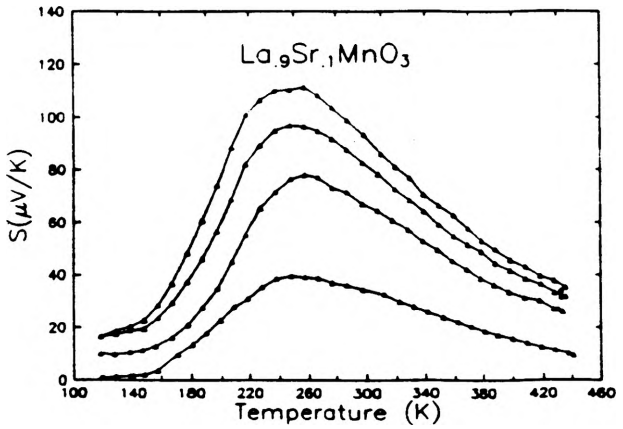

Figure 3 The Seebeck coefficient is scaled when the sample is removed and remounted

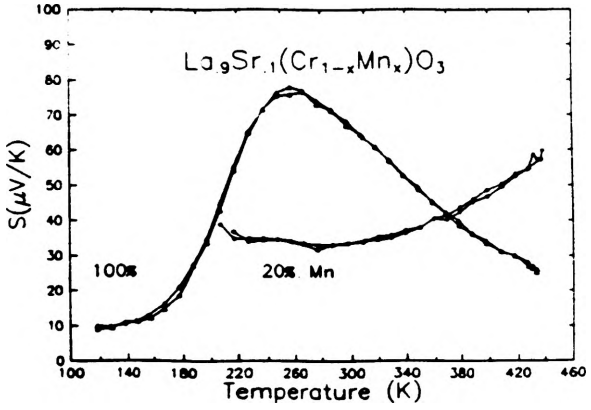

Figure 4 When the sample is not remounted the reproducibility is excellent

Although it would be possible to correct for the thermal impedance of the materials and junction, it would be much better to minimize such impedances. One way to lessen this is to use larger isothermal blocks (as with the third sample holder design). Another is by putting a silver paint on the samples. This greatly aids the electrical contact and, because of the polymeric binder in the paste, the paste can conform better to the isothermal block if it was not smooth. Using this method the remount-reproducibility is greatly improved ($\pm 15\mu V/K$). One thing to note is that the reproducibility when the sample is not removed is excellent ($\pm 2\mu V/K$) as shown in Figure 4.

EXPERIMENTAL RESULTS

Calibration

The apparatus was calibrated against two metals: chrome and cobalt. Even though these samples are not high impedance, the Seebeck coefficient in each is relatively small and therefore can test the limits of the apparatus. The cobalt sample (99.999%) was essentially ideal. It was a right cylinder about 1-1.5 cm long with a diameter of about 0.4 cm. The chrome sample (>99%) was much less ideal; it was 1.5 cm long, 0.5 cm at the maximum radius and shaped like a teardrop. The data in Figure 5 shows the effect of this geometry (and thus thermal impedance) on the Seebeck coefficient.

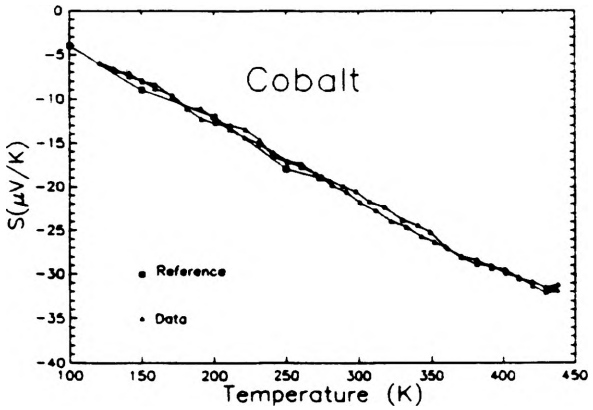

Figure 5 Cobalt Calibration

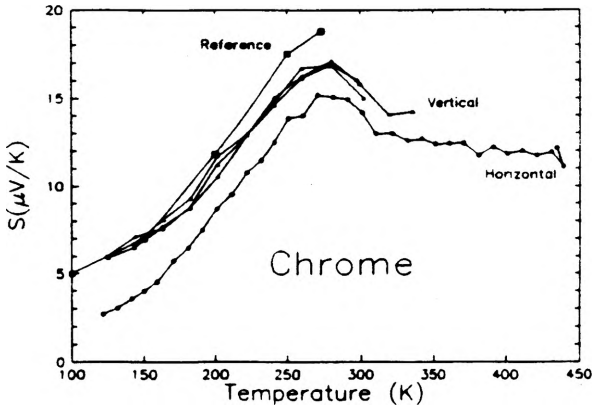

Figure 6 Chrome Calibration

$La_{.9}Sr_{.1}Cr_{1-x}Mn_xO_3$

The data from this series is shown in Figure 7. The most interesting sample in this series was $La_{.9}Sr_{.1}MnO_3$. The Seebeck coefficient falls from a high value at high temperatures to a lower value with a hump in it at the lower temperatures.

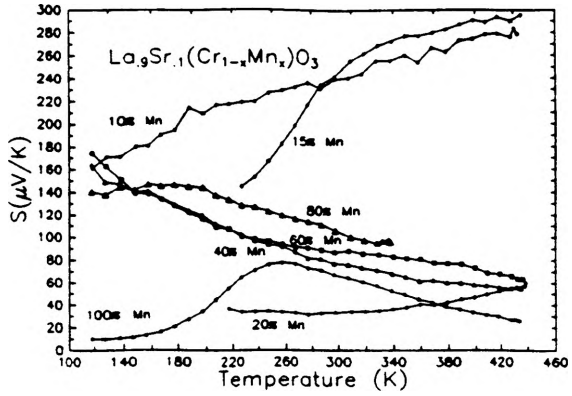

Figure 7

$LaCr_{1-x}Co_xO_3$

The data from this series is shown in Figure 8. This data is very interesting, especially those samples with $x > 60\%$. Scott Sehlin, a graduate physics student, was measuring the 100% Co sample from 1500 K to 300 K, where the value of the Seebeck coefficient is flat, but at around 400 K the value for the Seebeck coefficient dropped off very quickly (this is often the sign of a run which is no longer good) and he believed the data to be invalid below 450 K. When the sample was placed in this apparatus it was shown that the Seebeck coefficient did drop off very quickly and crossed zero. The 100% Co sample was then remeasured in his apparatus from 600 to 300 K and the agreement between the two apparati is excellent ($\pm 5\mu V/K$). Figure 9 shows two of the samples from this series.

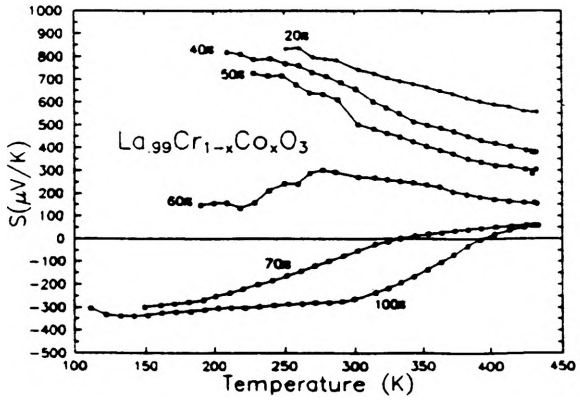

Figure 8

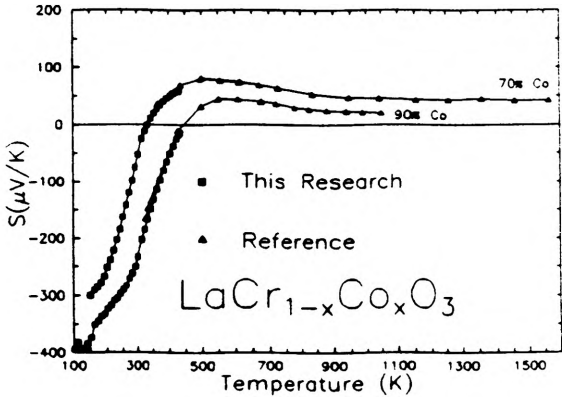

Figure 9

$La_{.9}Ca_{.1}Cr_{1-x}Co_xO_3$

At higher temperatures (> 1000 K) the Seebeck coefficient is more or less flat (small temperature dependence) and between 300-900 K, depending on the sample, the Seebeck coefficient rises to a higher value. In the temperature range covered by this apparatus, the samples with <40% Co are already flat, while 80% and 100% Co are still rising. One very interesting feature of this data set is the trend of the Seebeck coefficient toward 0 μV/K as T goes to absolute zero. This can be explained if there are a finite number of carriers, perhaps due to defects, as T goes to absolute zero because the entropy in the system goes to zero in a non-degenerate system.

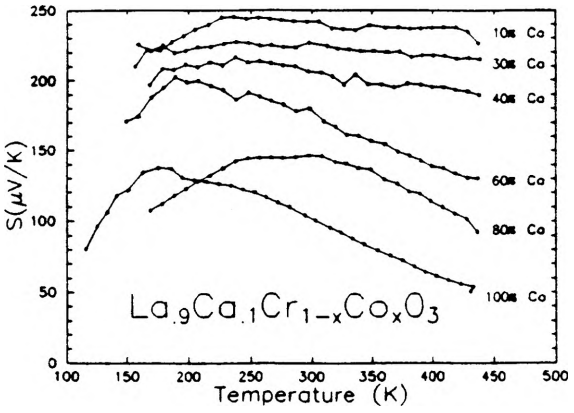

Figure 10

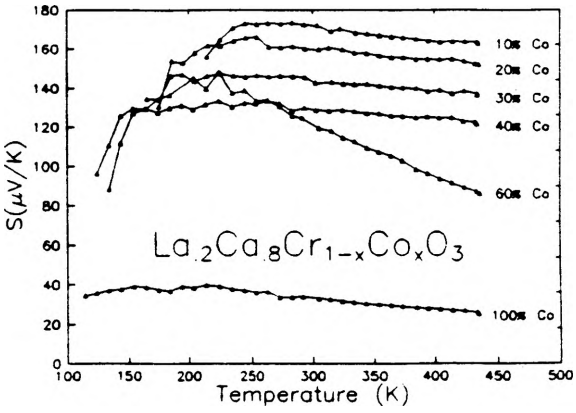

Figure 11

$La_{.2}Ca_{.2}Cr_{1-x}Co_xO_3$

The data from this series is shown in Figure 10. This data is very much like the $La_{.9}Ca_{.1}Cr_{1-x}Co_xO_3$ series except that the values are lower.

CONCLUSION

The thermal impedance problems associated with Seebeck coefficient measurements using thin, wide high resistivity samples have been extensively examined. Improved sample holders were designed and built which used silver paste to lower thermal impedances between the sample and the thermocouple block. The ideal thermal geometry is opposite to that required for electrical measurements in high resistivity material and a satisfactory compromise was reached.

Four series of conducting ceramics, with 5-7 samples each, were measured. Good agreement was achieved with other researchers and between the low and high temperature apparati at UMR.

ACKNOWLEDGEMENTS

I would like to thank Dr. Don Sparlin for his patience and wisdom in advising this project. I would also like to thank Scott Sehlin for providing the $La_{1-y}Ca_yCr_{1-x}Co_xO_3$ samples and Jason Hoerner, a Jackling Institute student, for writing all the graphics routines used.

REFERENCES

[1] Raffaelle, R., H. U. Anderson, D. M. Sparlin, and P. E. Parris, "Transport Anomalies in the High-temperature Hopping Conductivity and Thermopower of Sr-Doped La(Cr,Mn)O_3." Phys. Rev. B 42, 10A, 7991-99 (1991).

[2] Handbook of Chemistry and Physics, 56th edition, CRC Press, 1976. Page E-12

[3] Blatt, F. J. Thermoelectric Power of Metals, Plennum Press, 1976. Pages 180-181

Properties of buckminsterfullerene: analytic physical methods for verification of truncated icosahedral molecular structure

ABSTRACT

Jon R. Fox, Matthew L. Selinger, and David A. Thilker
Advanced Undergraduate Laboratory, Department of Physics, University of Missouri-Rolla, Rolla, Missouri 65401

March 23, 1992

Aspects pertinent to the confirmation of a specific molecular structure - buckminsterfullerene (C_{60}), the truncated icosahedral form of carbon - are examined. Absorption spectroscopy, nuclear magnetic resonance, scanning probe microscopy, and x-ray scattering are each covered. Nuclear magnetic resonance revealed a single peak, implying a truncated icosahedral structure. X-ray diffractometry (XRD) of the sample yielded a scattering pattern with sharp peaks. The XRD data loosely fit to an hcp lattice with lattice parameters a = 10.12 Å and c = 16.65 Å. Infrared spectroscopy revealed peaks indicative of the presence of two varieties of fullerite, C_{60} and C_{70}. Ultraviolet spectroscopy yielded the characteristic "camel" spectra. Visible spectroscopy measurements also agreed with previously reported observations. Auger analysis yielded no discernable difference from carbon graphite. STM/AFM analyses showed directly how our sample exhibited only a short-ranged packing order. A procedural description of buckminsterfullerene purification is given in detail.

NOTE: Abstract only included. Complete 43 page report on file in UMR Department of Physics.

UMR

OURE PAPERS

BORDER DETECTION OF SKIN TUMOR IMAGES

Salman Akhtar

Electrical Engineering

Abstract

Color border programs are used to try to obtain a border for skin tumors. A series of programs are used to obtain a color segmented image. This color segmented image can then be passed through a program that searches for the border, "Colborder.simple". Problems have occurred in trying to obtain the color segmented image. Normal images were used instead of the color segmented image as input to the color border detection program. The program was unsuccessful in finding the border.

Introduction

A line separating the skin tumor from healthy skin is referred to as the border. The border detection of skin tumor images is an important part of a research project which is trying to identify important features of skin tumor. The project proposes to identify skin tumor features in order to aid dermatologists in making a more accurate diagnoses.

Once the border has been found the programs can concentrate on features inside the border and they can ignore the skin outside the border. The features found can provide an indication if the tumor is malignant. If the border of the tumor is highly irregular it indicates a malignant tumor.

If the border detected is incorrect it is misleading in several ways. It gives an inaccurate irregularity index as well as providing an incorrect area for the subsequent programs which may try to find different features of the tumor. It may find features that are not a part of the tumor if the border includes the surrounding skin; it may miss some of the key features if part of the tumor is not included within the

border.

Border Detection

The first border detection program used radial search method on luminance image. In the original image each pixel includes red, green, and blue values, these can be converted to a gray scale luminance image by adding a weighted sum of the three values. The luminance border program searches radially from the center of the image to the edge. The search continues until a condition of a change in luminance followed by a sustained length is met. If no point is found than the restrictions are eased and the process is repeated until a point is found.

The above method has several disadvantages. By choosing the first point that satisfies the condition and not searching along the whole length of the radius the program looses an opportunity to find a better candidate. It takes a long time to process an image since the program may search several times along each radial line. A program which searches the radial line once and returns several candidates should be able to solve this problem.

The use of luminance instead of all three colors causes a substantial information loss which, if utilized, may lead to a more accurate border detection.

Color border detection

Colborder.simple tries to find the border by using a color segmented image with a small number of colors. This program outputs a data file containing the coordinates of the selected data points.

The colborder program requires that a color segmented image be provided to it for it to function correctly. It has not been possible to check the accuracy of the colborder program since a color segmented image could not be generated.

The color segmented image is generated by running eight programs. The programs are: avecolor.c, mask.c, spher_xform.c, find_covtrx.c, remap.c, seuccc.c, seuuccc.c, colfilter.c. The first three programs are functioning properly but from then on the programs produce unintelligible output.

When the original image is processed the first program it passes through is avecolor.c. This program takes as input a five hundred and twelve by five hundred and twelve image that is pixel interleaved. A pixel interleaved image is constructed by storing the red, green, and blue values of each pixel one after another. A four by four block of pixels is averaged to provide one pixel in the output image.

The mask.c looks at the feature file and masks out everything except the blocks which contain the tumor. The remaining image is written to an output file.

The spher_xform.c takes the image array and transforms it into spherical coordinates (Angle A / Angle B / Length). The image is then remaped. The output is the transformed, remaped image array.

The remap.c program takes an image array and the eigne vectors for the PCT transform (or any other linear transform matrix that may be desired). This program transforms an image array into the principle components transform and remaps to byte size (1-254). The output is a transformed and remaped image array.

Colborder.simple accepts as input a color segmented image. The user has the option to specify the coordinates of the center of the tumor. If not specified, the default value for center is the center of the image. The number of radii used for the radial search can also be specified, the default value used is sixty four.

Colborder.sample uses an algorithm that assumes that the origin of the radial search is the brightest color in the tumor. This program takes the upper left hand corner of the image as the origin. The x value of the pixels increases from left to right and is the column number. The y value of the pixels increases from top to bottom of the image and is the row number.

Colborder.simple uses a radial search and color information for determining four border candidates along each radii. A sustained length condition is specified which must be met before a point is considered a candidate. Colborder searches for changes in color segmented image which satisfy the sustained length condition. The point which has the greatest sustained length is chosen as the initial border candidate.

The radial length of the next radius is then compared to the previously chosen radius and the border point which has the least radial difference is chosen. This is repeated until a border point has been selected for each radii.

The accuracy of the colborder program is improved if the user limits the area of the search by placing a circle inside the tumor and another circle outside the tumor. The length of these radii can be found using another program and then passing the radii to colborder as the last two arguments in the command line.

Up to this point I have been unable find the errors in those programs. I am presently working on trying to debug those in order to obtain reasonable results.

When an unprocessed image was given to colborder.simple it was unable to find the border. If the correct point was found it was rejected because the difference in the radial length of the correct border point and the surrounding incorrect points was greater than the difference in the radial length of two incorrect points.

In order to obtain a correct border it is neccessary to provide the Colborder.simple with a color segmented image. I am currently working to this end.

"WORKING THE POLITICAL ENGINE": SAM ADAMS AND THE SPREAD OF REVOLUTION IN PROVINCIAL MASSACHUSETTS

KIRK G. BAST
DEPARTMENT OF HISTORY AND POLITICAL SCIENCE

Since the Revolutionary crisis with Britain began, people have debated Samuel Adam's role in America's break from the Empire. Currently, scholars are particularly interested in Adams' influence over both the people of Boston and other inhabitants of the Massachusetts Bay Colony, as they resisted British regulations. Was he able to manipulate crowd and mob behavior to enhance provincial fervor? Key to understanding Adams' influence is his conversion of rural Massachusetts to revolutionary sentiment. The purpose of this project is to assess Adam's impact as a propagandist from the mid-1760s to the early 1770s.

Historians endeavor to combine a diverse span of records into a cohesive picture. Unfortunately, time often tears gaps in the fabric of evidence. Such is the case with Samuel Adams, American Revolutionary, whose records are far from complete. Adams considered his documents "trifles", unworthy of preservation.[1] In an often quoted incident related by his cousin, John Adams, Sam Adams burned his letters to prevent subversive use of their contents.

Despite the scarcity of personal papers, it is possible to trace Adams' ascension to prominence beginning with his 1764 writing of the "Instructions" to the Boston Representatives. Although a Harvard graduate, failure dogged Adams in every profession he chose. Monetary matters seemed foreign to his Puritan nature. R.V. Harlow, an Adams' biographer, sketched the patriot's personality around his professional ineptitude. Harlow also argued that Adams' mental instability motivated his politics and his stance against the crown. According to Harlow, Adams developed an "inferiority complex" visible in his "neurotic" writings.[2] Although Harlow presented no examples of neurosis in Adams' writings, he repeatedly reiterated its influence on the patriot.

Despite Adams' recurrent failures, none of his writings show signs of mental illness. A stronger influence than insanity drove Adams. The religious heritage of John Winthrop and the Massachusetts Bay Colony made Adams' pen name "A Puritan", more than just a pseudonym. His Puritan heritage "gave him identity" and a sense of "Duty".[3] Adams sought

to follow the example of his forefathers and make Boston a "City on a Hill" for the rest of the world to follow. Religious piety, hard work, and basic freedoms for "Elect" citizens summarized Puritan ideals, and thus those of Adams.

The son of a wealthy deacon, Adams learned religion and politics from his father. Lacking capital, small farmers and businessmen of the colony established banks which backed currency with land rather than silver. After a short time, the banks were declared illegal, with investors remaining liable. As a substantial investor in the bank, the senior Adams remained accountable for numerous debts. Samuel inherited both a personal and political anti-establishment legacy from his father and the Deacon's economic difficulties associated with the Land Bank. The conflicting Silver Bank and Land Bank supporters drew political battle lines; the former led by the Boston merchant elite while the latter garnered backing from the provincial working classes.

Although the Land Bank supporters lost their struggle, it provided the Boston roots for the Country Party of James Otis.[4] Adams naturally joined the ranks of this party and became invaluable for his newspaper propaganda. He had previous experience with journalistic resistance. In 1748 Adams jointly started a newspaper, *The Independent Advertiser*, that accused Governor William Shirley of promoting the moral decay of the colony. During the "Era of Good Feelings" that prevailed in colonial politics under Governor Shirley, the maverick Adams stood out as an herald, preceding the future storm of revolt. He steadfastly wrote in opposition to the governor, even in these calm political times. Constant antagonism toward royal and elitist authority marked Adams' career.

Following the short gubernatorial tenure of Thomas Pownall which ended in 1760, Otis and Adams promoted dissent under new Governor Francis Bernard by gaining the support of numerous societies. Masonic groups and the Merchant Club influenced many, but the Caucus Club, as the Boston political machine, wielded the decisive power to choose town officeholders. Adams joined this group and thus took a larger and larger part in determining his own offices. Opposition views and positions formed in Club meetings were passed along to town meetings. The radicals used the Club for real decisions and the town meeting became their "rubber stamp."[5] The Boston Caucus Club also served as predecessor to the Committees of Correspondence by hosting Country party sentiment before dissemination throughout the province. Although vital, the Club lacked trans-Boston power allowing the Court party to control most colonial offices through a patronage system.

Any effective opposition to the Court faction necessitated non-Boston support. Boston held only 4 of 120 seats in the colonial lower house. With all their efforts, the Country party failed to awaken provincial Massachusetts to the 1764 Sugar Act. Traditional antagonism hampered unifying efforts, but Parliament provided the catalyst to revolt with the 1765 passage of the Stamp Act. To raise funds for the depleted British treasury, the Stamp Act required all official documents to bear a government stamp purchased from local agents of the crown. Events in this early crisis period exemplify many methods which Adams utilized

throughout the revolutionary era.

Adams employed diverse tactics to spread radicalism throughout the colony. Popular uprisings in Boston heightened rural awareness and worked to intimidate Loyalists, but the mobs could also damage the image of an oppressed, innocent Boston. The mob attacks of August 14 brought the resignation of Andrew Oliver as stamp master without major loss of property. Adams declared the attacks "ought to be forever remembered in America".[6] Not all mob activities received such praise. A drunken mob ransacked the home of Lieutenant Governor Thomas Hutchinson. Although he was an arch Tory, Hutchinson bore little relationship to this particular law, and the personal destruction of his home outraged many Bostonians and provincials. Adams avoided rousting up a possibly violent mob when he had an intelligent (partially literate) and reasoning public he could influence. "Violence & Submission," Adams later warned, "would at this time be equally fatal."[7] Some accused Adams of instigating the mobs and choosing their methods. Evidence clearly linked Adams to the demonstrations, however he avoided violence because of the counter-productive effects.

To prevent the martyrdom of Hutchinson in the eyes of both rural and Boston citizens, Adams resorted to a repeated tactic: lying. He fabricated a story implicating the lieutenant governor in the passage of the Stamp Act. Publication of this story and an Adams' letter to London which warded off imperial retribution minimized detrimental effects. Such skillful creation of propaganda to the point of lying marked Adams' use of the press.

Following the repeal of the Stamp Act, the first of numerous lulls in radical sentiment occurred. Victory on an issue brought the Loyalist goal of peace and quiet. During these periods Adams engineered dissent any way possible, such as by shifting criticism to local "oligarchs". During the Stamp Act crisis, Adams attacked Hutchinson's simultaneous officeholding and forced the Tory to resign his county judgeship. Adams continued in this vein condemning this practice.[8]

Imperial inaction left few rabble-rousing issues for Adams to exploit.[9] Fortunately, Parliament levied the Townsend Acts in late 1767. The Boston merchants retaliated by enacting a non-importation pact, an idea started in New York. Adams and the Whigs adopted this tactic as their own and initiated numerous boycotts beginning in 1768. Non-importation agreements harmed the London merchants and thus the Whigs generated economic pressure for Parliamentary concessions. These covenants held two difficulties for the Radicals. First, non-importation hurt Boston merchants as well as those in London. Second, Adams' Caucus Club could not implement them alone. Provincial participation was a prerequisite for any measure of success. Adams promoted support via the *Boston Gazette*. The printed voice of the Boston radicals, the *Gazette* influenced many people via its wide circulation. In numerous articles, Adams publicly berated opponents and praised those complying with the boycott.

The governor and the Whigs clashed again after the Whig controlled legislature drafted a statement addressed to the legislatures of the other colonies, opposing London's authority. Governor Bernard dissolved the legislature after the body refused to rescind the circular letter.

In response to this action to the stationing of troops in Boston, the Whigs called for an unprecedented convention of all provincial towns to discuss the supposed usurpation of colonial rights by the actions of Parliament and the governor. Whether or not the 1768 Convention served an additional purpose, it served as a model for the later more serious "Meeting of the People" in the Convention of 1772.[10]

The quartering of troops coincided with the calming of tensions. Traditionally apprehensive concerning standing armies, the colonists regarded the placement of professional soldiers in their homes as a threat to their personal liberties. Adams struck this emotional chord, haranguing the injustice of this occupation. New York newspapers began printing a "Journal of Events" relating alleged atrocities committed by British troops. Adams fabricated most of these stories, but they still swayed many readers. Throughout 1769, clashes between citizens and soldiers became a reality and that winter saw the death of a young boy. Adams virtually angelized the child in the *Gazette* and the funeral procession became a Whig rally. By March, Adams had the Bostonians incensed about the troops, and violence erupted. After weeks of enduring abusive taunts by Bostonians, British troops fired into an unarmed mob. The "Boston Massacre" outraged the entire town and Adams quickly forced concessions from the governor including the removal of the unit to prevent further bloodshed.

Following the Massacre, tensions again cooled, and as he had before, Adams provided invaluable maintenance of radical sentiment, prolonging political resentment fostered by the Massacre. He sought to end the old Boston/country rivalry and mistrust by recurrently reminding the outlying towns of the bloodshed wrought by the dreaded "lobsters" and that they too could suffer the humiliation of occupation.[11]

Complacency gripped the colony and signs of the radical fervor from the previous crisis all but disappeared. Adams needed a new vehicle to spread Radical views to the countryside. Adams had watched the rise and fall of correspondence societies in New York, and realized the value of such societies in marshaling grassroots support. Committees of Correspondence had been used before, but not to promote political actions. Adams needed a justification to form the network of committees. Through the fall of 1772, he authored numerous articles attacking the London plan to pay the salaries of judges.

The formation of the Boston Committee of Correspondence (BCC) defied conventional means of political opposition. To justify this unorthodox creation, the Whig controlled Boston town meeting petitioned the governor to allow the General Assembly to convene in response to the debate over judicial salaries. Predictably, Governor Hutchinson refused, thus granting Adams justification to form the BCC.[12] Adams summarized the impact of the refusal:

> our requests have been so reasonable that in refusing to comply with them he must have put himself in the wrong, . . . the Consequence of which will be, that such measures . . . will be more reconcilable even to cautious minds, & thus we may expect that Unanimity which we wish for.[13]

Indeed: "Put your enemies in the wrong" was Adams' first commandment in politics and he embodied it in all his actions. The BCC became the bugle for the Whig message and urged other towns to follow Boston's lead. During the winter of 1772, many provincial towns formed committees and stimulated reciprocal opposition sentiment. Through the BCC, Adams bridged the gap between Boston and the rest of the colony. His success at this endeavor is evident in the disappearance of the town versus country animosity endemic to Massachusetts politics. This union of Boston and the colony was never more important than after the passage of the Boston Port Act. Although evidence is mixed as to Adams role in the Tea Party, he maneuvered the situation into a stage play for his political use. Without the united coalition throughout the colony, Adams would have been unable to entertain such a confrontation.

Unlike Otis, who viewed his reforms within an imperial context, Adams recognized the vital importance of provincial Massachusetts. Boston and the BCC served as the hub of the revolutionary wheel in the colony. The metropolis channeled political sentiments (from itself and other towns) through the spokes of the Committees of Correspondence to the provincial rim. Adams and his creation, the BCC, exercised restraint in their unique, key position. Adams maintained a deference to rural "sovereignty" in their views. He marshaled rural support via this respect, some flattery, and constant media manipulation.[14] Because of his confidence in the power of the people he influenced, patience characterized Adams politics.

Historians continually debate the significance of Sam Adams.[15] They present diverse portrayals of him as a politically pathological liar, a "professional agitator" and controller of mobs, a "Pioneer in Propaganda," and a general troublemaker. Perhaps the most pertinent evaluations of Adams came from his opponents, such as Hutchinson and General Gage, who held unique perspectives on the patriot's activities. Both regarded Adams as the master rebel and only Adams and John Hancock were exempted from Gage's offer of amnesty.[16]

However, none of these poignant phrases captures the true nature of Adams. Motivated into politics in part to restore Puritan values and to challenge the heirs of his father's opponents, Adams recurrently reduced the struggle between colonial and imperial authority to local partisan clashes between himself and the colonial oligarchy. Adams resorted to this tactic often during calmer periods. During a crisis, he was simply one of many; but during lean times Adams proved indispensable to rekindling the Whig fire.

Far from being omnipotent, Adams often experienced setbacks and recovered. The Nullification Bill failure in October 1765, the initial rejection of the Solemn League and Covenant of 1774, the sporadic support and then defection by the Merchants' Club, all show limits on Adams' ability to control events during multiple crises. Indeed, Adams played an important role, but not as the head of a mob or a political oligarchy.

Through the BCC and the *Gazette*, Adams waged a decades long war of words. To

term him the "Pioneer in Propaganda" implies the prevalence of untruth, whereas Adams put forth his perception of the truth, successfully changing the view of others. Certainly the manipulation of public information remains key in political agitation, whether in Adams' period or during modern conflicts. Adams represents a revolutionary innovator of media use, and a constant member of the Revolutionary vanguard.

ACKNOWLEDGEMENTS

First and foremost I am indebted to Dr. Larry Gragg for his scholarly guidance and unending patience. Thanks to Robert Hobart for his constructive criticism. I received constant help from my emotional support team: Jeannette, Jules, and Nita. David Burwell, my word-processing guru deserves a new vehicle for his work. And finally, I am grateful to the OURE program for providing an avenue for undergraduate scholarship.

REFERENCES

1. Samuel Adams to Samuel Savage, Nov. 1, 1778. Quoted from Pauline Maier, *Old Revolutionaries: Political Lives in Age of Samuel Adams* (New York: Vintage Books, 1980), 35.

2. Ralph Harlow, *Samuel Adams: Promoter of the American Revolution* (New York: Holt and Co., 1923), 37, 170.

3. Maier, 42.

4. The Country Party refers to the group (headed initially by James Otis) which began opposition to first the Governor Francis Bernard administration and later imperial authority in general. The party backing the administration termed them "Whigs" (an English reference to the "Loyal Opposition" and later "Radicals" and also the insulting term "faction". Whig and Country Party are interchangeable terms; however the term Radicals is not inclusive of the entire opposition, only the more vocal group (including the "Loyal Nine") centered in Boston. As the mainstream of the opposition lost its effective leader, Otis, the Radicals under Adams took control until almost all Whigs were Radicals.

5. John Miller, *Sam Adams: Pioneer in Propaganda*. 2d ed., (Stanford: Stanford University Press, 1960), 39.

6. Samuel Adams, *The Writings of Samuel Adams*, edited by Harry Cushing (New York: Octagon Books, 1968), II 201.

7. Ibid., III 124.

8. Ibid., I 129.

9. John Miller, *Sam Adams: Pioneer in Propaganda*, 2d ed. (Stanford: Stanford University Press, 1960) 103.

10. See Miller, "The Massachusetts Convention of 1768", *New England Quarterly* VII, 445-474.

11. The *Gazette* is replete with examples of Adams allusions to the threat posed to the entire colony as well as the other colonies. For a typical example, see the article signed "Candidus" in the *Boston Gazette*, June 27, 1774.

12. For a detailed account of the formation of the BCC, see Richard D. Brown, *Revolutionary Politics in Massachusetts* (Cambridge: Harvard University Press, 1970), 38-57.

13. Samuel Adams, *The Writings of Samuel Adams*, edited by Harry Cushing (New York: Octagon Books, 1968), II 346.

14. For an example of his flattery and deference to the other towns, see "Candidus" in the *Gazette*, December 14, 1772.

15. For the best historiographic overview of the writings about Adams, see Maier, 8-16.

16. See references in Miller, 61; and Harlow, 69-70.

DESIGN AND DEVELOPMENT OF A SUPERCONDUCTING INDUCTION MOTOR

Terry Bowness
Dept. of Physics
University of Missouri-Rolla

ABSTRACT

The discovery of high-T_c superconductors has led to the development of a number of experimental superconducting motors. This report documents the design, construction, and methods of evaluating the performance of an induction motor with a high-T_c superconducting rotor. While others have utilized the Meissner effect, our superconducting motor works due to Lenz's law. In theory such a device will act as an induction motor only during start-up, after which its behavior is more like that of a synchronous machine. With a one-pole copper squirrel cage providing start-up torque two high-T_c discs encased in the rotor core act to bring the machine to synchronous speed.

INTRODUCTION

There has been a great deal of effort directed toward the development of higher-efficiency electrical machines. The idea of using superconducting components to achieve such goals is not new, but with the discovery of high-T_c Type II superconductors in 1986 interest in this area has been rekindled. Prior to this time the only known superconductors required liquid helium cooling systems which for many applications is simply too expensive. One of the chief advantages of the new materials is the relatively low cost of cooling with liquid nitrogen (LN_2). At this time, however, use of high-T_c superconductors is hindered by the limited number of physical forms in which they can be manufactured.

This report describes the development of a two-phase induction motor with a superconducting rotor, part of an ongoing undergraduate research effort at UMR. Such a device will in theory operate as an induction motor only during start-up, after which its behavior will be more like that of a synchronous machine.[1] In other words the small amount of slip characteristic of conventional induction motors goes to zero when the rotor reaches superconductivity. The rotor consists of two high-T_c $YBa_2Cu_3O_x$ discs surrounded by a single-pole copper squirrel cage, all encased in a laminated iron core. Increased efficiency as a result of the elimination of rotor power losses and hysteresis should be seen by comparing the operation of the same rotor with copper discs instead of the superconducting ones.

The theory of operation will be covered first in order to explain why the slip goes to zero and what the expected torque and power outputs should be. The design and implementation of the stator, power supply, rotor, and test apparatus are then described. Finally, an analysis of experimental data is included and compared to theoretical predictions.

THEORY

We will first consider the operation of a classical two-phase induction motor. The motor can be divided into two parts, the stator and the rotor (see Figure 1). The stator consists of four electromagnets placed 90 mechanical degrees apart. These magnets are powered by two a.c. voltage sources that are 90 electrical degrees out of phase, creating a rotating magnetic field. The rotor, centered between all four pole faces, is illustrated in Figures 2 and 3. As shown in these figures the rotor consists of a metallic "squirrel cage," generally copper, embedded in a

laminated iron core. The iron serves as a low-reluctance pathway through which the magnetic flux created by the stator may travel.

Even though each bar of the squirrel cage is connected to the same two end plates the rotor may be thought of as being composed of several discrete rectangular loops or poles. This is shown in Figure 4. The rotating **B** (magnetic) field created by the stator causes a change in the amount of flux passing through each loop. This induces a current in the conductor which works to oppose the change in flux (Lenz's law). The current loop creates a magnetic moment which, due to interaction with the rotating stator field, causes a torque about the axis of the rotor. See Appendix One for a derivation of the torque equation. The flux, Φ, linking one loop is given by the dot product of **B** and the area vector **A**, or $BA\cos\Theta$. If the **B** field rotates with constant angular velocity, w, then the torque on one pole will vary sinusoidally. The minimum number of poles required to create a constant torque is three; since there are two bars per pole most squirrel cages have at least six bars.

An important concept in induction motors is that of slip. The rotor of a conventional induction motor will never reach synchronous speed, w_s, i.e. the speed at which the **B** field rotates. Consider what would happen if somehow we did force the rotor to spin at w_s. At this point the current in the conductors of the squirrel cage would be zero since the flux linked by each loop would remain constant. With no current there is no torque, and with no torque the rotor will begin to slow down due to frictional forces. As the rotational velocity decreases, however, Φ begins to vary sinusoidally, inducing current and torque on the bars of the squirrel cage. There will be a speed at which this torque will balance out the frictional torque. The rotor will continue at that rate until the motor is connected to a load.[2] Slip is defined as the per unit difference between w_s and angular velocity of the rotor, w_r:

$$s = (w_s - w_r)/w_s \tag{1}$$

A common circuit model for the induction motor, the Steinmetz model, relates voltage and current characteristics to those of a transformer.[3] Shown in Figure 5a with its Thevinin equivalent circuit in Figure 5b, it is the basis for all the following equations. The output torque is given by[4]

$$\tau = \frac{2I_2^2 r_2(1-s)/s - P_{rot}}{w_s(1-s)} \tag{2}$$

where P_{rot} is the power loss due to air and rotational friction. The value for maximum torque will be[5]

$$\tau_{max} = 2\frac{\frac{V_i^2}{w_s}\left[\frac{jX_m}{r_1 + j(x_1 + X_m)}\right]^2 \frac{r_2}{s}}{\left(R_1 + \frac{r_2}{s}\right)^2 + (X_1 + x_2)^2} \tag{3}$$

which holds true for any value of r_2, however, for a given r_2 τ_{max} will occur at a particular slip:[6]

$$s_m = \frac{r_2}{\sqrt{R_1^2 + (X_1 + x_2)^2}} \qquad (4)$$

The mechanical power output and efficiency are simply

$$P_{out} = \tau \cdot w_s \cdot (1 - s) \qquad (5)$$

$$\epsilon = P_{out}/P_{in} \qquad (6)$$

with

$$P_{in} = V_1 \cdot I_1 \cdot \cos\Theta_p \qquad (7)$$

where Θ_p is the angle of the phasor impedance seen looking into the input terminals.

It is readily seen that these relationships fail to adequately describe the induction motor with a superconducting rotor. Because the rotor is superconducting its resistance and the slip, r_2 and s, are both zero. Substituting zero for the values of r_2 and s, the above equation for torque becomes the undefined quantity 0/0. Note, however, that for $r_2 = 0$ the slip at which τ_{max} occurs is zero, so it appears that there will indeed be no slip, however, a new expression is need to predict what the torque will be. At the time of this writing we have not completely derived this expression.

As described previously, the primary difference between the conventional and superconducting induction motors is in the rotor; all other components are essentially the same. A motor proposed by Brechna and Kronig employs two squirrel cages, one made from low-grade copper and the other from a superconductor.[7] Theirs was conceived before the advent of high-T_c type II materials, thus a cage of low-T_c niobium, zirconium, or niobium-tin alloy would present no problem other than the system for cooling with liquid helium. High-T_c superconductors are ceramic and therefore very brittle, however, and do not lend themselves readily to being milled or machined. A previous group at UMR working on this project attempted to have a squirrel cage cast from $YBa_2Cu_3O_x$ with no success.[8] For this reason our superconductors were left as discs and encased in an iron core with axes perpendicular to the axis of the rotor shaft as illustrated in Figure 6.

A one-pole copper squirrel cage provides torque during start-up. There can be no start-up torque with an r_2 of zero. This is demonstrated in equation (2) by letting $s = 1$ and $r_2 = 0$. Thus the copper provides the necessary resistance to accelerate the rotor from a standstill. As the rotor achieves minimum slip it is cooled to liquid nitrogen temperatures ($\approx$77 K). Synchronous speed is reached following a transient response as the rotor goes superconducting and the copper ceases to provide torque.[9] It was mentioned earlier that three poles are needed to produce a steady torque on the shaft, but our rotor has only one. Since a steady acceleration of the motor during start-up is not critical in such a small laboratory motor is was decided that one pole would suffice for experimental purposes.

To understand how the machine operates at synchronous speed a brief look at high-T_c

superconductors is in order. Superconductivity is dependent on not only temperature but also on magnetic field strength and current density within the sample. This is shown in Figure 7. Note that there are not one but two critical magnetic field strengths, H_{c1} and H_{c2}. Above H_{c2} there is no superconductivity. Below H_{c1} the sample will behave as a perfect superconductor in which all lines of magnetic flux are expelled from the sample.[10] This complete expulsion of flux from the interior of the superconducting sample is known as the Meissner effect.[11] In the region between H_{c1} and H_{c2} magnetic flux penetrates the sample as flux vortices. The sample remains a superconductor with zero resistance. Any attempt to change the flux density will result in increased vortex density within the sample.[12] If each flux vortex is pinned to imperfections in the sample the average field strength cannot change and a surface current is induced according to Lenz's law. If the flux vortices can easily move in and out of the superconducting sample, the eddy currents induced in the normal metal at the core of each vortex constitute a loss mechanism which creates an a.c. resistance. Strongly pinned flux vortices are necessary for lossless a.c. superconductor operation.[13]

Efforts to create a high-T_c superconducting motor in recent years have not been based on the above principles. Consider a sample cooled in the presence of a gradient field of strength greater then zero but below H_{c1}. Eddy currents acting to expel the internal flux will in turn produce a force on the sample. This idea was used by researchers at Sanyo in a simple Meissner motor in which the superconductors were mounted on the rotor.[14] Another group at the University of Arkansas, Fayetteville, employed superconductors as levitation bearings. Small magnets were mounted at the ends of the rotor shaft, which was levitated above high-T_c discs to achieve low bearing friction.[15]

Our superconducting induction motor does not make use of the Meissner effect, rather, it operates by Lenz's law. As explained previously the rotor is brought to within a few percent of synchronous speed before being cooled. The magnitude of the **H** field, H_0, will be between H_{c1} and H_{c2}. Initially the stator field will still rotate faster than the rotor, so from the point of view of the superconducting discs there is a changing flux density. Again, this induces eddy currents in the sample (Lenz's law) which act to maintain the internal flux density at B_o. These currents create a magnetic dipole which is stationary relative to the rotor itself, unlike the dipoles of the conventional motor which rotate slightly faster than the rotor. This fixed dipole enables the rotor to "catch up" with the stator field, transforming the device into a synchronous machine. Bringing the machine up to speed in this manner is quite similar to the way large industrial synchronous motors are started from a stand-still using auxiliary induction motors.[16]

DESIGN OF THE MOTOR AND TEST APPARATUS

The stator used in this research was designed and constructed by Beckman, Peacher, and Thornborrow, a previous UMR physics group working on this project.[17] Figure 7 illustrates its layout. The four poles are identical electromagnets of 500 turns each whose laminated iron cores measure 1.5" square in cross section. Power is provided to the stator with a two-phase function generator and a power amplifier. The function generator outputs two sinusoids with adjustable relative phase. Setting the phase for 90° will produce a **B** field rotating in one direction while setting it to 270° will rotate it the other way.

Our rotor design expands on that of Beckman et. al., shown in Figure 9, with the

addition of a one-pole squirrel cage and a cylindrical iron core. The squirrel cage provides starting torque while the iron core greatly reduces secondary leakage reactance, x_2. The result is the rotor shown in Figure 6.

A significant problem is created by the need to cool the rotor with liquid nitrogen. For the most efficient use of LN_2 it is best to insulate the rotor from the iron stator cores, which are moderate conductors of heat. To minimize leakage reactance x_2, however, the air gap between the rotor and stator needs to be made as small as possible. In the design by Brechna and Kronig the coolant, in their case liquid helium, is fed through a hollow rotor shaft to the rotor itself.[18] We opted instead to insulate the rotor in a foam-covered plastic container and simply pump LN_2 into the container (see Figure 10 for details). The flow of nitrogen is controlled by the power dissipated in a 30Ω resistor submerged in the large dewar. It was found that six to eight watts provides a flow of nitrogen sufficient to maintain superconductivity. This cooling system is advantageous over that of Brechna and Kronig in that it eliminates the need for a rotating seal on the end of the shaft, however it inevitably increases the width of the air gap.

Self-lubricated ball bearings are used to suspend the shaft. The biggest disadvantage to implementing this type of bearing is that they must be kept warm, preferably close to room temperature; rolling friction increases dramatically as the temperature of the lubricant is lowered. A 68Ω power resistor has been attached to each bearing with good thermal contact provided by silicon heat-sink compound. These resistors are inadequate when used alone, however, because of cold air escaping from the reservoir and blowing directly onto the bearings. For this reason two metal discs 1.5" in diameter with a .25" hole in the center are situated on the shaft just outside the reservoir. With these in place the two heaters work very well with about six watts supplied to each one.

To evaluate the performance of the superconducting induction motor it is necessary to measure the operating speed, the static torque, and the dynamic torque. A simple tachometer has been built which utilizes an interrupter module, illustrated in Figure 11. When the space between the arms of the module is unobstructed the unit outputs zero volts. If a solid object passes through it the output voltage goes to a positive d.c. value. As the rotor shaft turns the holes in the disc pass through the interrupter module, creating a series of short pulses which can be observed on an oscilloscope. Utilizing a frequency counter the frequency of the pulse train can be divided by the number of holes in the disc to obtain the rotor speed.

Measurement of the static torque, τ_s, is fairly simple. Figure 11 illustrates a means of performing this measurement. The spring constant, k, must be found first. With the spring attached to the shaft the motor is turned on and the distance, d, that the spring is stretched is found, which in turn will give the force F being exerted upon it. F is then multiplied by the radius of the rotor shaft, r, giving the value of τ_s.[19]

Finding τ_d, the dynamic torque, takes somewhat more effort. In Figure 12 the shaft is shown with a string wrapped around it a few times with one end tied to a mass and the other connected to a spring. The top of the spring is connected to a stationary object. Once the motor is running and the mass and spring are at fixed positions, the problem becomes one of statics. The frictional force, F_f, is equal to the force due to the spring minus the weight of the mass, W. τ_d is again the force tangent to the surface of the shaft times the shaft radius.

$$\tau_d = r \cdot (F_s - W) \quad (8)$$

EXPERIMENTAL RESULTS

The superconducting induction motor was tested with the rotor constructed by Beckman, Peacher, and Thornborrow. Maximum speed occurred when the stator field angular velocity was at or below 10 Hz although spinning of the rotor could be maintained with w_s as high as 40 Hz. While in theory there should have been no starting torque, the rotor did indeed start from a stand-still by itself when the stator field was at frequencies less than ten hertz. This can be attributed to the nature of the superconducting samples; these samples exhibit very little flux pinning, thus there was eddy current drag in the cores of the flux vortices. If the superconductors exhibited perfect flux pinning there would be no eddy current drag and therefore no net starting torque.[20]

Experimentation with a non-superconducting, one-pole rotor of dimensions similar to the new superconducting one indicated that the torque produced by our stator may be insufficient to overcome the new rotor's rather large moment of inertia. Unfortunately fabrication of the new rotor was not completed in time for it to be tested. If this research is continued it may be desirable to design and construct a smaller superconducting rotor.

CONCLUSIONS AND RECOMMENDATIONS

One of the most significant problems with our motor involved keeping the bearings warm. The ones used were self-lubricated ball bearings which became very lossy when the rotor was cooled. It was necessary to install baffles in addition to small heaters to reduce cooling by convection and conduction, respectively. It may therefore be worthwhile to look into alternative types of bearings, for example air bearings, which require no lubrication and operate with a minimal amount of friction.

There many improvements which can be made on our motor as well as a number of tests which have not yet been performed. The new rotor needs to be tested with superconducting discs that exhibit a high degree of flux pinning. It remains to be seen whether or not the motor will actually run at synchronous speed. Measurements of static and dynamic torque must be made. An expression for the torque on a superconducting disc in a rotating **B** field as a function of Θ should be developed. The resistance and reactance values of the Steinmetz circuit model could be determined from the blocked-rotor and no-load tests.[21] In general what is needed is more experimental data to determine exactly how the motor performs and how practical of a machine it really is.

ACKNOWLEDGEMENTS

Much of the knowledge and guidance behind this project has been patiently provided by Dr. Don M. Sparlin of the University of Missouri-Rolla Physics Department. Thanks also to Mr. Russell Summers for the design and construction of our stator power supply and interrupter module and to Mr. Charles McWhorter for his work in machining several of the vital motor components.

REFERENCES

1. H. Brechna and H. Kronig, "Three-phase induction motor with superconducting cage winding," IEEE Transaction on Magnetics **15(1)**, 715 (1979).
2. George McPherson and Robert D Laramore, An introduction to electrical machine and Transformers (John Wiley and Sons, New York, 1981), 2nd ed., Chap. 4, pp. 243-245.
3. McPherson and Laramore, 247.
4. McPherson and Laramore, 258.
5. McPherson and Laramore, 265.
6. McPherson and Laramore, 267.
7. Brechna and Kronig, 715.
8. D.M. Sparlin, University of Missouri-Rolla Physics Dept., private communication.
9. Brechna and Kronig, 715.
10. Raymond A. Serway, Superconducting supplement for physics for scientists and engineers (Saunders College Publishing, Chicago, 1988), 2nd ed., p. 16.
11. Serway, 10.
12. Serway, 15-17.
13. D.M. Sparlin, private communication.
14. A. Takeoka, A. Ishikawa, M. Suzuki, K. Niki, and Y. Kuwano, "Meissner motor using high-T_c ceramic superconductors," IEEE Transactions on Magnetics **25(2)**, 2511-2514 (1989).
15. David E. Weeks, "High-T_c superconducting levitation motor with laser commutator," Review of Scientific Instruments **61(1)**, 195-197 (1990).
16. McPherson and Laramore, Chap. 2, pp. 93-94.
17. A. Beckman, J.F. Peacher, and C. Thornborrow, UMR Physics Dept., "An induction motor using a high critical temperature superconductor motor."
18. Brechna and Kronig, 715.
19. Beckman, Peacher, and Thornborrow, 13.
20. D.M. Sparlin, private communication.
21. McPherson and Laramore, 276-281.

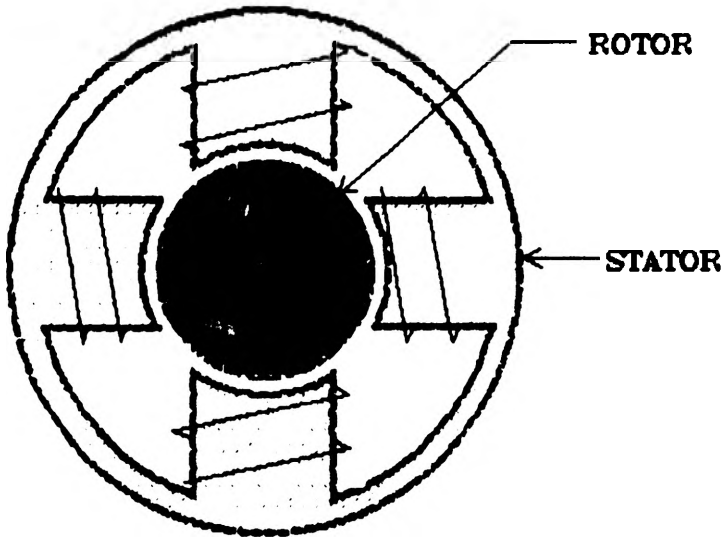

FIGURE 1--CONVENTIONAL INDUCTION MOTOR

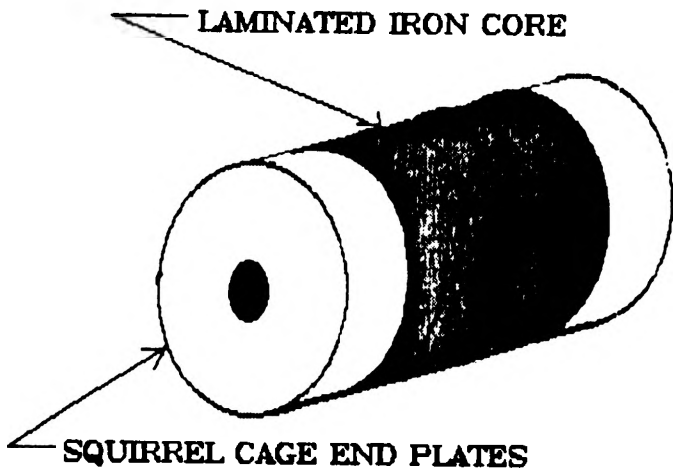

FIGURE 2--TYPICAL ROTOR

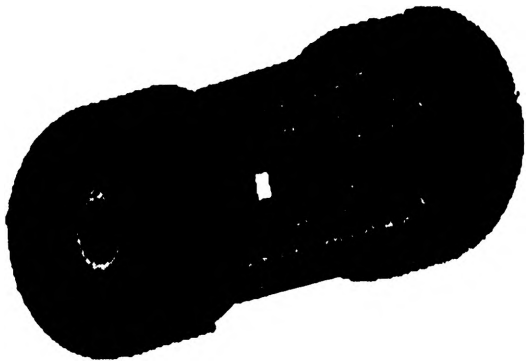

FIGURE 3--ROTOR SQUIRREL CAGE

ILLUSTRATION OF SQUIRREL CAGE AS THREE DISCRETE, ELECTRICALLY ISOLATED LOOPS

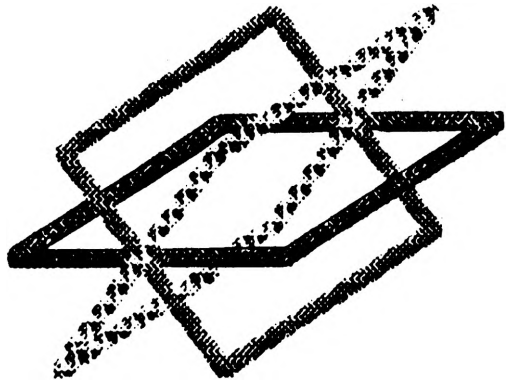

FIGURE 4

STEINMETZ CIRCUIT MODEL FOR THE INDUCTION MOTOR
(ONE PHASE)

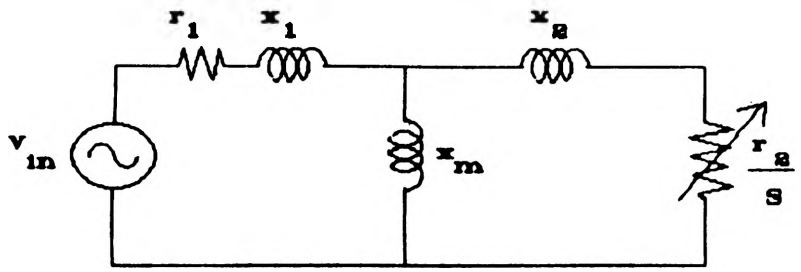

FIGURE 5a

THEVININ EQUIVALENT CIRCUIT

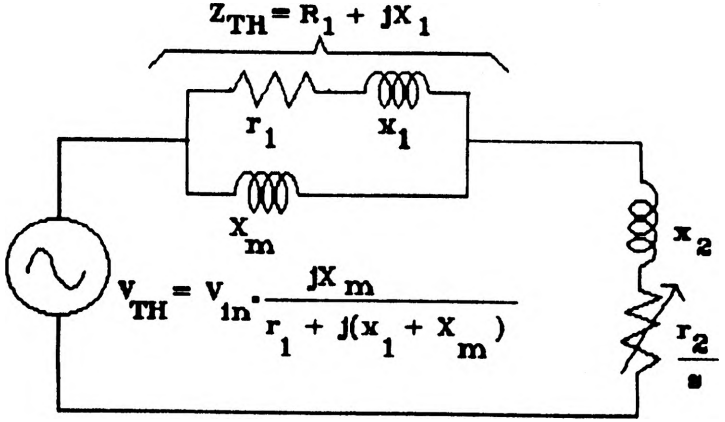

FIGURE 5b

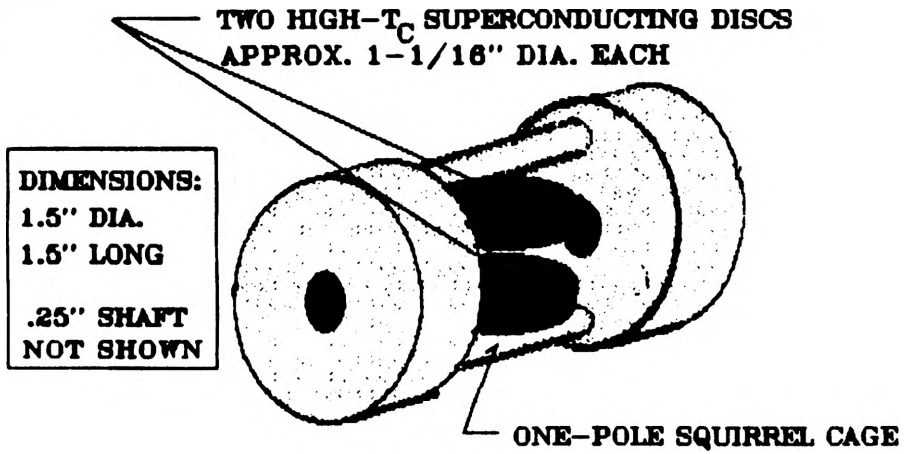

SQUIRREL CAGE AND SUPERCONDUCTING DISCS ENCASED IN LAMINATED IRON CORE AS IN FIGURE 1

FIGURE 6--SUPERCONDUCTING ROTOR

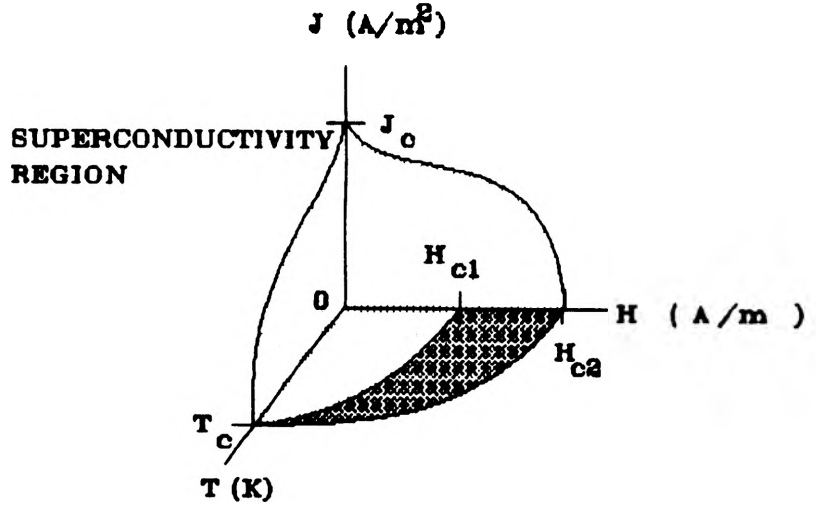

PLAID AREA REPRESENTS FIELD STRENGTHS AT WHICH FLUX PINNING OCCURS.

FIGURE 7

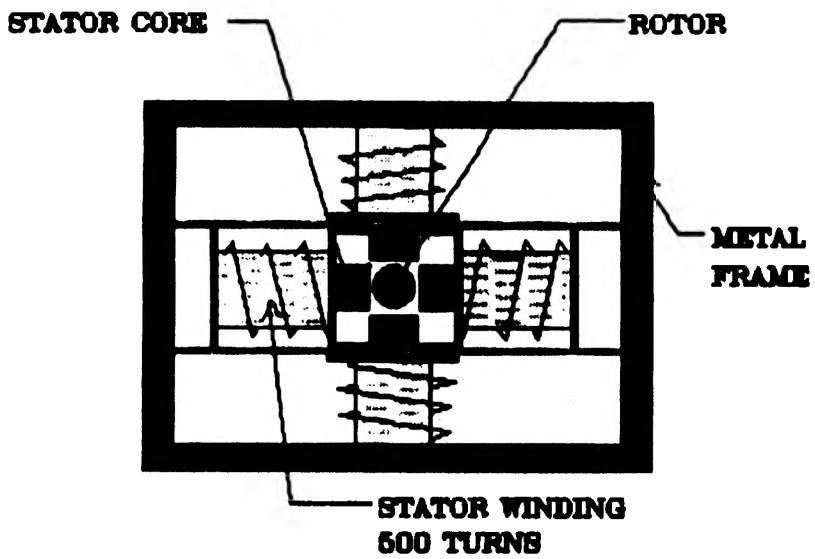

FIGURE 8--MOTOR LAYOUT

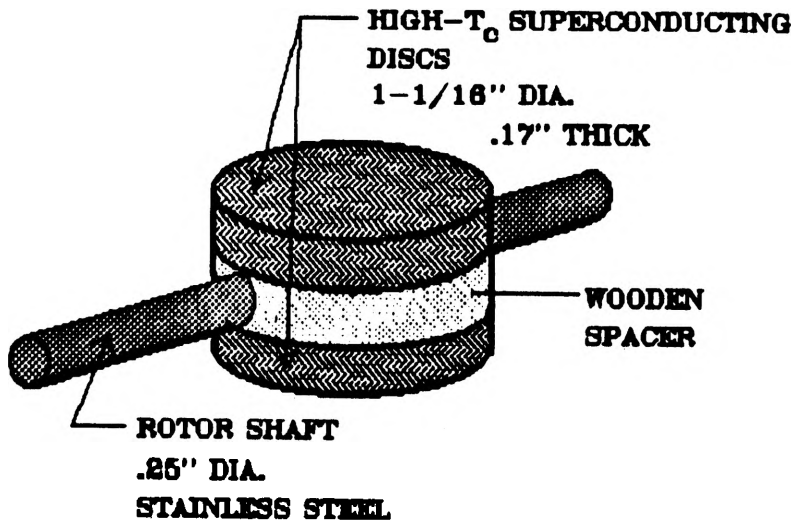

FIGURE 9--EARLY ROTOR DESIGN

TACHOMETER

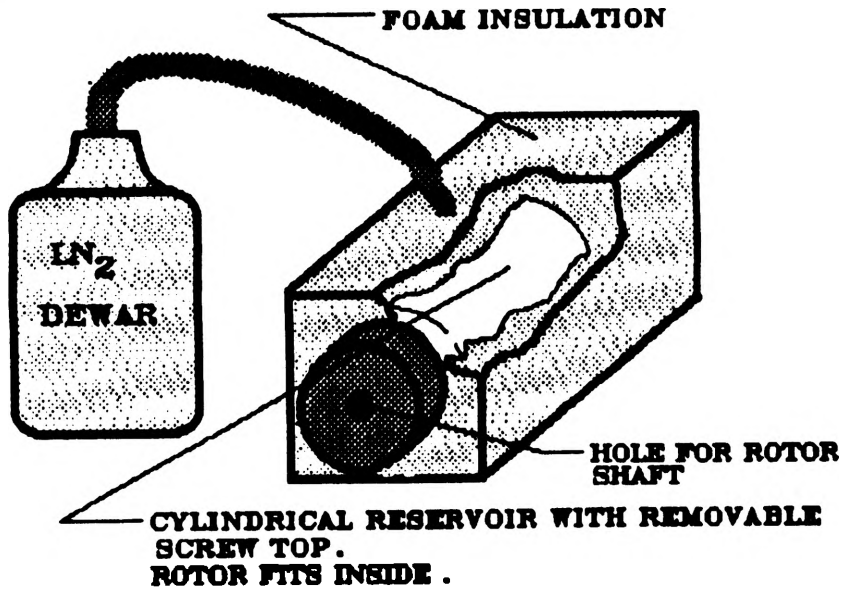

FIGURE 10: LN_2 COOLING SYSTEM

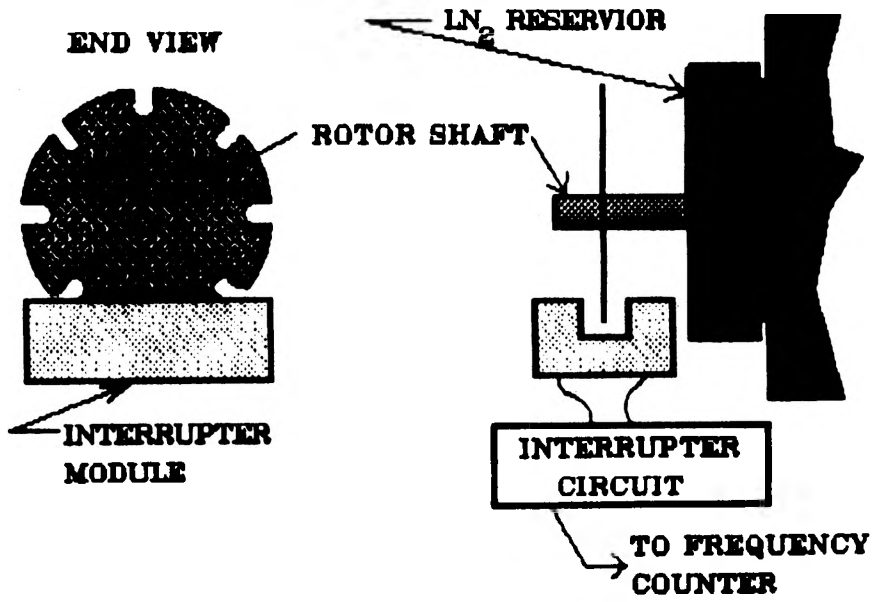

FIGURE 11

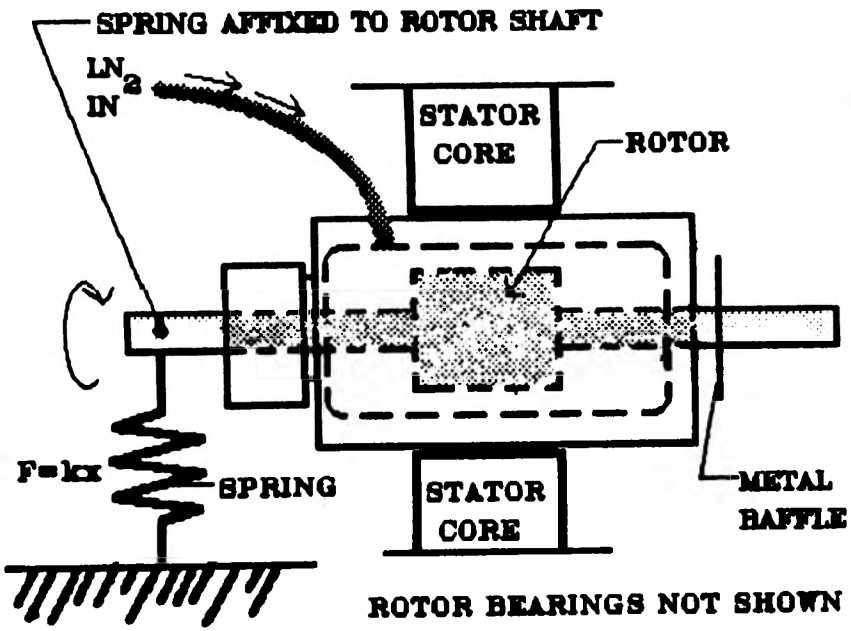

FIGURE 12
MEASUREMENT OF STATIC TORQUE

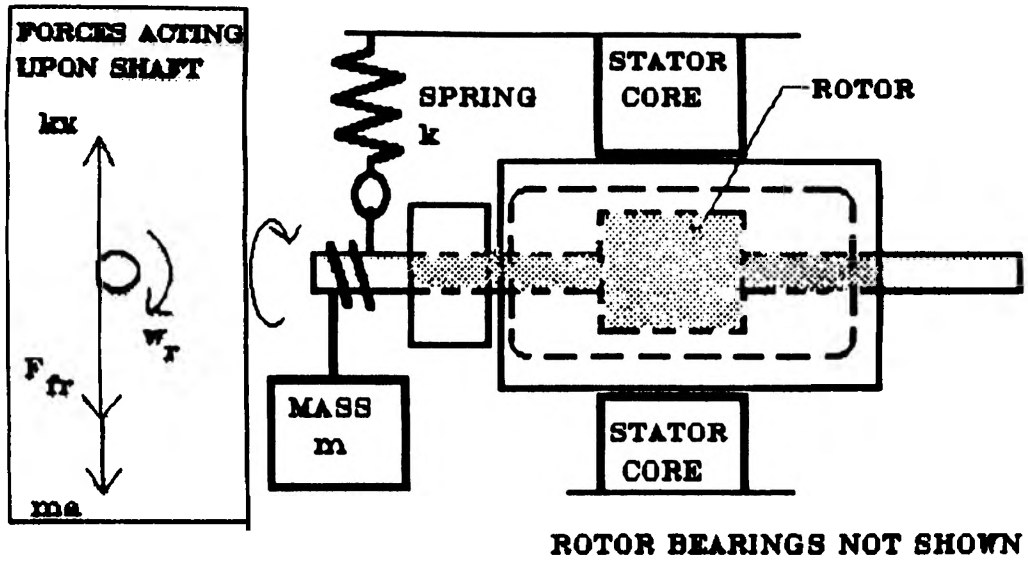

FIGURE 13
MEASUREMENT OF DYNAMIC TORQUE

APPENDIX ONE

Derivation of static torque on a conducting ring.

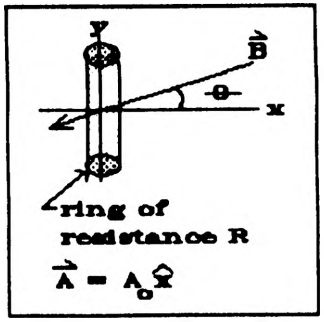

$$\vec{B}(t) = B_o(\hat{x}\cos(\omega t) + \hat{y}\sin(\omega t))$$

$$V(t) = -A_o\hat{z}\cdot\frac{d}{dt}B(t) = A_oB_o\omega(\sin(\omega t))$$

$$I(t) = V(t)/R$$

$$\vec{M}(t) = I(t)\vec{A} = V(t)\vec{A}/R$$

$$\vec{M}(t) = \hat{z}\frac{B_oA_o^2\omega}{R}\sin(\omega t)$$

$$\vec{\tau}(t) = \vec{M}(t)\times\vec{B}(t) = \hat{x}\frac{B_oA_o^2\omega}{R}\sin(\omega t)\times B_o(\hat{x}\cos(\omega t) + \hat{y}\sin(\omega t))$$

$$\vec{\tau}(t) = \hat{z}\frac{B_o^2A_o^2\omega}{R}\sin^2(\omega t)$$

DEVELOPMENT OF SOFTWARE FOR DETECTING CERTAIN KEY FEATURES IN SKIN TUMOR IMAGES

DANA M. BREWER
ELECTRICAL ENGINEERING

ABSTRACT

The goal of Dermvis is to develop a microprocessor-based system that will economically and clearly identify a skin tumor area and type. Dermvis is subdivided into various segments. This segment includes developing software, digitizing images, and manually defining borders in images. Manually drawing borders for digitized images creates bit-maps for average color analysis. Software is developed for determining the average color of the tumor and the surrounding tissue. Batch processing allows images to be analyzed in mass.

INTRODUCTION

Dermvis is the skin cancer project at the University of Missouri-Rolla with the purpose of developing a microprocessor-based system which will identify cancerous lesions. Once identified the cancerous tissue can be removed quickly.

There are seven types of skin cancers currently being considered: melanoma, dysplastic nevus, actinic keratosis (ak), squamous-cell carcinoma (scc), seborrheic keratosis (sk), basal-cell carcinoma (bcc), interdermal nevus (idn). Each genus has characteristics setting it apart from the others. High cure rates are achievable in all of these cancers if detected and treated early. Dermvis' goal is to develop software that will aid dermatologists in the early detection process.

PROJECT DEVELOPMENT

Digital Image Processing

A working image is obtained by taking pictures of the cancerous area and developing them into slides. Red, green, and blue Wratten gelatin filters and an NEC TI-23A camera are used to digitize slide images to produce bit-maps for analysis. (See Appendix C for complete equipment list).

Care should be taken to ensure accurate color depiction before digitizing. An average pixel value program, developed by

Robert McLean, is run to determine the percent difference between the colored filters while the camera is viewing the white translucent cover of the light box. A maximum of five percent difference is allowed. If the difference is greater than five percent, there is a greater risk in misidentifying the tumor class. Once acceptable color is achieved, image processing can begin.

An image is digitized by typing the following command from the keyboard.

digitize -Pc filename.pic

All image files are numbers followed by "n.pic" (e.g. 985n.pic).

The digitize program, also developed by Robert McLean, calls for focusing the image under the red filter. At the same focus, a picture of the image is taken with each filter. The result is a bit-mapped image displayed on an Androx ICS400-1A image processing board. The image focus and color is checked. If there is any question regarding the results, the necessary adjustments are made and the image re-digitized.

Each digitized image uses approximately 760 kilobytes of memory on the Solbourne 5/820 computer and file server. After storing several images temporarily in path "image/dermvis/home/dmb/images" all Dermvis group memory is depleted leaving other users without available storage space. The directory "im -> /spare200" replaced the previous path to free memory capacity for other users. The images were permanently stored on the magneto-optical read/write disk drive (eod) after write privileges were obtained.

It is important to note that all of the images stored on the eod have an identical compressed image available on the network in the directory

image/dermvis/images/compressed.

As a result of a mysterious eod failure, many hours of digitizing time were lost by failing to backup the images to network storage before deleting them from the temporary directory.

Border Identification

Part of the detection process consists of identifying the boundary of the cancerous area. A series of steps will show the bordering process.

It is first necessary to change directories to the eod to access the working images. Then, telnet from Solbourne to the PC images that need to be bordered. (Once experienced with the border program, approximately fifteen images per hour can be completed. It is recommended to border fifteen images, on average, to save time in the telnet process.)

At the C-prompt type "border". This will display a menu on the color monitor from which color images are retrieved,

bordered, and saved. Robert McLean wrote this program and modified it with suggestions from the research team. The modifications improved the quality and presentation of the border program and menu.

Once points are placed around the border and splined, the area within the tumor is specified. Each byte within the border is defined as a binary one and each byte outside the border as a binary zero. The point image is saved as "filename.pnt" and the binary image is saved as "filename.bin". It is this binary image that will be used in the program that determines the average color of the tumor and surrounding skin.

After several images are bordered, telnet back to Solbourne the "*.bin" and "*.pnt" files. The asterisk includes all files with the specified suffix. To save space, all binary and point files are compressed using

```
compress *.bin
compress *.pnt
```

and stored in

image/dermis/border/images/compressed

and

image/dermvis/border/points/compressed,

respectively. To finish the bordering process, telnet back to the PC and remove all image, binary, and point files for the next user.

All bordered images are checked for accuracy by Dr. Van Stoecker, dermatologist, and discussed with the researchers. Any alterations in the tumor boundary are made and the corrected binary and point images are saved, compressed, and stored in their respective directories.

Average Color Program and Analysis

Most tumors are nevi (i.e. moles) and lesions of which color is the most identifying mark. The "Bittest" program (Appendix A) is designed to find the average color. The first section of the program makes the variable assignments. One variable, "constant unsigned character mask[8]" will be logically "anded" with the previously digitized bit-mapped image. This will identify the bytes lying within the tumor for which the color must be averaged.

The next section of the program identifies any problems in accessing files or memory. The program stops and prints the error message corresponding to the problem.

After the proper files have been opened and memory allotted, average color analysis begins. Analysis begins by finding image resolution which determines the number of bytes in the image. For each byte there are eight bits and for each bit there are three possible colors represented, one for each color plane made

in the digitizing process. The program evaluates each pixel in the image and identifies it as tumor or non-tumor area. The average color of the tumor is determined by summing the color bits and dividing by the total tumor area.

"Bittest" was modified to determine the average color of the tissue defined as non-tumor. This process works the same as described in the previous paragraph. The average red in the cancerous tissue is red/area and the average red outside the tumor is redout/areaout.

The last section of the program prints the results of the analysis in a clearly identified manner.

Appendix B is a batch program designed to run a large quantity of images through the average color program. The batch program was written by Kishore Khemani and myself and is used to interface the average color program output to the color triangle program input. The statement "rm -f $output" removes any data that may be in the output file to clear it for subsequent processing. Thus, the output files are not appended to previous program runs.

The "while" loop in the batch program runs the range of the images input to the command line. It uncompresses the picture file and runs it through "Bittest", routing the output to the "set output" path. Finally, it re-compresses the picture file for storage on the network.

The second program is the color triangle developed by Kishore Khemani. This program converts the average color program output into rectangular coordinates and plots it on the color triangle. The triangle vertices represent red, green, and blue. The center of the triangle is represented by a white spot. As the software is further developed each tumor class will hopefully cluster in a specific area on the color triangle.

AREAS FOR FURTHER CONSIDERATION

It is important to back up the work. Many hours of digitizing could have been saved by compressing the images and storing them on the network prior to writing them to the eod. Eod problems and failures were investigated on several occasions and a root cause has yet to be found. Cost considerations make replacement of the eod unlikely.

It may be appropriate to consider a heat analysis of the cancerous area. A comparison of the heat differential between the cancerous area and non-cancerous area may aid in the border definition process. This would reduce the amount of time taken to manually define and check tumor boundaries. This type of analysis however, will take more funding and equipment than is presently available and is not feasible without outside sponsoring.

Another research possibility as an aid in border definition is use of magnetic resonance imaging (MRI). MRI applies strong magnetic fields and radio-frequency pulses to the soft tissues of the body. The image is transmitted to a monitor from which the

tissues may be analyzed for border, heat, luminescence, etc. This process is also costly, but may be possible with cooperation from the Phelps County Regional Hospital.

CONCLUSION

There is much frustration with the equipment. Without the eod working properly it is very difficult to acquire image files to test software development. The average color program works and all of the images have been bordered, except those most recently digitized.

Acknowledgments

Dr. Randy H. Moss, faculty advisor, provided me the opportunity to participate in the Dermvis research project.

Dr. W. Van Stoecker, dermatologist, initiated Dermvis and invited student research participation.

APPENDIX A
BITTEST

```
#include <stdio.h>
main(argc, argv)
int argc;
char *argv[];
{

  /*variable assignments*/

  FILE *image, *color;
  int i, xres, yres, done;

        /*color values for tumor*/
  long red, green, blue, area;

        /*color values for area outside the tumor*/
  long redout, greenout, blueout, areaout;

  unsigned char  tumor, r, g, b;
  const unsigned char mask[8]={128, 64, 32, 16, 8, 4, 2, 1};
  char *magic;

  /*error message for accessing program*/

  if (argc!=3)
  {
    fprintf(stderr,  "USAGE: %s bitfile picfile\n", argv[0]);
    return -1;
  }

  /*error message for accessing the image file*/

  image= fopen(argv[1], "r");
  if (image==NULL)
  {
      fprintf(stderr, "Something went wrong when opening image
file.\n");
    return -1;
  }

  /*error message for memory assignment*/

  magic= (char *) malloc(6);
  if (magic==NULL)
  {
        fprintf(stderr,  "Something went wrong when allocating
memory.\n");
    return -1;
  }
```

```
  /*error message for file type*/

  for (i=0; i<5; i++)
    magic[i]= (char) getc(image);
  magic[i]='\0';
  if (strcmp("FBMAP", magic)!=0)
  {
    fprintf(stderr, "This is not a bit map file.\n");
    return -1;
  }

  /*error message for accessing image file*/
  color= fopen(argv[2], "r");
  if (color==NULL)
  {
      fprintf(stderr, "Something went wrong when opening color
file.\n");
    return -1;
  }

   /*Once the other tests have been passed the average color
analysis begins.*/

  printf("This is a bit map file.\n\n");
  xres=getc(image);
  xres+=getc(image)<<8;
  yres=getc(image);
  yres+=getc(image)<<8;
  done=xres*yres;

        /*"done" is the number of bytes on the screen*/
  done=done/8;

        /*initializing tumor shades to zero*/
  red=green=blue=0;

        /*initializing area of tumor to zero*/
  area=0;

        /*initialize nontumor shades to zero*/
  redout=greenout=blueout=0;

        /*initialize nontumor area to zero*/
  areaout=0;

/*One time through the loop reads value of each color bit in the
byte for a total of "done" loops*/

  while(done>=0)
```

```
  {
    tumor=getc(image);
    done--;
    for(i=0; i<8; i++)
    {
      r=getc(color);
      g=getc(color);
      b=getc(color);

/*Find average color of the tumor tissue.*/

      if((tumor&mask[i])!=0)
      {
        red+=r;
        green+=g;
        blue+=b;
        area++;
      }

         /*Find the average color of the tissue surrounding the
tumor.*/

      else if(r>1.05*g && r>1.05*b && r>50)
      {
        redout+=r;
        greenout+=g;
        blueout+=b;
        areaout++;
      }
    }
  }
  printf("Average tissue color within the tumor for\n");
  printf("%s.\n\n", argv[1]);
  printf("Red %9.3f\n",(double) red/area);
  printf("Green %7.3f\n",(double) green/area);
  printf("Blue %8.3f\n\n",(double) blue/area);
  printf("Average tissue color outside the tumor.\n\n");
  printf("Red %9.3f\n", (double) redout/areaout);
  printf("Green %7.3f\n", (double) greenout/areaout);
  printf("Blue %8.3f\n", (double)blueout/areaout);
}
```

APPENDIX B
PROGRAM FOR BATCH PROCESSING

```
#! /bin/csh

#set any and all of the variables that will be used in this
#program

set output = /image/dermvis/home/dmb/src/skin/output
set image_dir = /eod
set bin_img_dir = /image/dermvis/border/images/compressed
set program = /image/dermvis/home/dmb/src/skin/bittest

#make sure the proper number of parameters were passed on the
#command line

if($#argv != 2) then
  echo "USAGE:  first_img last_img"
  exit -1
endif

#switch order of parameters if they were given in the wrong order

if ($1 > $2) then
  @ first = $2
  @ last  = $1
else
  @ first = $1
  @ last  = $2
endif

#start the batch

#remove the previous results

rm -r $output

#create a new result

while($first <= $last)
  if(-e $bin_img_dir"/"$first".bin.Z") then
    uncompress $bin_img_dir"/"$first".bin.Z"
                          $program      $bin_img_dir"/"$first".bin"
$image_dir"/"$first"n.pic" >> $output
    compress $bin_img_dir"/"$first".bin"
  endif
  @ first++
end
```

APPENDIX C
EQUIPMENT

Androx ICS400-1A image processing board
Solbourne 5/820 computer and file server
TrueVision ATVista 2M color frame-grabber board
20 MHz 80386-based AT-compatible computer
IDEK MF5015 color multi-sync monitor
NEC TI-23A camera
32 Mbyte RAM and 2 1024 Mbyte hard drives
Magneto-optical read/write disk drive (eod)
Red, green, and blue Wratten gelatin filters

ROBOTICS DEVELOPMENT AND DESIGN: OPTICAL AND COMPUTER CONTROLS

David E. Brown
EE Department

ABSTRACT

In industry today, the use of robotic systems is growing. They can be found in many diverse applications including washing dishes, assembling automobiles and carrying explosives. With such a wide range of applications, robotic systems are a very important division of engineering.

Designing such systems requires an interaction between different disciplines of engineering. In the work world, engineers are required to interrelate with other engineers of differing disciplines and backgrounds. This research was designed to implement this type of partnership and develop a project that required the knowledge of an electrical, a mechanical and a computer science engineer.

Using the Motorola M68HC11 microprocessor, this system is designed as a prototype for a self-contained robot. The robot will have the ability to learn paths and be remote-controlled. With a few modifications this robot would be ready to be adapted to a desired task.

This research investigates the application of this single board processor and the design process required to create a small robot with self-guidance capabilities.

INTRODUCTION

In engineering, the most important aspect of our education is the ability to put text book theory into solid working answers. This research promotes the practice of engineering in three different disciplines of engineering. The topic of robotics was chosen in order to benefit more from the interaction of electrical, mechanical and computer science engineering and the hands-on application of engineering.

The design and creation of a robot is a long process of decisions. The designer must decide on a general purpose that is flexible for the robot so that it will be flexible to many purposes. The purpose chosen then leads to the design of the carriage, drive train, controller, and communication between operator and robot control. This research contains the necessary design processes implemented to complete this project.

USING THE M68HC11EVB MICROCOMPUTER CONTROL BOARD

The center of this research fell on the use of a micro-controller as a central processing unit for the robot and its controls. The M68HC11EVB evaluation board is a flexible controller designed to interface with a personal computer or other controller for input. The board was chosen to act as a total processor on board the robot. The micro-processor was designed to read the inputs from the optical sensors and bump switches, process the information and translate it into a wave drive signal for the stepper motors.

The evaluation board is first connected to a personal computer for external control and monitoring. A cable was made to tie the terminal port of the M68HC11EVB to the com1: communications port of the computer. This cable is the RS-232 type cable similar to a parallel printer cable. The cable was configured to jump the ready line to the ready query line in order to maintain an open input at the computer. The cable was configured as shown below in Figure I.

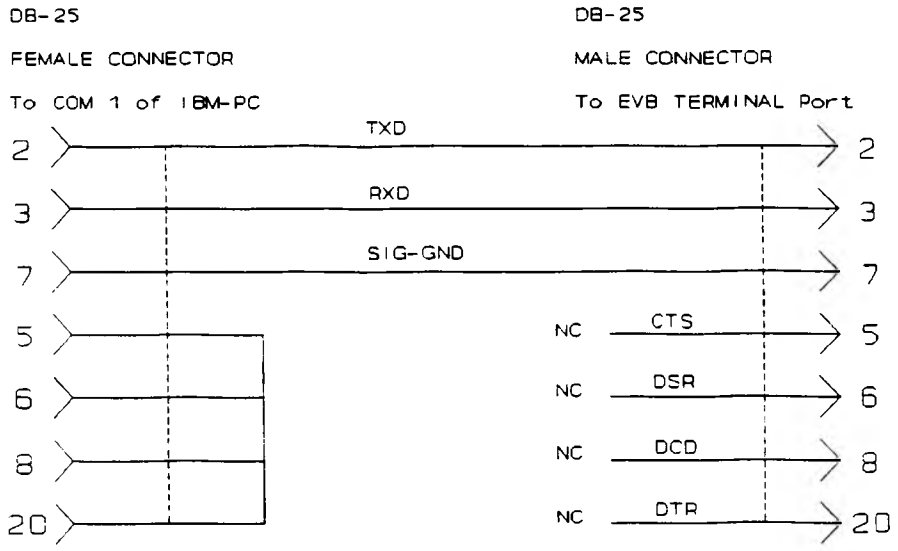

Figure 1: RS-232 Cable Configuration

The connection allows the board to communicate at all times with the computer and therefore the user [1].

Once the evaluation board is connected to the personal computer the input and output ports must be programmed. Ports A-E are each one designed for a specific purpose. The port A pins are configured PA0-PA2 as fixed input pins. Port pins PA3-PA6 are fixed output pins and PA7 is input/output configurable [2]. The Port A pins PA3-PA6 are used in the design as wheel one control output logic. Port B pins PB0-PB7 are configured as fixed output pins [2]. The Port B pins are used as wheel two control output logic. The Port C pins are configured in a complex all input, all output,

all input/output handshake or as a time-multiplexed address/data bus port [2]. Port C pins PC0-PC7 are used in the design as full input for optical sensors. This requires the control bit DDRC to be set to 0 to enable them as a full input port. Port D is configured in a similar manner as the Port C pins. To set the Port D pins as a full input port requires that the control bit DDRD is set to 0. The Port D pins are used as interrupt switches triggered by bump switches on the robot. The Port E pins are configured as fixed directional input pins that alternately function as an A-D converter [2]. The Port D pins have no function in the current design of the project. The pins are all TTL compatible for input and for output. A buffer is needed between the output and any circuitry to be driven since the board tends to be loaded down easily.

The micro-processor board also has specific power needs. A self contained power source designed to set next to the personal computer and tethered to the robot by a 30 foot cord was designed and built. The Power source used a simple design as shown in Figure 2.

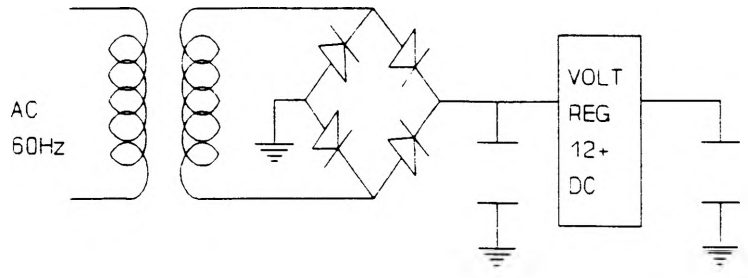

Figure 2: Power Supply Circuit

The capacitors were used to isolate all resonance or ripple out of the power to the computer board. The micro-processor requires 12 volts at .1A, -12 volts at .1A and 5 volts at .5A maximum currents.

The M68HC11EVB evaluation board is programmed using a language called BUFFALO (acronym meaning Bit User Friendly Aid to Logical Operation) [3]. The code is edited in a manageable text editor, such as Turbo C, and then assembled in a cross assembler provided with the board. The cross assembler creates a file filename.s19 which is downloaded using a communications program. The communications program used was KERMIT via the COM1 port [3]. One problem encountered was the board's limited memory. The program was unable to store long enough jump vectors to jump a sufficient number of lines and therefore required address vector jumps which are much more inconvenient. Code instructions can be found in the Reference Manual [2]. The program is not completed and will therefore be appended at a later date.

DESIGNING THE FRAME AND DRIVE SYSTEM

The design of the shape and size of the frame of the robot has a large impact on the other design parameters of the robot. The first step in designing the overall appearance is looking into other work that has already been done and also looking into the purpose of the project. In many catalogs, the use of a round body is utilized to keep the turning radius to a specific distance. The robot needed in this design only needs a predictable turning radius. Others use square designs or rectangles. The robot was designed as a rectangle for ease of placing the sensors and drive motors.

The next big decision to make is the material to use to build the prototype frame. The choice made in this research was aluminum. It is very workable and cheap. The electrical department also had a good supply of it already to purchase. The mechanical engineering department had the tools necessary for the tooling to be done. This made aluminum a good choice. The pieces for the original design were drafted and then cut and assembled. (Figure 3) The design also included a steel rod for the axle and poured and milled aluminum wheels.

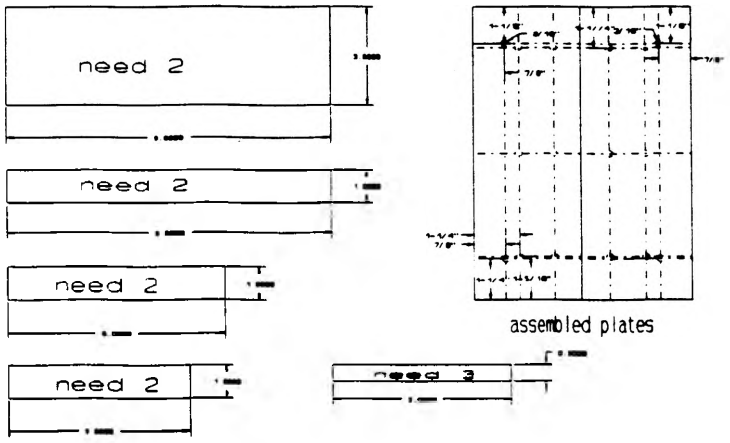

Figure 3: Metal for the Robot Frame

The drive system must be specified to the needs. The robot depends on the robot following commands and carrying them out with little error. There is no feedback of position since the design of a position measure is so difficult in a floor running robot. In order to avoid optical shaft encoder use on the robot, stepper motors were chosen. The motors were chosen on their ability to not slip after stepping and the ability of being strong enough to move the robot. The motors were found in a repossessed parts from old equipment catalog. The strength of 50 oz.in. holding torque was chosen and the steppers were driven as unipolar motors as shown in the EE313 lab manual [4]. This was a cheaper source than any other found. The creation of the mounts for the motor also took some time. The motors needed to stay stationary to ensure tight traction belts and no slippage. Straps were used to tie the motors to an angle with four face bolts to hold the motors.

Using the micro-processor to control the motors requires that there be some kind of switch between the motor power circuit and the TTL output of the board. A buffer is required to keep from loading down the board output power. The motors require five volts and 1 amp of current to energize each coil to be powered up. Unfortunately my first design failed to take into account the drain to source resistance of the VN6000 power MOSFET of approximately 4 ohms. This additional factor increased the voltage source requirements to 9 volts 1 amp per coil per motor. The circuit used to switch the motors is shown
below in Figure 4.

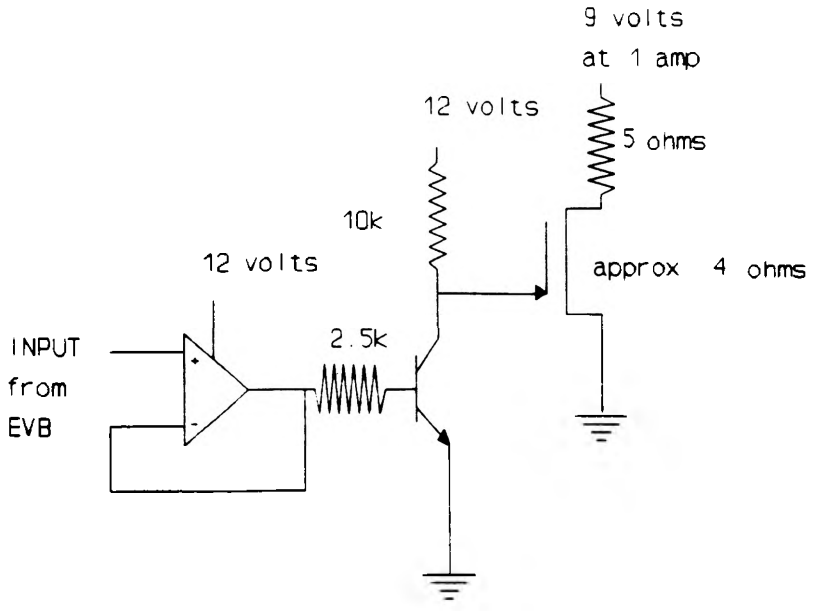

Figure 4: Motor Interfacing Circuit

DESIGNING THE OPTICAL SENSORS

One of the most interesting parts of this research is the optical sensing input devices. There is a wide variety of choices when choosing an optical sensor. The optical sensor type chosen for this project is the Infrared wavelength emitter and detector pair. A photodetector gives to wide a range of sensing and picks up all the light sources in a given room. The infrared sensors allow only the small wavelength around 880 to 975 nanometers to be an influence. Unfortunately the lighting in a room has a high percentage of infrared output [5].

To date, the optical sensors are still under research and design. The optical sensors will bias a bipolar junction transistor to turn on and give a five volt input to the micro-computer. The transistor will act as an amplifier with adjustable gain achieved by means of adjustable resistance in the base and emitter circuit. This will allow the sensitivity of the inputs to be varied for different lighting environments.

BUILDING A MAZE FOR THE ROBOT

The demonstration maze will be constructed as soon as the robot is complete and working. The maze is designed to simulate the use of the robot in an office building where it would possibly be programmed to pick up and deliver mail in the evenings or some other task. The maze will be made of movable walls to simulate any type of corner, room and/or hallway desired. The floor will contain a grid of holes where the walls will bolt down from underneath. Different lengths of wall will be made to be placed anywhere desired. The design is shown below in Figure 5.

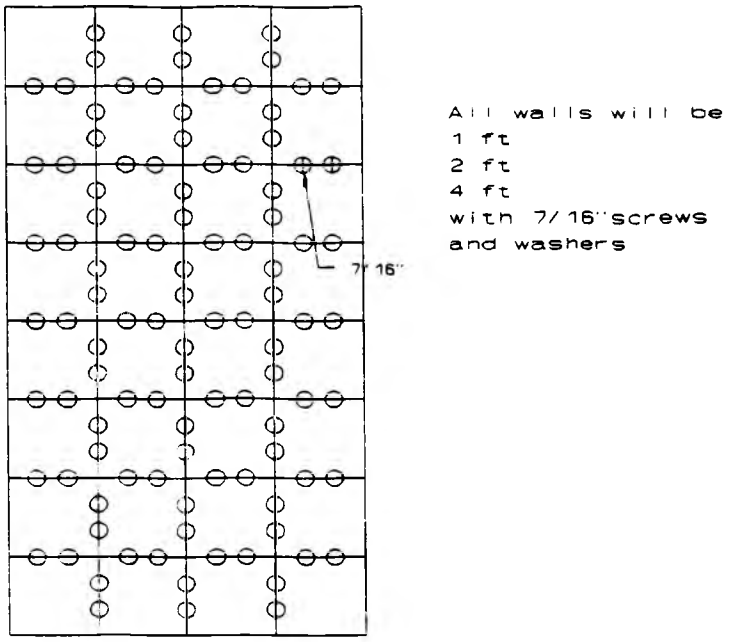

Figure 5: Demonstration Maze for Robot Exhibition

APPLICATIONS FOR RESEARCH

This research is useful in several areas. In places of business or health that humans really shouldn't go a robot can go. Hazardous waste containment someday will be done by robots. Area scavenging where a hand cannot reach. Getting the harvest in faster than man can.

This research was also a great learning tool for the people involved. We learned how to communicate with other engineers from different backgrounds and got a glimpse of what their training has been the past four years. The project also helped our understanding in what it takes to take an idea on paper and make it real. All of these are valuable market tools that must be developed in successful engineers of any discipline.

ACKNOWLEDGMENTS

I would like to thank Dr. Dawson who was my advisor and supporter.

I would also like to thank Dr. Watkins for his interest and advice in the work on this project.

I also appreciate the work of my fellow students Mike Gadbury (Undergraduate Computer Science Engineer) and Craig Potts (Undergraduate Mechanical Engineer) for their time and efforts.

BIBLIOGRAPHY

1. APPLICATIONS NOTE, M68XXXEVX/AN2, MAY 1990, MOTOROLA, PAGES 1-6.

2. HC11 REFERENCE MANUAL, 1990, MOTOROLA, PAGES 7-1 - 7-22, PAGES A-1 - A-113.

3. USER'S MANUAL,M68HC11EVB/D1, MOTOROLA, PAGES 3-1, A-1 - A-4.

4. EE313 LAB MANUAL, 1989, STEPPER DRIVES.

5. Dr Watkins, Electrical Engineering Dept.

STIFFNESS CHANGE EFFECTS ON STRUCTURE CONTROL SYSTEMS

R.J. FALKENRATH, CIVIL ENGINEERING DEPARTMENT

ABSTRACT

This paper contains the results of a computer analysis performed on a two-dimensional model structure, in which the structure response was found under dynamic loading conditions. A structural dynamics program (BASIC) was modified to perform its analysis on a two-dimensional structure with a control system modelled into it. The modified program was then used to determine whether a change in the stiffness of the structure would cause the control algorithm to be ineffective for the structure. In light of the limited scope of the analysis (two-dimensional model with constant applied force on one story), the results indicate that a control algorithm, which dampens the adverse response of the structure under dynamic loading, will continue to be effective if there is a measurable (25%) increase or decrease in the stiffness of the structure.

INTRODUCTION

The basic objective of this research project was to determine whether the control algorithm used to dampen the response of a structure under dynamic loading conditions would be effective if the stiffness of the structure was drastically changed. This problem was simplified by using a two-dimensional model structure and a BASIC program in performing the analysis.

In progressing from the conception of the project to its finish, three major tasks had to be undertaken. First, a working understanding of structural dynamics and the modelling of structural control systems had to be gained. This subject is not in the current curriculum. Second, the BASIC program written by Mario Paz had to be decoded and adapted to perform its analysis using a control algorithm, modelling a structure with a control system [1]. Hand calculations were performed to check the original and adapted programs. Third, a model structure was chosen and the stiffness analysis was performed.

The analysis was performed on a model structure of two stories, thus the scope of the project is limited. A two-dimensional analysis was performed because it displayed the

concepts behind the analysis, without incurring the vast complexity involved in the analysis of higher dimensional structures. Simplifying conditions were established such that the results would be representative, but not past the scope of the time constraints.

THEORY

The analysis was based on structural dynamics with the structure modeled as a mass system with stiffness resisting the displacement of the stories. Viscous damping was neglected for this analysis (C=0). The time dependent force equations for the two-dimensional system are functions of the mass, m, stiffness, k, acceleration, $\ddot{x}$, and displacement, x, and are represented in Figure 1.

$$F_1 = m_1\ddot{x}_1 + k_1x_1 - k_2(x_2 - x_1) = 0$$

$$F_2 = m_2\ddot{x}_2 + k_2(x_2 - x_1) = 0$$

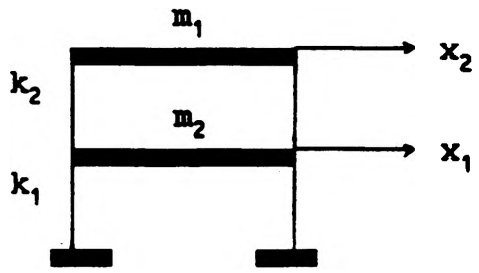

Figure 1. Model two-dimensional structure.

The control forces, U are added to the above force equations, at a short time increment, dt, after the initial forces are applied, as follows:

$$F_1'(t+dt) = F_1(t+dt) + U_1(t)$$

$$F_2'(t+dt) = F_2(t+dt) + U_2(t)$$

The control forces at one time increment are a function of the velocity, $\dot{x}$ caused by the forces at the previous time increment. They are also a function of the mass, m, time increment, dt, and the control algorithm inputs, Q and R. All Q's were set at unity so that only a scaled R value had to be input into the equation. All R's were set equal for this same reason. The control forces are as follows:

$$U_1(t) = (dt / 2)[Q / (R * m_1)] * x_1(t)$$

$$U_2(t) = (dt / 2)[Q / (R * m_2)] * x_2(t) - U_1(t)$$

A force applied to the second story adds another component to the force equation and causes the accelerations, velocities, and displacements, of which the control forces work to counteract.

METHODOLOGY

The project was divided into three phases. The first phase consisted of learning enough about structural dynamics and structural control systems to perform the project. This was accomplished by the study of references on the subject [1,2,3,4]. Reading and problem assignments were given by the faculty advisor. The faculty advisor monitored the progress and decided when the next phase of the project could be engaged.

The second phase of the project began with the task of decoding the BASIC structural analysis program[1]. This was accomplished by checking the results of a text problem performed using the program with hand calculations [1]. After an understanding of the program was gained, the source code had to be adapted to accept the use of a control algorithm for a two story mass structure with control on both floors. This too was checked upon completion by hand calculations.

The third phase of the project involved using a model structure, finding a control algorithm input value to maximize the dampening effects of the control, checking if the control worked for other forcing functions, and finally, performing the stiffness parameter study. An example problem was used in which the mass, stiffness, and damping matrices were known [1].

PROBLEM 18.1. Determine the response of a two-degree-of-freedom system excited by a constant force of magnitude 10 Kips and duration 0.3 seconds acting on the second coordinate. The stiffness, mass and damping matrices of the system are:

$$[K] = \begin{bmatrix} 75 & -44.3 \\ -44.3 & 44.3 \end{bmatrix} \text{(k/in)}$$

$$[M] = \begin{bmatrix} 0.136 & 0 \\ 0 & 0.066 \end{bmatrix} \text{(k} \cdot \text{sec}^2\text{/in)},$$

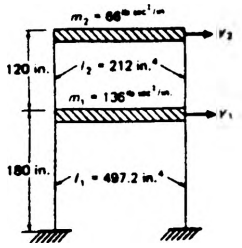

Figure 2. Example Problem.

A constant applied force was used for the forcing function in the determination of the control algorithm input value and the final stiffness parameter study. An optimum control algorithm input value was found by iteration. Increasing and decreasing forcing functions were used to make sure that the input value was optimum for forcing functions that were not constant. The stiffness parameter study involved the increasing and decreasing of the stiffness of the model structure by 5% increments up to 125% and down to 75% of the original stiffness.

RESULTS

The computer analysis results are in the form of a time history printout, showing for each time step and each story, the incremental force, control force, displacement, velocity, and acceleration response of the structure to the applied dynamic force. To find the optimum control algorithm input value, all five of the data outputs were compared to the output for the structure without control. Of the data, the forces developed at the different stories and the displacement of each story are the most important analysis results. The data is best presented by plotting, on the same graph, the output from the structure without control and the output from the structure with control versus time.

Figures 3. and 4. display the response forces, as a function of time, for story 1 and 2, respectively. These are the response forces developed in the structure under a constant applied force to story 2. Notice that the control dampens the adverse effects of the applied force and that story 2 developed larger forces than did story 1.

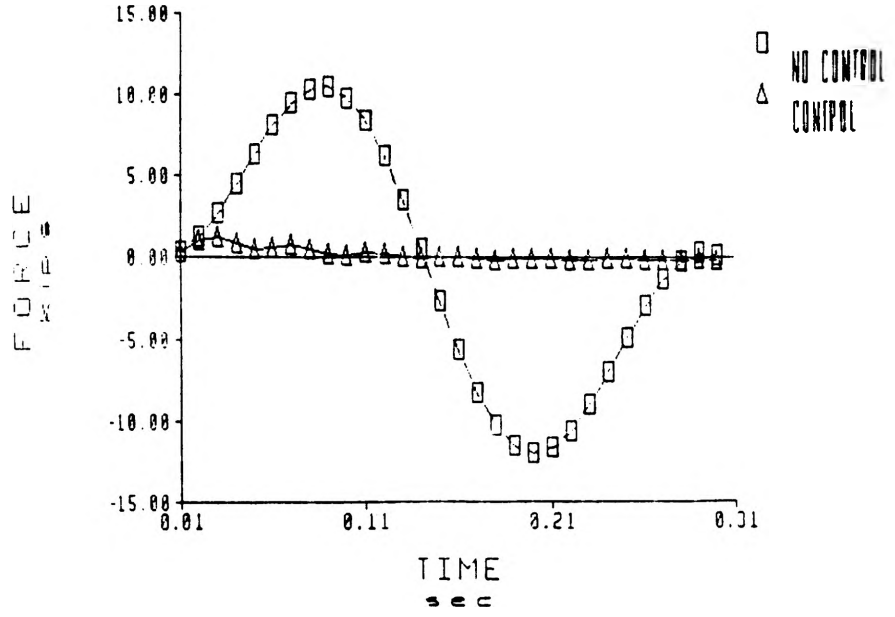

Figure 3. Response Forces of Story 1 Under a Constant Applied Force to Story 2, With and Without Control.

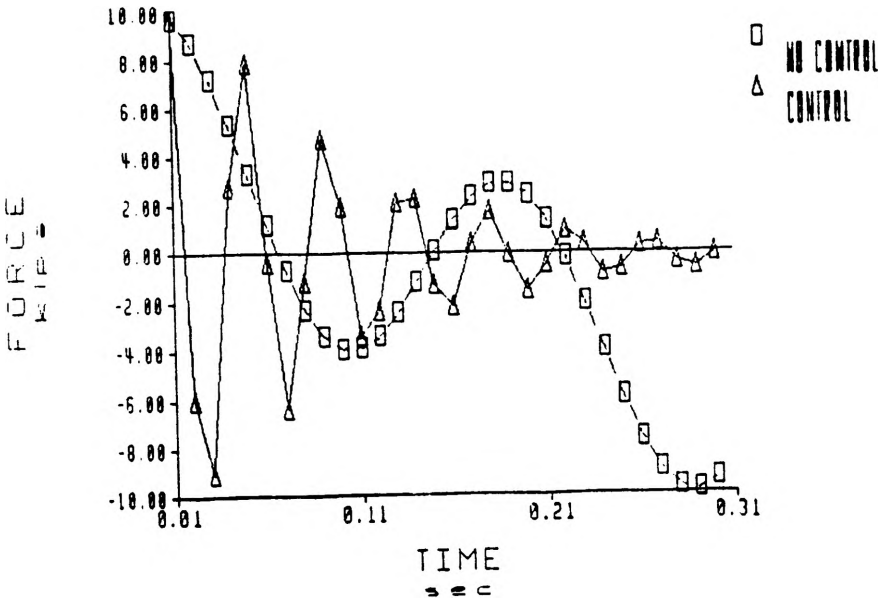

Figure 4. Response Forces of Story 2 Under a Constant Applied Force to Story 2, With and Without Control.

Figures 5. and 6. show the displacements, as a function of time, for story 1 and 2, respectively. These are the displacements corresponding to the application of a constant force to story 2. In comparison with Figure 3. and 4., the response forces and displacements follow the same shaped function of time. This is not true for the velocity and acceleration responses, however.

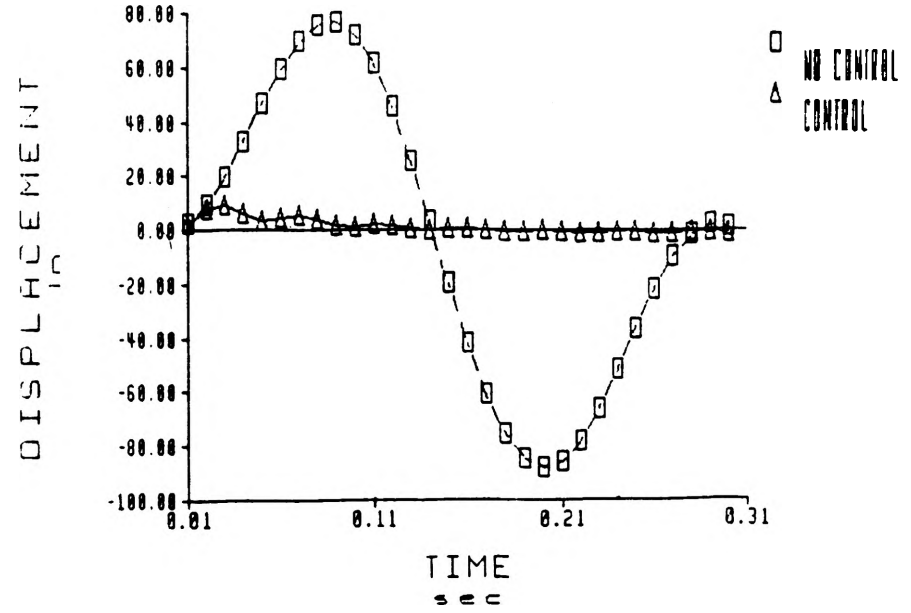

Figure 5. Displacement of Story 1 Under a Constant Applied Force to Story 2, With and Without Control.

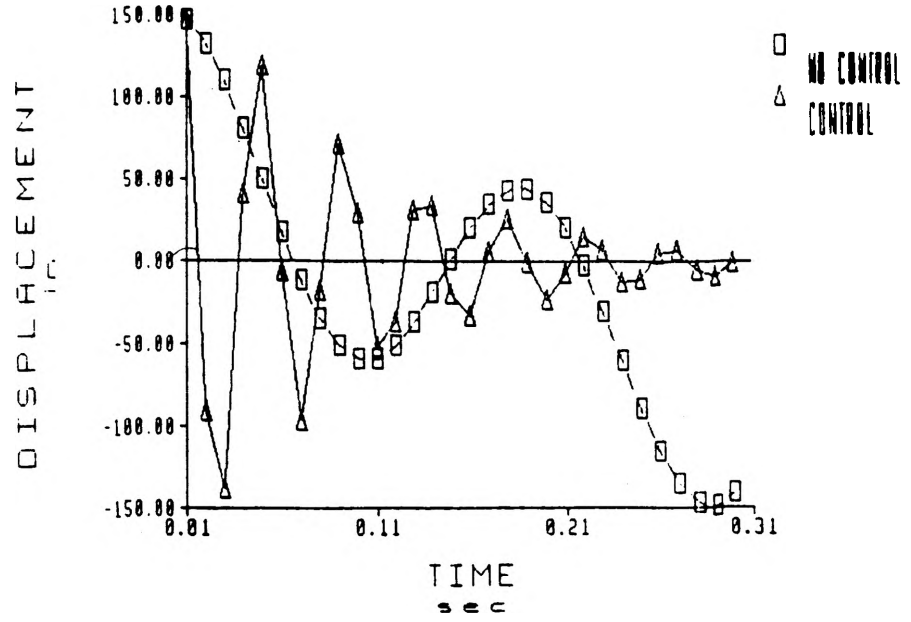

Figure 6. Displacement of Story 2 Under a Constant Applied Force to Story 2, With and Without Control.

Figure 7. displays the control forces of stories 1 and 2, propagated under a constant applied force on story 2. It can be seen that the control forces develop opposite to the response forces, as they should by definition.

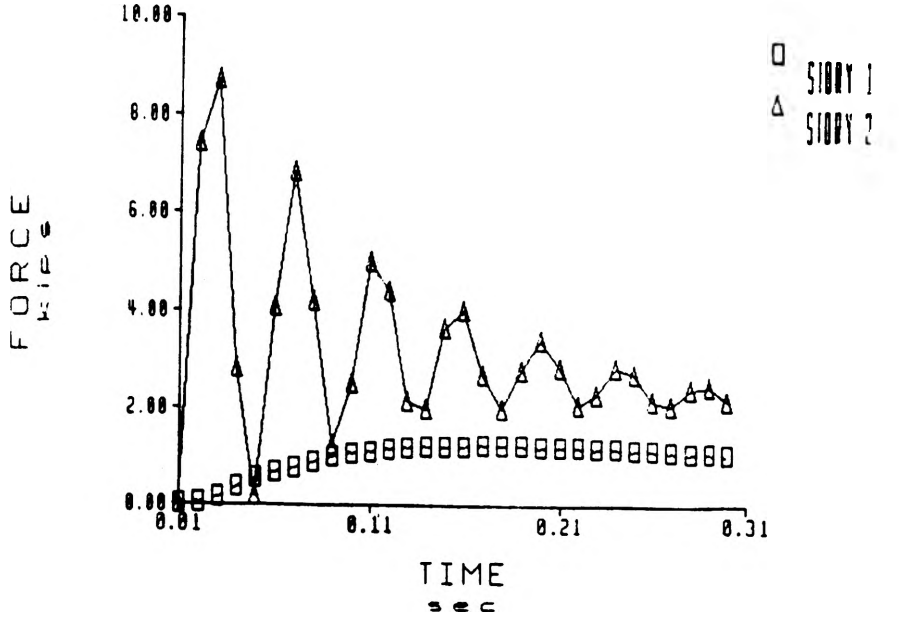

Figure 7. Control Forces of Stories 1 and 2 Under a Constant Applied Force.

The stiffness parameter study produced results of which the worst cases are presented in Figure 8. and 9. The response forces for a constant applied force on story 2, at 75, 100, and 125 percent of the original stiffness, are plotted as functions of time for story 1 and 2, respectfully. In that the displacements follow the same shaped curve, they have not been presented here.

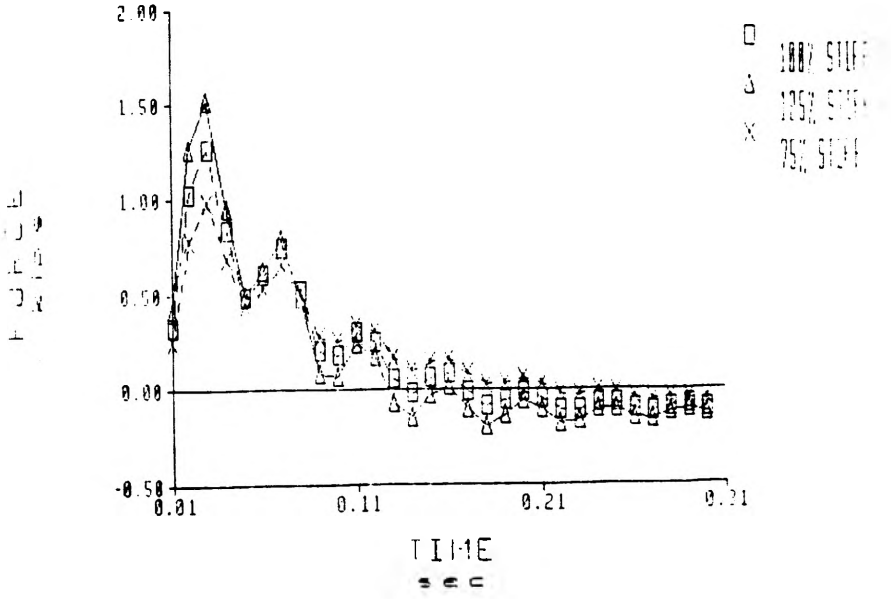

Figure 8. Response Forces of Story 1 Under a Constant Applied Force to Story 2, for 75, 100, and 125 Percent of the Original Stiffness.

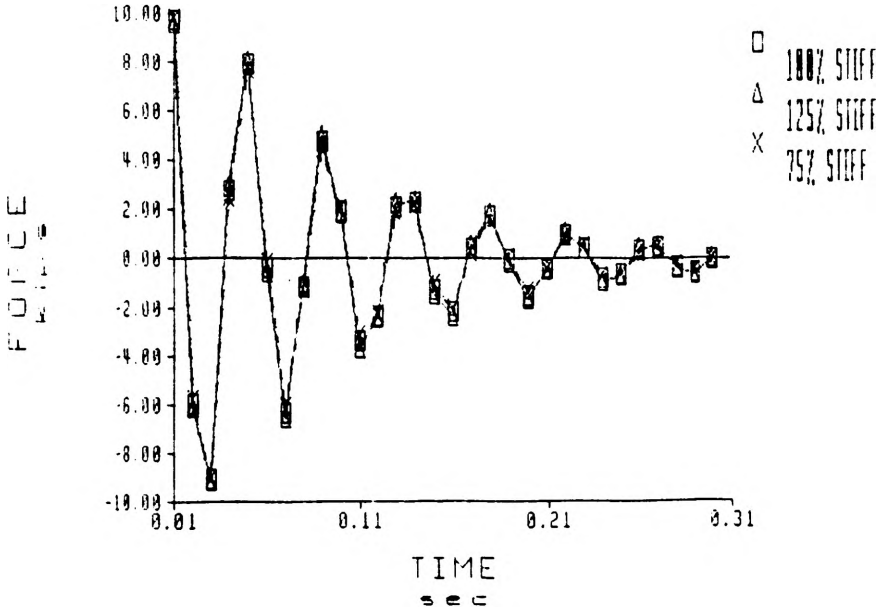

Figure 9. Response Forces of Story 2 Under a Constant Applied Force to Story 2, for 75, 100, and 125 Percent of the Original Stiffness.

CONCLUSIONS

The results of this project show that for a modelled structure, the control algorithm, once set for optimum control, will not be measurably effected by a change in the stiffness of the structure. Whether or not this holds true for real structures is beyond the scope of this project, but the fact that there are structures with control systems in operation today is an indication that it could be applicable. If the results of this project are pertinent to real structures, then those structures with control systems are not in danger of failure due to a change in stiffness causing the control system to break down. This is both legally and ethically important to the engineers designing and installing control systems in structures as well as the owners and occupants of those structures.

ACKNOWLEDGEMENTS

The faculty advisor for this project was former University of Missouri-Rolla professor of Civil Engineering, Dr. C.P. Pantelides. Dr. Pantelides has published papers on the subject of structures with control systems, and is knowledgeable in the field of structural dynamics [4]. Without his knowledge, ideas, and guidance this project would not have been made possible.

REFERENCES

1. M. Paz, Microcomputer-Aided Engineering: Structural Dynamics. New York: Van Nostrand Reinhold, 1986.
2. Warburton, G.B. The Dynamical Behaviour of Structures. 2nd ed. Oxford, England: Pergamon, 1976.
3. Hibbeler, R.C. Structural Analysis. 2nd ed. New York: Macmillan, 1990.
4. Pantelides, C.P. "Computer-Controlled Structures." Computers & Structures. Vol. 34, No. 5, pp. 715-725 Oxford, England: Pergamon, 1990.

INSTANT CENTERS OF VELOCITY IN A KINEMATICALLY INTELLIGENT BLACKBOARD ENVIRONMENT

R. Jeff Fensterman Mechanical Engineering Department

ABSTRACT

This project was part of a continuing expansion of a graphical software environment called "Skimp", originally developed by Dr. J. K. Nisbett.[1] The final version of this software package will allow the kinematic concepts of an introductory machine dynamics class to be taught exclusively on a blackboard sized projected computer screen. This software package will be used as a teaching aid in the classroom as well as a tutorial for students outside the classroom.

The scope of this project was limited to the concept of instant centers of velocity. This portion is a subroutine accessible during the regular execution of the program. The subroutine has three modes of operation which include automatic, automatic with construction lines, and tutorial.

INTRODUCTION

Background

The graphical software environment called "SKIMP" was originally developed by Dr. J.K. Nisbett as part of his Master's thesis at the University of Texas at Arlington. The scope of Dr. Nisbett's original program was limited to the construction and animation of various planar linkages. This original work allowed the construction of planar linkages, not limited to the standard four bar linkages, using both revolute and prismatic joints. Though initially limited to pre-processing for analysis through the computer aided sketching of mechanisms, Dr. Nisbett recognized the potential of an expanded version of this software as both a teaching aid and tutorial.

Theory

The instantaneous center of velocity is defined as the instantaneous location of a pair of coincident points of two different rigid bodies for which the absolute velocities of the two points are equal.[2] By the definition, the pin joints P_{12}, P_{23}, P_{34}, and P_{14}, are instant centers between the links they connect (see figure 1). Body 2 and Body 3 are two rigid bodies which have a pair of coincident points. The pin joint is a point on both bodies. These points are coincident and the absolute velocity for the points on both bodies are equal. A similar argument can be made for all remaining pin joints.

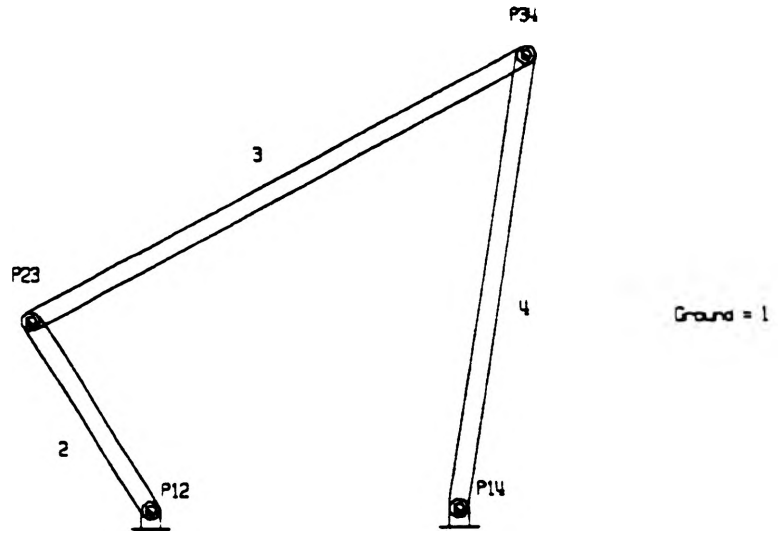

Figure 1. Standard Four Bar Linkage

For the case of straight line sliding motion between two links, the instant center of velocity will be on a line normal to the motion at a distance of infinity (see Figure 2).

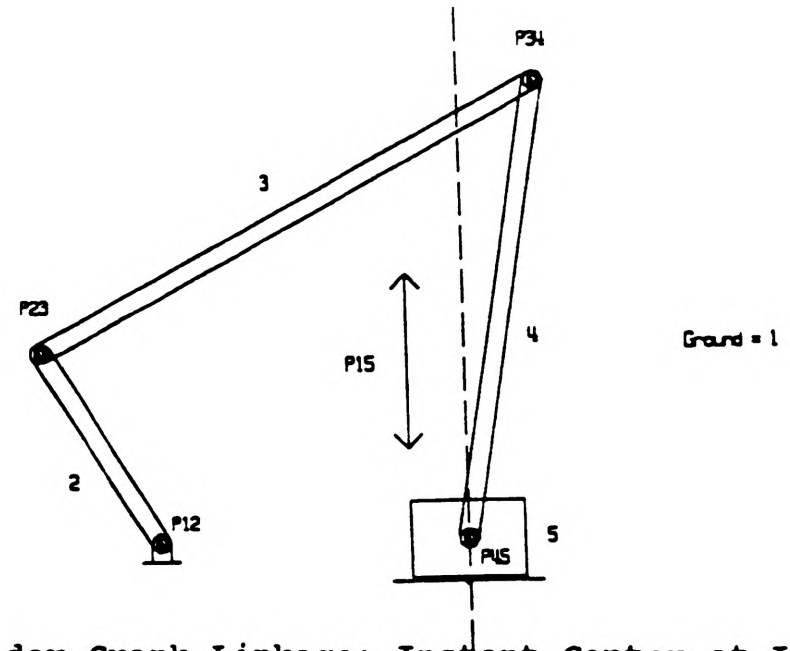

Figure 2. Slider Crank Linkage: Instant Center at Infinity

This is a known instant center of velocity which is equivalent to a pin joint connecting the two bodies at infinity.

For each linkage there are N number of instant centers as defined by Equation (1) where n is equal to the number of links in the mechanism.[2]

$$N = \frac{n(n-1)}{2} \quad (1)$$

Instant centers of velocity that are not found by obvious application of the definition are located by applying the Aronhold-Kennedy Theorem of three centers. This theorem states that the three instant centers shared by three rigid bodies in relative motion to one another (connected or not) all lie on the same straight line.[2] Body 2 (see Figure 1) is part of two sets of three rigid bodies for which this theorem can be applied. Body 2 has relative motion with bodies 3 and 4, as well as bodies 1 (ground) and 4. Applying the theorem to the first set of rigid bodies, bodies 2,3 and 4, leads to the conclusion that the instant center of velocity between bodies 2 and 4 lies somewhere on the line that passes through instant centers P_{23} and P_{34} (see Figure 3).

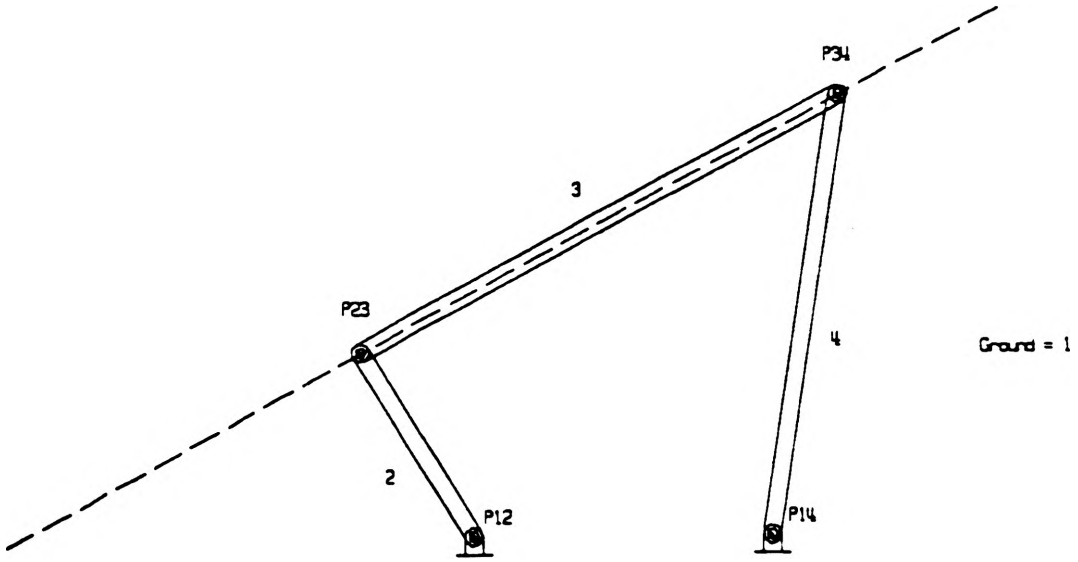

Figure 3. First Application of Aronhold-Kennedy Theorem

The exact location of the instant center of velocity between bodies 2 and 4 can now be determined by applying the theorem to the second set of rigid bodies, bodies 1,2 and 4. The instant center P_{24} lies on a line that passes through instant centers P_{12} and P_{14}. These points are two of the three instant centers shared by the three bodies in relative motion, bodies 1,2 and 4 (see Figure 4). The instant center P_{24} is then located at the intersection of the two lines formed by the application of the Aronhold - Kennedy Theorem of three centers. It is instructive to note that each time the theorem was applied, it was done through existing instant

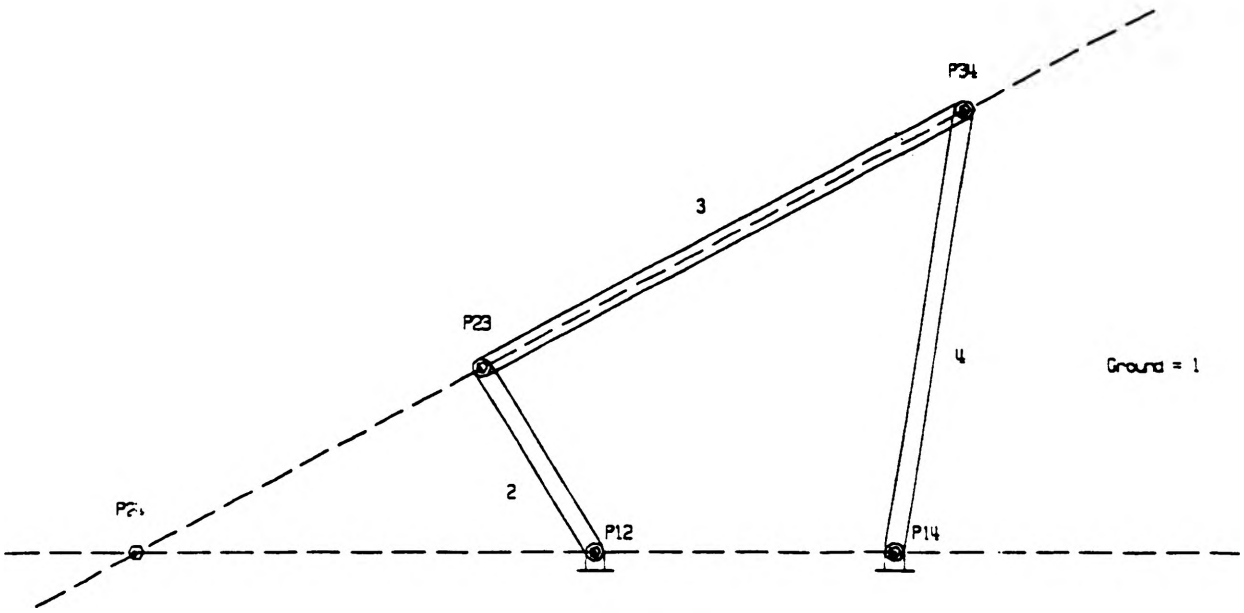

Figure 4. Second Application of Aronhold-Kennedy Theorm

centers which contained the subscript 2 and the subscript 4, together with a subscript which was common to both instant centers. By repeated application of this theorem all N number of instant centers of velocity can be found.

The best method for keeping track of which instant centers have been found is to space the link numbers around the perimeter of a circle and connect the link numbers corresponding to the subscripts of known instant centers (see Figure 5).

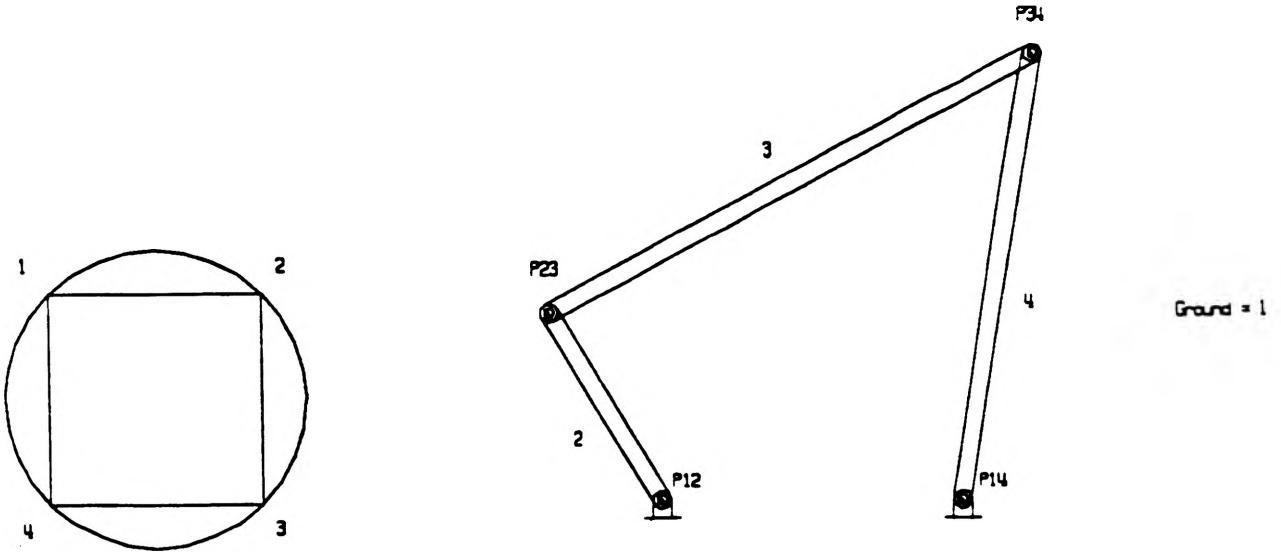

Figure 5. Instant Center Circle

As each unknown instant center location is attempted to be found using the Aronhold-Kennedy Theorem, a dotted line connecting the link numbers corresponding to the subscript of the instant center in question is drawn. The endpoints of any two lines that form a triangle with the dotted line define the subscripts of known instant centers. It is through these instant centers that the construction lines are formed using the Aronhold-Kennedy Theorem to define the location of the unknown instant center (see Figure 6).

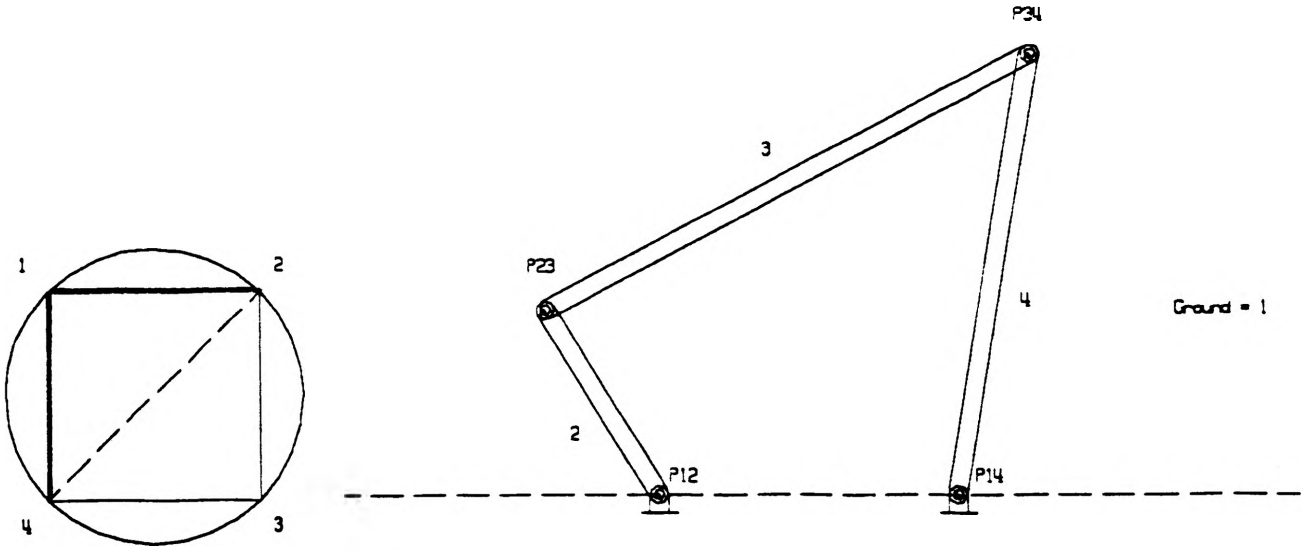

Figure 6. Instant Center circle and Aronhold-Kennedy Theorem

PROGRAM METHODOLOGY

Background

To begin the project it was necessary to convert the existing graphical subroutines of the program "SKIMP" to equivalent subroutines using GRFLIB [3] and SPECTRE.[4] This collection of graphical subroutines are in wide use and existing documentation was available. The instant centers of velocity subroutine begins by making use of three existing subroutines called jtype1, jtype2 and findunkn. These subroutines were written by J. Hair, D. Millar and S. Koehr [5] as a part of a senior level design class. The subroutine jtype1 determines the location of instant centers for grounded joints. The subroutine jtype2 determines the location of instant centers for pinned joints. The subroutine findunkn determines the location of unknown centers of velocity using the Aronhold-Kennedy Theorem of three centers. All three subroutines store the global x and y coordinate of the instant centers in a 3 by N array. The first component of each element is a flag to determine whether the location of that particular instant center is known.

Automatic With Construction Lines

This portion of the subroutine allows the step by step graphical determination of all instant centers of velocity of a

mechanism. It begins after the main program "SKIMP" has sketched the mechanism. The subroutine is activated through the pull down menu labeled "Instant Centers". In this pull down menu are sub-menus whose titles are the three modes of operation: automatic, automatic with construction lines (automatic w/lines), and tutorial. (see Figure 7).

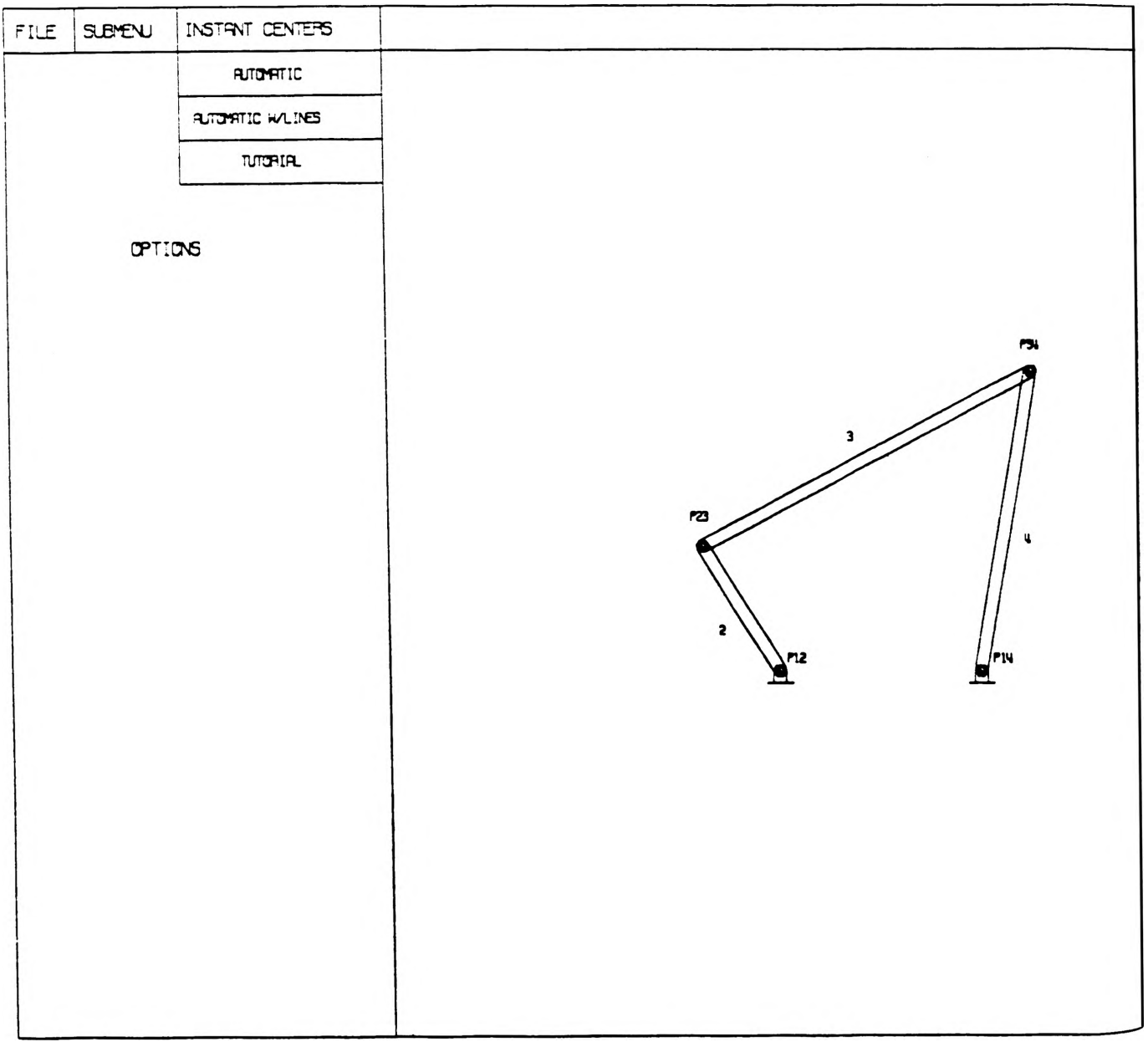

Figure 7. Skimp Environment: Instant Center Pull Down Menu

When the cursor is held on the label automatic w/lines and released the instant center circle will appear in the left window, with a line connecting all known instant centers. A pop-up menu will also appear which lists the N number of instant centers. Next to each instant center is a toggle switch for both the construction lines and the instant center (see Figure 8).

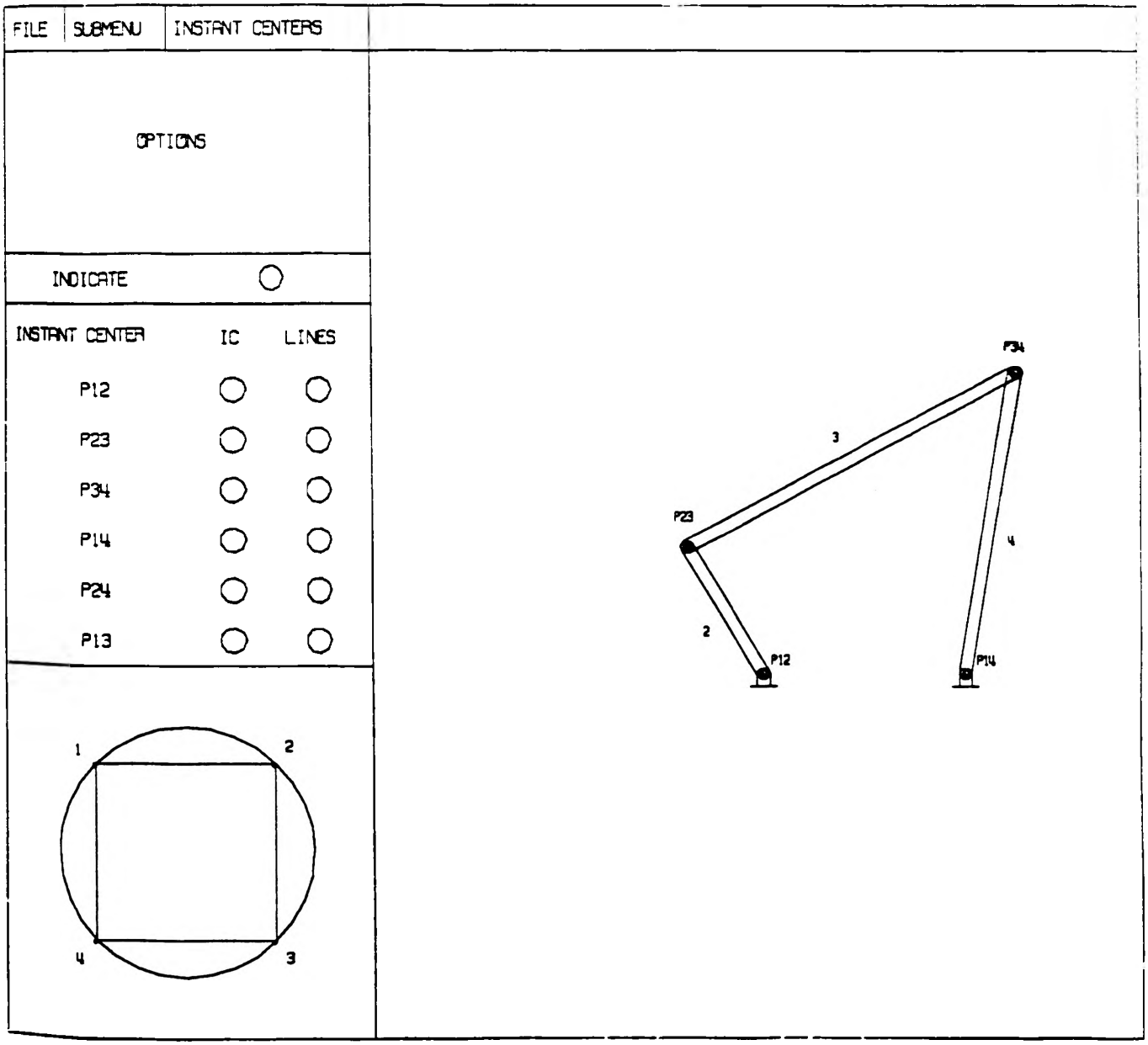

Figure 8. Skimp Environment: Automatic W/Lines

After each instant center is found the construction lines can be turned off so the screen is not cluttered when the remaining instant centers are found. As shown in the figure there is also a switch labeled "indicate". When this switch is activated, it allows the user to indicate with the cursor which particular line or instant center is to be turned off.

The subroutine findunkn has been altered to find one unknown instant center at a time and to have a keystroke pause between each application of the Aronhold-Kennedy Theorem. When the construction line is drawn through two known instant centers, the line, as well as the two legs of the triangle on the instant center circle which define the known instant centers blink on and off. This is to insure the student understands the connection between the instant center circle and the application of the Aronhold-Kennedy Theorem.

The exact location of the instant center is calculated by determining the slope and intercept of each construction line and setting the equations of the lines equal to each other and solving for their common point. A subroutine called trim is then called which calculates the length between the new instant center and the instant centers through which each construction line passes. The shortest length is the portion of the construction line which will remain on the screen. The construction line is then drawn in the background color and the shortest length is then redrawn (see Figure 9). This is repeated with a keystroke pause between each step until all instant centers of velocity are found.

Automatic

This subroutine is also available through the pull down menu. It calculates the location of all instant centers of velocity, then displays them (see Figure 10). A pop-up menu with a list of the N number of instant centers appears in the left window. A single toggle switch is next to each label allowing each to be turned on or off depending on their present state. There are also switches labeled: all on, all off, and indicate.

Tutorial

The tutorial subroutine operates in much the same way as the subroutine automatic w/lines. The most notable exception is that the choice of which known instant centers are used in applying the Aronhold-Kennedy Theorem is determined by the user and not the computer. Upon activating the subroutine, again via the pull down menu, the same pop-up menus appear in the left window as did in the subroutine automatic w/lines. An added pop-up menu will appear in the left window with the N number of instant centers as labels, as well as a single switch labeled "help". There will be two switches for each label under the headings "find" and "using". The student will be able to choose the unknown instant center to be located, then choose two instant centers under the heading "using" which will be used for the first application of the Aronhold-Kennedy Theorem. The student will then be prompted whether this construction line should then be drawn. Upon answering yes, an additional prompt asking for the second two instant centers through which the mixed construction line will be drawn. The student will once again be prompted as to whether this construction line will be

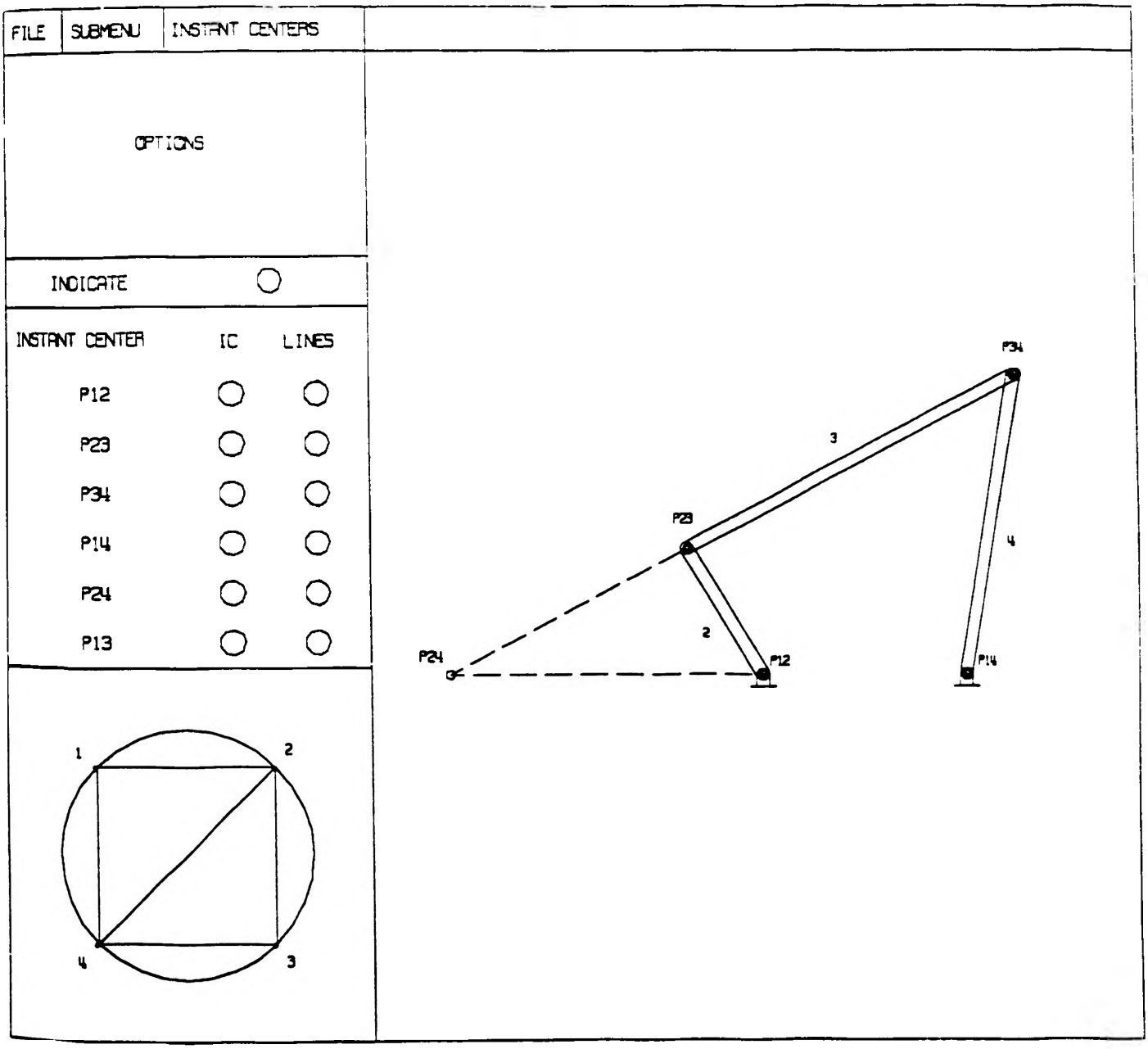

Figure 9. Skimp Environment: Finding Unknown Instant Center

drawn. The instant center circle will highlight the legs of the triangle which denote the known instant centers through which the respective construction lines have been drawn. This subroutine will allow the student to make errors and when the "help" switch is activated, the computer will delete each step with a keystroke

pause between each deletion, back to the point at which the mistake was made.

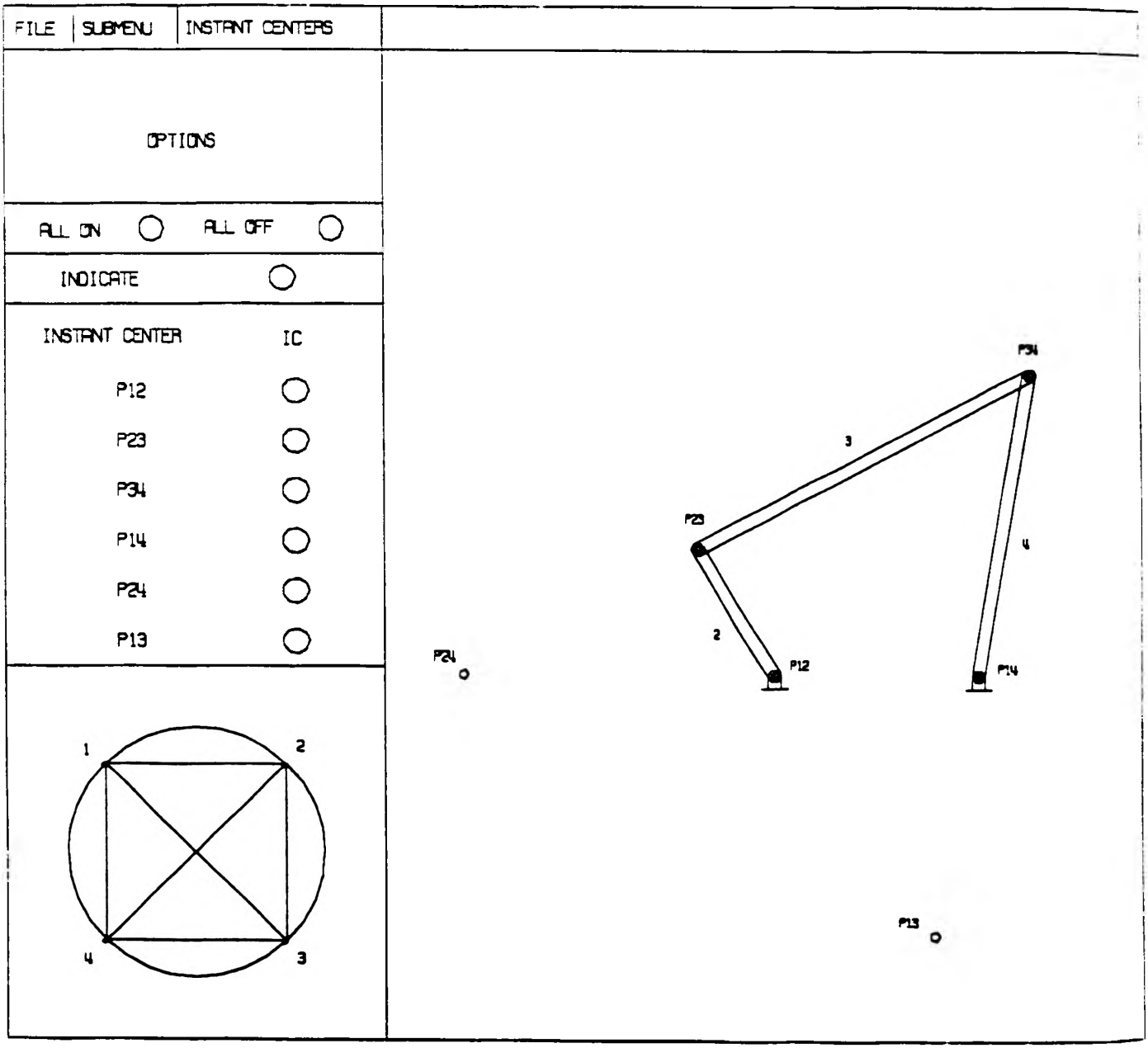

Figure 10. Skimp Environment: Automatic

CONCLUSIONS

The purpose of this project was to create a subroutine for the graphical software environment called "Skimp". This subroutine is a prototype for one module of the Kinematically Intelligent Blackboard project of Dr. J.K. Nisbett. The subroutine was responsible for teaching the concept of Instant Centers of Velocity on a blackboard sized projected computer screen. It incorporated the Aronhold-Kennedy Theorem of Three Centers which graphically determines the location of unknown instant centers by intersecting construction lines drawn through known instant centers. The subroutine has three modes of operation which include Automatic, Automatic W/Lines, and Tutorial.

One of the largest problems faced by students is not with the understanding of basic concepts such as instant centers of velocity, but the time constraint which does not allow these concepts to be applied in varying problem configurations. The greatest advantage to using the instant centers of velocity subroutine is that the classroom will not be hindered by the time constraint normally associated with traditional teaching methods.

The student will find the program valuable as a tutorial, a method for verifying solutions, and a record of lectures. The tutorial portion of the program will serve the students as their own personal tutor, available whenever the student has questions.

This subroutine is also useful in teaching concepts of machine dynamics related to instant centers of velocity. Concepts such as velocity ratios and velocity polygons can be more fully understood by using the instant centers of velocity subroutine.

Though this program has only been used in the classroom for demonstration purposes it is hoped that using the program to teach concepts of machine dynamics will benefit both instructor and student. The next step in the development is the continued expansion of the prototype and classroom testing.

REFERENCES

1. "An Interactive Graphical Computer Approach to Planar Linkages", J.K. Nisbett, M.S. Thesis, University of Texas at Arlington, 1986.

2. Theory of Machines and Mechanisms, J.E. Shigley and J.J. Uicker, McGraw-Hill, 1980,pp 95 to 102.

3. Grflib Users Manual, Version 3.0, Wes Barris, University of Minnesota.

4. Spectre: Subroutines Providing Event Control and Tracking Resources Efficiently, Version 1.6, Wes Barris, University of Minnesota.

5. Senior Design Project, J. Hair, D. Miller, and S. Koehr, University of Missouri- Rolla, 1990.

COMPUTER SOFTWARE CONTROL OF A THREE-JOINT MODEL ROBOT

John W. Fierke
Department of Electrical Engineering

ABSTRACT

The general scope of the computer program to control a three-joint model robot is presented. Several existing and potential sources of difficulty are also mentioned. For all specific explanations the reader is referred to the thesis papers of Richard Wainwright [1] and Eric Stelzer [2]. This presentation merely adheres to the description of the software to control the robot using the existing information contained in these two papers

INTRODUCTION

The purpose of this project was to make the Electrical Engineering Department's Fishertechnik model robot functional through the use of an IBM PC. It was desired to have it operate as it was originally designed to operate on an Apple microcomputer, as described by Richard Wainwright [1] and Eric Stelzer [2].

The software control of the robot is the primary concern of this paper. However, the software greatly hinges upon the design of the existing auxiliary interface card, which has seemed to pose the majority of the difficulty of this project. This card was not accompanied by any documentation of any sort, no schematic, no description. The greatest concern of the author was to discover how the edge connectors of the card interfaced with the connectors on the card slots of the IBM, and also to learn the actual addresses of the slot connectors so as to be able to communicate with the card (This has been postponed as the author has been on co-op, away from all the materials).

The card's primary component is an ADC0808CCN Analog-to-Digital converter made by National Semiconductor Corporation [3]. Its function is to convert the voltages across the potentiometers on the joints of the robot into numerical values corresponding to positions of the arms.

Along with these pieces of information and the descriptions by Wainwright[1] and Stelzer[2], it was decided to move on and devise a "skeleton" program to handle the desired operations of the robot without actually knowing the true addresses of the interface card. It essentially "steps through" all the processes for the sake of having a base to build upon once the addressing problem is conquered. Some small, specific subroutines have been created to manipulate non-critical, unused memory locations,

treating them as the actual output and input addresses. These subroutines simulate the robot's motion and provide all the necessary values that would be experienced, were there an actual robot attached, so that the various calculations can be performed and verified. This simulation is still under development and is useful only for the present until time can be devoted to the robot itself at the lab in Rolla. Only then can the pertinent modifications be made and the true results observed.

Turbo Pascal was chosen as the programming language for its structure and high level language characteristics in order that the program could be more easily altered or updated in the future.

Although the primary function of the model robot is to act in a "machine vision" capacity; identify an object on a conveyor belt, calculate the point of intersection, move to pick it up, and deposit it in a corresponding bin; it should also be capable of performing several specific operations and the user should have control of most of its parameters such as speed, direction, and position and be able to either provide a finite set of points through which to move the robot or have the computer execute a calculated set of moves to reach a desired position.

Following is a general description of the design and operation of the Robotics Command System (RCS) and some of its existing and potential disadvantages.

THE ROBOTICS COMMAND SYSTEM
ROBOT STATUS WINDOW

In keeping with Stelzer's design, most of the features he mentions as being part of his Robotics Operating System (i.e. MOVE, LEARN, CALIBRATE, Path Segments, Path Buffers, and Speed Control) have been implemented with various modifications. This program is not be command-line based but resembles the display in Figure 1.

This is the operating environment for the user and allows for complete visualization of all of the robot's present parameters and the demands put upon it. The top portion, the Robot Status Window (RSW), remains fixed at the top of the screen and is constantly updated to relate the robot's present values. Following are the parameters displayed in the RSW :

Mode

Mode depicts that the hardware controller switch is either in the Computer (C) position, which transfers control to the computer, or in the Manual (M) position, allowing manipulation of the robot with the controls on the hardware controller. The particular mode that it is in is checked upon every attempt to output or input information so as to determine if the computer can proceed with its operation or not. The corresponding letter in the display will be highlighted.

```
*****************************************
*                                       *
*    ROBOTICS COMMAND SYSTEM (RCS)      *
*                                       *
*****************************************

*************************************************************************
*                                                                       *
*  MODE : C/M  POSITION  Cart : (x)___ (y)___ (z)___                    *
*                        Joint : (1)___ (2)___ (3)___    MAGNET : ON/OFF *
*               SPEED (%)      : (1)___ (2)___ (3)___                  *
*                                                                       *
*************************************************************************
```

#	Command	Coordinates	System	Speed	Options	Elbow	Time
1	MOVE	0,0,0	J	100		RU	
2		12,5,-10	C	50	H400		
3	LPICK	0,0,0	J				
4		15,4,15	C			LD	
5		0,0,0	J	75			
6	E						
7	CALIB						
8	A						

Figure 1. The Robot Command System Window

Position

This portion of the RSW displays the position of the manipulator as it moves in both Cartesian and joint coordinates. The Cartesian coordinates; x, y, z; are expressed in centimeters and the joint coordinates; J1, J2, J3; in degrees. The joint coordinates are obtained directly from reading the position of the three pots and converting the resulting values (each can range from 0 to 255) into degrees by applying a conversion factor of 340 degrees/255. (340 degrees due to the physical limitations of the joints as explained by Stelzer[2]. This RSW feature has the definite potential of slowing down the program and thus the smooth operation of the robot, because upon each sampling of the robot's position, the computer must convert the positions into degrees, convert the degrees into Cartesian values, and print all six values on the screen.

Speed

It is intended to also display the actual speed of each joint as small compensations are made to correct the position of each joint due to the effects of friction and gravity. Constantly updated values such as speed and position may have to be changed to be updated only once for a certain number of inputs to speed up operation. The speed will initially be determined by the user, but in given time intervals throughout the movement of the manipulator the computer will compare the robot's present position (obtained by reading each joint's potentiometer voltage) to its expected position (calculated using the equation $p_k = v_k*t + c_k$, in the manner described by Stelzer[2]; p is the

expected position of joint k, v_k is the newly calculated velocity of joint k, t is the time elapsed, and c_k is the starting position of joint k.) and make appropriate speed adjustments to each motor. In this manner the robot will best reach its destination smoothly and as quickly as possible.

Magnet

This information is merely a means of identifying at a certain moment if the manipulator's electromagnet is activated or not, as is instructed by the user.

THE ROBOTICS COMMAND SYSTEM
ROBOT COMMAND WINDOW

In this portion of the screen the user is allowed to command the robot to complete a certain action while also providing various options. Each request is contained on one line of the RCS table as shown in Figure 1. For example, for command #1, the user would enter 'MOVE', tab to the next column, enter a set of coordinates '0, 0, 0', tab, signify which coordinate system was to be used 'J' for Joint coordinates, tab, provide the desired percent of full speed '100', tab, any other available options, tab, the elbow configuration 'RU'-Right elbow Up, then press Enter to execute the command or tab to the next line, in order to make a list of commands to execute later.

At this point the most important aspects of the RCW are Command, Coordinates, System, and Speed. Options, Elbow, and Time will be developed at a later time.

Command

Currently, the user can enter one of four instructions in the Command column-Move, L(earn), or Calib(rate) and A(uto).

Move

The Move command is used to initiate a move of the manipulator from its current position to a designated point specified in either Cartesian or Joint coordinates. If desired, the Move command may be omitted, as is shown on lines 2, 4, and 5 in Figure 1, and CS will take for granted that a move is desired since this will be the most commonly used command.

Learn

The Learn command is used in such a manner as to create a file on disk in which to store a series of commands to execute at any later time. The user merely follows the L with the desired filename in which to store the upcoming commands. Some or all the moves may be designated by switching the pulse-width modulator to the manual mode and positioning it using the controls on the box. By merely pressing enter, the present coordinates of the manipulator will be stored and printed on the appropriate line. The user may end the Learning session by entering an 'E' for Exit in the command column, upon which the file is stored on disk. Then to initiate those stored moves, the user must enter the name of the file in the command column.

Calibrate

This command is used for designating the "zero" position of the robot. When the command is entered the user must manually position the robot in the desired "zero" position and press enter to identify the robot's position to the computer. This position will replace the previous calibrated position and will be referenced upon each startup until it is re-calibrated.

Auto

When the user enters an 'A' in the command column this sends the robot into fully automatic operation, or "Machine Vision" mode as mentioned previously, in that the robot is only actuated upon the breaking of the light beam to the first photo cell on the conveyor belt. In this case, the inputs from the photo cells are considered and the path to the pickup point and the drop bins are stored in a special predetermined file.

Coordinates and System

The user may specify his coordinates for a move in either Cartesian or Joint coordinates by merely placing either a C or a J in the Coords column. The program deals directly with coordinates in degrees, so no conversion is necessary for Joint coordinates. If Cartesian coordinates are specified, these x-y-z values are converted to Joint coordinates through the use of the solutions of the Kinematic equations as described by Stelzer [2].

Speed

This option allows the user to set the overall operation speed of all three motors. For example, if the speed of motor 1 is 100% of full speed, motor 2 is 30%, and motor 3 is 80%, a speed value of 100 would maintain these speeds, but, for instance, a value of 50 would slow each motor to half its set speeds (i.e., motor 1-50%, motor 2-15%, motor 3-40%). When omitted, the default value used will be 50%.

The author regrets how unspecific this report may appear, but the majority of the material has already been stated by either Wainwright [1] or Stelzer [2]. The extent of this author's work was in designing and programming the software to accomplish the tasks mentioned. It was believed that discussing the program code would not prove to be useful in a report of this nature. Hopefully, the program will soon speak for itself.

ACKNOWLEDGMENTS

I wish to express my thanks to Dr. Randy Moss for the time and effort he offered. I would also like to thank Mr. Bob Dopher and Mr. Jim Ross for their extensive technical advice.

REFERENCES

1. Stelzer, E. H., "A Control Program and Operating System for a Three Joint Robot Arm on an Apple Microcomputer," M.S. Thesis, University of Missouri-Rolla, 1982.

2. Wainwright, R.E., "Microprocessor Control of a Model Robot System using Programmable Pulse Width Modulation," M.S. Thesis, University of Missouri-Rolla, 1982.

3. National Semiconductor Corporation, Semiconductor Databook, The ADC0808CCN Analog-to-Digital Converter, p. 48-58, 1989.

THERMAL BUCKLING OF COMPOSITE TUBES

S. Fulkerson
Mechanical Engineering

ABSTRACT

The object was to design and initiate the use of a fixture capable of testing for pre-buckling deflections in a composite tube under thermal loading. The fixture is to be used on a continuing basis to test three types of composites: (1) glass/epoxy, (2) Kevlar/epoxy, and (3) graphite/epoxy. The course of action chosen was to adapt a fixture designed by Tim Streb and Steve Fulkerson in the spring of 1991. The fixture was completed, and one test was performed. An added responsibility was to initiate a course of action such that the volumetric percentage of fiber in the composite may be determined.

INTRODUCTION

A composite consists of a fiber and a matrix. The combination of a strong fibers with a dense matrix gives composites properties unlike any pure material. The objective of the assignment was to design and initiate the use of a fixture capable of measuring axial and lateral deflections when thermally loaded. The fixture needed to be capable of handling temperature up to 400 degrees Fahrenheit and remain rigid. Also, the fixture needed to be capable of supporting measuring equipment for future mechanical loadings. A secondary objective of the research was to determine the best method of finding the fiber volume fraction of cured composites. This involved investigations into organic chemistry and high magnification viewing devices. The thermal test conducted used ten strain gages, a ten band bridge, a strain indicator, two thermocouples, a thermometer, and four dial indicators. A Stabil-Therm Recirculating Utility Oven was used for the thermal environment. The equipment was to allow for measuring induced load on the composite in addition to finding when pre-buckling deformations occurred. Buckling in axially loaded tubes has been theoretically predicted and experimentally shown to occur by axisymmetric ripples [1]. The purpose of this research was to measure such a rippling effect.

DESIGN AND RESULTS

Procedure for Fiber Volume Fraction

Three distinct procedures were investigated to determine the fiber volume fraction of the material. The initial procedure used for the glass composite was to insert a small section of a completed tube in a test oven and burn off the epoxy matrix. Knowing the initial and final weights as well as the density of

each material allowed a calculation of the fiber volume fraction of the original sample. However, when this procedure was suggested for the Kevlar and graphite epoxy, several chemists and ceramic engineers suggested using some alternative method. Since Kevlar and graphite are organic compounds, they would burn off at temperatures required to burn off the epoxy.

The next method suggested was to chemically remove the epoxy with nitric and/or sulfuric acid. This technique was outlined in an ASTM standard [2]. However, the supplier of the Kevlar composite material objected to such a procedure. The supplier said such tests were inaccurate and that other methods should be investigated.

As it was necessary to measure for air voids in the composite for related research by M. Farhadinia [3], it was suggested that the two assignments be combined. Farhadinia found that the university possessed an optical device capable of achieving both goals. A typical cross-section of the cured composite was cured into a surrounding matrix. This cylindrical unit was then highly polished, and high resolution photographs were taken and processed by a computer. The computer calculated the void and fiber percentage as a function of cross sectional area. When the results from the glass burnout test were compared to the optical method, a high correlation was present. Therefore, the technique chosen was the optical method.

Fixture Design

The fixture designed for the experiment involved the adaptation of a previously designed fixture by the author and T. Streb [4]. The original fixture was designed to measure thermal and mechanical loading of composite tubes. Alterations necessary included the attachment of four deflection dial indicators in a plane normal to the axis of symmetry. The dial indicators were to be placed every ninety degrees around the midpoint of the composite and be capable of measuring the horizontal deflections of axial loading. Photographs of the original design may be seen in figures 1 and 2. Figure 1 shows the setup for thermal loading. Four bars with strain gages mounted in the center restrain the composite from axially expanding. The strain gages allow for the measuring of the induced load created by the elevated temperatures (after correcting for the thermal expansion of the fixture). Figure 2 shows the setup for mechanical loading. The bottom plate is fixed. The top piece is attached to the moving head of an MTS machine. An intermediate plate allows for the adjustment of the angle of compression to ensure uniform loading around the perimeter of the composite. A sketch of the final design for thermal loading may be seen partially assembled in figure 3. The design required parts capable of being attached to an end plate for thermal loading and to the intermediate plate for mechanical loading. Four identical parts attach to the plate around the composite. Each L-shaped piece holds one dial indicator.

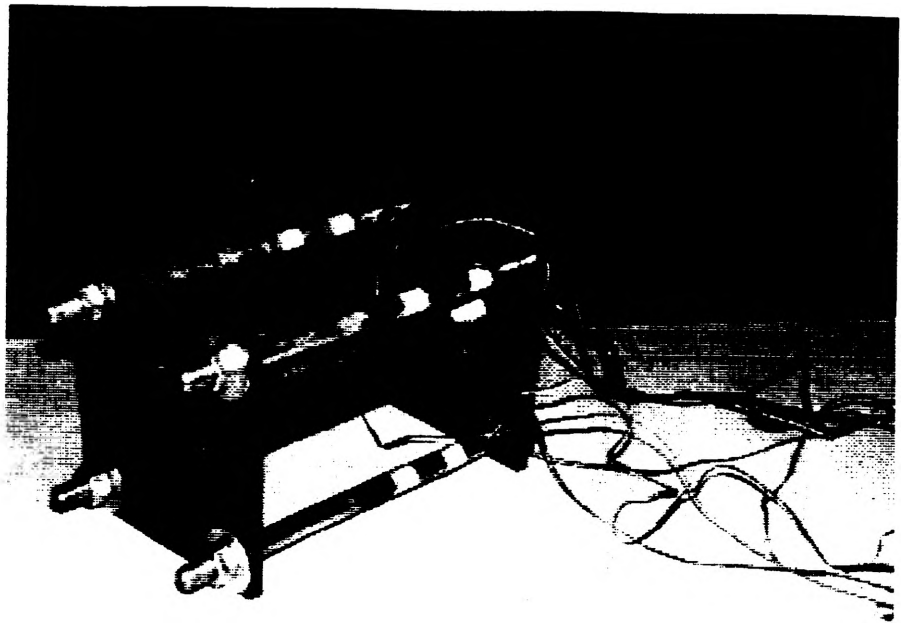

Figure 1. Fixture for Thermal Loading

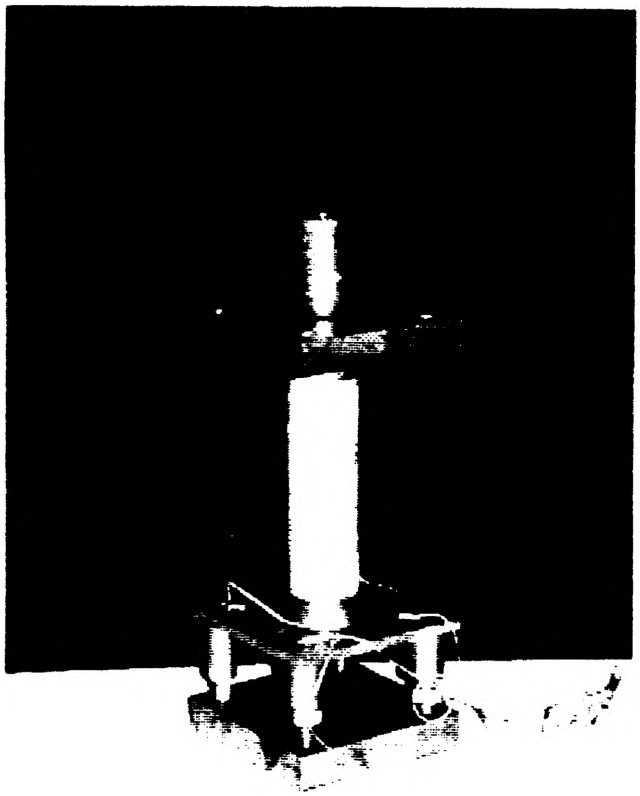

Figure 2. Fixture for Mechanical Loading

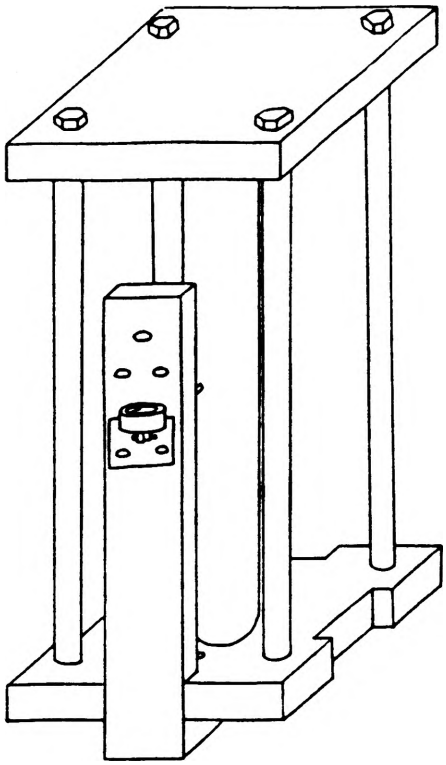

Figure 3. Partially Assembled Fixture for Thermal Buckling Test

Testing

For testing, a three layer, glass/epoxy sample was selected. Its fibers were parallel to the axis of symmetry. Four strain gages were glued to the vertical bars and six strain gages were fixed. Four deflection dial indicators were mounted, and two thermocouples were attached to the apparatus. A calibration was performed to find the natural effect of the elevated temperature on the involved systems. This was performed with no load. Finally, testing was initiated. The four bolts were tightened to a "snug" fit. The strain was zeroed, and it was assumed the induced force was negligible. The fixture was placed in the oven and heating was commenced.

RESULTS

The results were poor. No induced load was measured in the test. This was disappointing since significant loading was seen for previous tests with the fixture sans the added equipment. When testing was performed in April 1991, loads surpassed 20 kN for a similar temperature range. However, the sample tested then was a five layer Kevlar composite with circumferential fibers. Also, the previous sample was noticeably stiffer. Figures 4, 5, and 6 display the measured strain in three of the four vertical bolts versus temperature for both the calibration and experimental runs. Little difference is seen between the two curves. This clearly

indicates no load was induced. An apparent error was made in the calibration curve of the remaining bolt. Though the source of the error is unknown, it can easily be remedied by simply running another calibration of the gage. Strain results for the gages attached to the sample indicated similar trends in the failure to measure induced loads.

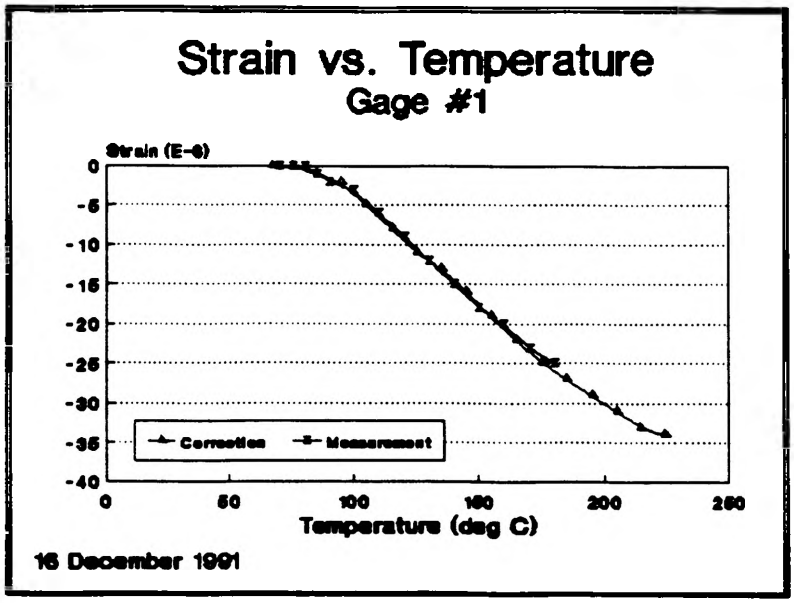

Figure 4. Strain versus Temperature for Vertical Support #1 in Thermal Buckling Test

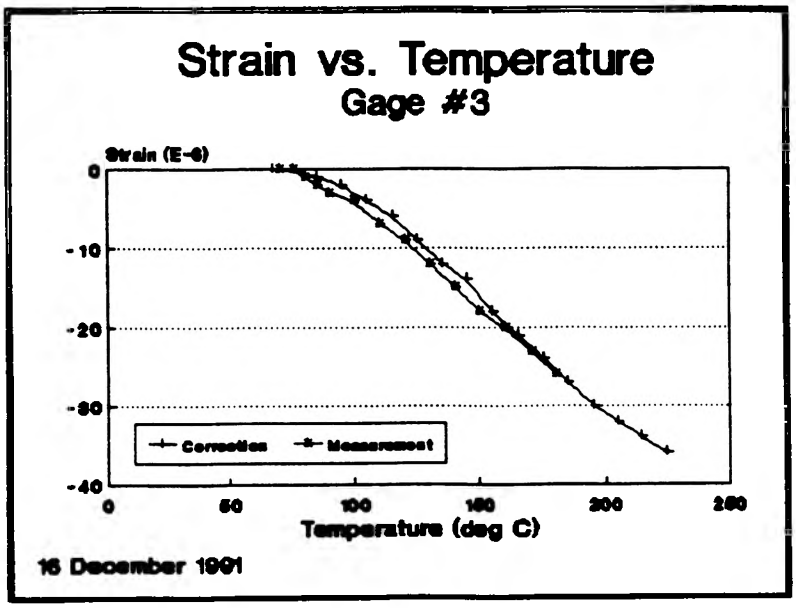

Figure 5. Strain versus Temperature for Vertical Support #3 in Thermal Pre-Buckling Test

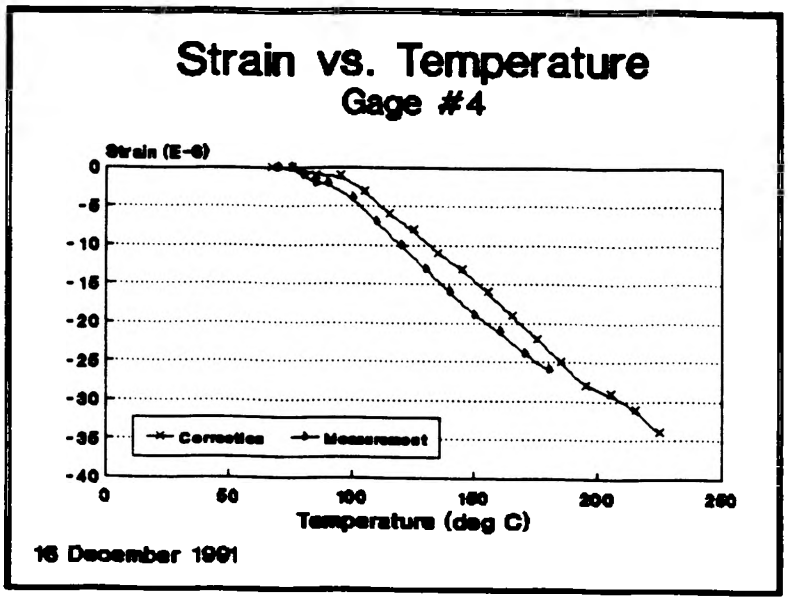

Figure 6. Strain Versus Temperature for Vertical Support #4 in Thermal Pre-Buckling Test

Several possible causes exist for the lack of successful results. One suggested cause is that the bars were too stiff for the sample measured. Glass composites are inherently weaker than Kevlar composites, so to expect similar result ranges may be unreasonable. Another possible cause is that the bolts may not have been securely fixed to the ends. The planned method of solving the problem is to utilize the dial indicator supports to fix the two plates together. This would allow for an exact parallel alignment and secure joining of the two plates. However, the author's concern is in the difficulty of measuring the induced load. Clearly, loads are difficult to compute when strain indicators are attached to a rectangular cross section with several holes drilled through its cross section. Also, unless new supports are made, small extensions are necessary to span the extra distance to the top plate. If the induced load is of any interest, the author suggests using bolts with a smaller cross section rather than opting for joining the plates with the gage supports.

CONCLUSION

While only one test was performed, the information acquired will certainly help future students at the University of Missouri-Rolla. A fixture was designed for current and future use and a simple method of determining percentage by volume of fiber in composites was found. Overall, the author feels grateful that he was able to continue his senior design project as it allowed for good experience with a rapidly expanding field.

REFERENCES

[1] S. Krishnakumar and C. G. Foster, Measurement of Axisymmetric Prebuckling Deformations in Axially Compressed Cylindrical Shells, Experimental Mechanics. March (1991), 47-51.

[2] ASTM D 3171-76, Standard Test Method for Fiber Content of Resin-Matrix Composites by Matrix Digestion, American Society for Testing and Materials. April (1990), 1-3.

[3] M. Farhadinia. title unknown. Thesis. U of Missouri-Rolla, 1992.

[4] T. Streb and S. Fulkerson, Compression Testing of Composite Tubes, unpublished paper, 29 April (1991).

OPPORTUNITY FOR UNDERGRADUATE RESEARCH PROJECT REPORT

"COMPUTER-MODELING OF A LIQUID FUEL SPRAY"

By: Clement R. Goodin, Jr.

Mechanical Engineering Department

ABSTRACT

This project was designed to find an accurate and convenient method of computing fuel spray parameters. The project centers around an experimental setup which basically fires a laser beam through a fuel spray mist. A concentric ring detector then measures energy from the scattered light.

A computer code was written which solves a governing equation to give computed values of the energy from scattered light. Comparison of the experimental energy and the computed energy tells how well the fuel parameters of the computer model matches those of the real spray of the experiment. An iteration technique then manipulates the computer model until the unknown parameters are solved for.

The computer code designed here works very well with calibration or known data. However, actual test data causes the computer code to crash. New techniques and approaches are currently being employed to salvage the code.

A specific liquid fuel spray exits a specific type of injector with certain repeatable and consistent parameters. The overall objective of this project is to repeatedly measure these characteristics with a high degree of accuracy and convenience.

Fuel sprays studied here are modeled as "Rosin-Rammler" (RR) distributions. The RR distribution is given as:

$$V(D)=\frac{\delta D^{\delta-1}}{D\delta}\ Exp\ \{-(D/\bar{D})^{\delta}\} \tag{1}$$

where $\bar{D}$, the mean droplet diameter, and δ, the distribution width parameter, are constants for a particular fuel spray as mentioned above. These parameters are the points of interest here.

When a fuel spray exits an injector, the spray is made up of spherical droplets, ranging normally from 5 to 200 microns in diameter. The mean droplet diameter, as the name implies, is more or less an average droplet diameter. The distribution width parameter is a dimensionless relative gauge of the size of each class of droplets.

The project centers around the experimental setup of Figure 1. In this experiment, a laser beam is directed through a projected fuel spray flow, scattering light. This scattered light is detected by a flat, concentric ring detector (Figure 2) which detects the light as energy, given by:

$$Energy = L_{ik} = C\int_0^{\infty}\left\{\left[J_o^2+J_1^2\right]\alpha\theta^i - \left[J_o^2+J_1^2\right]\alpha\theta_k\right\}\frac{1}{D}V(D)\,dD \tag{2}$$

This expression gives the energy incident upon the i^{th} ring.

(Note: For a more complete and in-depth discussion of the above points, see Dr. J.A. Drallmeier's M.S. and PhD. theses.)

The energy given by Equation 2 is measurable and is recorded data. Note, however, the containment of V(D), the size distribution, in the integral of Equation 2. The distribution is unknown and, to be solved for, must be assumed. Several distributions have been suggested by various researchers. As noted, this project assumed the function to be a Rosin-Rammler distribution, given by Equation 1. This is a widely accepted assumption.

Note also in Equation 2 the α term. α is given by:

$$\alpha = \frac{\pi D}{\lambda} \tag{3}$$

The dependence of α upon drop diameter, D, makes equation 2 all the more complicated (λ is wavelength of the laser light, a known constant). In addition, α is an argument of the Bessel functions, complicating matters further still. Also, note the θ term in Equation 2. $(\theta_i - \theta_t)$ is the angle from the bottom of the ring to the top of the ring.

The anticipated method of solving for $\bar{D}$ and δ is to begin by making educated guesses for these two parameters. These values will be inserted into Equation 2 and the corresponding energies calculated. After comparison of the calculated energy values and those obtained from experiment, adjustments will be made in $\bar{D}$ and δ and the process repeated. Eventually, computed energy values and experimental energy values should match and thus, $\bar{D}$ and δ of the fuel spray is known.

Although this appears as a cookbook operation, Equation 2 is a difficult equation to solve. A computer code was written which accomplished this. The energy values produced by the code were checked against energy data obtained from a calibration reticle. A calibration reticle is a very thin gold foil slide which has been precisely etched. The gold is etched away to leave a known number of known diameter particles, thereby simulating fuel drops an a slide. With all numbers of particles and particle diameters known, the $\bar{D}$ and δ parameters of the RR distribution equation are also known.

The code written solved Equation 2 by representing the integral with a Simpson Rule approximation from calculus. The code also computes Bessel functions as needed. Bessel function values were checked against those of a CRC handbook. The integral is evaluated from a minimum diameter to a maximum diameter, instead of zero to infinity.

The energy values given by the code matched very well with experimental energy measurement of the calibration reticle. For this reason it was decided that output of the code was plausible and the code should be integrated into a larger code, with the purpose of performing the iterative solving procedure.

Since there are two unknowns at hand, namely $\bar{D}$ and δ, the iterative solution procedure is required to be a "non-linear" best fit routine. The method employed in this project is that laid out in chapter 14 of Numerical Recipes, by B.P. Flannery, et al. This method is basically a statistical analysis of the energy data and the two unknown parameters we seek. The analysis was realized with computer code by computing an error residual and partial derivatives of the particular function with respect to the unknown parameters. With

these values, the analysis is designed to compute incremental values of $\bar{D}$ and δ which are used to create a better fit to the inputted experimental data. In short, the code constantly reduces the error residual and drives $\bar{D}$ and δ to values which most agree with the inputted energy curve.

The code was completed and was tested again with calibration reticle data. This was done by using energy data from the reticle as a data base and inputting $\bar{D}$ and δ values which were known to be incorrect. The code performed superbly and quickly iterated to the correct $\bar{D}$ and δ values. The code has not, however, proved successful with real test data. The iteration code "blows up" or crashes most of the time it encounters real test data.

The code's success with calibration data provides us with confidence that it's defects can be cured. We are currently trying a couple of different things, such as normalized data and a different, although still Rosin-Rammler, distribution function.

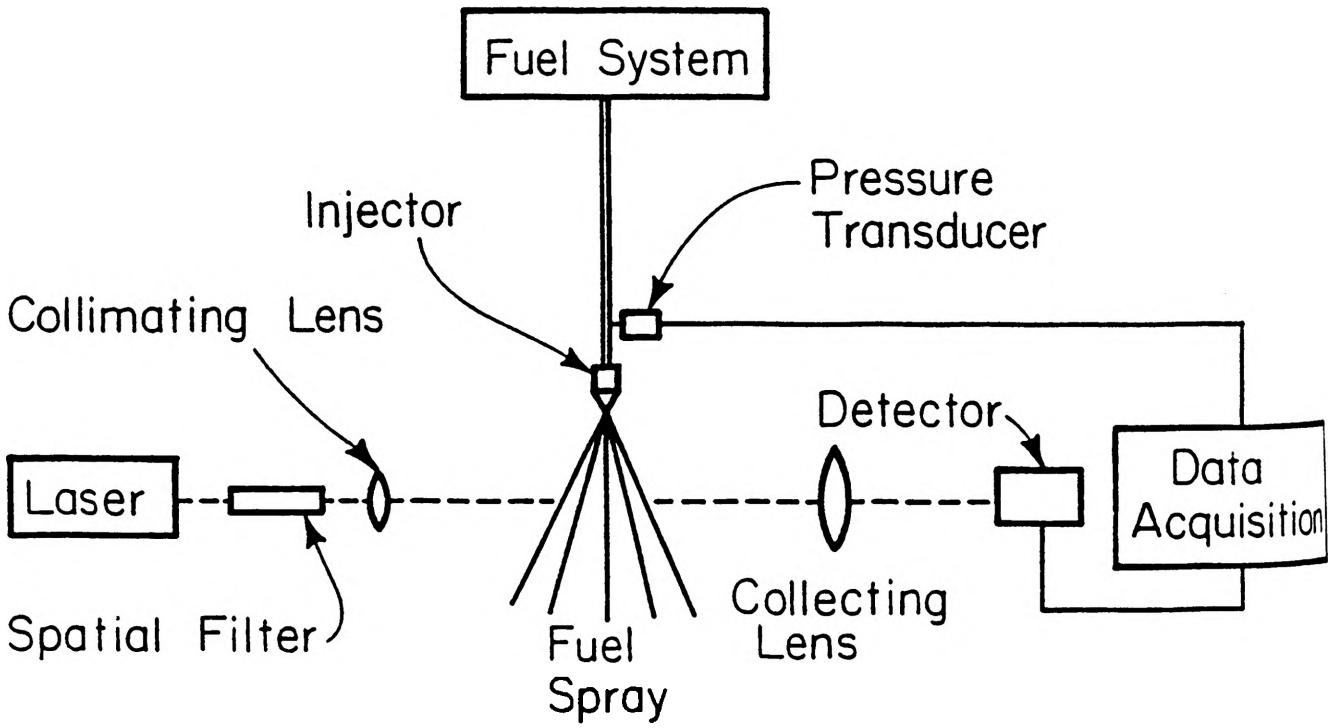

Figure 1) Experiment Setup

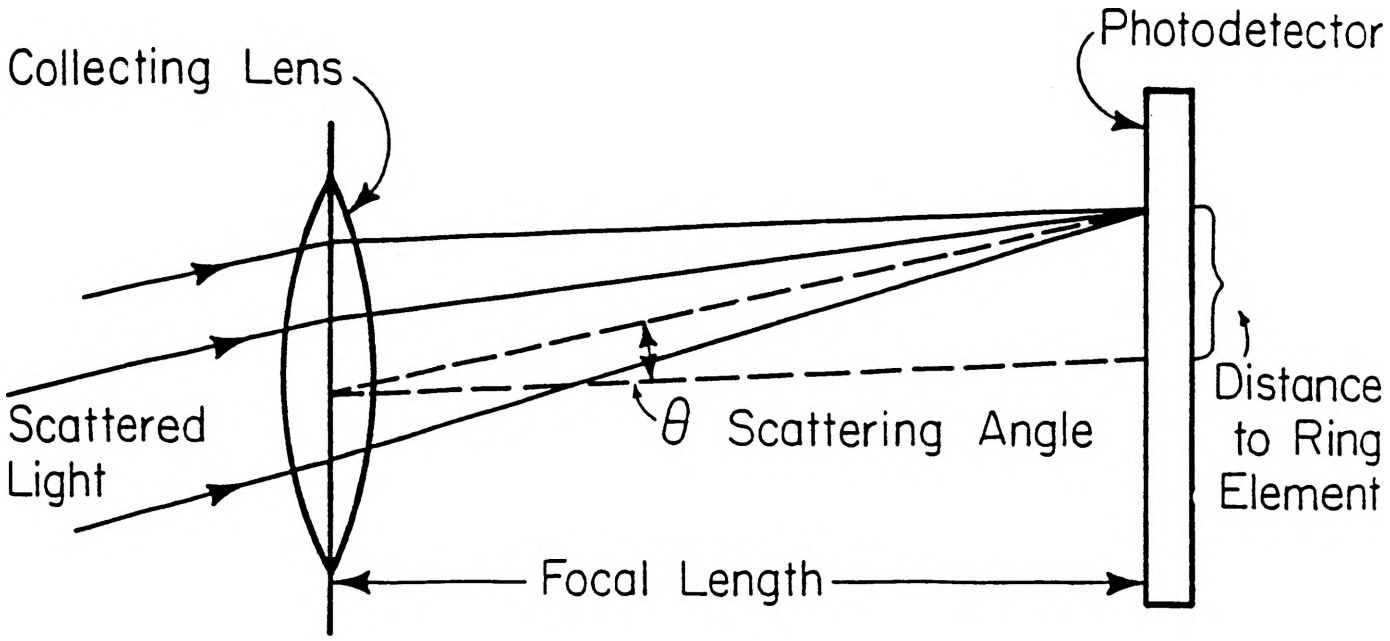

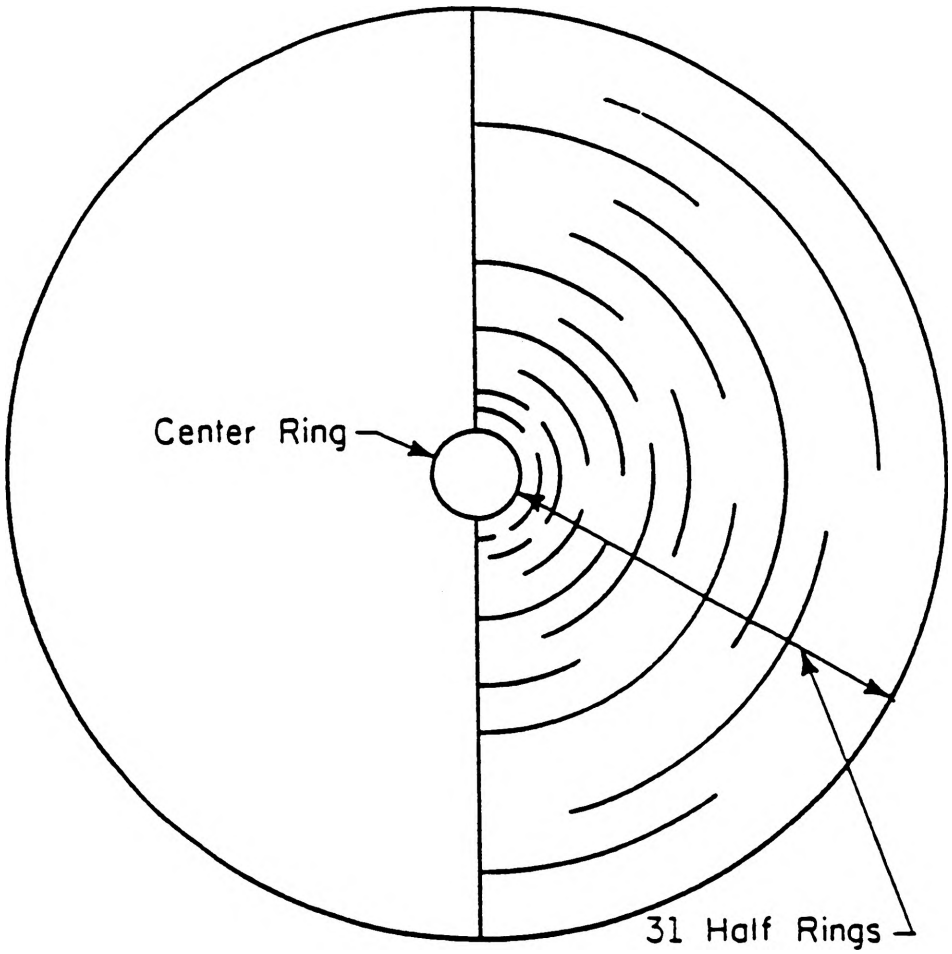

Figure 2) Ring Detector

A DEVELOPMENT OF A MONTE CARLO METHOD FOR THE DETERMINATION OF THE GAMMA RAY DETECTING EFFICIENCY OF A GERMANIUM DETECTOR

Author: Wayne T. Greene
Date: 25 March 1992

The determination of gamma ray transport has proven difficult to handle by ordinary methods. The use of the Monte Carlo method for the transport of various gamma rays impinging upon a detector has provided an accurate way to describe the gamma ray detection phenomenon. Using the Monte Carlo method, a procedure has been developed to describe all gamma ray interactions with the material of which the detector is made. The gamma ray detection efficiency is determined by computing the ratio of the gamma particles that interact and leave a certain minimum energy in the detector divided by the number of gamma particles emitted by the source.

INTRODUCTION:

The detection efficiency of a detector is defined as the ratio of the number of photons detected divided by the number of photons emitted by the source. The number of photons detected depends on the gammas that interact in the detector and deposit a certain minimum energy in it. This minimum energy is related to the minimum electronic pulse that can be recorded.

To date, there has not been developed a good method to determine very accurately the efficiency of a gamma ray detector. This is a major concern to fields such as health physics and if left unaddressed this problem may lead to incorrect radiation doses for radiation workers and members of the public.

The basis of the Monte Carlo method is the use of the Random Walk procedure. Random Walk is an expression used for the random implementation of various factors in the calculation of the possible events describing a particle's motion. To accomplish this end, a computer simulation of the history of the incident particle which is in our case a gamma ray (or photon) was developed in relation to another particle which the photon will then interact with. A random number generation scheme is utilized to determine a random number between the values zero and one. This number, once generated, will then be used in the decision making process regarding all events describing the photon position, energy, direction of motion, and type of interaction.

1.0. THE DETECTOR:

A Geranium (Ge) crystal was assumed to be used as the detector. The size of the crystal is variable such that it may be used as an input parameter for the calculations within the program.

2.0. THE MONTE CARLO SIMULATION:

2.1. The Types of Interactions:

In following the history of each photon as it moves through the detector there are many types of interactions that need to be addressed. In this work, the following three were considered:

A. Photoelectric Effect
B. Compton Effect
C. Pair Production.

A. Photoelectric Effect: As illustrated in **Figure 1**, a photon is traveling and soon collides with an atom in its path. The atom recoils from the impact and emits an electron from either its outer or inner shell. If this electron is emitted from the outer shell, we will simply have an electron flying off in one direction with the atom continuing to proceed in the direction of its recoil. This is just a simple case of Ionization of an atom and our interest in this matter is terminated. However, if the electron emitted from the collision originates from the atoms inner shell, then a hole is left in its wake within the inner shell where the electron originally occupied. Since this is an unstable condition for an atom, another electron will fall from an outer shell to fill the void left in the inner shell. This collapse of an electron to an inner shell will produce an x-ray which will then be emitted from the atom. This x-ray is very important to our calculation since it carries part of the gamma ray energy. Photoelectric interaction is dominant for photon energies less than 1 Mev.

B. The Compton Effect: As illustrated in **Figure 1**, a photon is traveling and collides with a free electron. From the collision with the electron, the photon will lose some of its energy in the form of kinetic energy to the electron and will have a lower amount of energy than it had prior to the collision. This type of interaction is dominant for photon energies from 0.5 Mev to 5 Mev..

C. The Pair Production Effect: As illustrated in **Figure 1:** a photon collides with a nucleus. This causes the nucleus to totally absorb the energy of the photon but being unable to contain this abundant energy, the nucleus breaks apart and forms an electron - positron pair. The positron proceeds only a short distance when Annihilation occurs. In this process, the positron collides with another free electron, and the two particles are both converted into two separate photons with an energy of .511 Mev each. This type of interaction occurs at energies above 1.02 Mev..

These three effects represent the major interactions the photon will encounter as it moves through the detector. To determine which type of effect will occur one uses the individuals cross sections (probabilities) along with a random number. Assume the following:

$$\mu_1 = \textit{probability of photoelectric} \qquad (1)$$

μ_2 = *probability of Compton* (2)

μ_3 = *probability of pair production* (3)

μ_t = *total interaction probability* (4)

$$\mu_t = \mu_1 + \mu_2 + \mu_3 \quad (5)$$

The following algorithm is then used:

$RN <= \mu_1 / \mu_t$,	*Photoelectric effect occurred*
$\mu_1/\mu_t < RN < (\mu_1+\mu_2)/\mu_t$,	*Compton effect occurred*
$RN > (\mu_1 + \mu_2)/\mu_t$,	*Pair Production occurred*

Depending on the interaction, the program branches off and records energy deposited, and particles still alive along with their energy, direction of motion, and position. The attenuation coefficients (probabilities) μ are functions of energy. They are tabulated at certain fixed energy values. To obtain the values of the coefficients for energies not on the table, an interpolation scheme is used which may be linear or more elaborate like cubic spline interpolation.

2.2. The Location Of The Photon:

It is extremely important to know the location of the photon relative to the detector boundaries. To achieve this, two coordinate systems are set up. The first is a fixed coordinate system with the z axis placed at the center of the cylindrical detector (see **Figure 2**). The second is a frame of reference moving along with the particle and having the z axis always coinciding with the direction of motion of the photon. To obtain the coordinates of the position of the particle in the fixed system, a transformation is employed as shown in **Figure 3**. If a photon has an interaction at point 2, to transform this location to the fixed reference frame, the angle position 2 makes with the z-axis of the fixed reference frame is given the value $\theta 1$ and the projection of point 2 onto the x-y plane with the angle between the x-axis and the projection is known as $\phi 1$. Using the following equations a determination for the direction cosines α, β, and γ may be found:

$$\mu = cos\theta 2 \quad (6)$$

$$\alpha = sin\theta 1 * cos\phi 1 \quad (7)$$

$$\beta = sin\theta 1 * sin\phi 1 \quad (8)$$

$$\gamma = cos\theta 1 \quad (9)$$

After the above values have been found, the initial values of the x, y, and z coordinates may be located using the following equations:

$$x = r_{12} * \sin\theta 1 * \cos\phi 1 = r_{12} * \alpha \qquad (10)$$

$$y = r_{12} * \sin\theta 1 * \sin\phi 1 = r_{12} * \beta \qquad (11)$$

$$z = r_{12} * \cos\theta 1 = r_{12} * \gamma \qquad (12)$$

This calculation determines point 2, the first point away from the z-axis. The determination of point 3 as illustrated in the **Figure 3** is handled in a similar manner, except that the equations are slightly changed. The direction cosines α', β', γ' of the direction r_{23} are now determined and the new coordinates x_3, y_3, z_3 are obtained as shown at the bottom of **Figure 3**.

2.3. Methods For Killing the Photon:

To avoid going into an infinite "loop", a decision must be made to place limits upon the life of each particle. These limits are I Absorption, II. Failure To Reach Detector, III. Energy Falls Below a Set Limit, IV. Leaving the Detector Volume.

The decision for absorption is based on the type of interaction. Photoelectric and pair production lead to photon absorption, while Compton does not.

After a Compton interaction, the photon survives with reduced energy. Clearly, there is a possibility for a photon to have numerous Compton interactions with a corresponding energy reduction after every such collision. Since in practice there is always some energy below which the photon cannot produce a pulse that can be recorded, it is a waste of effort to follow such a particle forever. A decision is made to consider the particle lost (dead) after its energy falls below a certain limit which is taken to be in the range of 10 - 1 KeV.

The present status of this work is this: All the parts of the program have been written but no results for the detector efficiency have been obtained. This work will be continued until such time as the detector's efficiency may be determined.

CONCLUSION:

The use of the Monte Carlo method is a good way to accurately take into account all the possible interactions as well as complex geometries which may be encountered when one studies particles. For the calculation of the gamma ray detection efficiency, the Monte Carlo method may be applied successfully for any size and detector shape and for any gamma energy range.

APPENDIX

LISTED FIGURES CITED IN DISCUSSION

FIGURE 1: INTERACTIONS

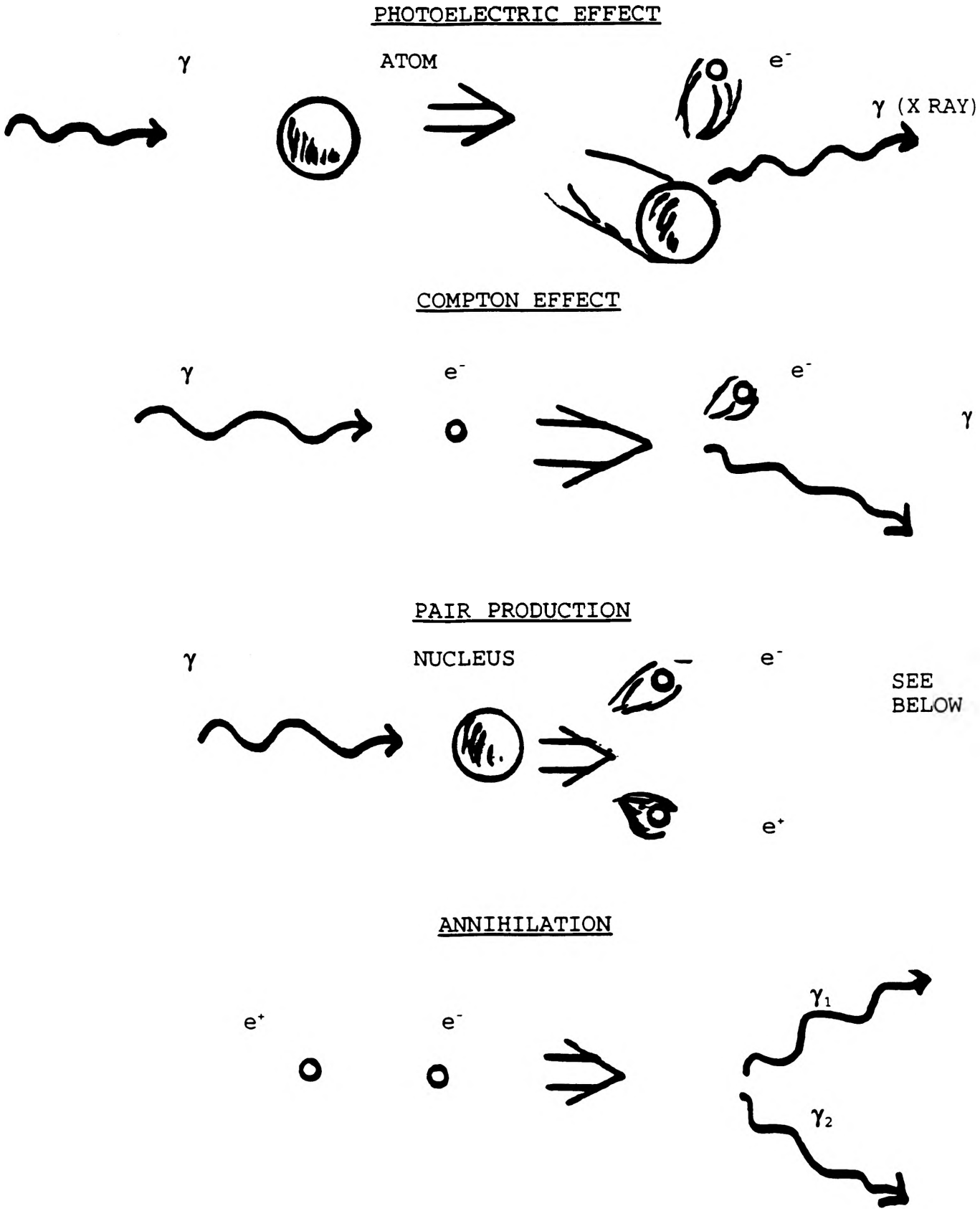

FIGURE 2: SOURCE PRODUCTION VS GAMMA DETECTION

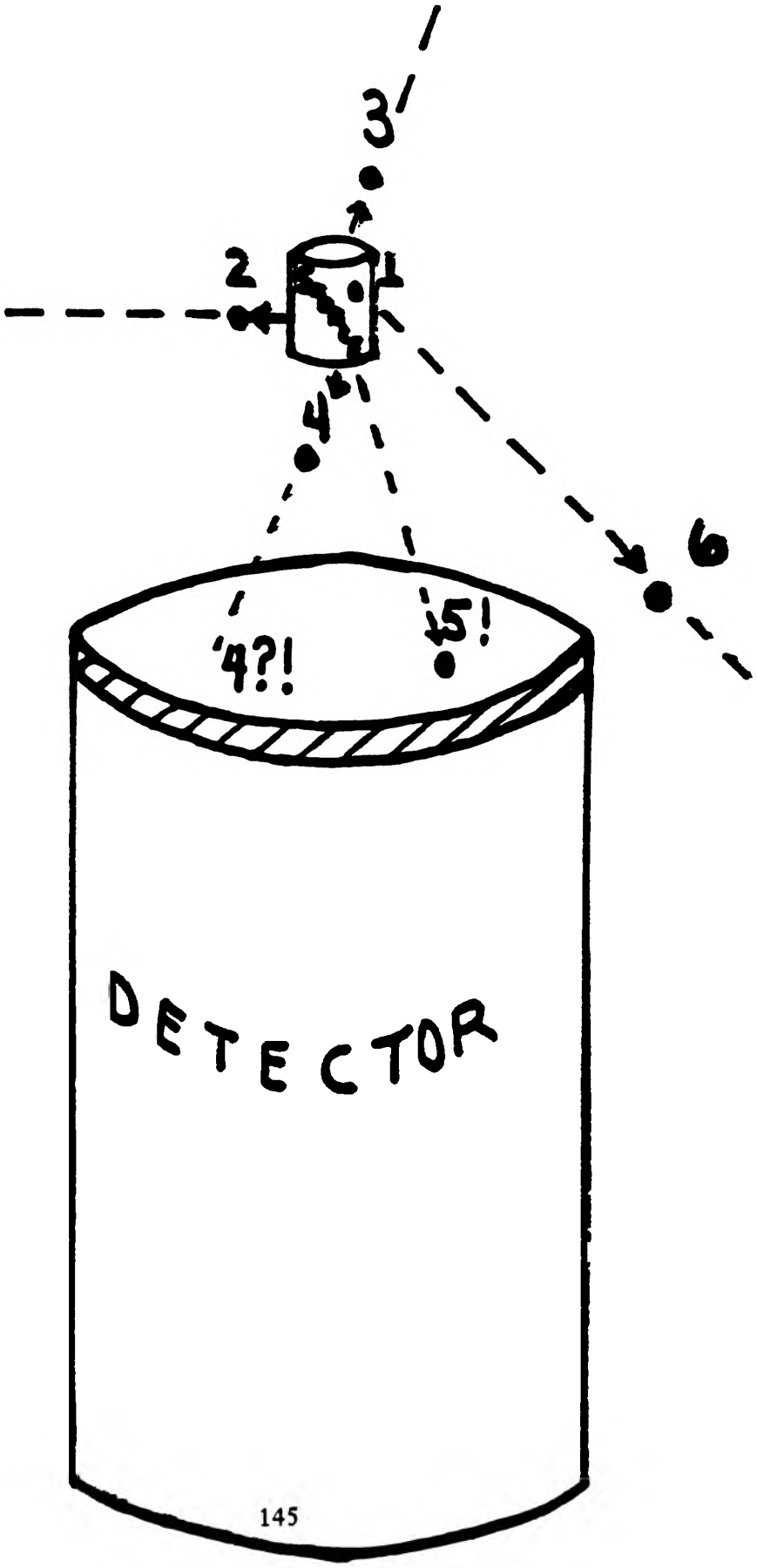

FIGURE 3: ROTATION OF COORDINATES

Assuming that the cosine of the polar angle of scattering is μ, the azimuthal angle is ϕ, and the direction cosines of the initial direction are α, β, and γ, then the direction cosines of the scattered photon, which are designated by α', β', and γ', are calculated as shown in Fig. 13.

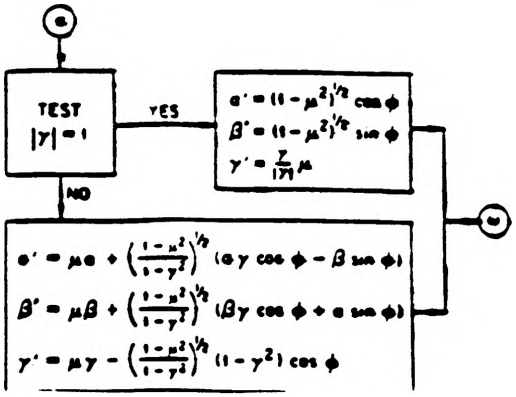

α', β', γ' are direction cosines with respect to the fixed coodinate system

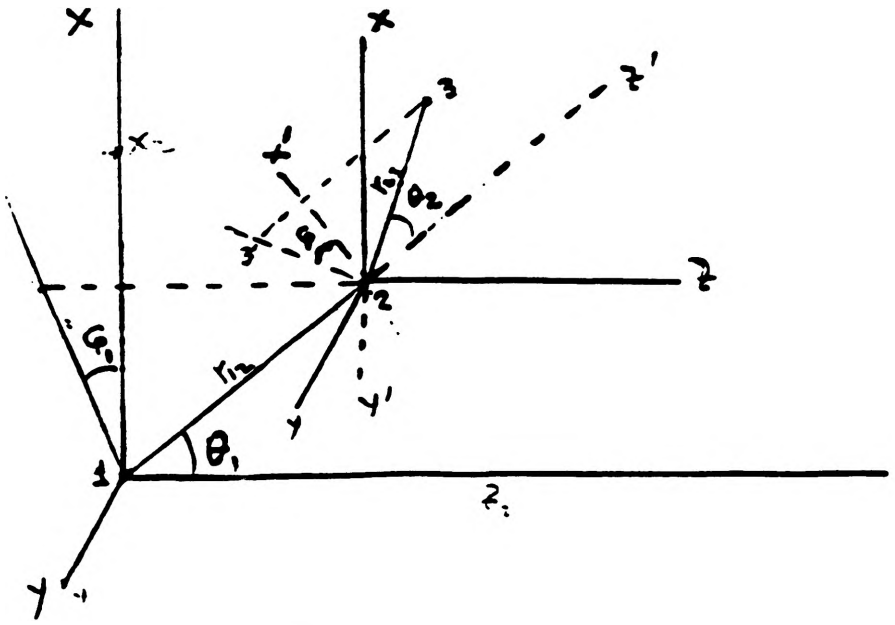

$\mu = cos\theta_2$

$\alpha = sin\theta_1 * cos\phi_1$

$\beta = sin\theta_1 * sin\phi_1$

$\gamma = cos\theta_1$

If $\gamma = 1$, this means $\theta_1 = 0$ and the equations for α', β', γ' are simpler to solve.

NEW COORDINATES

$$x_3 = x_2 + r_{23}\alpha' \qquad x_2 = r_{12}sin\theta_1 cos\phi_1 = r_{12}\alpha$$

$$y_3 = y_2 + r_{23}\beta' \qquad y_2 = r_{12}sin\theta_1 sin\phi_1 = r_{12}\beta$$

$$z_3 = z_2 + r_{23}\gamma' \qquad z_2 = r_{12}cos\theta_1 = r_{12}\gamma$$

Microcomputer Control of a Model Robot System

David N. Ilges

Electrical Engineering Department

ABSTRACT

The project involved creating an interface board that would allow an I.B.M.- AT computer to control a model robotic system already in existence. The I.B.M.- AT computer was then to be programmed in Pascal such that the model robotic system could perform various path movements and functions.

The interface board involved taking various digital outputs from the computer and converting them to analog control signals or use them to turn devices off and on. The interface board also would collect inputs from the robotic system and convert these analog values back to digital words.

INTRODUCTION

Since the robotic system to be used in this experiment had been designed by a previous graduate level Electrical Engineering student, the problem was to decipher what was needed by the system in order for it to run properly. The data left by the student was very poor and outdated since updates to the system had been made after the information he had written down was done. It was decided to use an I.B.M.- AT due to its incredible clock speed, availability and computing power. In order to take advantage of the power available from the Intel '386 processor, an interface board needed to be designed that could utilize all of its advantages.

The interface board was designed to accomodate input signals from the robotic system from the two infrared detector circuits and from the potentiometers associated with the three joints of the robotic arm used to remove parts from the conveyor belt. The board must also accomodate output signals from the computer and change these to control signals with analog outputs in order to control the speed and position of the joints of the robotic signal such that the arm can be positioned correctly. Another signal to be controlled is the magnetic coil at the end of the robotic arm extension in order to energize it.

The interface board contains an analog to digital convertor in order to process information obtained from the potentiometers associated with the motors on the robotic system.

The control functions not accomplished using hardware implementations will be done with the control program being written in Pascal. These functions include the path and velocity calculations that need to be made in order to move the robotic arm into position smoothly and accurately. This software part of the control system enables many functions normally implemented in the hardware to be accomplished in a manor that allows them to be updated and changed any time a new revision for improvement comes along.

PROCEDURE

The process of designing the interface board involved first determining what communication pins needed to be used to convey data from the computer to the interface card. The pinout connections for the I.B.M.- AT computer interface cards are shown in Figure 1 below. These pin configurations labeled in Figure 1 are the actual ones that are to be used.

Pinout Configuration

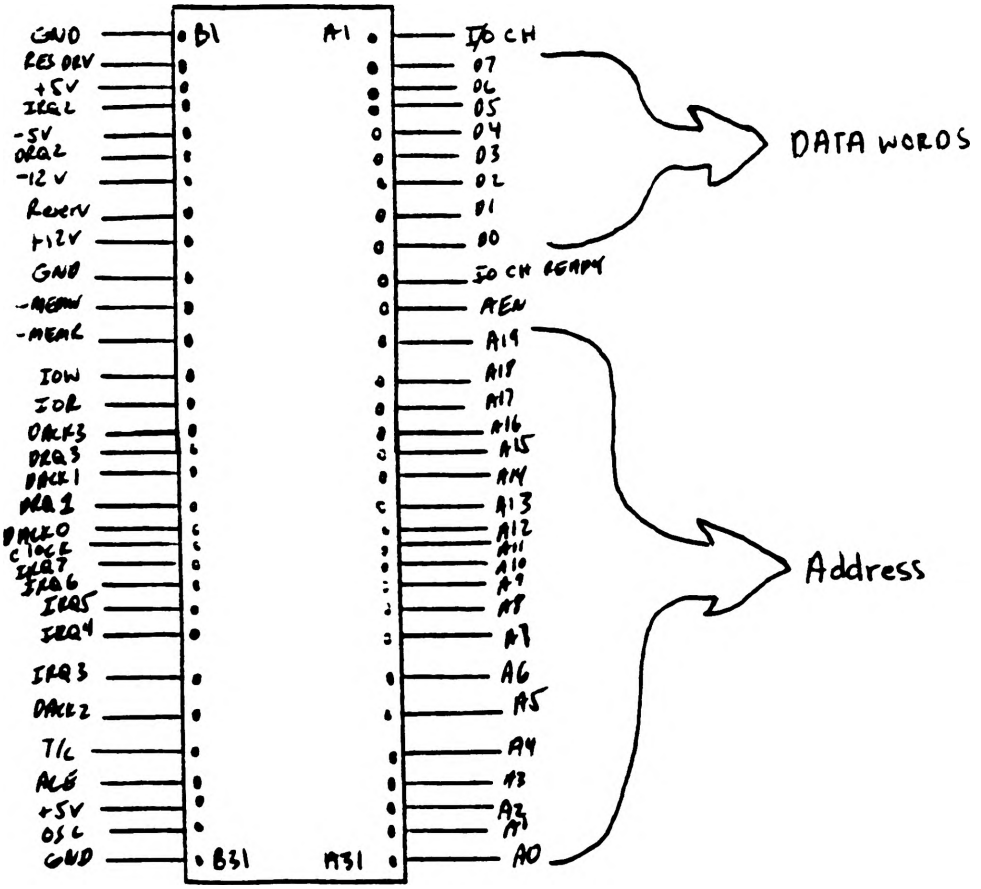

Figure 1

Once the data is taken from the computer it is to be stored in a register, this information is then either used to turn a device on or off or it is sent to the pulse width modulation circuitry already in place and contains information on the velocity at which a particular moter should move. The adreesing scheme involves using a sixteen bit word and using part of it to determine device selection and the other part to convey information on the desired speed and/or action to be taken. The sixteen bit word is shown in figure two and the information carried in each bit is labeled.

Computer Word

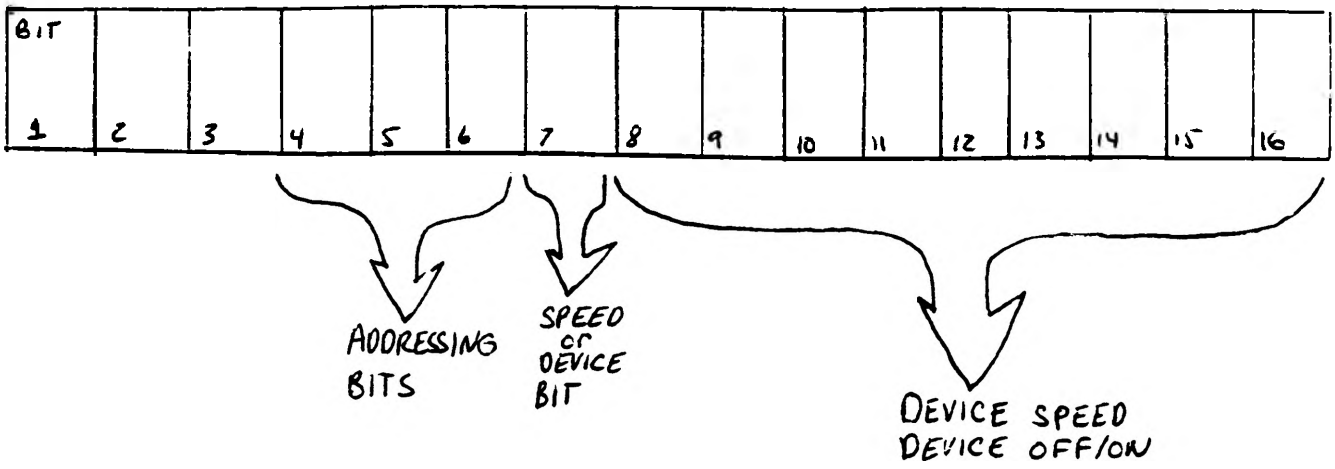

Figure 2

The computer program is to be set up in such a way that the program continually checks the status of the particular potentiometers alternately with outputting control information when device speed or status needs to be updated. This method of polling the inputs should still be quick enough to allow good control response of the robotic system.

When an output is checked such as the potentiometer, the analog signal obtained needs to be converted to a signal that the computer can understand. This is solved by sampling each input every 10 milliseconds alternately and running the input through an analog to digital converter in order to display the position in a digital word. The analog to digital converter used in this experiment is an 8 bit converter which gives a resolution that is accurate enough to work very well with the system setup. Since the analog to digital converter is a National Semiconductor ADC0808 it has eight channels multiplexed such that all inputs can be checked fairly closely together. The maximum delay time associated with the convertor is approximately 116 microseconds. This fast enough to give accurate results since the motor velocities used with this robot are not great enough to cause position changes that would need faster times.

A real time clock is used on the interface board in order

to reduce some of the software requirements of the system and to allow afaster sampling process to be used. The real time clock is to be used in order to provide the computer with a method of timing for the necessary sampling. The clock has an adjustable sampling period which is controlled by a potentiometer on the circuit board. The clock is implemented using a pair of monostable multivibrators in such a fashion that each one will remain at its peak stable value until it is retriggered by the decay of the RC time-constant.

The overall design of the interface board and the routing of signals through it can be seen in Figure 3. This figure gives general information and signal flow information and provides an overview of what function the interface board serves in the whole scheme of the system.

Signal Flow

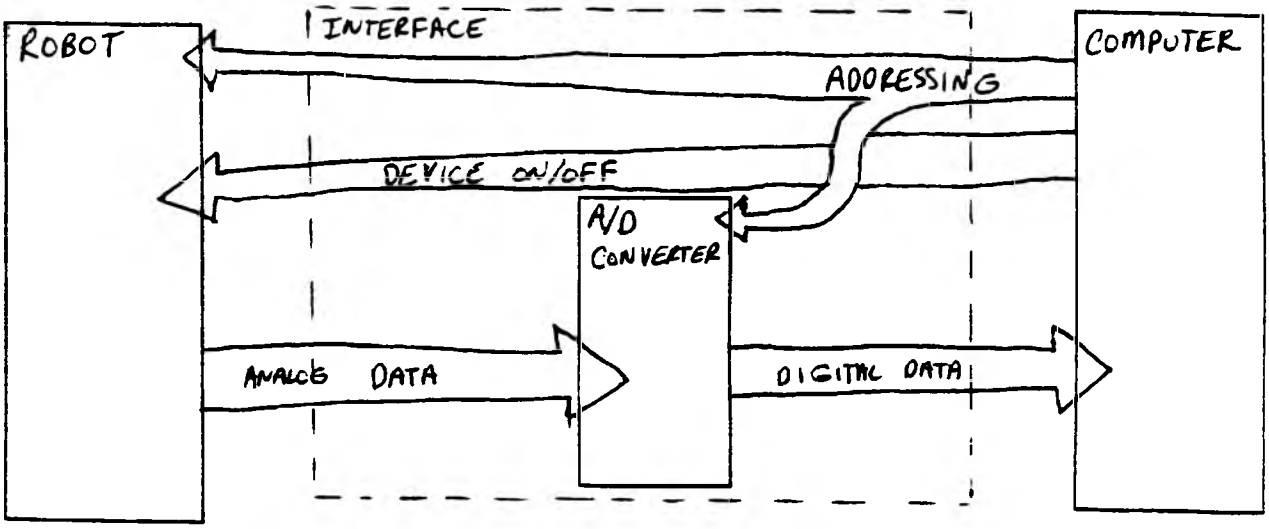

Figure 3

The above figure confirms the function that the interface board serves and allows for an understanding of how the sytem works.

CONCLUSION

This experiment has involved successfully designing an interface board that accomplished the desired control functions needed to allow a model robotic system to successfully operate. This board used the computer outputs and then processed them such that they would control the motors used to move the robotic arm into position. The inputs are sampled at a frequency determined by the real time clock and are fed back to the computer control program and processed such that any change in device speed or status that needs to be made can be done via the computer

outputs. These inputs are read by the analog to digital converter and changed into digital words in order for the computer to understand them and process the data. The interface board works up to design criteria and meets its requirements.

ACKNOWLEDGEMENTS

I wish to thank many individuals for there help in accomplishing this project. There contributions and support would not have made this project possible.

I would like to thank most of all Dr. Randy Moss who was my faculty advisor on the project and whose guidance and expertise is greatly appreciated.

I would like to thank my partner who was in charge of writing the control program, John Fierke. His continual insights and efforts made the design of the board much more feasible.

I would like to thank Jim Dopher for his assistance in the soldering of parts and advise on where to obtain information on particular points necessary to the completion of the project.

I would like to thank Kurt Hambacker for his advise on interfacing schemes and connections associated with the I.B.M. computers.

The Simulation of Tool Path Generation in Milling for Machining Processes

Rickey W. Jennings
Department of Mechanical Engineering

ABSTRACT

This paper is a report on the progress of this project to create a complete CAD/CAM system. The paper describes the introduction to the simulation package called Vericut. It also discusses the integration of the three packages: AutoCad version 11, PCAPT with APTGEN, and Vericut. The progress of the project to this point is only to the integration of the three packages. The paper also indicates the work which still needs to be completed. The key point of which is the menu system which is the final step in the project.

INTRODUCTION

The purpose of this paper is to give the progress on my project of "The Simulation of Tool Path Generation in Milling for Machining Processes". The objective of this project is to create a CAD/CAM system for use in Computerized Numerically Controlled (CNC) milling processes. This project involves the integration of several PC based software packages which can perform the desired function of the system. The system is ran on an IBM P/S 2 and the entire system is to be contained in the one unit. The main function of this system is to simulate tool paths for milling processes and the Vericut tool path simulation program [1] is used to perform this function of the system. Several possible packages or combinations of packages can be used to create the geometry and tool path data for the system. The initial package chosen to create the necessary geometry and tool path data for input into Vericut is E-Z-Mill [2]. The E-Z-Mill package, however, has a limited geometrical capabilities and is loaded on the IBM AT computers in the computer lab which makes it a less than ideal choice for the system. For these reasons I only used the E-Z-Mill package as a method for an introduction to the Vericut package.

In order to create the complete system the combination of AutoCad version 11 [3] and PCAPT [4] is used to create the necessary input into Vericut. The diagram of the method of integration of the three packages is shown in figure 1 on the next page.

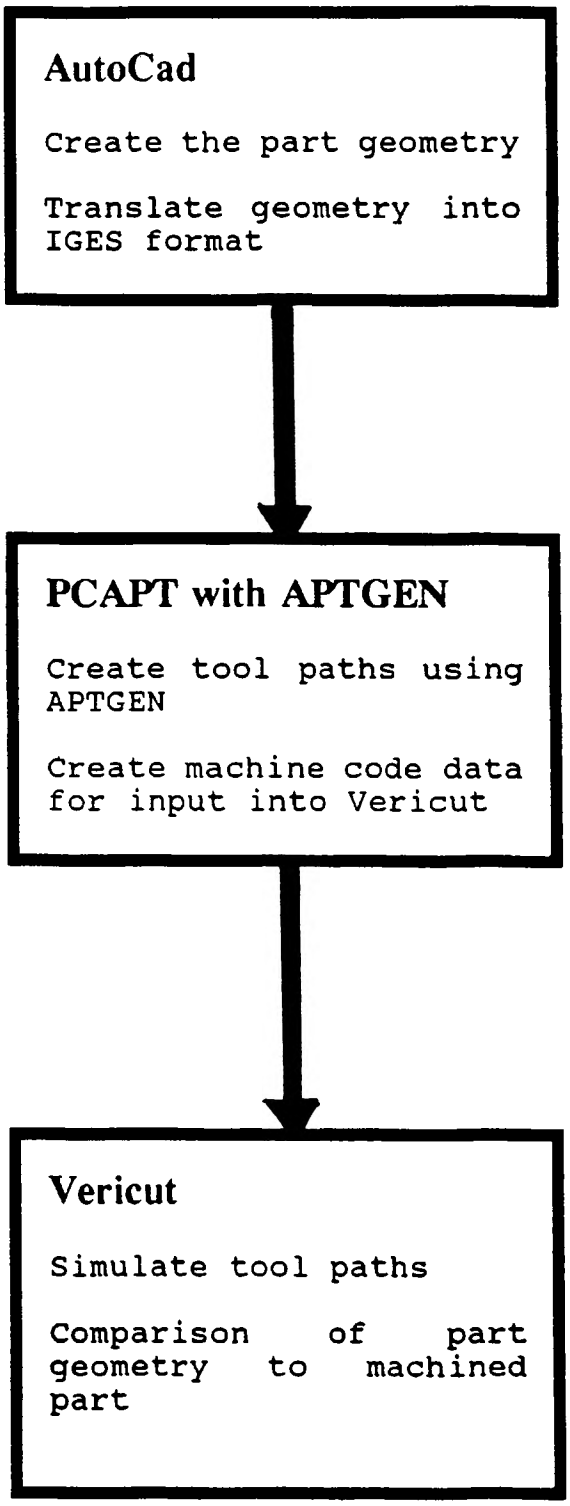

Figure 1. Schematic Of CAD/CAM System

AutoCad is a very flexible system with solid modelling capability and creates the necessary Initial Graphics Exchange Specification (IGES) format for input into PCAPT. PCAPT is the package which produces the tool path information which is used as the input into Vericut and eventually the input into the NC milling machine. PCAPT takes the IGES input from AutoCad and through the use of the AptGen program within creates the tool paths.

INTRODUCTION TO VERICUT

Creation of Geometry and Tool Paths Using E-Z-Mill

The first step of the project was to familiarize myself with the Vericut package. This was accomplished by creating simple objects using E-Z-Mill located in the AT computers in room ME 217. The geometric entities were created using the geometry function of E-Z-Mill [2].The geometric entities were created by defining the points, lines, and circles which make up the entity. The geometry created by E-Z-Mill was then used to create the tool paths.

The tool paths were created next using the geometry already created. The next step was to enter the part program section of E-Z-Mill [2] in which the tool paths were defined. The type of cutting operation must be chosen first upon entrance into this section. Then the tool parameters and the depth of cut must be set-up using the appropriate menu choices. Once the tool parameters have been set the tool path can be defined. This was accomplished by choosing the points and other geometric entities in a clockwise direction around the object. This process was repeated multiple times, each time moving the cutter in a distance equal to the cutter radius, to cut the part to its final dimensions.

Once the tool paths were defined the Post module of E-Z-Mill [2] was entered and the CNC program was created. The program was created by using the file BOSS8I [2] which contain the necessary CNC information which was required by E-Z-Mill [2]. The output was a listing of machine code. A sample of this machine code is shown below.

```
N5G70G75G90
'BLOCK1      23-FEB-92'
'MILL1'
'TOOL NUMBER:1       SPINDLE RPM:1000'
N25G0X0Y0T1M6
N30X-1.25Y2.0
N35Z0.05
N40G1Z-2.0F5.0
```

Figure 2. Machine Code Produced By E-Z-Mill

This machine code can then used as the input for Vericut.

Tool Path Simulation Using Vericut

The code which Vericut uses to simulate the machining process is an ASCI file, which is similar to the clprint file created by many APT programs, and an example is shown below [1].

```
PARTNO THIS IS A SAMPLE TOOL PATH FILE
COOLNT/ON
SPINDL/500,CLW
CUTTER/10,0,0,0,0,0,18
FEDRAT/100.0
FROM/10.,-6.,5.
GOTO/10.,0.,5.
GOTO/40.,0.,16.
FEDRAT/10.0
GOTO/40.,5.,16.
GOTO/10.,5.,16.
GOTO/10.,10.,16.
GOTO/40.,10.,16.
GOTO/40.,21.,16.
GOTO/10.,21.,16.
COOLNT/OFF
SPINDL/OFF
```

Figure 3. Example Of The ASCI File Used By Vericut

The file created by E-Z-Mill, however, is in machine code which is not directly readable by Vericut. Therefore the machine code from E-Z-Mill must be converted into an ASCI file and this is accomplished though the use of the Revpost program in Vericut [1]. Before the Revpost program can be ran the proper codes for the specific post-processor which is used to create the machine code. Upon entering the Revpost program the codes can be checked and changed to match those used by the post-processor. A file corresponding to the post-processor is now created and is used to convert the machine code into an equivalent ASCI file as shown above. It is now necessary to create a tool library for Vericut to access when running the part program. The tool library is created using the MS-DOS editor [5] and is as follows.

```
CUTTER/1,0,0,0,0,0,5
CUTTER/.5,0,0,0,0,0,5
CUTTER/.5,.25,0,0,0,0,5
CUTTER/1,.125,0,0,0,0,5
```

Figure 4. Tool Library File For Vericut

The tool library file contains the specifications for the cutters which are used in the part program.

Once the file is translated we are ready to enter Vericut. Upon entering Vericut you are presented with the following screen [1].

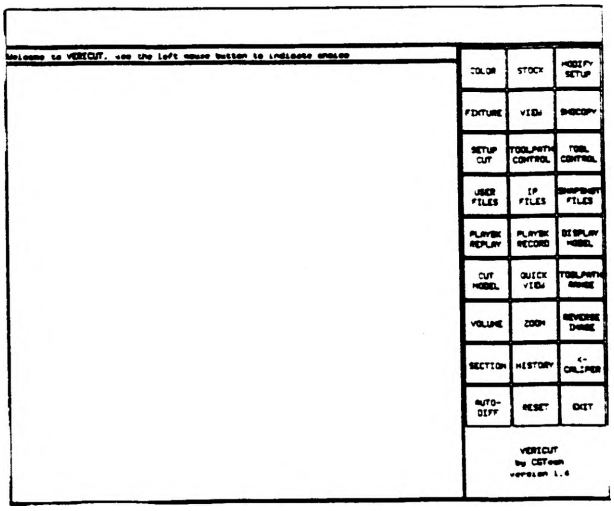

Figure 5. Vericut Screen

The Vericut program is ran using the mouse as the main interface tool. The first step once in Vericut is to indicate the appropriate tool path and tool library files. Once these have been entered in the proper areas in the Vericut the program is ready to be executed. First, however, you must input the stock dimensions into the stock set-up. Next click the display model icon to display the stock for machining.

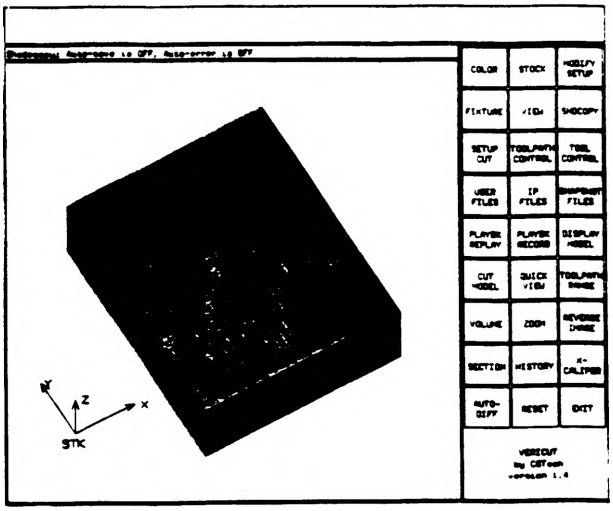

Figure 6. Stock Display

Once the stock is displayed the cut model icon is clicked to execute the machining process. Once the machining is complete the finished part is displayed.

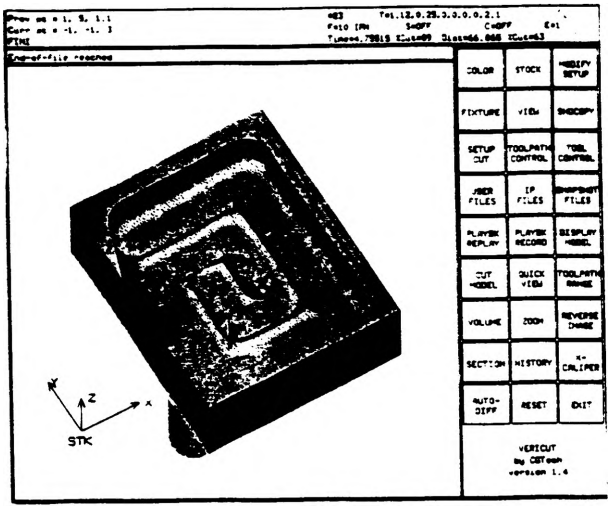

Figure 7. Finished Part

This concluded the introduction to Vericut and the skills developed are used in the integration of the three software packages chosen for the CAD/CAM system.

INTEGRATION OF SOFTWARE

The purpose of this project was to create a complete CAD/CAM system and for this the following packages were used.

1. AutoCad version 11
2. PCAPT with APTGEN
3. Vericut

Creation of Geometry Using AutoCad

The use of AutoCad to create the required geometry is because AutoCad is a very versatile CAD package with solid modeling capabilities. The geometry created using AutoCad must be converted to IGES format for input into APTGEN in PCAPT. At this time I have not completed the work for the AutoCad portion of the system. This section of the integration is to be finished by the end of April.

Creation of Tool Paths Using PCAPT With APTGEN

Once the geometry has been completed in AutoCad and has been converted into IGES format we are ready define the tool paths. In order to gain an understanding of the workings of PCAPT and APTGEN sample parts were designed using the geometry function with in APTGEN. Creating the required geometry in APTGEN is a tedious

process which can be accomplished much more easily in AutoCad. An example of the geometry created by APTGEN is shown below.

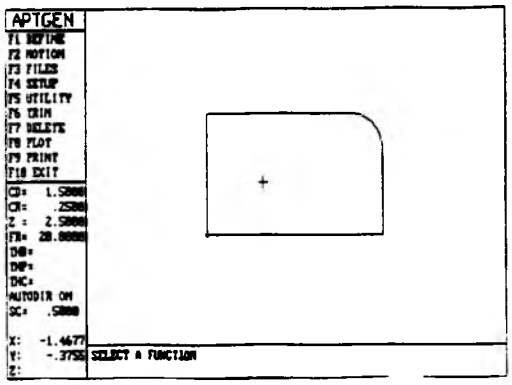

Figure 8. Geometry Produced by APTGEN

The advantage to using APTGEN comes in the easy of defining the tool paths. The method of assigning tool paths in APTGEN is as follows. The cutter size is defined using the "TOOLCHG" function [4]. First you must assign the starting point of the tool and then you use the "Startup" command to bring the cutter to the cutting surface [4]. Then the cutter path is created by simply picking the surfaces which are to be machined in the process with the mouse. A tool path which was defined is shown below.

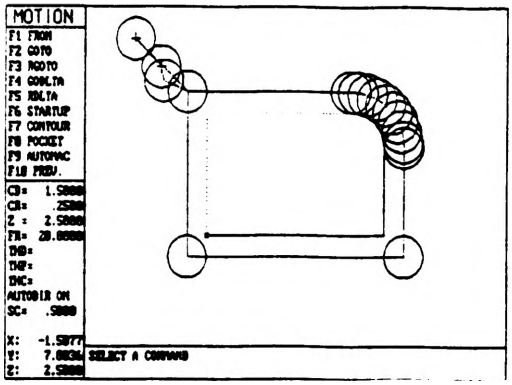

Figure 9. Tool Path Defined by APTGEN

Once the tool path was defined by APTGEN the part program was executed and the machine code was produced by PCAPT. The post processor which created the machine code was GMILL1 [5]. This code created by GMILL1 is much the same as the machine data produced by E-Z-Mill and can be translated using the Revpost [1].
Once the code is converted it can be executed in Vericut to see the machining which has been defined.

FUTURE WORK TO COMPLETE THE SYSTEM

The intention of this project is to create a complete CAD/CAM system including the simulation of the cutting process. In order to complete the system a menu system and program is to be designed so that the three packages will act as a single system. The menu and program will access each package when the appropriate number is chosen and will facilitate the transfer of the files between the packages. The menu is intended to be very user-friendly and to simplify the design process.

The other addition to the system will be the use of the geometric interface which is in Vericut [1]. This interface will take a solid model created by AutoCad and convert into the format recognized by Vericut. This solid model will be used in the "auto-difference" function [1] in Vericut to compare the desired shape to what is obtained in the cutting process.

CONCLUSIONS

The purpose of the project is to produce a complete CAD/CAM system. Once the project is finished a very complete CAD/CAM system will be produced. The system will have very wide uses including use as an aide in design projects and use as a teaching aide in manufacturing and design classes.

ACKNOWLEDGMENTS

I would like to thank my advisor Dr. Lu for his help and support of this project.

REFERENCES

1) Vericut Manual version 1.4, CGTech, 1991

2) E-Z-Mill Manual

3) AutoCad version 11 Manual

4) PCAPT Manual version 3.2, N/C Software, 1990

5) GMILL1 Manual

IMPLEMENTATION OF TI545 IN AIR PRESSURE CONTROL

Kenneth D. Kangas

Electrical Engineering Department

ABSTRACT

The Texas Instruments Model 545 programmable logic controller is used to control the air pressure in a heating/ventilation simulator designed and built for a classroom experiment station. Through the use of the PLC's built-in PID algorithm, the pressure in the duct was controlled to within a 2% tolerance and over 72% of the sensor range for a load setting of 10%. The theory of PID controllers and their application to this problem are discussed. Also, the configuration of the simulator, and plans for future work are described.

THEORY

The Proportional-Integral-Derivative (PID) controller, because of its simplicity and effectiveness, is one of the most widely used control schemes in industry. Fundamentally, the PID is a feedback loop with three terms in the feedback transfer function: proportional, integral, and derivative. The proportional term responds to changes in the process variable, but a P controller settles at an offset value that is different from the process set-point. The integral term remedies this problem by responding to the integral of the difference between set-point and process variable values. However, in some circumstances, the integral term can saturate the controller and render it useless. The use of an integral reset coefficient can fix this problem. The derivative term is added in some situations for faster response and better damping characteristics.

SYSTEM DESCRIPTION

The heating/ventilation simulator (see Figure 1) consists of a piece of ordinary air ducting with a 3-phase blower on one end, a heating element inside, and a variable opening on the other end to simulate varying loads on the H/V system. The blower is driven by an Allen Bradley variable-frequency motor drive, with a range of 0.5 to

60 Hertz. The drive frequency is controlled by a 0-10 Volt analog signal from the PLC. An Omega pressure sensor with a range of 0-1" H_2O is located close to the opening and sends a 4-20 mA analog signal to the PLC.

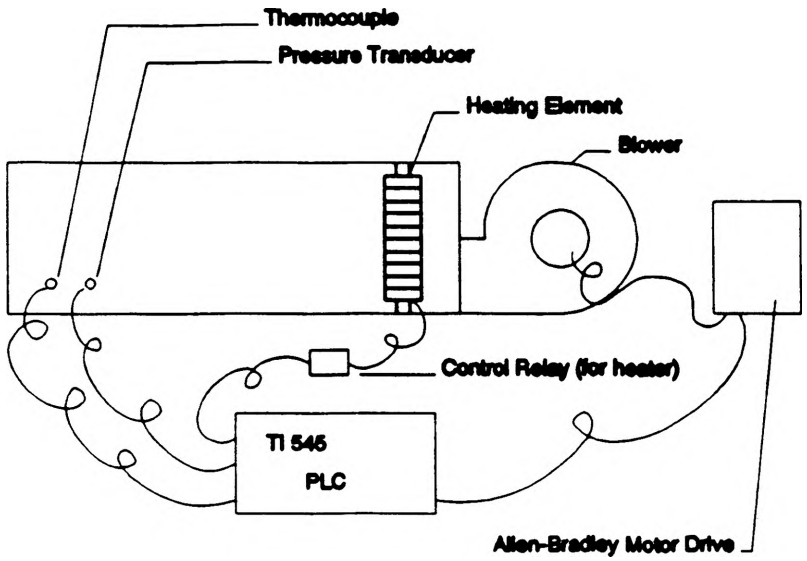

Figure 1

CONTROL

There are three primary parameters which affect the pressure inside the duct: (1) the speed of the blower, (2) the load setting, and (3) the temperature in the duct. To simplify the investigation, the load was considered to be a system disturbance and not controllable by the PLC. Also, the effect of temperature on the pressure was neglected. In essence, the duct air pressure was considered to be a direct function of only the speed of the blower. The block diagram of this simplified system is shown in Figure 2.

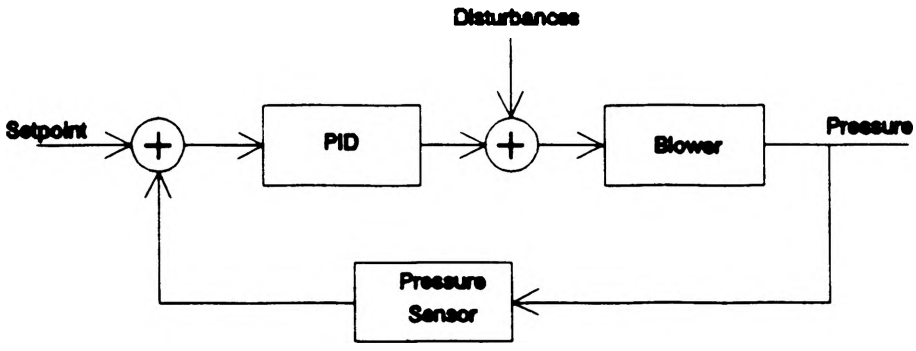

Figure 2

The Laplace transform of the PID loop is given by equation 1.

$$M = K_c (E + E/(T_i s) + CT_d s) + M_x/s \quad (1)$$

Where:

M = PID loop output
E = Set point - process variable
C = Process variable (pressure in duct)
M_x = Loop output when E=0
K_c = Proportional Gain
T_i = Reset coefficient
T_d = Derivative coefficient

As was mentioned before, the PLC has a pre-programmed PID algorithm so that the application engineer has only to "fill in the blanks" to set up and tune the controller. The set-point is held in a special dedicated variable called LSPX (where X is the loop number, 1-64.) In this case, the process variable (C) is contained in WX49, which is the address of the analog pressure sensor value after A-D conversion. The parameters K_c, T_i, and T_d are directly entered into the PID loop table (Appendix A.) It was found that values of 0.75, 0.09, and 0, respectively, gave the best performance. T_d was set to zero because taking the derivative of the inherently noisy pressure signal puts wild swings into the loop output. This effectively classifies this control as a PI control rather than a PID.

PERFORMANCE

The PI controller is not aggressively tuned and the settling time equals the rise time. There is no sinusoidal "bouncing" around the set point, so once it is within tolerance, it stays within tolerance. Table 1 shows the 95% rise times when the set point was changed in a step from 10% to another value. For each measurement, the system was allowed to settle at the 10% point before input of the new set-point value. The control was able to hold the process variable to within 1.3% of the set point. In the table, t_r is given in seconds, set-points are given in hundredths of an inch of water (which corresponds to percent of sensor range.)

TABLE 1: RISE TIMES

New Set Point	t_r
15	14
20	22
25	27
30	29
40	29
50	30
60	30
72	30

PROGRAMMING

The basic programming tools of the PLC logic are discrete and analog inputs and outputs, control relays, timers, counters, math special functions, and various bit and word manipulation functions. Most of the programming of this project was accomplished in math special functions. The ladder listing and special function listing are in Appendix A.

The basic operation of the system is to use a selector switch (X3, X4, X5, X6) to choose one of two pressure set-points (or one of two temperature set-points in the future.) Then using momentary push buttons (X7-up,X8-down,) the set point is incremented up or down by one percent. The value is displayed on an LED readout (Y17-Y24.) When the START button (X1) is pressed the value from the display is loaded into LSP1 (the PID algorithm's dedicated set-point address,) the loop is set to automatic mode, and the control relay (Y29) for the frequency drive is turned on. The set point may be changed at any time with no effect on the loop until the START button is pressed. Pressing the STOP button (X2) turns off the freq. drive relay and takes the PID loop out of automatic mode. The two lamps (Y26, Y28) are turned on and off by the control loop flag (C106) which shows the sign of the E in the loop. For example, if the system is stepped to 60 from a value of 20, the Error (set-point - process variable) will be positive until the process variable becomes greater than the set-point. This was handy for tuning, since one could see the system was settled when the two lights began blinking back and forth rapidly.

FUTURE WORK

Plans for future experimentation consist mainly of developing a temperature control loop, a better user interface, and perhaps implementing a fuzzy controller to replace the PID algorithm. All three of these will be totally software changes, as the temperature control hardware is already in place.

The most immediate of these projects will be the temperature control loop. It will be almost identical in structure to the pressure control loop except that the heating element (driven by a relay) is either off or on. There is no analog control of the heating hardware. Therefore a proportional time control scheme will be implemented, where the output from the PID will go to a math function which will calculate a duty cycle for the heating element. One of the issues to be resolved in this problem will be finding the optimum period of the off/on total cycle.

CONCLUSION

By holding the pressure to within 1.3% of the set point, PLC PID controller has proven its viability to an HVAC application. The ease with which the application engineer is able to assemble a working system highlights the flexibility and explains the popularity of the industrial programmable logic controller.

ACKNOWLEDGMENTS

I would like to thank those whose help has made this project possible:

Dr. Kelvin Erickson -- Faculty Advisor

Marvin "Eddie" Light and Donald "Frosty" Foster for building the platform

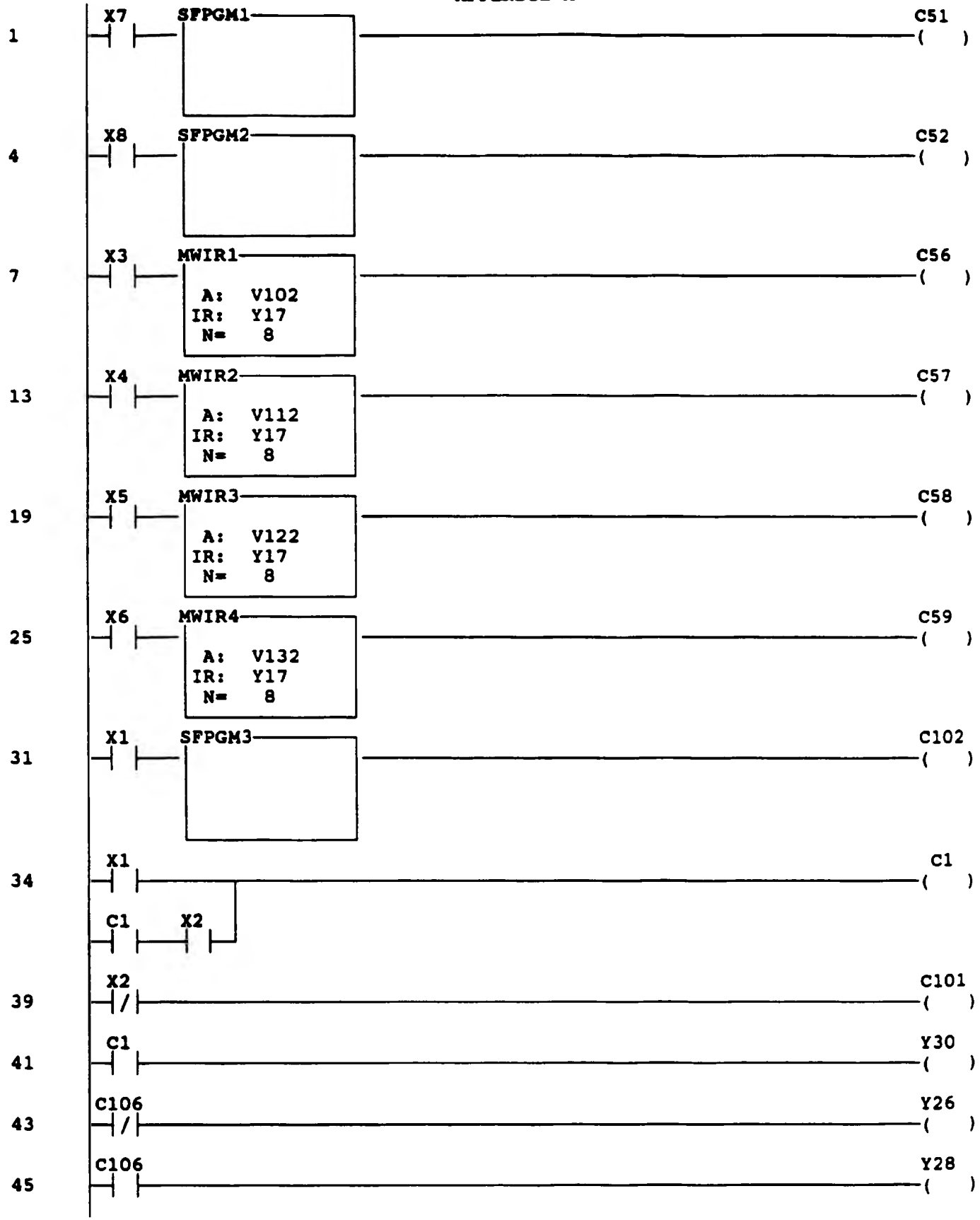
1
X7
SFPGM1
C51
4
X8
SFPGM2
C52
7
X3
MWIR1
A: V102
IR: Y17
N= 8
C56
13
X4
MWIR2
A: V112
IR: Y17
N= 8
C57
19
X5
MWIR3
A: V122
IR: Y17
N= 8
C58
25
X6
MWIR4
A: V132
IR: Y17
N= 8
C59
31
X1
SFPGM3
C102
34
X1
C1
C1
X2
39
X2
C101
41
C1
Y30
43
C106
Y26
45
C106
Y28

```
    PID LOOP   1  TITLE: PRESSURE

  POS/VEL PID ALGORITHM: POS
     LOOP VFLAG ADDRESS: C101
     SAMPLE RATE (SECS): +0.10000

PROCESS VARIABLE ADDRESS: WX49
        PV RANGE:  LOW = +20.0000
                   HIGH = +100.000

          PV IS BIPOLAR: NO
      SQUARE ROOT OF PV: NO
       20% OFFSET ON PV: YES

    LOOP OUTPUT ADDRESS: WY57
      OUTPUT IS BIPOLAR: NO
  20% OFFSET ON OUTPUT: NO

  RAMP/SOAK PROGRAMMED: NO
      RAMP/SOAK FOR SP: NO


        ALARM DEADBAND: +2.00000

  MONITOR LOW-LOW/HI-HI: NO
      MONITOR LOW/HIGH: NO
  PV ALARMS:   LOW-LOW = +41.0000
                   LOW = +45.0000
                  HIGH = +55.0000
             HIGH-HIGH = +59.0000

          REMOTE SETPOINT: NONE
    CLAMP SP LIMITS:  LOW = +20.0000
                     HIGH = +100.000

                LOOP GAIN: +0.75000
     RESET (INTEGRAL TIME): +0.09000
   RATE (DERIVATIVE TIME): +0.00000
              FREEZE BIAS: NO

 DERIVATIVE GAIN LIMITING: NO
    LIMITING COEFFICIENT: +10.0000

  SPECIAL CALCULATION ON: NONE
        SPECIAL FUNCTION: NONE

           LOCK SETPOINT: NO
        LOCK AUTO/MANUAL: NO
            LOCK CASCADE: NO

         ERROR OPERATION: NONE
          REVERSE ACTING: NO

       MONITOR DEVIATION: NO
 DEVIATION ALARM: YELLOW = +3.00000
                  ORANGE = +5.00000

  MONITOR RATE OF CHANGE: NO
    RATE OF CHANGE ALARM: +0.00000

  MONITOR BROKEN XMITTER: NO
```

```
TITLE: SETPT.UP                                                SF PROGRAM    1
                    CONTINUE ON ERROR (Y,N): NO
                ERROR STATUS ADDR (Y,C,WY,V): V50 - V52
                     PROGRAM TYPE (N,P,C,R): PRIORITY
                           CYCLE TIME (SEC): 0.0
```

```
00001 *        INCREMENTS HIGH TEMP SET-POINT WITH
               ACTIVATION OF UP/DOWN SWITCHES
00002 IF       X3
00003 MATH     V101 := V101 + 1
00004 ENDIF
00005 IF       V101 > 99
00006 MATH     V101 := 99
00007 ENDIF
00008 BINBCD    BINARY INPUT..: V101            BCD RESULT....: V102
00009 IF       X4
00010 MATH     V111 := V111 + 1
00011 ENDIF
00012 IF       V111 > 99
00013 MATH     V111 := 99
00014 ENDIF
00015 BINBCD    BINARY INPUT..: V111            BCD RESULT....: V112
00016 IF       X5
00017 MATH     V121 := V121 + 1
00018 ENDIF
00019 IF       V121 > 99
00020 MATH     V121 := 99
00021 ENDIF
00022 BINBCD    BINARY INPUT..: V121            BCD RESULT....: V122
00023 IF       X6
00024 MATH     V131 := V131 + 1
00025 ENDIF
00026 IF       V131 > 99
00027 MATH     V131 := 99
00028 ENDIF
00029 BINBCD    BINARY INPUT..: V131            BCD RESULT....: V132
****  END ****
```

```
TITLE: SETPT.DN                                                SF PROGRAM    2
                    CONTINUE ON ERROR (Y,N): NO
                ERROR STATUS ADDR (Y,C,WY,V): V53 - V55
                     PROGRAM TYPE (N,P,C,R): PRIORITY
                           CYCLE TIME (SEC): 0.0
```

```
00001 *         INCREMENTS HIGH TEMP SET-POINT WITH
                ACTIVATION OF UP/DOWN SWITCHES
00002 IF        X3
00003 MATH      V101 := V101 - 1
00004 ENDIF
00005 IF        V101 < 10
00006 MATH      V101 := 10
00007 ENDIF
00008 BINBCD     BINARY INPUT..: V101              BCD RESULT....: V102
00009 IF        X4
00010 MATH      V111 := V111 - 1
00011 ENDIF
00012 IF        V111 < 10
00013 MATH      V111 := 10
00014 ENDIF
00015 BINBCD     BINARY INPUT..: V111              BCD RESULT....: V112
00016 IF        X5
00017 MATH      V121 := V121 - 1
00018 ENDIF
00019 IF        V121 < 10
00020 MATH      V121 := 10
00021 ENDIF
00022 BINBCD     BINARY INPUT..: V121              BCD RESULT....: V122
00023 IF        X6
00024 MATH      V131 := V131 - 1
00025 ENDIF
00026 IF        V131 < 10
00027 MATH      V131 := 10
00028 ENDIF
00029 BINBCD     BINARY INPUT..: V131              BCD RESULT....: V132
****  END ****
```

```
TITLE: LOOPS.ON                                                SF PROGRAM    3
                    CONTINUE ON ERROR (Y,N): NO
                ERROR STATUS ADDR (Y,C,WY,V): V56 - V58
                     PROGRAM TYPE (N,P,C,R): PRIORITY
                           CYCLE TIME (SEC): 0.0
```

```
00001 *         SETS LOOPS' REMOTE SET-POINTS TO THE
                VALUES CORRESPONDING TO POSITION OF THE
                ROTARY SWITCH
00002 IF        X3
00003 MATH      V210 := V101
00004 ENDIF
00005 IF        X4
00006 MATH      V210 := V111
00007 ENDIF
00008 IF        X5
00009 UNSCALE    SCALED INPUT..: V121          BINARY RESULT.: LSP1
                 LOW LIMIT.....: 0.0           HIGH LIMIT....: 100.0
                 20% OFFSET....: NO            BIPOLAR.......: NO
00010 ENDIF
00011 IF        X6
00012 UNSCALE    SCALED INPUT..: V131          BINARY RESULT.: LSP1
                 LOW LIMIT.....: 0.0           HIGH LIMIT....: 100.0
                 20% OFFSET....: NO            BIPOLAR.......: NO
00013 ENDIF
****  END ****
```

THE EFFECT OF SELF-RATED ATTRACTIVENESS ON PERSONAL AND INTERPERSONAL FUNCTIONING

Bonnie Mathis & Robert L. Montgomery
Department of Psychology

ABSTRACT

Self-ratings of one's own physical attractiveness among 455 students (311 male and 144 female) were compared with their scores on a scale measuring personality (the California Psychological Inventory) and subjective perceptions of their body weight. In addition, they completed two measures of shyness; the Social Provisions scale (Russell & Cutrona, 1984); the Student Adjustment to College Questionnaire (Baker & Siryk, 1984); and the Interpersonal Betrayal Scale. For both sexes, self-rated physical attractiveness correlated significantly with (a) all seven folk scales (dominance, capacity for status, sociability, social presence, self-acceptance, independence, and empathy) on Cluster I (extraversion) of the CPI; (b) two of the three vectors on the CPI: v.1 (intraversion) and v.2 (openness to norms); (c) shyness; and (d) having a boyfriend or a girlfriend. Self-rated physical attractiveness affected females, but not males with Social Provisions and perceived body weight.

INTRODUCTION

One of the most widely cited research conclusions in social psychology is summarized by Dion, Berscheid, and Walster's (1972) claim that, in people's perceptions of others, "what is beautiful is good" (p. 285). This statement linking beauty and goodness suggests a stereotype in which physically attractive individuals are believed to possess a variety of positive personal qualities. Dion et al. (1972) had subjects rate facial photographs selected on the basis of judge's agreement. The pictured individuals were low, medium, or high in physical attractiveness. Subjects' ratings of the people in the photographs pertained to various personality traits as well as to life outcomes such as marital happiness and career success. To the extent the pictured individuals were physically attractive, the subjects ascribed more favorable personality traits and more successful life outcomes.

This paradigm has guided many subsequent investigations, and a large body of research exists on the attractiveness stereotype. Most reviews of this literature are in agreement -- the "beauty-is-good" stereotype is a strong and general phenomenon (Adams, 1982; Alley & Hildebrandt, 1988; Berscheid, 1981; Berscheid & Walster, 1974; Dion, 1981; Hatfield & Sprecher, 1986). Secondary sources (e.g., introductory social psychology textbooks) have likewise treated the beauty-is-good stereotype as a homogeneous, potent, and firmly established phenomenon. Although the general concensus is that an attractive target leads perceivers to make strong inferences of personality goodness, some reviewers have noted exceptions to this phenomenon. Dion (1981) suggested that the beauty-is-good effect is strongest for measures of social competence and interpersonal ease, and Bassili (1981) reached a similar conclusion, arguing that the core of the physical attractiveness stereotype is social vitality or extraversion. In a recent meta analysis of this literature, Eagly, Ashmore, Makhijani, and Longo (1991), similarly, found that the effect may not be as wide-ranging as previously thought. Eagly et al., (1991) found the effect to

be limited primarily to the domains of social competence, and it had only intermediate effects in the area of potency, adjustment, and near zero effects on integrity and concern for others.

Nearly all research on attractiveness has used observer's assessments of a target's attractiveness. Self-ratings by the targets, themselves, of their own attractiveness, have been all but absent in the field. Moreover, ratings between self and others generally lack agreement. Patzer (1985, p.24), in fact, states that "self-measures of physical attractiveness do not work," and others note the low correlations between self-ratings and ratings by others (Downs & Wright, 1982). Balban (1981) found inter-rater reliability among observers to be .89, while reliability between self-ratings and others' ratings was .22. Other investigations (Stroebe, Insko, Thompson, and Layton, 1971; Adams, 1977) have found similar results.

A discrepancy as large as the one found between self-ratings of physical attractiveness and others' ratings raises an intriguing question. Why should such a disparity exist? In general, self-reports serve as legitimate sources of data and are treated as such. In addition, research indicates a widely applicable standard (though not quite universal) of human beauty. Even infants of four months of age respond differentially to an attractive versus an unattractive human face, and children at the age of four years and older have been shown to use the same criteria as adults in deciding who is, and is not, attractive. With such a highly developed set of perceptual and judgmental faculties so attuned with the "rest of the world" when judging the physical appearance of others, why would people be unable to apply these same standards when asked to judge themselves? Some evidence (Gurman & Balban, 1990; Montgomery, Haemmerlie, & Edwards, 1991) suggests, that except for those who are extremely attractive, many of us engage in a "self-serving" bias. That is, we see ourselves as being more attractive than we really are, at least in comparison to how we would be rated by a set of uninvolved independent judges. Moreover, this self-serving bias could function as an adaptive illusion. Stated otherwise, the belief we are more attractive than reality permits may benefit us in terms of self-esteem maintenance, personality integration, our interpersonal functioning, and in having a more active engagement with life.

The purpose of this study was to see if positive self-ratings of physical attractiveness may not, in fact, be of benefit. This was accomplished by having students rate themselves in attractiveness on a 1 to 10 scale and by comparing these scores with those made on the California Psychological Inventory (CPI), a well-known, valid, and reliable test of personality. In addition, self-rated physical attractiveness scores were compared to the scores made on two measures of shyness and on the Interpersonal Betrayal Scale (IBS) -- a test that we used to assess integrity. In addition, we wanted to see how one's self-rated physical attractiveness might impact other aspects in an individual's life -- one's adjustment to college, the number and types of friends one had, and the variety, quantity, and quality of social support provided by each of these friends. In general, we expected that the effects of physical attractiveness, as rated by oneself, would be limited primarily to the domain of extraversion, social competence, and interpersonal ease, and have only intermediate effects in the area of adjustment and social support. Finally, self-rated physical attractiveness was expected to have near zero effects on integrity and/or concern for others.

The CPI, a widely used and well-researched measure of personality (Anastasi, 1988), has 20 "folk concept" scales that measure a variety of personality traits. These "folk concept" scales are similar to the traits that an average person would use when describing himself or herself, or that independent observers might use when describing an average person. Factor analytic studies show the existence of five main factors that cut across the 20 "folk concept" scales. Gough (1987) has labeled these Extraversion, Control, Flexibility, Concensuality, and Femininity/Masculinity. The latest, 1987 version of the CPI also identifies three thematic vectors which underlie the inventory. Persons scoring high on v.1 are introverted, inwardly oriented, and reserved. Persons high on v.2 are conscientious, self-disciplined, and rule following. And persons scoring high on v.3 are reflective, capable, and optimistic concerning their present and future status. In general, self-rated physical attractiveness was expected to be highly related to the extraversion factor and v.1 of the CPI, and also to other traits assessed by the CPI, though to a much smaller extent.

With regard to shyness, previous research suggests a substantial correlation with it and self-rated physical attractiveness (in a negative direction), but a near zero correlation with shyness and ratings of physical attractiveness by independent observers (Cheek & Melchior, 1990; Garcia,

Stinson, Ickes, Bissonette, & Briggs, 1991; Jones, Briggs, & Smith, 1986). Because of the focus on self-rated physical attractiveness in this study, a significant negative relationship with shyness and physical attractiveness was expected. With regard to one's social life, as assessed by the Social Provisions Scale (SPS; Russell & Cutrona, 1984), we expected that those who viewed themselves as attractive would have a larger network of friends (particularly nonkin), more contact with each of those friends, and greater quantity, quality, and variety of social provisions being met with each friend.

Finally, we were interested in seeing if self-rated physically attractive people viewed themselves as less overweight (Rodin, 1984). Several studies have found that the perception of being overweight is related to having low levels of self-esteem and that this relationship may be stronger for females than for males. In general, we expected to replicate this result. That is, people who saw themselves as unattractive would similarly see themselves as being more overweight, and these effects would be more dramatic for women than men.

METHOD

Subjects and Procedures Subjects were undergraduate general psychology student class volunteers required to participate in 3 hours of psychology research as part of the class they were taking. This particular project took approximately 2 hours and it occurred outside of the normal classroom setting in a Psychology Laboratory. Students typically participated together in groups of 5 to 12.

College students (455: 311 males and 144 females[1]) rated their own physical attractiveness on a 1 to 10 scale, gave their height and weight, and completed the CPI (Gough, 1987). Students also indicated whether or not they saw themselves as being overweight on a 1 to 5 point scale with a "3" being normal or average in weight. In addition, the height and weight information they provided was, in turn, compared by the investigators with a "Metropolitan Life Insurance Chart" listing for medium builds, to determine whether or not they were over- or under-weight. To reduce the fatigue factor of taking too may tests in one setting, the two shyness measures (Social Avoidance and Distress: Watson & Friend, 1969; Social Reticence: Jones, 1987) were given to only 160 of the subjects. The Social Provisions Scale (Russell & Cutrona, 1984) and the Interpersonal Betrayal Scale (Jones, 1988) was given to 320. And the Student Adjustment to College Questionnaire (Baker & Siryk, 1984) was given to 225 of the 455 students.

Preliminary analysis of the physical attractiveness measure indicated the existence of a strong "self-serving" bias for the majority of students. On a 1 to 10 point rating scale, eighty-two percent of the 455 students rated themselves above 5, or the midpoint or average; 13% rated themselves right at the midpoint; and only 5% rated themselves below average.

Validity and Reliability of the Measures

California Psychological Inventory. The CPI was developed specifically for use with normal adult populations. It draws nearly half of its 462 items from the MMPI. Retest reliability scores (median of .70 for an interval of over a year) as well as internal consistency reliability coefficients (median alpha coefficient of .73) for the individual 20 "folk concept" scales compare favorably with those found with other personality inventories (Gough, 1987, p. 31).

The SRS and the SAD are both reliable measures of shyness (Jones, et al., 1986). The SRS has an alpha coefficient of .91 and a test-retest correlation of .87 over an eight week period. Its inter-item correlations average .36. The SAD has an alpha coefficient of .90 and a test-retest correlation of .68 over four weeks, and its inter-item correlations average .25.

The Social Provisions Scale, based on Robert Weiss's (1974) theory of social relationships, involves six social functions or provisions that could be obtained in relationships with others. Although all six might be needed for individuals to feel adequately supported and to avoid loneliness, different ones could be more crucial at different stages of one's life cycle. The six relational provisions are (a) attachment, a sense of emotional closeness and security, usually provided by a spouse or lover; (b) social integration, a sense of belonging to a group of people

who share common interests and recreational activities, usually obtained from friends; (c) reassurance of worth, an acknowledgment of one's competence and skill, usually obtained from coworkers; (d) reliable alliance, the assurance that one can count on others for assistance under any circumstance, often obtained from family members; (e) guidance, advice and information, usually obtained from teachers, mentors, or parent figures; and (f) opportunity for nurturance, a sense of responsibility for the well-being of another, often obtained from one's children. Internal consistency for the total score on the SPS is relatively high, ranging from .85 to .92 across a variety of populations (Russell & Cutrona, 1984). Alpha coefficients for the individual subscales range from .64 to .76, and factor analysis has confirmed a six-factor structure that corresponds to the six social provisions.

The Student Adaptation to College Questionnaire, developed by Baker and Siryk (1984) and published by Western Psychological Services (1989), was employed as a measure of adjustment to college and it contained 52 items. Students rated their estimated level of adjustment on a 9-point rating continuum. A higher score indicated better adjustment. The four subscales of the test included academic adjustment (18 items), social adjustment (14 items), personal-emotional adjustment (10) items, and Goal Commitment (8 items). The sum of the scores for all items yielded a measure of overall adjustment to college. Baker and Siryk (1984) reported internal consistency measures of reliability in the .90's for the full SACQ scale score, the .80's for the academic adjustment and social adjustment subscales, and the .70's for the personal-emotional subscale. Validity data reported by Baker and Siryk (1984) indicates significant relationships between the subscales and numerous relevant independent criteria: the personal-emotional subscale and being known to a psychological services center; the academic adjustment scale and freshman year grade point average and subsequent election to Phi Beta Kappa; and the social adjustment subscale and a campus activities checklist and decisions regarding applications for dormitory assistant positions.

The Interpersonal Betrayal Scale (Jones, 1988) is a 40 item scale consisting of three subscales, mole, terrorist, and spy and assesses the likelihood that an individual will betray friends and acquaintances. Not much is known yet about the validity and reliability of this particular scale.

RESULTS

Data were analyzed first using Pearson product moment correlations among self-rated attractiveness scores and on scores on the 20 CPI "folk" traits and three vectors, the SAD and SRS measures of shyness, the 24 SPS measures, estimates of being over-weight, the SACQ, and the IBS. Following this analysis, a series of multivariate and univariate analyses of variance were performed to see if reliable effects could be attributed to male/female differences.

Pearson's r correlation of Perceived Attractiveness with CPI, Shyness, Social Support, Weight Student Adjustment to College, and Betrayal. As can be seen in Table I, self-ratings of physical attractiveness correlated with 9 of the 20 CPI scales and with v.1 ($r = -.30$, $p < .001$) and v.2 ($r = .11$, $p < .05$) but not with v.3 ($r = -.05$). For shyness, one's self-rated physical attractiveness correlated significantly with both the SAD, $r = -.26$, $p < .001$, and the Social Reticence, $r = -.29$, $p < .05$) scales. With regard to social support only two dimensions out of a possible 24 were statistically significant. Those viewing themselves as physically attractive were more likely to have a boyfriend/girlfriend ($r = .25$, $p < .001$), and (related to this component of their social lives) they were more likely to maintain a higher mean total mean frequency of contact with nonkin people concerning their needs for attachment ($r = .19$, $p < .05$). One's weight as rated and/or perceived by themself on the 1 to 5 scale, was inversely ($r = -.12$, $p < .01$) and significantly correlated with self-rated attractiveness. The perception of one's weight also correlated positively with actual weight ($r = .26$, $p < .001$) and with weight as defined by the Metropolitan Life Insurance chart ($r = .37$, $p < .001$). Neither actual weight ($r = -.06$), nor one's weight relative to others, as determined from the Metropolitan Life Insurance chart ($r = -.01$), however, were correlated with self-ratings of attractiveness. With regard to adjustment to college, self-rated attractiveness was related to social adjustment ($r = .14$, $p < .05$), but not to academic adjustment,

personal adjustment, or goal commitment. Self-rated attractiveness was unrelated to the Interpersonal Betrayal Scale as a whole, and to each of its individual subscales.

TABLE I: PEARSON r CORRELATIONS WITH PERCEIVED ATTRACTIVENESS

Calif. Psych. Inv.	**Physical Attractiveness**
Dominance	.26***
Capacity for Status	.12**
Sociability	.28***
Social Presence	.18***
Self-Acceptance	.22***
Independence	.21***
Empathy	.10*
Responsibility	.00
Socialization	.04
Self-Control	-.12**
Good Impression	-.03
Well-being	.12**
Achievement via Conformity	.04
Tolerance	-.04
Achievement via Independence	-.03
Flexibility	-.09
Intellectual Efficiency	.01
Psychological Mindedness	.05
Communality	.08
Femininity	-.08
Vector 1 (Internality)	-.30***
Vector 2 (Norm-favoring)	.11*
Vector 3 (Self-realization)	-.05
Shyness	
Social Avoidance & Distress	-.26***
Social Reticence	-.29***
Social Provisions Scale	
Boyfriend/Girlfriend	.25**
Mean Freq. Contact with nonkin for attachment needs	.19*
Weight	
Actual Weight	-.06
Perceived Weight	-.12***
Metropolitan Chart Weight	-.01
Interpersonal Betrayal Scale	-.02
Mole	-.04
Terrorist	.01
Spy	-.00
Student Adjustment to College	.10
Academic Adjustment	.04
Social Adjustment	.14*
Personal Adjustment	.06
Goal Commitment	.08

*p< .05 **p < .01 ***p< .001

Self-rated Attractiveness x Male / Female differences on the CPI factors, vectors, and scales. To determine if any of the five CPI factors (Extraversion, Control, Flexibility, Concensuality, Femininity/Masculinity) were related to self-rated attractiveness ratings, and if they were differentially affected by male / female differences, a Perceived Attractiveness x Sex (Top 50%/

Bottom 50%[2] x Male/Female) multivariate analysis of variance was performed on each of the five CPI clusters. Results are summarized in Table II.

TABLE II. MULTIVARIATE AND UNIVARIATE MAIN EFFECTS FOR LOW VS. HIGH SELF-RATED PHYSICAL ATTRACTIVENESS X SEX GROUPS ON CPI FACTORS, VECTORS, AND SCALES[a]

	Physical Attractiveness Means				Sex Means			
	Low	High	F	p	Male	Female	F	p
Factor I (Extravers.)	-	-	3.6	.0009	-	-	1.0	.42
Dominance	51.8	54.0	15.6	.0001	51.8	54.0	4.2	.04
Capacity for status	49.0	50.0	2.7	.10	49.0	50.0	1.5	.22
Sociability	52.0	54.0	20.5	.0001	52.0	53.8	5.0	.03
Social presence	51.1	53.0	8.5	.0001	51.1	52.5	1.6	.21
Self-acceptance	52.7	54.9	10.8	.001	52.7	54.9	5.1	.03
Independence	49.8	51.0	10.2	.002	50.0	51.0	2.4	.12
Empathy	50.6	51.4.4	.3	.62	50.6	51.4	.6	.43
Factor II (Control)	-	-	2.6	.01	-	-	.4	.89
Responsibility	47.7	47.9	.3	.58	48.0	48.0	.7	.41
Socialization	48.9	49.5	.3	.59	49.3	49.2	.0	.94
Self-control	44.9	45.4	.1	.22	44.5	44.7	.1	.81
Good impression	45.1	45.3	.0	.92	45.1	45.6	.7	.42
Well-being	45.5	48.0	6.4	.01	47.0	47.4	.2	.70
Tolerance	49.6	48.7	.1	.81	48.8	49.5	.0	.86
Achievement by con	49.3	50.1	1.5	.22	49.9	49.7	.1	.74
Factor III (Flexibility)	-	-	.8	.53	-	-	2.1	.06
Tolerance	49.6	48.7	.1	.81	48.8	49.5	.0	.86
Achievement by ind	51.2	51.0	.1	.77	51.3	50.4	2.4	.13
Flexibility	50.9	48.8	2.2	.14	49.8	49.1	1.3	.26
Intellectual effic.	47.3	47.4	.1	.73	47.8	46.4	4.0	.05
Psychol. mindedn.	49.7	50.4	.5	.46	50.2	50.1	.0	.96
Factor IV (Consensual)	-	-	1.9	.12	-	-	.9	.45
Communality	52.3	53.3	1.5	.23	52.7	53.6	1.9	.17
Responsibility	47.7	47.9	.3	.59	48.0	47.5	.7	.41
Socialization	49.0	49.5	.3	.59	49.3	49.2	.0	.94
Well-being	45.5	48.0	6.4	.01	47.0	47.4	.2	.70
Factor V (F / M)	46.2	45.9	.0	.91	46.1	45.6	.7	.41
Vectors	-	-	5.1	.002	-	-	.9	.47
v.1 (Introverted)	16.9	14.6	10.3	.001	13.5	18.2	.4	.52
v.2 (Rule-follow.)	21.2	22.5	5.5	.02	22.6	21.2	1.9	.17
v.3 (Self-realiz.)	34.0	33.2	.3	.61	35.7	30.8	.3	.61

A strong significant multivariate main effect for self-rated attractiveness ($p < .0009$) was found for Cluster I (extraversion) and a moderately strong multivariate main effect ($p < .01$) was found for Cluster II (control), but a significant main effect for self-rated attractiveness was not found in

a Multivariate effects are underlined and univariate effects are not.

Cluster III (flexibility), Cluster IV (consensuality), or Cluster V (femininity). Sex and the interaction effect of self-rated attractiveness with sex were not significant at the multivariate level.

A strong significant, univariate main effect for self-rated physical attractiveness was found on five of seven scales (dominance, sociability, social presence, self-acceptance, and independence) in Cluster I (extraversion). With Cluster II, out of seven scales, only Well-being ($p < .01$) was statistically significant. Self-rated physical attractiveness had no significant effect on any of the remaining 14 scales. Furthermore, among individual univariate analyses, no significant interactions with sex were found on any of the 20 scales, and male/female differences were found on only four scales. The females were significantly higher than males on dominance, sociability, independence, and intellectual efficiency. Overall, these results strongly suggest that the effect of one's self-rated attractiveness was primarily limited to the area of extraversion and/or social competence.

A multivariate analysis of the Vectors associated with the CPI indicated a strong multivariate main effect for self-rated attractiveness ($p < .002$), but no significant effects for sex or for the interaction of sex with self-rated attractiveness. For the univariate analyses, significant main effects for sex or interactions with sex were not found. A strong univariate main effect ($p < .001$) for self-rated attractiveness was found with v.1 (introversion), and a weaker one ($p < .02$) was found with v.2 (openness to rules or norms), but no significant effect was found with v.3 (the vector assessing self-realization). Again, this suggests that the effect of one's perceived physical attractiveness was primarily limited to the area of extraversion and/or social competence.

Self-rated Attractiveness x Male/Female differences and Shyness.

A series of univariate analyses of variance (Top 50% / Bottom 50% x Male / Female) were also conducted on the shyness measures. Subjects scoring high on the 1 to 10 scale measure of attractiveness reported less shyness on the Social Reticence Scale than did low scoring subjects ($F = 7.16$, $p < .008$, high $M = 46.0$, low $M = 52.3$) and on the SAD scale ($F = 7.46$, $p < .007$; high $M = 6.1$, low $M = 9.6$). Neither male/female differences, however, nor the interaction of sex with attractiveness were significant for either Social Reticence or the SAD scales. These results also strongly suggested a link between one's self-rated attractiveness and extraversion, social competence, and interpersonal ease.

Self-rated Attractiveness x Male/Female differences in Social Support.

On the Social Provisions Scale, only two significant main effects were found for physical attractiveness. Self-rated highly attractive people are more likely than low ($F = 3.96$, $p < .05$, high $M = .5$, low $M = .3$) to have a friend of the opposite sex (boyfriend/ girlfriend), and (related to this) they were more likely to maintain a higher total mean frequency of contact with nonkin people concerning attachment needs ($F = 4.09$, $p < .05$, high $M = 4.6$, low $M = 3.9$).

Numerous main effects for sex were found in the SPS results (See Table III). While females did not differ from males in total network size or total mean frequency of contact, they did differ from males in the types of provisions received -- both in number and in frequency. Nurturance was received from a larger number of kin people by females than by males, and females also had a greater frequency of contact with each kin person for purposes of social integration, guidance, reassurance of worth, and a reliable alliance. In addition, significant interactions were found (See Table IV) between self-rated attractiveness and sex on the SPS for total kin nurturance ($F = 3.97$, $p < .05$), and for total attachment needs met by nonkin ($F = 5.67$, $p < .02$). With regard to nurturance, for males, self-rated attractiveness was unrelated (high $M = 1.8$, low $M = 1.7$) to the total number of kin providing it. For females, however, this was not the case. Females viewing themselves as attractive had significantly fewer kin providing nurturance than females who saw themselves as unattractive (high $M = 2.0$, low $M = 3.2$) and suggests that unattractive females relied more on kin for nurturance than attractive females. With regard to attachment provisions by nonkin, for males, there was no statistically significant difference between those seeing themselves as attractive or unattractive (high $M = 1.4$, low $M = 1.9$), but for females there was. Females who saw themselves as more attractive had significantly more nonkin people ($p < .05$) who satisfied attachment needs than did females who saw themselves as unattractive (high $M = 1.8$, low $M = .9$). These results indicated that females with high self-rated attractiveness scores had fewer nurturance needs met by kin, but more of their attachment needs met by nonkin than females with

low self-rated attractiveness scores. Overall, self-rated attractiveness was of importance to a female and relatively unimportant to a male with regard to these two social provisions.

TABLE III. MAIN EFFECTS ON THE SPS FOR SEX

	SPS Means Male	Female	F	p
Number Provisions by Kin				
Nurturance	1.8	2.5	5.45	.02
Frequency Provisions by Kin				
Social integration	3.0	3.9	4.24	.01
Guidance	4.0	5.0	8.76	.003
Reassurance of worth	3.7	4.8	7.50	.007
Reliable Alliance	3.6	4.7	7.12	.009

TABLE IV. SIGNIFICANT INTERACTION EFFECTS OF PERCEIVED ATTRACTION X SEX ON THE SPS

	SPS Means Male	Female	F	p
Number				
Total Kin Providing Nurturance				
Low Attractive	1.7	3.2	3.97	.05
High Attractive	1.8	2.0		
Total Nonkin Providing Attachment				
Low Attractive	1.9	.9	5.67	.02
High Attractive	1.4	1.8		

Self-rated Attractiveness x Male/Female differences and Weight

With regard to actual weight, males (M = 167.4) in the sample, not surprisingly, weighed significantly more, $F(1, 447) = 144.94$, $p < .001$, than females (M = 132.8). In addition, a significant Attractiveness x Sex interaction, $F(1,447) = 5.01$, $p < .03$, indicated that males and females differed with regard to the relationship between actual weight and their self-rated attractiveness. Among males, self-rated attractiveness was unrelated to one's real weight (high M

= 167.1, low M = 167.2). Among females, on the other hand, those giving themselves higher self-ratings for physical attractiveness, weighed significantly less (high M = 128.5, low M = 140.3).

With regard to a perception of being overweight, females (M = 3.7) scored significantly higher, F(1,447) = 5.83, p < .02, than males (M = 3.5). A significant self-rated physical attractiveness x sex interaction, F(1,447) = 4.08, p < .04, moreover, indicated that males and females differed with regard to the perception of being overweight and self-ratings of physical attractiveness. Among males, the perception of being overweight was unrelated to one's self-rated physical attractiveness (high M = 3.5, low M = 3.5), but among females it was. Females rating themselves as low in attractiveness, saw themselves as significantly more overweight (high M = 3.5, low M = 4.1) on a 1 to 5 scale (with 3 being normal weight).

By comparing the height/weight figures provided by each subject with the Metropolitan Life Insurance chart, it was also possible to determine if subjects actually were overweight. Overall, the results indicated males (M = 3.1) were relatively more overweight, F(1,447) = 3.86, p < .05, than females (M = 2.6). Again the self-rated attractiveness x sex interaction was also significant, F(1,447) = 3.86, p < .05. A simple effects analysis of this interaction indicated that while self-rated attractiveness was unrelated to weight among males (high M = 3.2, low M = 3.1), among females, self-rated physical attractiveness was significantly (p < .05) and negatively related to being over-weight. In other words, those females who saw themselves as more attractive, were significantly thinner (high M = 2.5, low M = 2.9). In fact, those females who saw themselves as unattractive and overweight were only slightly below (M = 2.9) normal weight with regard to the Metropolitan chart, while those who saw themselves as most attractive were significantly (M = 2.5) below normal weight -- at least as determined by the chart.

Perceived Attractiveness x Male/Female differences for IBS and Student Adjustment to College

For the Interpersonal Betrayal Scale (IBS), neither the main effects of physical attractiveness, F(1,316) =1.46, p < .22, Sex, F(1,316) = 1.77, p < .18, nor their interaction, F(1,316) = .13, p < .71, were significant. These results are consistent with the meta analysis of Eagly et al., (1991) where physical attractiveness, as rated by independent observers, had near zero effects on integrity and concern for others.

For the Student Adjustment to College Questionnaire, neither the main effects of physical attractiveness, F(1,222) =1.29, p < .26, Sex, F(1,222) = .60, p < .44, nor their interaction, F(1,222) = .13, p < .71, were significant. Further, on each of the subscales (Academic Adjustment, Social Adjustment, Personal Adjustment , and Goal Commitment), neither main effects nor their interactions were significant. These results suggested that self-rated physical attractiveness had little bearing on a student's adjustment to college.

DISCUSSION

In some instances, for both males and females, self-rated physical attractiveness significantly affected personality and interpersonal relationships. These instances included (a) all seven folk scales (dominance, capacity for status, sociability, social presence, self-acceptance, independence, and empathy) on Cluster I (extraversion) of the CPI; (b) two of the three vectors on the CPI: v.1 (intraversion) and v.2 (openness to norms); (c) shyness; and (d) having a boyfriend or a girlfriend.

In other instances self-rated physical attractiveness affected females, but not males (i.e., a significant Attractiveness x Sex interaction occurred). These instances included (a) social provisions in the areas of nurturance and attachment, and (b) both perceived and actual weight. In the area of Social Provisions, self-rated unattractive females received greater nurturance from kin and had fewer attachment needs met from nonkin than did attractive females. For males, self-rated attractiveness had little impact on either nurturance or attachment. With regard to weight, the thinner females were, the higher they rated themselves on the self-rated attractiveness scale. Although the males in this sample were more likely to actually be overweight, the females in this sample were more likely to perceive that they were overweight. For males, self-rated physical

attractiveness was unrelated to weight. In fact, the evidence indicated that those females who considered themselves to be the most attractivewere significantly below normal weight.

In other instances, only sex differences differences were found, and these differences were unrelated to self-rated physical attractiveness. For example, males were generally taller and they weighed more; and females relied on kin more for the social provisions of social integration, guidance, nurturance, reassurance of worth, and for having a reliable alliance than males.

Finally, there were instances in which neither self-rated physical attractiveness nor being a male or female made a difference. These included (a) several of the CPI "folk" scales & v.3 (personal integration); (b) several of the dimensions assessed by the Social Provisions Scale; (c) one's adjustment to college as measured by the Student Adjustment to College Questionnaire; and (d) one's propensity toward betrayal as measured by the Interpersonal Betrayal Scale.

Overall, self-ratings of physical attractiveness chiefly affected the domain of extraversion, perceived social competence, and interpersonal ease, but not integrity, self-realization, adjustment, sensitivity to others, or concern for others. In general, it would seem that a positive, self-serving bias, as it pertains to self-rated physical attractiveness, does serve the role of an adaptive illusion, but its domain of beneffectance is largely circumscribed to the areas of extraversion, perceived social competence, and interpersonal ease. Other than having an opposite sex friend (i.e., a boy or girl friend), this beneffectance did not extend into personal relationships (either in terms of quantity or quality), nor to one's adjustment to college, levels of personal integration, integrity, nor to other domains. Thus, while the effect of self-rated attractiveness may be fairly potent as it relates to the area of perceived social competence, it does not have much of an effect in other areas.

FOOTNOTES

[1] The male/female ratio of 3:1 closely mirrors that of the student body population where the study took place.

[2] Previous studies are mixed in whether they compare only those subjects who score extremely high or low (e.g., top vs. bottom 25%), or whether they compare all subjects. The advantage of selecting participants with extreme scores is that it increases the likelihood of uncovering a relationship. However, this increase in power is achieved by artificially inflating the magnitude of a relationship. Because an analysis of only the extremes would not provide an accurate estimate of the size of the effects being studied, we elected to present the data including all subjects.

REFERENCES

Adams, G. R. (1977). Physical attractiveness research: Toward a developmental social psychology of beauty. Human Development, 20, 217-239.

Adams, G. R. (1982). Physical attractiveness. In A. G. Miller (Ed.), In the eye of the beholder: Contemporary issues in stereotyping (pp. 253-304). New York: Praeger.

Alley, T. R., & Hildebrandt, K. A. (1988). Determinants and consequences of facial aesthetics. In T. R. Alley (Ed.), Social and applied aspects of perceiving faces (pp.110-140). Hillsdale, NJ: Erlbaum.

Anastasi, A. (1988). Psychological Testing. New York: MacMillan.

Baker, R. W., & Siryk, B. (1984). Measuring adjustment to college. Journal of Counseling Psychology, 31, 179-189.

Balban M. (1981). Accuracy in self-evaluation of physical attractiveness as a function of self-esteem and defensiveness. Dissertation Abstracts International, 42, 3488-B, 1982.

Bassili, J. N. (1981). The attractiveness stereotype: Goodness or glamour? Basic and Applied Social Psychology, 2, 123-133.

Berscheid, E. (1981). A review of the psychological effects of physical attractiveness. In G. W. Lucker, K. A. Ribbens, & J. A. McNamara (Eds.), Psychological aspects of facial form (pp. 1-23). Ann Arbor, MI: Center for Human Growth.

Berscheid, E., & Walster, E. (1974). Physical attractiveness. In L. Berkowitz (Ed.) Advances in experimental social psychology, 7. New York: Academic Press.

Berscheid, E., & Walster, E. (1978). Interpersonal attraction (2nd ed.). Reading, Mass.: Addison-Wesley.
Cheek, J. M., & Melchior, L. A. (1990). Shyness, self-esteem, an self-consciousness. In H. Leitenberg (Ed.), Handbook of social and evaluative anxiety (pp. 47-82). New York: Plenum Press.
Dion, K. K. (1981). Physical attractiveness, sex roles, and heterosexual attraction. In M. Cook (Ed.), The bases of human sexual attraction (pp. 3-22). London: Academic Press.
Dion, K. K., Berscheid, E., & Walster, E. (1972). What is beautiful is good. Journal of Personality and Social Psychology, 24, 285-290.
Downs, A. C., & Wright, A. D. (1982). Differential conceptions of attractiveness: Subjective and objective ratings. Psychological Reports, 50, 282.
Eagly, A. H., Ashmore, R. D., Makhijani, M. G., & Longo, L. C. (1991). What is beautiful is good...: A meta-analytic review of research on the physical attractiveness stereotype. Psychological Bulletin, 110, 109-128.
Garcia, S., Stinson, L., Ickes, W., Bissonnette, V., Briggs, S. R. (1991). Shyness and physical attractiveness in mixed-sex dyads. Journal of Personality and Social Psychology, 61, 35-49.
Gough, H. G. (1987) California Psychological Inventory. Palo Alto: Consulting Psychologists Press.
Gurman, E. & Balban, M. (1990). Self-evaluation of physical attractiveness as a function of self-esteem and defensiveness. Journal of Social Behavior and Personality, 5, 575-580.
Hatfield, E., & Sprecher, S. (1986). Mirror, mirror: The importance of looks in everyday life. Albany: State University of New York Press.
Jones, W. H. (1987) Social Reticence Scale (SRS): A measure of shyness. Palo Alto: Consulting Psychologists Press.
Jones, W. H. (1988). Psychological and interpersonal issues in betrayal and treachery. International Conference on Personal Relationships, Vancouver, B. C. Canada.
Jones, W. H., Briggs, S. R., & Smith, T. G. (1986). Shyness: Conceptualization and measurement. Journal of Personality and Social Psychology, 51, 626-639.
Montgomery, R. L., Haemmerlie, F. M., & Edwards, M. (1991). Social, personal, and interpersonal deficits in socially anxious people. Journal of Social Behavior and Personality, 6, 859-872.
Patzer, G. L. (1985). The physical attractiveness phenomenon. New York: Plenum Press.
Rodin, J. (1984). Fear of fatness: A risk factor model of Bulemia. Invited speaker. American Psychological Association meeting, Toronto, Canada.
Russell, D., & Cutrona, C. E. (1984, August). The provisions of social relationships and adaptation to stress. Paper presented at the American Psychological Association convention, Toronto, Ontario, Canada.
Stroebe, W., Insko, C. A., Thompson, V. D., & Layton B. D. (1971). Effects of physical attractiveness, attitude similarity, and sex on various aspects of interpersonal attraction. Journal of Personality and Social Psychology, 19, 79-91.
Watson, D., & Friend, R. (1969). Measurement of social-evaluative anxiety. Journal of Consulting and Clinical Psychology, 33, 448-457.
Weiss, R. (1974). The provisions of social relationships. In Z. Rubin (Ed.), Doing unto others (pp. 17-26). Englewood Cliff, NJ: Prentice Hall.

MEMBER STIFFNESS AND CONTACT PRESSURE DISTRIBUTION OF BOLTED JOINTS

Matthew L. McKay
Department of Mechanical Engineering
University of Missouri-Rolla

ABSTRACT

Member stiffness and the stress distributions in the bolts and members of bolted joints have been calculated for various bolt sizes, as well as thicknesses and materials of the members. The finite element method has been used to calculate the displacements and the stress distributions in the components of the bolted joint. Using axisymmetric elements, the bolted joint could be analyzed as a two dimensional problem. Member stiffness ratios were calculated from the finite element results and compared with those calculated by an existing commonly used theory. The values were comparable for conditions where the theory could be applied. In addition, by developing a new yet similar theory which takes into account the bolt clearances, even better results could be achieved. Formulas and dimensionless curves which can be used to estimate the member stiffness ratios for several kinds of bolted joints are presented.

INTRODUCTION

The bolted joint is a type of mechanical connection which is used commonly for the construction of many types of structures. In fact, bolted joints are important in most of the mechanical devices and machines used in modern society. When a bolt is used to connect two members as in Figure 1, the bolt is normally preloaded with an initial tensile load. The purpose of the preload is to place the bolted member components in compression for better resistance to either static or cyclic external loads and to create force between the parts or members so that the shear loads can be resisted by friction forces. Variations in the magnitude of the tensile preload on a bolted joint can produce dramatic differences in the cyclic life of the connection. Accurate predictions of member stiffnesses are essential for determining proper preloads.

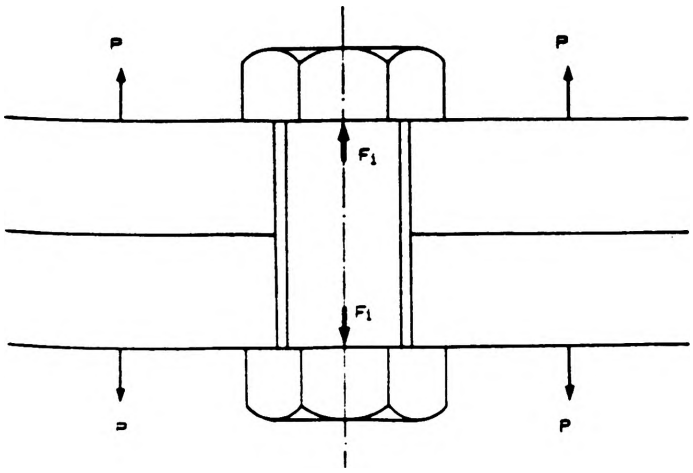

Figure 1. A Bolted Joint

When the external load P is applied to a bolted joint under initial preload F_i, the resultant force in the bolt, F_b, is

$$F_b = \frac{k_b P}{k_b + k_m} + F_i \qquad (1)$$

and that of the connected members, F_m, is

$$F_m = \frac{k_m P}{k_b + k_m} - F_i \qquad (2)$$

where k_b is the stiffness of the bolt and k_m is the stiffness of the members. Thus, the stiffnesses of the bolt and members are needed for the calculation of the resultant force in the bolt and the members of the joint when an external load is applied to the members. The stiffness of the bolt is determined from the ratio of the force applied on the bolt to the deflection of the bolt produced by the force, i.e.

$$k_b = \frac{F_b}{\delta_b} = \frac{AE}{L} \qquad (3)$$

where F_b is the applied force, δ_b is the deflection, E is the modulus of elasticity, L is the length of the bolt, and A is the cross sectional area based on the nominal diameter.

However, the determination of the stiffness of the members presents more difficulties, and past analytical and experimental attempts to calculate it have been only partially successful and widely varying. Better understanding of the forces, stresses, and deformations of bolted joints is necessary if member stiffnesses are to be accurately calculated.

Several authors have suggested both theoretical and experimental methods to determine member stiffnesses and pressure distribution between the members of bolted joints. Early work, however, centered on single plate pressure distributions [1 - 5]. Gould and Mikic [6] and also Tang and Deng [7] have used finite element analysis (FEA) to find the pressure distribution between the members. However, in these studies, the bolts were not modeled. Osman et al. discussed a design method for calculating an optimal bolt diameter and suggested that a hollow cylinder with outside diameter 1.5 times the bolt diameter be used for determining the area under compression and thus the member stiffness [8]. Edwards and McKee cite the Association of German Engineers' suggestion to determine the member stiffness using an equivalent cylindrical area dependent on the size of the joint [9]. Ito et al. [10], using ultrasonic techniques, suggested the use of Rotscher's pressure cone method [11] for stiffness calculation with variable cone angles typically larger than those so far theoretically calculated by other authors. Shigley and Mitchell [12] and Shigley and Mischke [13] have proposed a simpler method, described in the next section, by using a standard cone angle of 30° to 45°. Little [14] and Osgood [15] indicate that more conservative results will be realized with the use of the smaller 30° angle which will generally preclude overestimation of the clamping stiffness and, as seen in (1), will also prevent overestimation of the allowable force taken by the bolt. However, many times this approach will not give an accurate representation of the member stiffness in the joint.

Grosse and Mitchell [16] give a general discussion of nonlinearities in bolted joints due to the application of external loads as well as bolt thread and interfacial friction. Detailed consideration of these effects will require further research.

The object of the current research is to:

(1) provide rules for the calculation of the member stiffnesses of a class of bolted joints with multiple connected layers of different materials,

(2) further clarify the influence of member thicknesses, material properties of the members, and the diameter of the bolt on the contact pressure distribution of various bolted joints that fall within the class of joints considered,

(3) and to develop a better understanding of the effects that the bolt clearance has on member stiffness calculations.

Basic Theory

When circular plates of the same thickness are connected to each other by a bolt, the plates are subjected to a compressive force, F_m. Figure 2 shows the upper plate in compression.

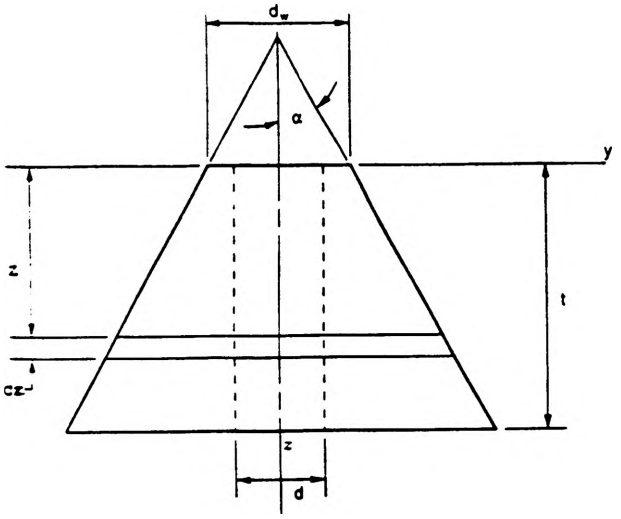

Figure 2. Pressure Distribution Confined to Frustum of Hollow Cone

The deflection of an element of the cone of thickness dz due to the compressive force is given by

$$d\delta_m = \frac{F_m dz}{EA} \qquad (4)$$

The area of the element can be expressed as

$$A = \pi(r_o^2 - r_i^2)$$

By substituting the appropriate data from the figure and expanding, this can equally be expressed as

$$A = \pi\left[\left(z\tan\alpha + \frac{d_w+d}{2}\right)\left(z\tan\alpha + \frac{d_w-d}{2}\right)\right] \qquad (5)$$

Substituting (5) into (4) and integrating from 0 to t results in an expression for the deflection as

$$\delta_m = \frac{F_m}{\pi E d \tan\alpha} \ln\left[\frac{(2t\tan\alpha + d_w-d)(d_w+d)}{(2t\tan\alpha + d_w+d)(d_w-d)}\right] \qquad (6)$$

Thus, the stiffness of a single frustum is

$$k_m = \frac{F_m}{\delta_m} = \frac{\pi E d \tan\alpha}{\ln\left[\frac{(2t\tan\alpha + d_w-d)(d_w+d)}{(2t\tan\alpha + d_w-d)(d_w+d)}\right]} \qquad (7)$$

Model

Figure 3 shows the finite element model of the bolted joint. Assuming only one bolt we can treat the problem as one having axial symmetry. Then because of axial symmetry, only

half of the bolt joint need be modeled. It has been assumed that the bolt has been cut at the parting line and the distributed load, q, which represents the preload, F_i, in the bolt, has been applied at the cut surfaces as shown in Figure 3(a). The existence of average clearance between the bolt and the hole of the members as recommended in the Machinery's Handbook [17] has been used to avoid interference between the bolt and the members due to radial deformation. Axisymmetric, quadratic, quadrilateral elements have been used as the type of element for the finite element analysis. The centroidal axis of the elements is the z-axis.

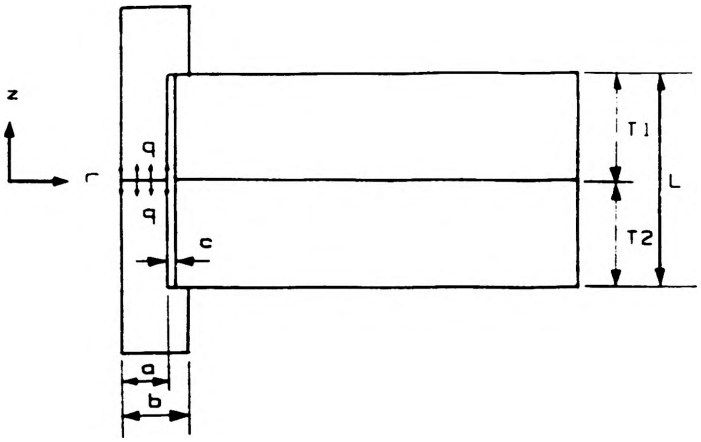

(a) Basic Model

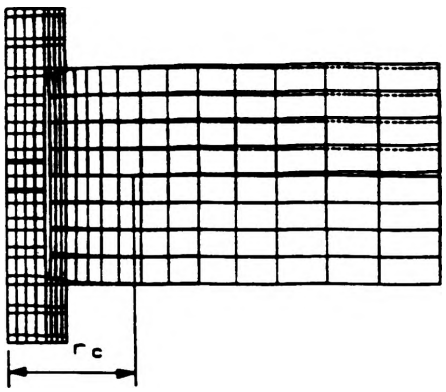

(b) Separation of the Members

Figure 3. Finite Element Model

When a preload has been applied to a bolt the members are in contact for a certain region radially near the connected part of the bolt and the members. However, for the region somewhat distant from the connected part, there occurs a separation between the two members. Figure 3(b) shows the members in contact for the distance r_c and separated beyond that distance after deformation. Further study of the generated FEA stress results could show where this separation occurs. This topic is not addressed in this paper.

Displacements and stresses in the axial z direction were used for the calculation of member stiffness. There were a number of nodal points along the contacting portion of the bolt and members. The average displacement of those nodal points in the z direction was used to calculate the stiffness of the members by dividing the member force (preload) by the average displacement. The member force, F_m, equals the preload, F_i, when there is no externally applied load, P, on the joint (see (2)). The contact pressure distribution is the stress distribution in the z direction at the nodal points in the contacting region of the two members. As noted above, the stresses are compressive in the contacting portion.

Five sizes of metric hex head bolts were modeled as fasteners for the bolted joints of this study: M8, M12, M16, M20, and M24. A medium fit was used as the clearance hole diameter corresponding to each bolt. The clearance between the bolt and the hole was 1 mm except for the case of the M8 bolt where 0.5 mm was specified.

The thicknesses of the upper members were 12, 16, and 20 mm respectively, and the thickness of the lower member was fixed at 20 mm for most of the work. In order to study the more general case, various combinations of the thicknesses of the members were investigated for M16 bolts. In these cases, the ratios of the member thicknesses were 0.6, 0.8, and 1.0, although the actual thicknesses were different for each case.

Steel, Aluminum, and Cast Iron were used as the materials of the connected members.

The combination of the materials were: (i) Aluminum/Steel, (ii) Steel/Steel, (iii) Cast Iron/Steel, (iv) Aluminum/Aluminum, and (v) Cast Iron/Cast Iron.

DISCUSSION OF RESULTS

A large number of models were analyzed by finite element methods to find the displacements in the z direction for the contact areas of the members and the stress distribution in bolt and members. An average of the member displacements δ_m under the head of the bolt was used to calculate the member stiffness k_m, i.e.

$$k_m = \frac{F_m}{\delta_m} \tag{8}$$

where $F_m = F_i$ is the initial force applied to the cross-section of the bolt. The member stiffnesses of various models under the initial force of $F_i = 1000$ N are shown in Table I.

TABLE I. MEMBER STIFFNESS OF BOLTED JOINTS

Bolt Diameter (mm)	Thickness Ratio of Members	Member Stiffness (MN/mm) for Al/St	St/St	Ci/St	Al/Al	Ci/Ci
8	12/20	1.387	2.511	1.790	0.910	1.352
	16/20	1.340	2.490	1.754	0.902	1.340
	20/20	1.306	2.458	1.719	0.890	1.321
12	12/20	1.868	3.418	2.440	1.217	1.809
	16/20	1.809	3.337	2.348	1.200	1.788
	20/20	1.736	3.300	2.288	1.180	1.756
16	12/20	2.832	5.103	3.640	1.818	2.701
	16/20	2.658	4.904	3.472	1.775	2.638
	20/20	2.537	4.772	3.342	1.717	2.573
20	12/20	4.013	6.940	5.112	2.546	3.766
	16/20	3.690	6.743	4.805	2.452	3.642
	20/20	3.471	6.519	4.566	2.366	3.514
24	12/20	5.464	9.346	6.940	3.435	5.089
	16/20	4.933	8.937	6.402	3.268	4.845
	20/20	4.577	8.562	6.013	3.124	4.636

* Al: Aluminum, St: Steel, Ci: Cast Iron

Comparison of the stiffness ratios calculated by FEA to the basic theory results mentioned earlier as Rotscher's pressure cone method is shown in Figure 4 as a function of the ratio of total member thickness L to the bolt diameter as

$$K = \frac{k_m}{Ed} \tag{9}$$

where E is the modulus of the material and d is the nominal diameter of the bolt. (The 45° cone

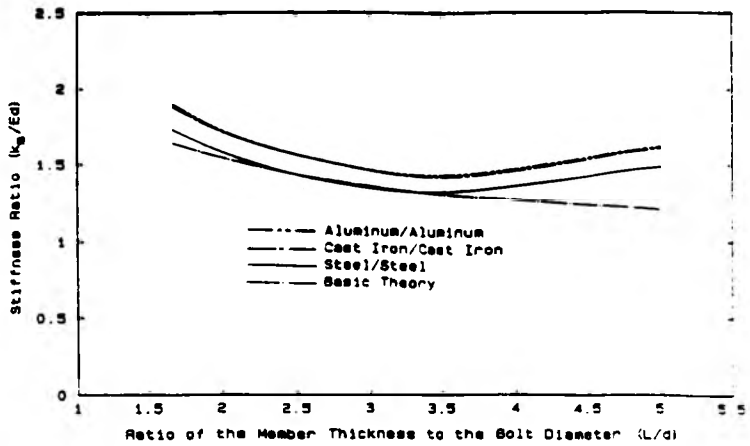

Figure 4. Comparison of Member Stiffness Ratio (Basic Theory vs. FEA)

angle was applied.) If the materials of the two members are different, the stiffness ratio in (9) cannot be calculated because the modulus of the material is different for each member of the bolted joint. Therefore, only the stiffness ratios for the cases of the same material members are given in Figure 4. Table II has been included below to compare the member stiffnesses of joints, composed of different materials, with the basic theory.

TABLE II. COMPARISON OF BASIC THEORY AND FEA MEMBER STIFFNESSES

Bolt Diameter (mm)	Thickness Ratio of Members	Member Stiffness (MN/mm) for Al/St			Ci/St		
		Basic* Theory	FEA	Relative Error	Basic* Theory	FEA	Relative Error
8	12/20	1.085	1.387	(21.8)	1.434	1.790	(19.9)
	16/20	1.031	1.340	(23.1)	1.370	1.754	(21.9)
12	12/20	1.826	1.868	(2.2)	2.404	2.440	(1.5)
	16/20	1.708	1.809	(5.6)	2.266	2.348	(3.5)
16	12/20	2.692	2.832	(4.9)	3.536	3.640	(2.9)
	16/20	2.488	2.658	(6.4)	3.298	3.472	(5.0)
20	12/20	3.682	4.013	(8.1)	4.824	5.112	(5.6)
	16/20	3.369	3.690	(8.7)	4.463	4.805	(7.1)
24	12/20	4.793	5.464	(12.3)	6.269	6.940	(9.7)
	16/20	4.351	4.933	(11.8)	5.758	6.402	(10.1)

* The Basic Theory was applied using a 45° cone angle.

The differences between the stiffness ratios calculated by the finite element analysis and the basic theory are relatively small for the M12 through M24 bolts. Especially for the Steel/Steel model, the stiffness ratio was found to be almost the same as the values from the basic theory. However, for the model with the M8 bolt, large differences were found indicating that the influence of the clearance between the bolt and the hole on the results is quite significant. The greater deviations are a direct result of using the different clearance.

The basic theory assumes that d_w of equations (5), (6) and (7) is equal to 1.5 times the bolt diameter, d. Thus, by introducing the use of the hole diameter with the stated clearances

rather than the bolt diameter of the classical model, significant deviations between the two sets of basic theory results are achieved.

As discussed earlier, the current trend in applying the basic theory is to use a cone angle of 30° to estimate the member stiffness. If the current method is to be applied, however, it was shown above that indeed the 45° angle better represents the pressure distribution. Moreover, if the theory is adapted to handle the clearances, the angle increases even more. By using a linear regression technique, it was found that an angle of closer to 51° better fits the pressure distribution for the bolt sizes, plate thicknesses, and materials used in this study. The benefits in applying the new theory are two-fold. The actual pressure distribution can be more realistically determined when the material in the clearance zone is not considered in the calculations, and, the data fits tighter across a broader range of bolt sizes. For example, when the clearances are neglected, linear fitting indicates that the optimum angle for calculation of Steel/Steel member stiffness ranges from 45° to 47° for the M12 through M24 bolts. However, by not neglecting the clearances this range is reduced by a factor of two. These results are highlighted in Table III and were similar for the other material cases.

TABLE III. COMPARISON OF BASIC THEORY RESULTS TO FEA RESULTS WITH AND WITHOUT CONSIDERING BOLT CLEARANCES (Steel/Steel)

Bolt Diameter (mm)	Clearance (mm)	Cone Angle	
		Classical	Clearance
12	1.0	45°	50°
16	1.0	45°	49°
20	1.0	46°	49°
24	1.0	47°	50°

Figures 5 and 6 on the following page show the stiffness ratios of the members as a function of the thickness ratios, and represent the Steel and Cast Iron cases, respectively. For each case, the thickness of the lower member was fixed at 20 mm and the thicknesses of the upper member varied from 12 to 20 mm. Typically, the stiffness ratio decreases almost linearly as thickness ratio increases. The stiffness ratios in the models with the larger bolt sizes are generally larger than the stiffness ratios with smaller bolt sizes. However, for the case with the M8 bolt, this rule cannot be applied because the clearance is different from the other cases as mentioned previously. Similar results were also obtained for Aluminum.

Formulas which can be used to predict the stiffness ratios of the members for various thicknesses and member materials have been developed from these results. Since the changes of the stiffness ratios are almost linear, functions of second order are sufficient to represent the values. The values of the coefficients in the form of

$$K = ax^2 + bx + c \qquad (10)$$

where x is the thickness of the upper material divided by the thickness of the lower material (20 mm), are summarized in Table IV on the following page.

For more general application, some additional models with the M8 bolt and steel members were investigated, i.e., the upper members with thicknesses of 6, 8, and 10 mm were

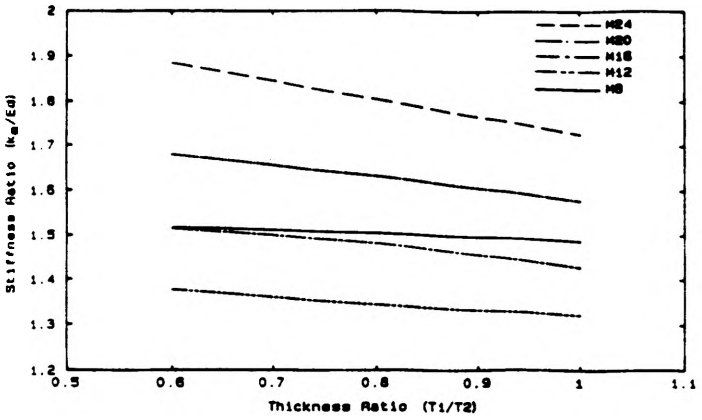

Figure 5. Member Stiffness Ratio vs. Thickness Ratio (Steel)

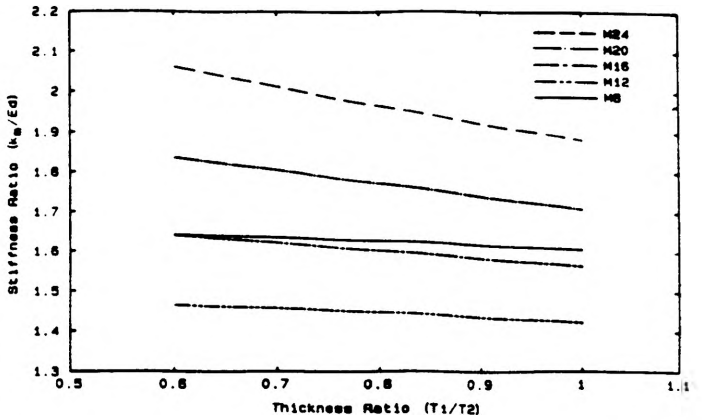

Figure 6. Member Stiffness Ratio vs. Thickness Ratio (Cast Iron)

TABLE IV. COEFFICIENTS OF THE FORMULA* TO CALCULATE THE MEMBER STIFFNESS RATIOS

Bolt Size	Member** Material	a	b	c
M8	Steel	-7.538E-2	4.060E-2	1.521E+0
	Cast Iron	-8.708E-2	4.683E-2	1.645E+0
	Aluminum	-1.000E-1	6.558E-2	1.656E+0
M12	Steel	1.120E-1	-3.170E-1	1.527E+0
	Cast Iron	-1.113E-2	7.253E-2	1.462E+0
	Aluminum	-2.500E-2	-6.937E-2	1.529E+0
M16	Steel	-2.750E-1	2.210E-1	1.482E+0
	Cast Iron	-1.198E-2	-1.730E-1	1.748E+0
	Aluminum	-1.750E-1	4.967E-2	1.689E+0
M20	Steel	-7.537E-2	-1.340E-1	1.786E+0
	Cast Iron	2.540E-2	-3.610E-1	2.042E+0
	Aluminum	7.462E-2	-4.490E-1	2.099E+0
M24	Steel	7.511E-1	-5.150E-1	2.165E+0
	Cast Iron	2.010E-1	-7.760E-1	2.455E+0
	Aluminum	1.750E-1	-7.550E-1	2.477E+0

* Formula: $K = ax^2 + bx + c$ where $K = k_m/Ed$, $x = T1/T2$

** $E_{St} = 20.678E4\ (N/mm^2)$

$E_{Ci} = 10.290E4\ (N/mm^2)$

$E_{Al} = 6.860E4\ (N/mm^2)$

combined with a lower member of 10 mm thickness, and upper members of 18, 24, and 30 mm were combined with a lower plate of 30 mm thickness, respectively. Figure 7 shows the comparison of the stiffness ratios of these models. The stiffness ratios of the models with thinner lower members is higher than the stiffness ratios of the models with thicker lower members and they decrease almost linearly as the thickness ratio increases.

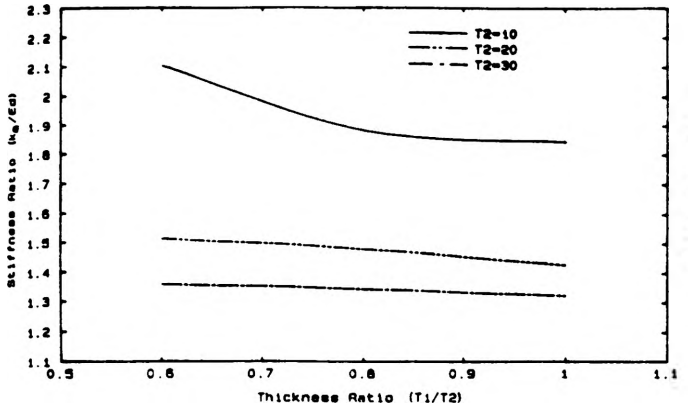

Figure 7. Comparison of Member Stiffness Ratio (M16 bolt)

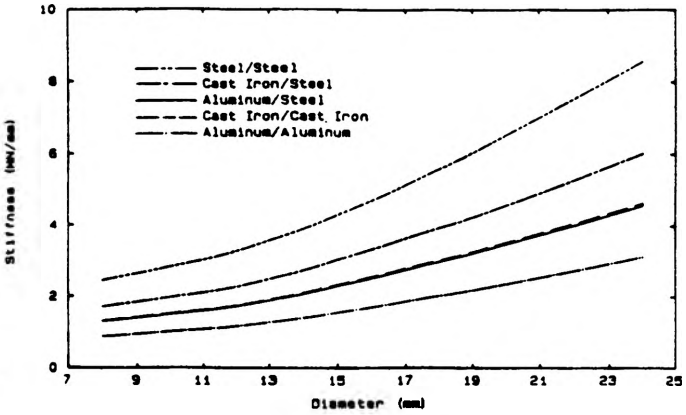

Figure 8. Member Stiffness vs. Bolt Diameter (20/20)

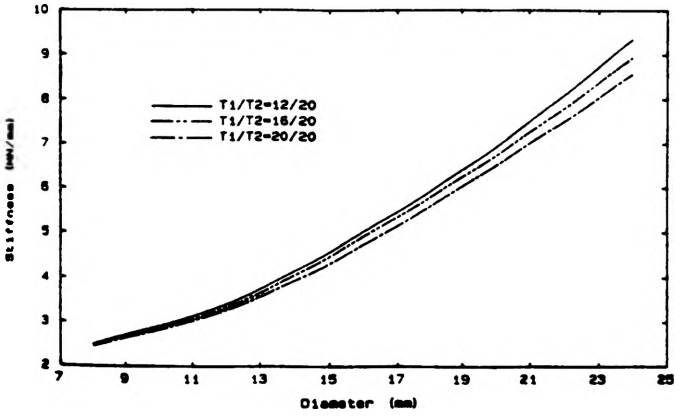

Figure 9. Member Stiffness vs. Bolt Diameter (Steel/Steel)

Figures 8 and 9 show how the stiffness of the members varies as a function of bolt diameter. The stiffness of the members always increases smoothly as the diameter increases. Figure 8 confirms that the larger the sum of the moduli of the members, the larger the stiffness. The differences between the stiffnesses is small for various size top plates as the bolt diameter is small, but increases as the diameter gets bigger. This is illustrated in Figure 9. Similar results for different materials and thickness ratios were evident.

CONCLUSIONS

Formulas which can be used to predict the member stiffness ratios for various kinds of bolted joints are presented in Table IV. The following observations were made in the course of conducting this study:

- The influence of the clearance between the bolt and hole in calculating the member stiffness is significant. Better results can be achieved by incorporating clearance values into the basic theory.
- The member stiffness ratios decrease almost linearly as the thickness ratios of the members increase.
- The member stiffness ratio of the bolted joints with thinner total member thickness is higher than that of the bolted joints with thicker total member thickness although the thickness ratios are the same.
- The member stiffness always increases smoothly as the bolt diameter increases.

- If the sum of the moduli of the members is increased, the member stiffness is increased.

ACKNOWLEDGMENTS

Much of the work for this study was a continuation on the previous work of Dr. Terry Lehnhoff (research advisor) and Kwang Ko, part of which was submitted to *Trans. of ASME* for publication in February 1992.

REFERENCES

1. Sneddon, I. N., 1946, "The Elastic Stresses Produced in a Thick Plate by the Application of Pressure to Its Free Surface," *Proceedings of the Cambridge Philosophical Society*, Cambridge, England, Vol. 42, PP. 260-271.
2. Greenwood, J. A., "The Elastic Stresses Produced in the Mid-Plane of a Slab by Pressure Applied Symmetrically at Its Surface," *Proceedings of the Cambridge Philosophical Society*, Cambridge, England, Vol. 60, pp. 159-169.
3. Nelson, C. W., 1962, "Further Considerations of the Thick Plate Problem with Axially Symmetric Loading," *Journal of Applied Mechanics*, Vol. 29, *Trans. ASME*, Series E, Vol. 84, pp. 91-98.
4. Lardner, T. J., June 1965, "Stresses in a Thick Plate with Axially Symmetric Loading," *Journal of Applied Mechanics, Trans. ASME*, Series E, Vol. 32, pp. 458-459.
5. Fernlund, I., 1961, "A Method to Calculate the Pressure Between Bolted or Riveted Plates," *Transaction of Charmers University of Technology*, Gothenburg, Sweden, No. 245.
6. Gould, M. M. and Mikic, B. B., August 1972, "Areas of Contact and Pressure Distribution in Bolted Joints," *Trans. ASME*, pp. 864-870.
7. Tang, J. and Deng, Z., November 1988, "Better Stress and Stiffness Estimates for Bolted Joints," *Machine Design.*
8. Osman, M. O., Mansour, W. M., and Dukkipati, R. V., 1976, "On the Design of Bolted Connections with Gaskets Subjected to Fatigue Loading," ASME Paper No. 76-DET-57.
9. Edwards, K. J. and McKee, R. B., 1991, *Fundamentals of Mechanical Component Design*, McGraw-Hill, 1st Ed.
10. Ito, Y., Toyoda, J., and Nagada, S., 1977, "Interface Pressure Distribution in a Bolt-Flange Assembly," ASME Paper No. 77-WA/DE-11.
11. Rotscher, F., 1927, *Die Maschinelemente*, Springer Verlag, Berlin.
12. Shigley, J. E. and Mitchell, C. R., 1983, *Mechanical Engineering Design*, McGraw-Hill, 4th Ed.
13. Shigley, J. E. and Mischke, C. R., *Mechanical Engineering Design*, McGraw-Hill, 5th Ed.
14. Little, R. E., November 1967, "Bolted Joints: How Much Give?," *Machine Design*, pp. 338-339.
15. Osgood, C. C., October 1970, "Saving Weight on Bolted Joints," *Machine Design*, pp. 338-339.
16. Grosse, I. R. and Mitchell, L. D., September 1990, "Nonlinear Axial Stiffness Characteristics of Axisymmetric Bolted Joints," *Trans. ASME*, Vol. 112, pp. 442-449.
17. *Machinery's Handbook*, 1988, Industrial Press, Inc., Twenty-Third Edition, pp. 1665-1666.

THERMALLY INDUCED STRESSES IN MICRO-CHIP MOUNTING DEVICES

K. J. Mikulcik
Mechanical Engineering Department

ABSTRACT

Microchip thermal stress due to the temperature change related to the mounting of a chip to its lead frame was investigated by moire interferometry. Large scale models were made, and the problems of applying a grating to this model at high temperature were addressed without success. Further possibilities, however, remain to be attempted. Moire interferometry was successfully used at room temperature by examining mechanically relieved residual stresses. The results agreed with an analytical approach to stress analysis and also to a finite element analysis. A practical solution to the problem of peeling was found.

INTRODUCTION

Thermal stresses in microchips present a problem when microchips are large, which creates a high aspect ratio, and when there is a large temperature drop. The microchip which is made of silicon has a very low coefficient of thermal expansion, whereas the lead frame to which it is mounted is usually a metal with a high coefficient of thermal expansion. In the case of this research the lead frame is copper which has a relatively high coefficient of thermal expansion. When the silicon chip is mounted to the copper a bimetallic strip is created which bends as the temperature changes. This causes stresses that tend to peel the silicon chip from its mount at the chip's edges.

The purpose of this research is to examine the stresses in a microchip due to the curing process of the epoxy by which it is attached to its lead frame. This was accomplished by creating a large scale model of a microchip and analyzing the stress field of a cross-section of the chip by moire interferometry. Moire interferometry is a strain measurement technique by which a strain field on a flat surface is determined by examining the interference pattern between a virtual grating and an actual grating on the surface after strain. The virtual grating is the

interference pattern of two coherent beams of laser light at right angles. The resulting interference pattern is at the same frequency as the actual grating before strain. Thus fringes or nodes are produced as the strain of the actual grating causes its frequency to change. Sensitivity of measurement is highest with gratings of high frequency. The frequency of the gratings used was 1200 per inch.

The results of this analysis were compared to a finite element analysis of the chip model. The finite element program used was MSC Nastran.

RESEARCH

To begin research, existing microchips were sliced to examine the cross section of a typical microchip on its mounting. After slicing three integrated circuits, it was determined that the chips being examined were too small to show appreciable thermal strain, even with moire interferometry. Furthermore, the chip's aspect ratio, approximately four to one, was too low for bending to occur. To measure the thermal effects on a microchip, larger dimensions were needed to use moire interferometry, and a higher aspect ratio, corresponding to a larger chip, was also needed. Therefore, materials were obtained to make a model of the largest dimensions possible for the most accurate measurements of strain.

A model was made by attaching with epoxy a piece of silicon from a 6 inch diameter silicon wafer to a plate of copper. The dimensions of the model were 2.8 inches by 3 inches with thicknesses of silicon, epoxy and copper being .033 in, .003 in and .1255 in respectively. The thickness of the epoxy was maintained by inserting between the silicon and copper mylar sheets as shims. The curing temperature was 150 Celsius so that upon cooling the resulting model showed appreciable thermal strain, for the model curved as a bimetallic strip does. Next, a thin cross section was cut from the middle of the chip model so that a strain field could be measured by moire interferometry.

Two methods of thermal stress analysis were investigated. The first method was to apply a grating that is on zerodur, a material that has a coefficient of thermal expansion of zero, at high temperature and then examine the fringe pattern upon cooling. The second method was to apply a grating after cooling and relieve the stresses mechanically after which a fringe pattern was observed.

A method was sought to apply a grating at 150 Celsius, the curing temperature of the microchip adhesive. The grating molds available were composed of silicon rubber, phenolic resin and photoresist. Photoresist does not hold

its integrity at high temperature, therefore it was not investigated as a mold at high temperature. Silicon definitely holds its integrity at high temperature. Phenolic resin needed to be investigated. Phenolic resin gratings were examined at various temperatures up to 227 Celsius. Up to 163 Celsius the phenolic resin grating appeared adequate for moire interferometry with the only adverse effects from temperature being a darkening of color and a lessoning of diffraction. Therefore, phenolic resin and silicon were used in attempts to apply a grating at 150 Celsius.

Phenolic resin gratings can be made from a silicon mold with ease at room temperature since silicon and phenolic resin do not adhere. Silicon gratings should be able to be made from phenolic resin gratings. However, this was not the case in our lab. Phenolic resin inhibited the curing of silicon. Many attempts were made at replicating silicon gratings at various temperatures but none worked satisfactorily. The best results were obtained at low temperatures. Apparently phenolic resin gives off a substance that inhibits the curing of silicon.

This lead to attempts to isolate the curing silicon from the phenolic resin. A coating (SS4177) from G.E. Silicones to inhibit the substance given off by phenolic resin was used and found to be inadequate. Photoflo was used in a similar way, and the same results were obtained.

The next step was to determine if aluminum layers could be used to isolate the curing substance, silicon, from the grating mold substance, phenolic resin. Aluminum foil could not be used since it is too thick, so the aluminum had to be vacuum deposited. An experiment was performed to determine if silicon adhesive would cure on a grating of phenolic resin with one layer of vacuum deposited aluminum. The silicon cured, but it stuck to the aluminum too strongly and the two layers could not be separated.

A possibility for relieving the problem of adhesion is to apply two layers of aluminum separated by a layer of aluminum oxide. This is the method used when the grating is made from photoresist. Many attempts were made at creating a phenolic resin grating with two layers of aluminum. However, it was discovered that the vacuum depositing machine at our facilities was defective. So a piece of zerodur with a phenolic resin grating was sent to Virginia Tech to obtain suitable aluminum layers. This piece was used in applying a layer of aluminum grating to one of the models at 150 Celsius. The results were poor since the phenolic resin degraded and the silicon did not adhere evenly. The possibility remains that a similar experiment with phenolic resin being replaced by silicon would be successful since silicon does not degrade at 150 Celsius.

Without any real success from high temperature application of a grating, attention was turned to a more conventional method of residual strain analysis. This was the technique of mechanical stress removal. Experiments were performed to determine the effectiveness of various different slicing techniques for relieving residual stresses.

The first attempt to determine residual stresses involved removing the silicon from the copper by machining it away with a diamond cutter. The results were totally inconclusive. A different attempt was made at removing the copper from the silicon and a photo was taken of the result. See Figure 1 for the U field fringe pattern and Figure 2 for the V field fringe pattern.

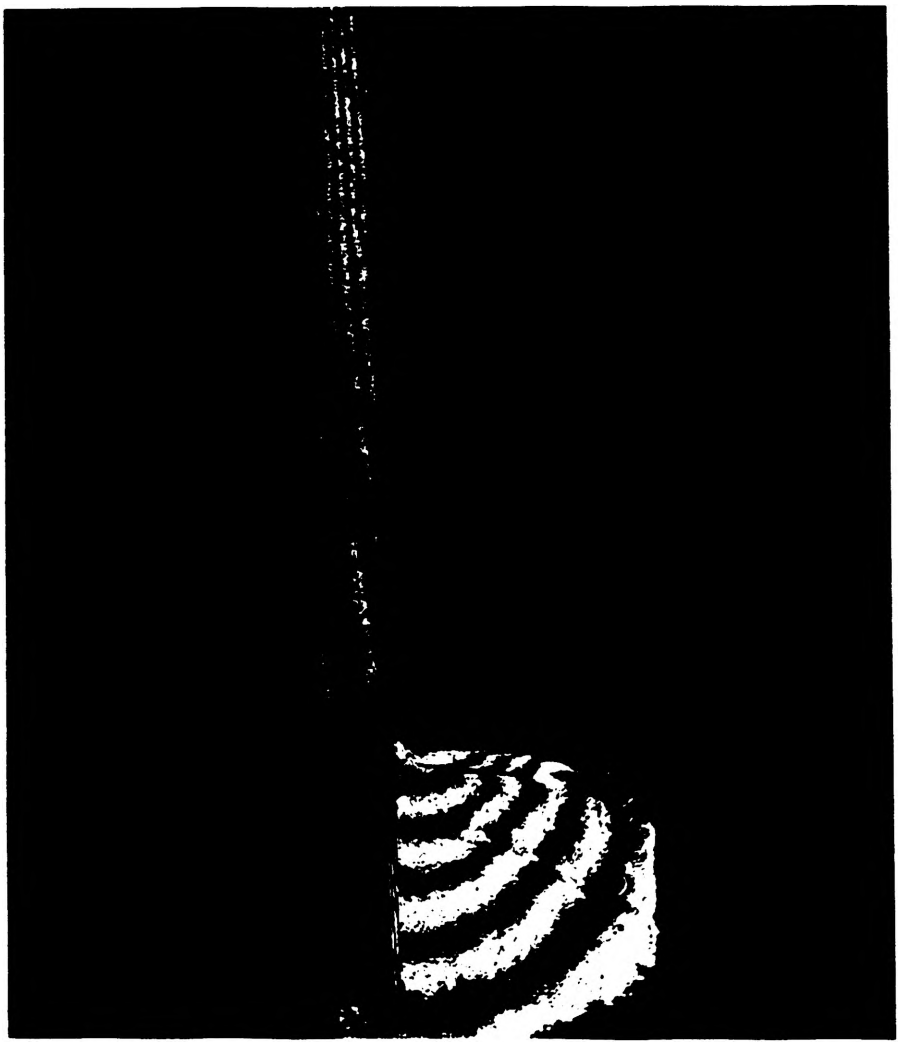

Figure 1. U Field Fringe Pattern

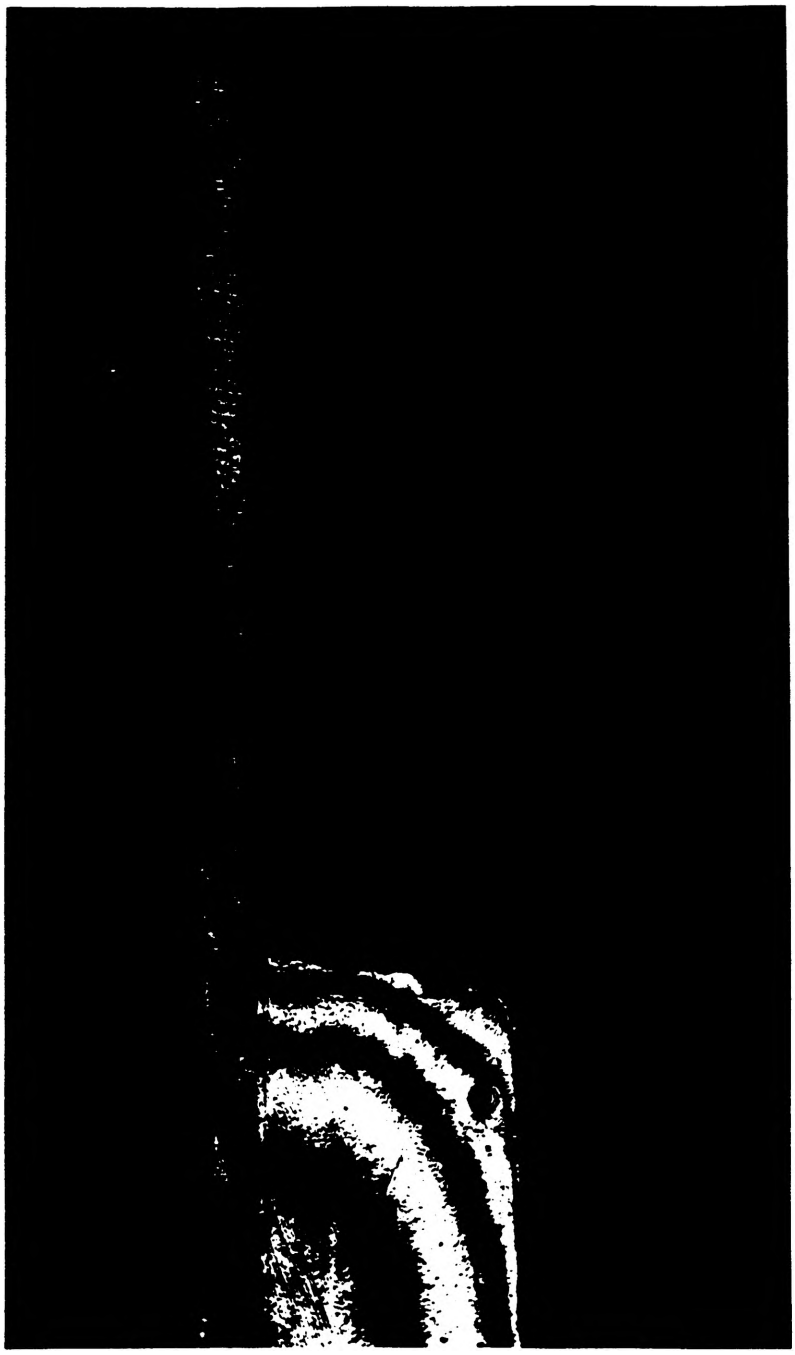

Figure 2. V Field Fringe Pattern

Although the photograph of the U field shows high shear stress near the edge of the copper, the results are poor since a null field was not obtained and a great deal of rotation occurred.

The second and final attempt at strain measurement was to examine the residual stresses at the midpoint of the microchip model. The first step was to photograph the

microchip model cross-section to obtain a null field. See Figures 3 and 4.

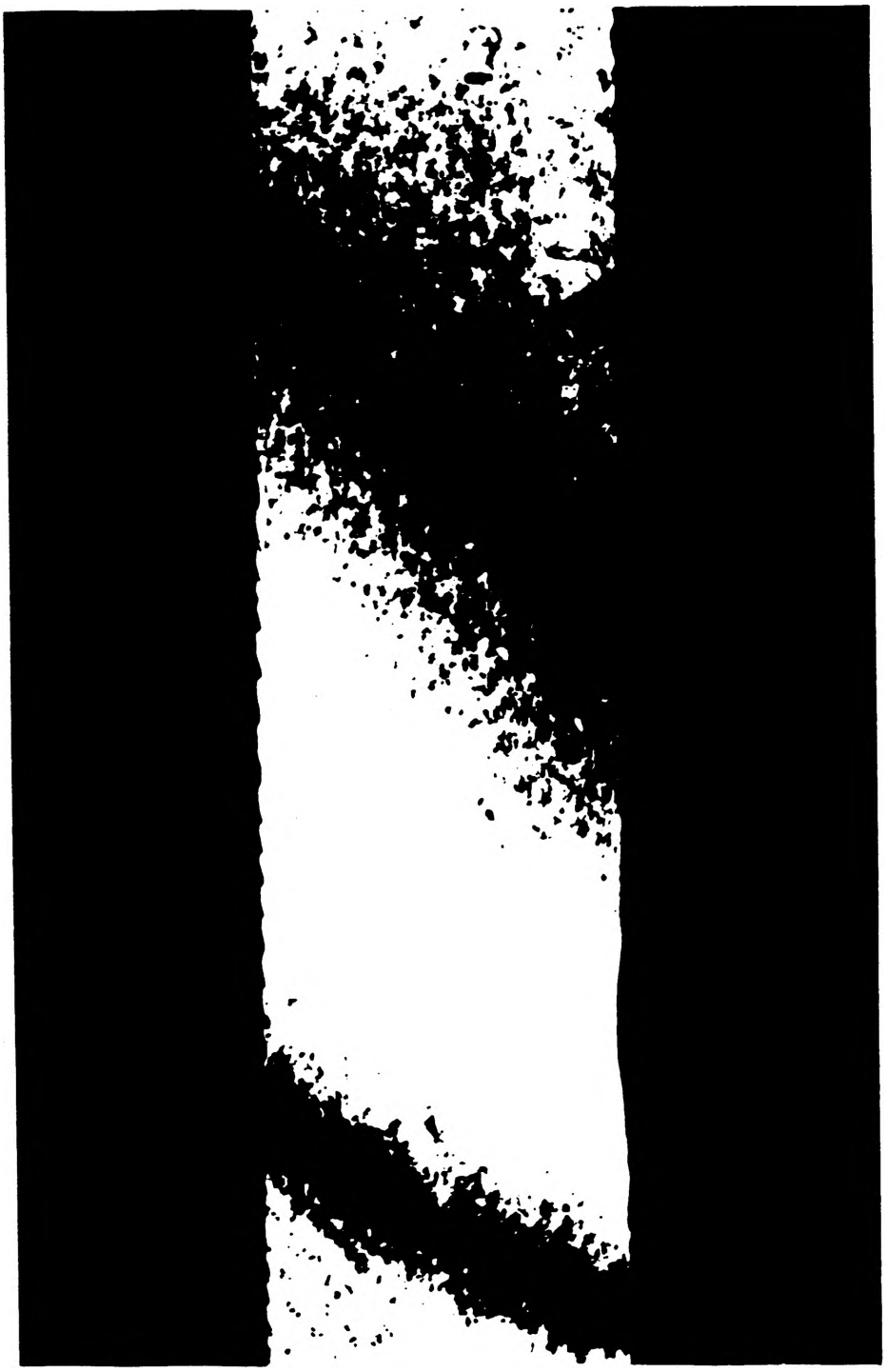

Figure 3. U Field (Null)

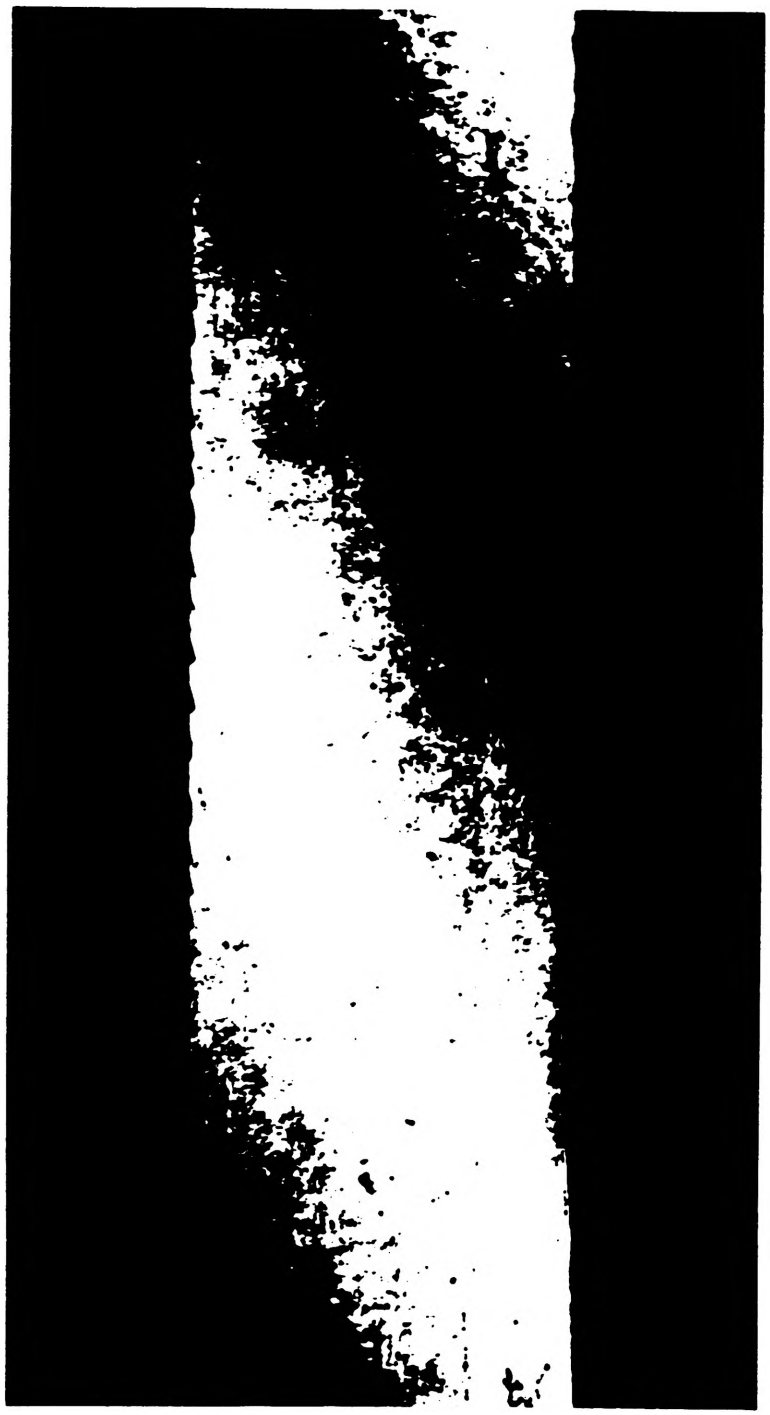

Figure 4. V Field (Null)

The notch on the right side of each photograph indicates where the cut was to be made. Next a cut was made along the centerline of the model perpendicular to the layers. This cut relieved the stresses at the centerline at the edge of

the cut. As would be expected, Figure 5, the U field photo, shows very little stress in the U direction.

Figure 5. U Field of Cut Model

The only change is a small amount of shear stress at the epoxy and some rotation. The V field, however, shows a definite pattern of stress. See Figure 6 on the following page. The silicon is in a state of compression, and it shows three fringe orders of strain. Quantitatively this amount of strain is small since the stress is not completely relieved, but qualitatively it agrees with theory. The next layer is a layer of epoxy. This layer shows a very large amount of shear strain, near 1.67 inches per inch. But this does not indicate an extremely high stress since the elastic modulus of the epoxy is on the order of 6.5^5 psi. The

Figure 6. V Field of Cut Model

copper is in both tension and compression. Adjacent to the epoxy the copper is in tension, and the fringe pattern shows this tension relieved. Between the epoxy and the right edge the stress changes to compression which is a maximum at the right edge.

This compression at the right edge of the copper is a limiting factor for the bending of the specimen. This part of the copper is resisting the moment created by the part of the copper in tension and the silicon which is in

compression.

A finite element analysis was done for comparison of the stresses in the model. See Figure 7 for the graphic side view. This graph shows the elements before and after thermal loading.

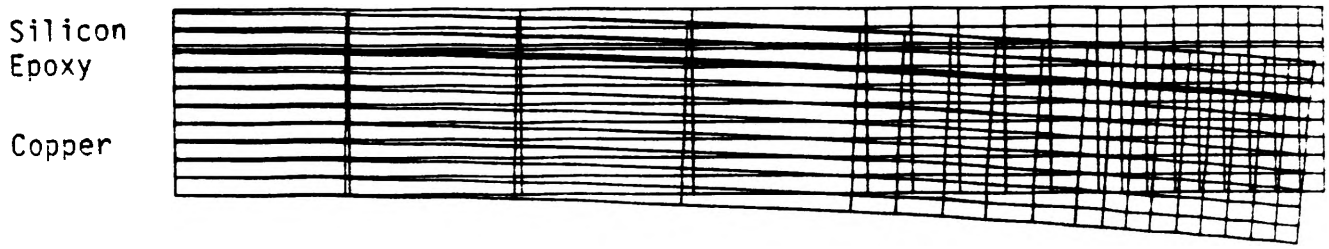

Figure 7. Finite Element Side View

This analysis agrees with the results of the stress release due to the centerline cut of the actual model. Both the model and the analysis show appreciable bending. See Figure 8 for the stress profile.

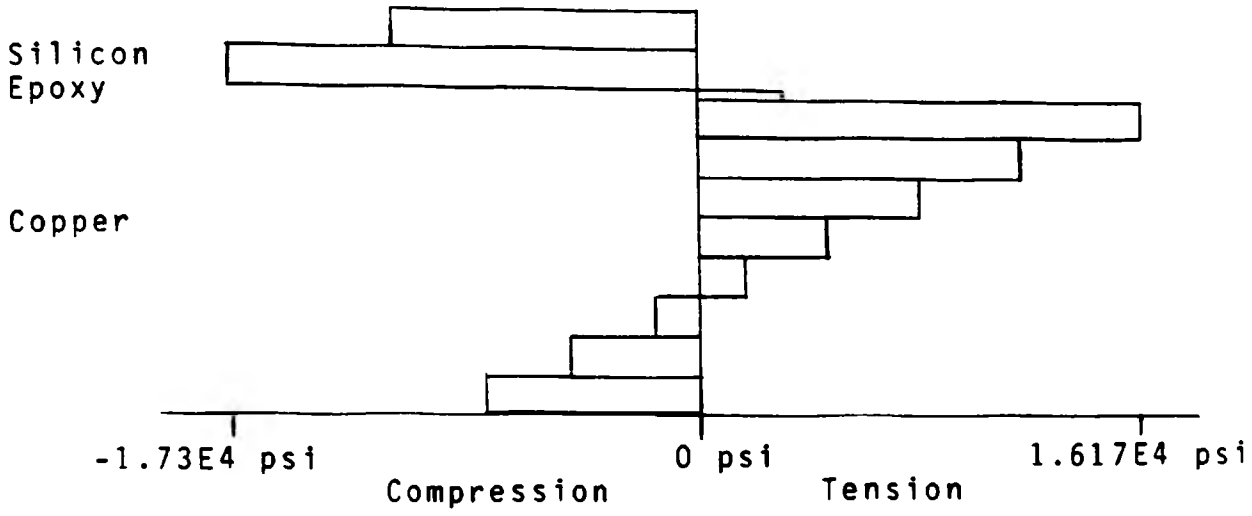

Figure 8. Stress Profile of the Finite Element Model at the Centerline

This profile shows a linear variation of stress in the copper, and this linearity is in agreement with an analytical model.

CONCLUSIONS

In conclusion, the results of the centerline cut experiment show that it is possible to reduce the stresses that a microchip would undergo at very low temperatures. If another chip of silicon were to be attached to the opposite side of the copper lead frame, a symmetric situation would arise, and the bending would be eliminated. This would eliminate the possibility of peeling and reduce the amount of normal stress in the silicon and reduce the amount of shear stress that the adhesive would experience. Unfortunately, time did not allow for the production of a modified model with an extra layer of silicon for symmetry, nor did it allow for an attempt to apply an aluminum layer from a silicon grating at high temperature.

ACKNOWLEDGMENTS

I thank Dr. Duksung Joh for his assistance and guidance in basic research especially in experimental techniques and for the use of his lab. I also thank Kook Yun Byun for his cooperation and help with moire interferometry and the use of Nastran. I also thank Patrick O'Mahony for his help with Nastran.

STATIC AND DYNAMIC TESTING OF SERPENTINE BELT DRIVE TENSIONERS

JOHN W. MINOR DEPARTMENT OF MECHANICAL ENGINEERING

ABSTRACT

Serpentine belt drive tensioners are used in virtually every model of automobile produced today. Limited testing has been done to see how the tensioner performs under certain situations. In each case outside influences were either not accounted for or considered not to influence the way the tensioner performed in a given situation. By developing new ways of testing tensioners for static and dynamic characteristics separately, the influence each trait has on the performance of the tensioner can be exactly gauged.

INTRODUCTION

The days of automotive engines with multiple belts are gone. Today virtually all of the new automobiles produced in the world use a single polyrib belt to drive the peripheral engine components (i.e. fan, water pump, alternator, etc.). With the change in the belt drive system came a change in the way tension was kept in the belt. In the multiple belt system, tension in each individual belt was set by the adjustment of the position of the specific component that was being driven by the belt. With the advent of the single belt drive, also called the serpentine belt drive, a new component was introduced: the serpentine belt drive tensioner. Tensioners consist of a belt pulley mounted on one end of an arm with a very stiff torsional spring attached to the pivot end of the arm. Tension is kept in the belt, by the tensioner, by moving the arm and thus loading the spring and allowing the pulley to push on the belt between the pulleys of two of the peripheral engine components.

Since the tensioner is used to supply a force to the belt which induces tension, the tensioner exhibits a dependance on static load. Also, due to the fact that an automotive engine is a large source of vibration and the main forcing component in the tensioner is a spring, the effect of vibrations on the tensioner is of great concern.

Experimental Background and Scope

Limited testing of the tensioners has been done by the research and development division of Dayco Industries in Springfield, Missouri. Dayco is the major manufacturer of tensioners for the Ford Motor Company. At Dayco the dynamic

characteristics of the tensioners were tested on a stationary engine. Testing the dynamic response in this manner may have introduced the elastic characteristics of the belt and thus the dynamic characteristics of just the tensioner may not have been tested. The static load response was tested by directly attaching an air cylinder to the arm of the tensioner. By testing static characteristics this way the effects on the tensioner due to the tension in the belt and the placement of the surrounding components were totally neglected.

The goal of this research is to test the static and dynamic characteristics of only the tensioner in a typical application. This can be easily done by using a steel strapping material in place of the polyrib belt to eliminate any elasticity effects the belt would introduce. Also, by simulating nearby components both the dynamic and static characteristics of the tensioner can be measured in an environment that imitates an actual application. To develop overall characteristics many different tensioners from numerous production runs will be tested.

Fixture design

Using information which described the position of the engine components in relation to the center of the crankshaft pulley, the positions of the required components were laid out, see figure 1. An attachment was added to the lower portion of the main fixture that would allow the fixture to be elevated off the floor such that the free end of the steel strap could be attached to a weight hanger or a vibration source. Since static forces of up to 200 pounds and vibration forces are used in the experiment the fixture had to be quite strong so that it would not introduce any unwanted effects. Therefore, the fixture box was made out of half inch steel plate and the components were braced well to make the entire setup rigid.

The steel used in the fixture parts that were built in the Mechanical Engineering shop was paid for with the money provided by the OURE. All other parts were provided by Dayco, free of charge, or built in my home shop using scrap materials. Instrumentation was built from used parts and therefore cost nothing also.

STATIC CHARACTERISTICS

By using a weight hanger suspended from the free end of the steel strap the static response of a tensioner was tested. Large weights averaging about fifteen pounds and small weights of exactly five pounds were added until the tensioner reached full displacement. Then the weights were removed to see if the tensioner exhibited the same sort of static response in this setup as it did in the setup used by Dayco.

Results

The tensioner shown in figure 2 was used on an engine by Dayco during testing, thus, it contained some amount of wear. In the figure each line represents

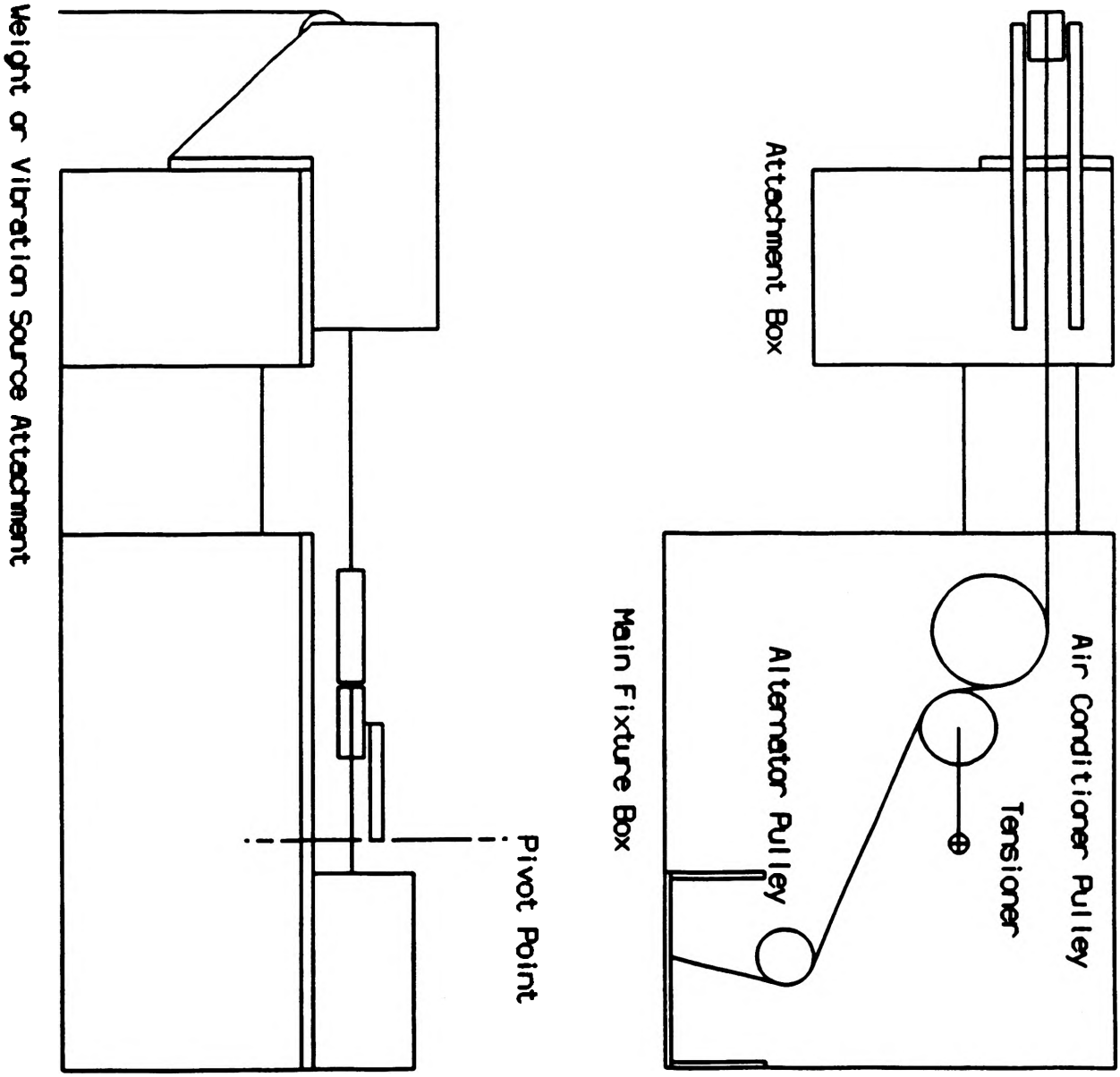

Figure 1: Schematic Layout of the Test Fixture

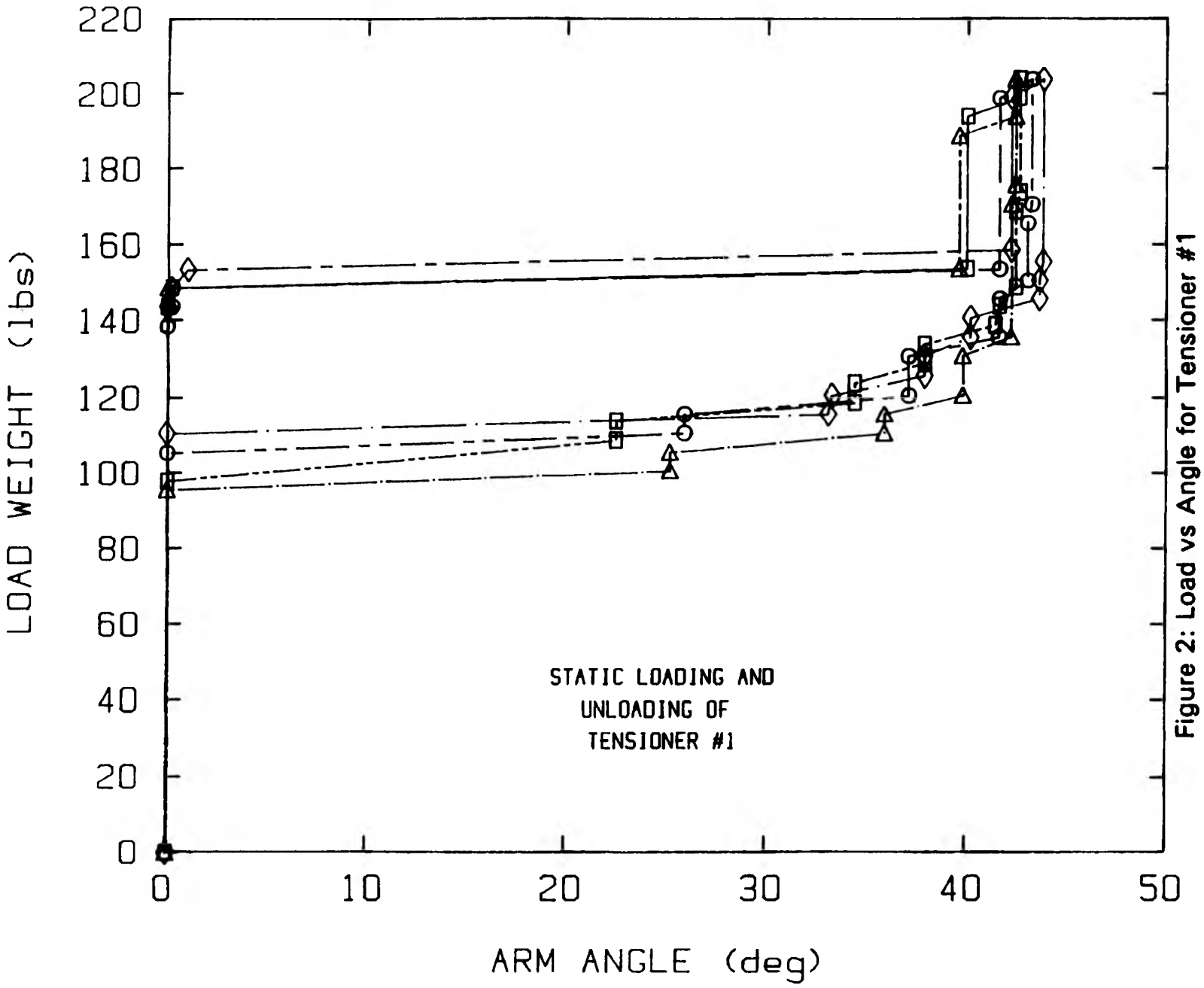

Figure 2: Load vs Angle for Tensioner #1

a loading and unloading of the tensioner. From the figure it is easy to see that the tensioner arm does not move until a large amount of weight is contained upon the weight hanger and with the addition of only five pounds the tensioner goes to virtually full displacement. This is nothing like the smooth loading curve that Dayco produced when loading a tensioner by their method [1]. However, the part of the graph that corresponds to the unloading of the tensioner is approximately equivalent to the unloading curve found by Dayco. The only difference in the unloading portion is that in the setup used by Dayco the tensioner gradually reached zero displacement whereas here the tensioner quickly moves to zero displacement after a certain amount of weight is removed.

In figures 3, 4, and 5 new tensioners directly from the production plant were tested. These tensioners were given an initial displacement to see if a change in the way the tensioner loaded was evident. Each tensioner loaded without moving until a certain weight was reached and then displaced to its full displacement. Unloading each tensioner proceeded in the same fashion as tensioner one.

Conclusions

Due to the way that the tensioner loaded, it is easy to see that the way a tensioner loads is highly dependent on the environment in which it is loaded. Also, the load at which the tensioner will displace depends on the age of the tensioner. Tensioner one displaces at a much lower load than either of the other three tensioners. However, looking at all four figures the unloading lines are virtually the same for all four tensioners and the maximum displacement angles are also relatively the same. Thus, if the tension in the belt close to the point where the addition of a small amount of load would cause full displacement and the tension were to be somehow increased, due to the addition of a load (i.e. turning on the automobile's air conditioner) or by increasing the speed of the engine, momentary loss of tension would occur causing belt squall.

DYNAMIC CHARACTERISTICS

Due to the trouble in getting tensioners and other parts no dynamic testing was done at this point in the experimentation. Testing of the dynamic characteristics will be done at some point by applying a vibrating force to the steel strap with a tensioner in its normal running angle, approximately 18.5 degrees, by either the use of a vibration exciter or other vibration source. The vibration testing will seek out any resonance characteristics or other parameters associated with vibrating systems.

FUTURE TESTING

At the present time static testing on six more tensioners is in progress. At the conclusion of this round of static testing, some dynamic testing will be done in order

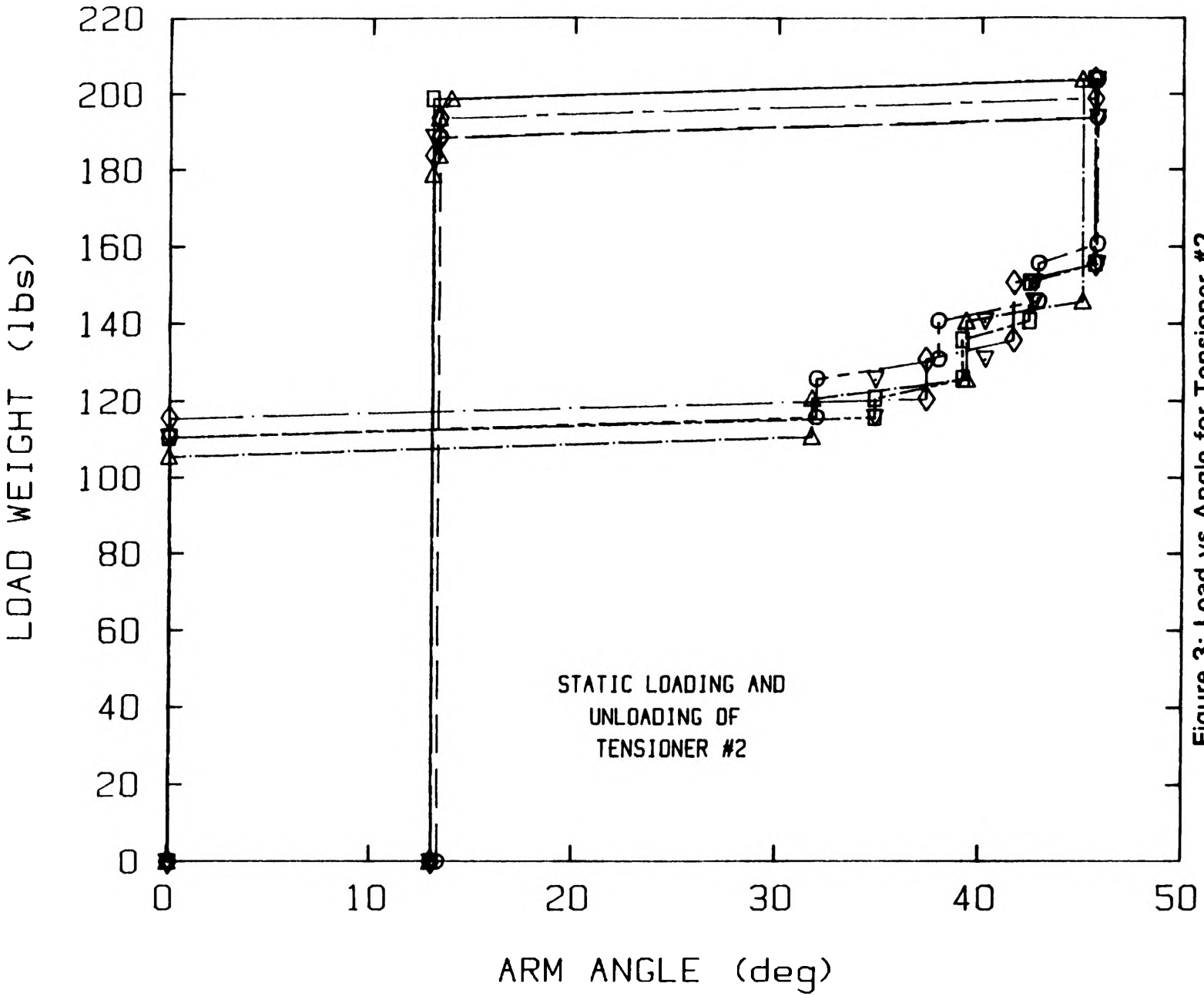

Figure 3: Load vs Angle for Tensioner #2

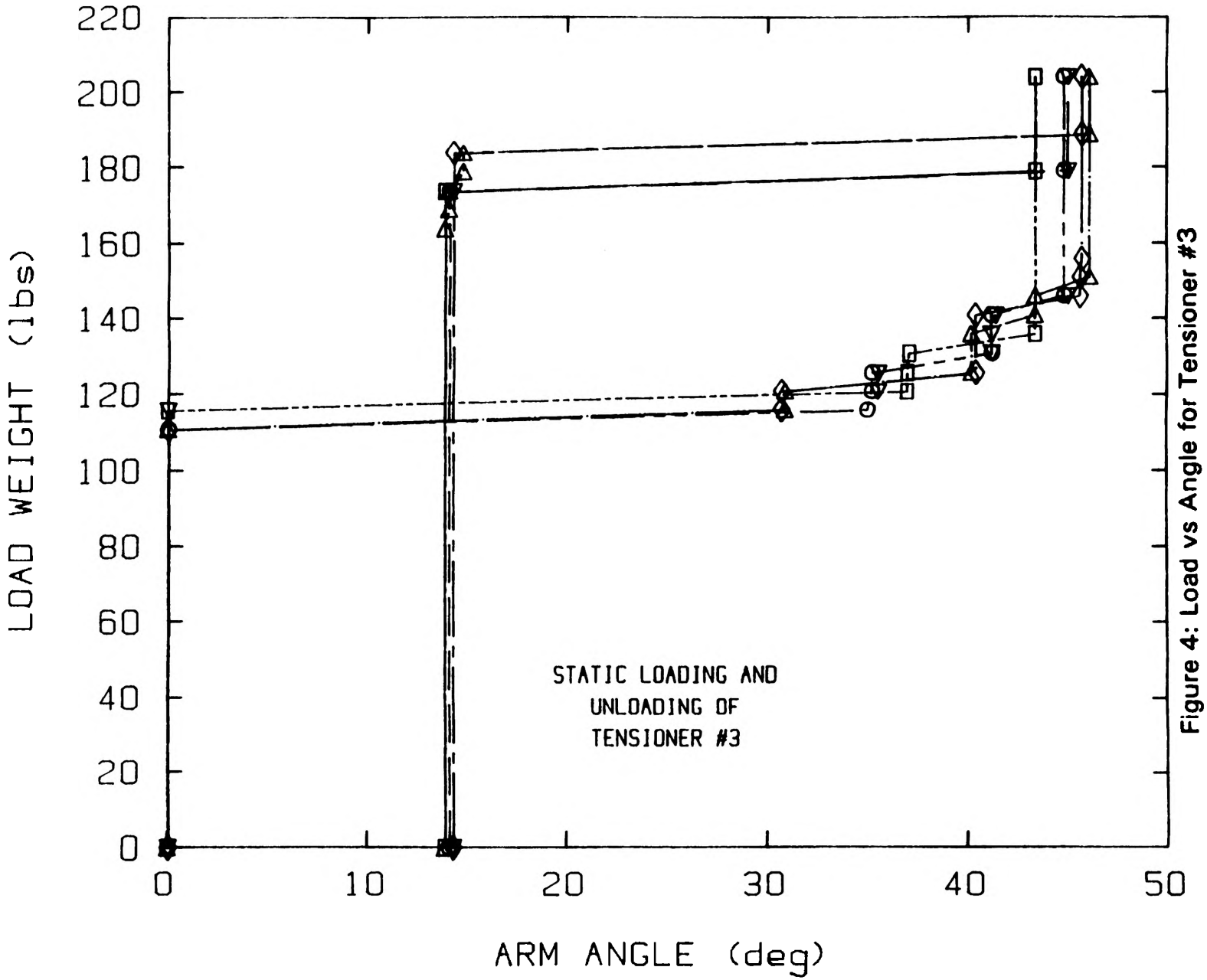

Figure 4: Load vs Angle for Tensioner #3

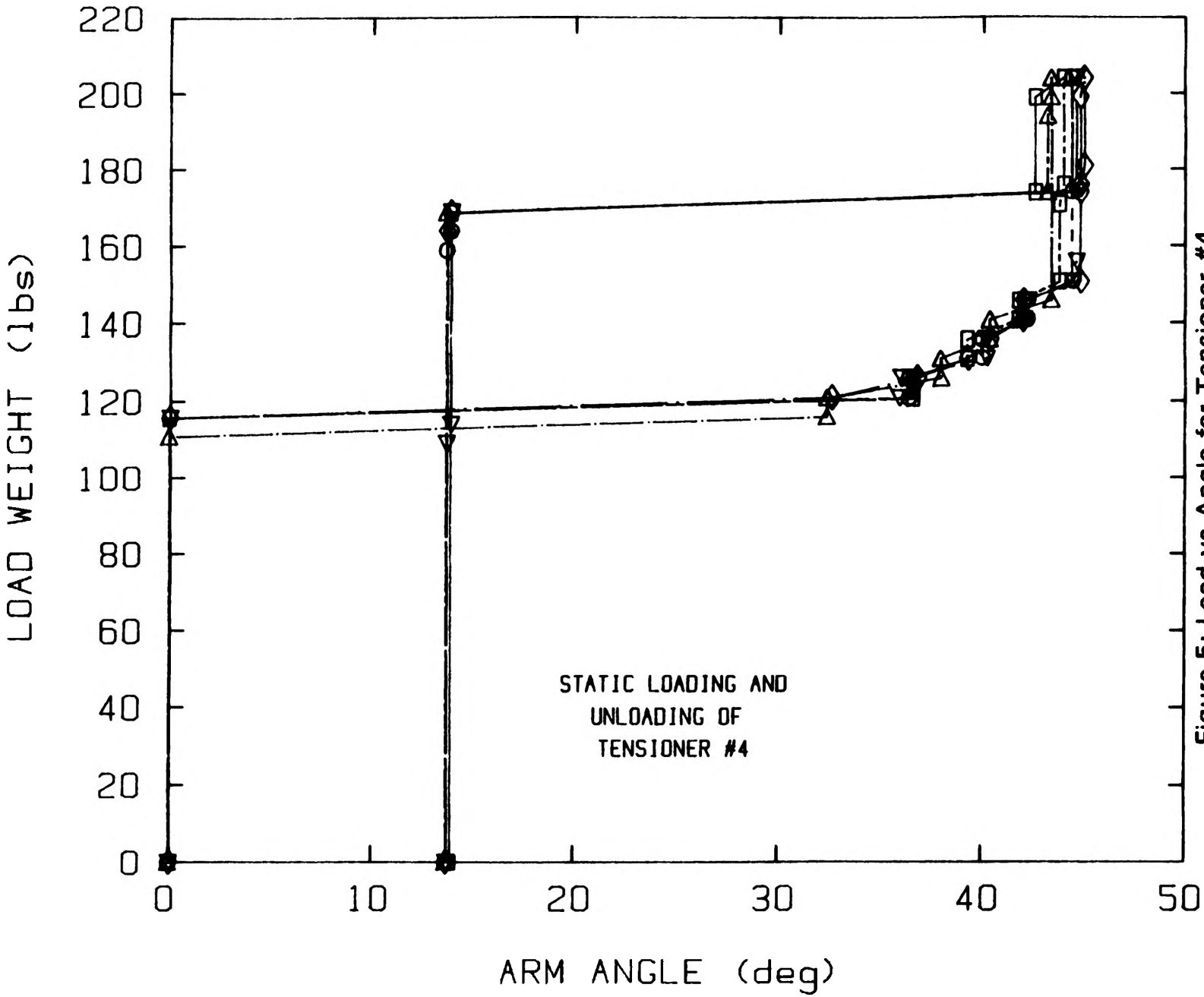

Figure 5: Load vs Angle for Tensioner #4

to come up with a basis for later testing of the dynamic characteristics of the tensioners. Work will continue until the end of the semester as part of my honors research in the Department of Mechanical Engineering. Also, due to the constant changing of tensioner design, more research on this topic could be done by others in coming semesters.

ACKNOWLEDGMENTS

I would like to thank the following people for their help in this research project:
Dr. C. R. Barker, faculty advisor, for his help in getting me started with the research and helping me solve any problems.
Dr. William F. Breig and Dayco for supplying me with the needed layout information and the test tensioners.
Mr. Bob Hribar for building the majority of the fixture.

REFERENCES

1. Barker, C. R., Oliver, L. R., and Breig, W. F., "Dynamic Analysis of Belt Drive Tension Forces During Rapid Engine Acceleration", SAE Technical Paper 910687, February, 1991.

MIELNIK PROBABILITY SPACES AND FUNCTIONAL EQUATIONS

J. J. Mitchell
Mathematics Department

ABSTRACT

The invariance properties of the solutions of those functional equations naturally occurring in the construction of Mielnik probability spaces are studied, and in turn are related to one another. In particular, the possibilities for fixed points of these solutions are found, and the relationships between these results are discussed. The two functional equations studied include a representation of the generalized parallelogram law and an equation used in the modeling of polarization phenomena. The main result of the paper lies in the extention of previous research on Mielnik probability spaces to a higher dimension, as well as a discussion of their applicability in characterizing inner product spaces.

INTRODUCTION

In [1], G. Birkhoff and J. von Neumann confronted the problem of finding a fundamental set of axioms which would ensure the use of orthogonal projectors in Hilbert space as a representation of quantum logic propositions. C. Piron [2], assuming weak semimodularity, showed that it is possible to represent yes-no measurements by orthogonal projectors in some unitary spaces. The insufficiency of this approach was later noted by Mielnik [3], who instead proposed a geometric foundation to quantum mechanics. To do so, Mielnik introduced an abstract space of states in which to construct his geometric theory. Let S be a nonempty set and p a real-valued function defined on SxS such that the following three axioms hold.

Axiom A: $0 \leq p(a,b) \leq 1$ and $p(a,b)=1$ if and only if $a=b$.

Axiom B: $p(a,b) = p(b,a)$.

The third axiom deals with the property of orthogonality. Two elements $a \in S$ and $b \in S$ are said to be orthogonal if $p(a,b) = 0$. An orthogonal system of S is defined as a subset $R \subseteq S$ such that any two distinct elements of R are orthogonal. A maximal orthogonal system, or basis, is an orthogonal system which cannot be contained within any larger orthogonal system in S. The existence of at least one basis in S is a consequence of Zorn's lemma. In [3], Mielnik proved the uniqueness of the number of elements contained in a basis. Thus, the usual definition of dimension is applicable to the set S. With this concept of basis, Axiom C may be formulated as follows.

Axiom C: For each basis $R \subseteq S$ and for each $x \in S$, $\sum_{r \in R} p(x,r)=1$.

These three axioms form the foundation of a Mielnik probability space, as indicated in the following definition.

Definition: A Mielnik probability space (S,p) consists of a nonempty set S and a real-valued function p defined on SxS such that axioms A, B, and C hold.

FUNCTIONAL EQUATIONS IN MIELNIK PROBABILITY SPACES

The Generalized Parallelogram Law.

Let [0,2] be the domain of f, and let [0,1] be the range of f. Further, let f be continuous and strictly increasing, and let f(0)=0 and f(2)=1. We denote the class of all such functions F.

Let [0,2] be both the domain and range of g. Further, let g be continuous and strictly decreasing with g(0)=2 and g(2)=0. We denote the class of all such function G. In [4], Stanojević examined those $f \in F$ and $g \in G$ that satisfied the functional equation

$$f+fog=1 \qquad (1)$$

where fog(t) = f(g(t)). Stanojević was able to generalize the parallelogram law as a test for an inner product space using the above functional equation, and then went on to characterize these inner product spaces in terms of Mielnik probability spaces. The following result from [4] guarantees the existence of solutions to (1).

Lemma 1. (C. V. Stanojević) Let $f \in F$ Then there exists a $g \in G$ such that (1) holds.

We now proceed to examine the invariance properties of those $f \in F$ and $g \in G$ that together satisfy (1).

Lemma 2. Let $f \in F$ and $g \in G$ satisfy (1). Every such g has a unique fixed point.

Proof. First note that Lemma 1 guarantees the existence of solutions to (1). Now, the continuity of f guarantees that f takes on all values in [0,1]. Further, the monotonicity of f results in f being a one-to-one function, and so f attains each value in [0,1] exactly once. Thus, consider $x \in [0,2]$ such that f(x)=1/2. Then

$$f(x) + fog(x) = 1 \text{ implies } fog(x) = 1/2.$$

But,

$$f(x) = 1/2 \text{ and } fog(x) = 1/2 \text{ implies that } g(x) = x$$

since f is one-to-one. Thus, g has at least one fixed point. We now show the uniqueness of this fixed point. Suppose that x and y are fixed by g. Then (1) immediately reduces to

$$f(x) = 1/2 \text{ and } f(y) = 1/2.$$

Again, due to the one-to-one nature of f, we have x = y. Hence, the fixed point of g is unique, and the proof is complete.
From the proof of Lemma 2, we have established the following result.

Lemma 3. Let $f \in F$ and $g \in G$ satisfy (1). Then $g(x) = x$ if and only if $f(x) = 1/2$.

An interesting consequence of these lemmas is the following theorem.

Theorem 1. Let $f \in F$ and $g \in G$ satisfy (1). Then the unique common fixed point for all such f and g is x=1/2.

Proof. From Lemma 3, if g fixes x then $f(x) = 1/2$. Thus, if f is also to fix x, we must have $x = 1/2$. In no other instance can both f and g fix a value simultaneously. Thus the unique common fixed point is $x = 1/2$. It appears from this development that $x = 1/2$ represents some center point of symmetry.

A Functional Equation Related to Polarization Phenomena.

In [5], Stanojević and Guccione introduced the following functional equation in an effort to offer a very general class of probability functions to be applied to modeling polarization phenomena. This equation, given by

$$\phi(t) + \phi(1-t) = 1, \qquad (2)$$

is applied by setting the probability function p(x,y) to by

$$p(x,y) = \phi \circ f(\|x+y\|),$$

where $f \in F$. From here on, we denote the class of all such functions ϕ from [0,1] onto [0,1] satisfying (2) by Φ. Further, in our consideration of applying this functional equation to polarization phenomena, we will denote the subclass $\Phi_1 \subseteq \Phi$ where Φ_1 is the set of all strictly increasing, continuous functions satisfying (2). Noting the obvious existence of a solution to (2) given by $\phi(t)=t$, we now proceed with an investigation of the invariance properties of this functional equation.

Theorem 2. Every $\phi \subseteq \Phi$ has at least one fixed point, namely t = 1/2.

Proof. Direct substitution of $t = 1/2$ into (2) verifies $\phi(1/2) = 1/2$.

Theorem 3. Let $\phi \in \Phi$ and suppose t is fixed by ϕ. Then (1-t) is also fixed by ϕ.

Proof. Since $\phi(t) = t$, we have from (2) that $t + \phi(1-t) = 1$. Thus, $\phi(1-t) = 1-t$, and the proof is complete.

It is to be noted that a more complete characterization of Φ was given in [5], where it was proposed that every $\phi \in \Phi$ was of the form

$$\phi(t) = h(t-1/2) + 1/2,$$

where h is an odd function defined on $[-1/2,1/2]$. These same fixed point theorems follow readily from this observation as well.
An interesting result is obtained by considering the application of this functional equation to polarization phenomena. Letting $p(x,y) = \phi o f(\|x+y\|)$, we have the following theorem, which links the invariance properties of the two functional equations.

Theorem 4. Let N be a real inner product space, S its unit sphere, $f \in F$, $g \in G$, and $\phi \in \Phi_1$. Further, let $p(x,y) = \phi o f(\|x+y\|)$ define a probability function for $x,y \in S$. Then ϕ attains the fixed point at $t = 1/2$ when and only when g takes on its unique fixed point.

Proof. The verification that (S,p) results in a Mielnik probability space of dimension 2 was accomplished by Stanojević and Guccione in [5]. Thus, the probability space axioms hold. It is immediate that the bases are of the form $\{x,-x\}$. Hence, from Axiom C, we have

$$p(x,y) + p(x,-y) = 1 \Rightarrow$$

$$\phi o f(\|x+y\|) + \phi o f(\|x-y\|) = 1.$$

Now, ϕ satisfies (2), so $f(\|x-y\|) = 1 - f(\|x+y\|)$. From Lemma 1, there exists a $g \in G$ such that $f(\|x-y\|) = fog(\|x+y\|)$. Let $z=\|x+y\|$. Clearly, z takes on all the values in the interval $[0,2]$. Thus, we may now write

$$\phi(f(z)) + \phi(fog(z)) = 1, \text{ or}$$

$$\phi(f(z)) + \phi(1-f(z)) = 1. \qquad (3)$$

Suppose ϕ takes on the central fixed point at z. Then $f(z) = 1/2$, and from Lemma 3, $g(z) = z$.
Conversely, suppose $g(z) = z$. Again from Lemma 3, $f(z) = 1/2$, and (3) reduces to show that ϕ takes on the central fixed point.

A FOUR-DIMENSIONAL PROBABILITY SPACE

Let N be a complex normed linear space, and let S be its unit sphere. Further, let $f \in F$ and for all $x,y \in S$ let

$$D_1 = D_1(x,y) = f(\|x-y\|)f(\|x-iy\|)f(\|x+iy\|),$$

$$D_2 = D_2(x,y) = f(\|x-y\|)f(\|x+y\|)f(\|x-iy\|),$$

$$D_3 = D_3(x,y) = f(\|x-y\|)f(\|x+y\|)f(\|x+iy\|),$$

$$D_4 = D_4(x,y) = f(\|x+y\|)f(\|x-iy\|)f(\|x+iy\|).$$

Theorem 4. For all $x,y \in S$, let

$$p(x,y) = D_4 /(D_1 + D_2 + D_3 + D_4).$$

Then (S,p) is a probability space of dimension 4.

Proof. We divide the proof into sections verifying the probability space axioms.

Axiom A. Notice that $D_1 + D_2 + D_3 + D_4$ is never zero. For, assuming the contrary, each D_i would have to be zero since the range of f contains no negative values. But, $f(t) = 0$ if and only if $t = 0$. Thus, each D_i must contain the common term $f(0)$. However, the D_i do not all share a common term, so it is impossible for each D_i to be zero simultaneously. Thus, $p(x,y)$ is well defined.

Now, since the range of f can take on only nonnegative values, we have $D_i \geq 0$ for each $i \in \{1,2,3,4\}$ and $D_4 \leq D_1 + D_2 + D_3 + D_4$. Thus, $0 \leq p(x,y) \leq 1$.

Consider $p(x,x)$. $D_1 = D_2 = D_3 = 0$ since $f(\|x-x\|) = f(0) = 0$, and so

$$p(x,x) = D_4 /D_4 = 1.$$

Conversely, suppose $p(x,y) = 1$. Then $D_4 = D_1 + D_2 + D_3 + D_4$. Hence, $D_1 = D_2 = D_3 = 0$. Again, this can only occur if each of D_1, D_2, and D_3 contain the common term $f(0)$. The only term common to D_1, D_2, and D_3 is $f(\|x-y\|)$. Thus, $\|x-y\| = 0$, and so $x=y$.

We have thus shown that $0 \leq p(x,y) \leq 1$ and $p(x,y) = 1$ if and only if $x=y$. Thus, Axiom A holds.

Axiom B. We must show $p(x,y) = p(y,x)$. We start by showing that D_4 is invariant on interchanging x and y. Clearly, $f(\|x+y\|)$ remains unchanged due to the commutativity of addition in N. Now, $|i| = 1$, so $\|y-ix\| = \|iy-i^2x\| = \|iy + x\| = \|x + iy\|$. Similarly, $\|y+ix\| = \|x-iy\|$. Thus, upon interchanging x and y, we have $f(\|y-ix\|) = f(\|x+iy\|)$ and $f(\|y+ix\|) = f(\|x-iy\|)$. Hence, D_4 is invariant under the interchanging of x and y.

Using the same procedure (multiplying through by i when necessary), it is found that D_1 remains invariant while D_2 becomes

D_3 and vice versa when x and y are interchanged. Thus, ΣD_i is itself invariant. Thus, p(x,y) = p(y,x), and Axiom B holds.

Axiom C. The bases in this instance are of the form

$$B = \{b,-b,ib,-ib\}.$$

To see this, note that since each two distinct elements of an orthogonal system have a zero transitional probability, we must have $D_4=0$ for any two orthogonal elements. It follows, since $D_4=0$ if and only if it contains a term of the form f(0), that if r and s are orthogonal, then r = -s or r = ±is. The form of the bases B immediately follows. We now formulate the sum required for Axiom C. Upon direct substitution into p(x,y) and summing, we find that $\Sigma_{b\in B}$ p(x,b) = 1, and so Axiom C holds also. Thus, the axioms of a probability space are satisfied, and so (S,p) is a probability space. From the verification of Axiom C, we have that (S,p) is of dimension 4. This proof is complete.

Future Research.

The extension of a probability space structure to n dimensions has already been accomplished in a manner similar to the specific four dimensional case presented here. The significance of these results is that it can be shown that these higher dimensional probability spaces can not be used as a characterization of inner product spaces as the two dimensional spaces were by Stanojević. The extension to the n dimensional case and the inability of probability spaces of higher dimension to characterize inner product spaces will be presented in an upcoming paper. The applicability of Mielnik probability spaces to physical phenomena as well as the significance of the invariance properties of the functional equations used in their construction offer interesting avenues of future research to follow up on.

ACKNOWLEDGEMENTS

The author wishes to acknowledge Dr. C. V. Stanojević for his guidance and advice, and for pointing to this topic as an area of research.

REFERENCES

1. G. Birkhoff and J. von Neumann, The logic of quantum mechanics, Ann. of Math. (2) 37 (1936), 823-843.

2. C. Piron, Axiomatique quantique, Helv. Phys. Acta 37 (1964), 439-468. MR 34 #3894.

3. B. Mielnik, Geometry of quantum states, Comm. Math. Phys. 9 (1968), 55-80. MR 37 #7156.

4. C. V. Stanojević, Mielnik probability spaces and characterization of inner product spaces, Trans. Amer. Math. Soc. 183 (1973), 441-448. MR 48 #6904.

5. S. J. Guccione, Jr. and C. V. Stanojević, A class of functional equations and mielnik probability spaces, Proc. Amer. Math. Soc. (2) 59 (1976), 317-320.

CYCLODEXTRIN STATIONARY PHASES FOR THE GAS-SOLID CHROMATOGRAPHIC SEPARATION OF HYDROCARBONS

Chris A. Monge
Department of Ceramic Engineering

ABSTRACT

Cyclodextrin, bonded to silica gel and used as a gas-solid chromatographic stationary phase provides a practical and efficient means for separating a wide variety of C_1-C_7 hydrocarbons at ambient to elevated temperatures. Conditioning the columns at high temperature (300°C) for several hours increased efficiency and resolution. The adsorption of these light hydrocarbons involves a multiple retention mechanism. Evaluation of the columns and an analogous silica gel column with hydrocarbon standards is reported. Capacity factors and chromatograms are presented for these GSC stationary phases.

INTRODUCTION

Gas-solid chromatography (GSC), introduced in 1941 by Martin and Synge [1] is a widely used technique for the separation of light hydrocarbon and permanent gases. Compared with gas-liquid chromatography (GLC), GSC stationary phases (GSC SPs) have a comparatively larger surface area [2] and this results in excessive retention times for large molecules. For lower molecular weight compounds, GLC has little selectivity, and is seldom used. For separation of these low molecular weight molecules, packed columns, and more recently, porous layer open tubular (PLOT) or support coated open tubular (SCOT) [3][4][5] columns are the main choices. Many GSC stationary phases have been cited as separating light hydrocarbons, including molecular sieves [6][7], alumina and silica gel [8][9][10], porous polymers [11][12][13][14][15] and charcoal [16][17][18]. Elution order for adsorption columns vary by stationary phase polarity [19]. Compounds are separated by boiling point on non-polar columns, while on polar stationary phases, in an analogous series, triple bonded compounds are retained stronger than double bonds which are retained stronger than saturated compounds.

A GSC SP used for separating higher boiling compounds along with geometric isomers is composed of cyclodextrin on an inert support [20]. Presently, many researchers are reporting the use of derivatized cyclodextrins as GLC chiral SPs for the separation of enantiomers, diastereomers, and geometric isomers [21][22][23][24]. Cyclodextrins are cyclic oligosaccharides; D(+)-glucopyranose units linked alpha (1,4). The three most common CDs are the alpha, beta and gamma (α, β and γ), which are differentiated by the number of glucopyranose subunits (6, 7 and 8, respectively). The cyclized glucopyranose units form a conical shaped structure, with secondary hydroxyls (12 for α–CD) surrounding the wider end and primary hydroxyls (6 for α–CD) opposite. The top and bottom of the structure are polar, due to the hydroxyl groups, while the interior of the cavity is apolar.

The alpha and beta-cyclodextrin cavities are on the order of 4.5 and 7 Å, respectively, and molecules with appropriate sizes can form a host/guest inclusion complex. Mechanistic studies involving CDs [25][26] and derivatized CDs [27] have cited multiple retention mechanisms. These studies were done on compounds (hydrocarbons, chlorocarbons, aromatics, etc.) in which a tight fitting host/guest complex could be obtained. For aliphatic hydrocarbons, dispersive forces are responsible for inclusion. With these forces, a guest in close proximity to the CD is required since the dispersive force diminishes with the reciprocal of the sixth power of distance. Inclusion complexes of α–CD and lower hydrocarbons (methane, ethylene, propane, butane) in solution are formed when the gases are held at a high pressure for several days[28]. The crystalline complexes are very stable for long periods of time and contain 0.6-1.2 mole of gas per mole of CD. Similarly, lower noble gases (helium, neon and argon) do not to form an inclusion complex with α–CD, where the larger members of the group (krypton and xenon) do form inclusions under high pressure [29]. Acetylated cyclodextrins have much steric bulk, and inclusion is difficult to obtain .

EXPERIMENTAL

Instrumentation

A Hewlett-Packard (Avondale, PA, USA) 5890 Series II gas chromatograph equipped with a packed column injection port, flame ionization detector, and a liquid nitrogen cryogenic coolant system was utilized in this study. The injector and detector were set at 200°C. The oven temperature program was 30°C for 2 minutes, then increasing at 7.5°C/minute to 200°C. The program was terminated with the last eluting peak. Data collection was accomplished with a Hewlett-Packard 3396B Series II integrator. Helium was used as the carrier gas for all separations, with a flow rate of approximately 10 mL/minute. The void retention time for the columns was measured with repetitive injections of (150 µL) hydrogen. Hamilton gas tight syringes

were used for all injections.

Stationary Phases

Stationary phases were obtained from Advanced Separation Technologies, Inc. (Whippany, NJ). All separations were accomplished on 40 μm silica supports (preparative HPLC supports). The SPs were: Cyclobond I (CBI), Cyclobond I Acetylated (CBI AC), Cyclobond III (CBIII), Cyclobond III Acetylated (CBIII AC), silica gel, silica gel containing the 6-10 atom epoxy terminated linkage [30][31] used to bond cyclodextrin to silica gel (Epoxy) and CBI with a high stationary phase density (HIGH). Cyclobond I is β-cyclodextrin and Cyclobond III is α-cyclodextrin. SPs were packed into three foot by one eighth inch OD (3'x$^1/_8$"), 2.1 mm ID stainless steel tubing (Supelco, Bellefonte, PA). All columns were prepared by dry packing, using tapping or vibrating to ensure tight packing. Approximately 1.5 grams of stationary phase was packed into each three foot column.

Chemicals

Reagents were obtained from Aldrich Chemical Company, Inc. (Milwaukee, WI): 1,3-butadiene (29,503-5), 1-butene (29,505-1), cis-2-butene (29,507-8), cyclopentane (15,476-8), 2,2-dimethyl butane (D15,140-8), 2,3-dimethyl butane (D15,160-2), 2,3-dimethyl pentane (D17,320-7), 2-methyl pentane (M6,580-7), 2-methyl propene (or isobutylene) (29,546-9) and trans-2-butene (29,508-6); Matheson Gas Company, Inc. (East Rutherford, NJ): propylene; Phillips Petroleum Company (Bartlesville, OK): 2,2-dimethyl propane; Scott Specialty Gases (Plumsteadville, PA): (1000 ppm C_1-C_6 n-alkanes (can mix 236), 100 ppm C_2-C_6 olefins (can mix 222), 10 ppm C_2-C_4 alkynes (can mix 30), 10 ppm branched paraffins (can mix 2), 10 ppm C_4 + isomers (can mix 55) and hydrogen (can 108). Liquids were sampled in their headspace, and gases were sampled directly or from gas sampling bulbs. Approximately 2 μL of headspace above liquids was injected into the GC. Gas mixture injection volumes varied with the concentration of the blend.

RESULTS AND DISCUSSION

Six gas-solid chromatographic stationary phases, along with silica gel as a comparison, were evaluated in terms of retention and separation characteristics of light hydrocarbons. The GSC SPs evaluated were based upon cyclodextrin (CD), either alpha or beta. These phases consisted of three native and two derivatized CD phases along with the hydrolitically stable epoxy terminated linkage which connects CD to the silica gel. SPs were attached to 40 μm (325/400 mesh) spherical silica gel.

The stationary phases were activated at 280-300°C for several hours before testing commenced. Conditioning of the SP removed water and any residual solvent remaining

from the CD bonding step. It was observed that better efficiency occurred after conditioning. Table 1 lists the capacity factors for the compounds by SP. Hydrogen was used as the dead (void) time for all calculations. Native CDs have longer retention times (larger capacity factors, k') than acetylated CDs, with the high surface density β CD (HIGH) having the largest k' values. HIGH had the longest retention times for every compound tested. The data in Table II (K' values, arranged by compound boiling point) indicates that triple bonds are adsorbed stronger than double bonds, which are adsorbed stronger than single bonded materials (like the silica gel SP), and not eluted by boiling point. The trend observed when comparing the data from the silica gel column to the CD phases is the silica gel column had the lowest k' values for saturated compounds, but the k' ratio between silica gel and HIGH significantly decreased as unsaturation was introduced into a compound series (i.e. propane, propene and propyne); CD columns retained unsaturated compounds to a lesser extent then the silica gel column. The SPs tested thus can be considered moderately polar.

Alkanes are not tightly adsorbed on silica gel, and their retention times are minimal. When CDs are bonded to silica gel, the retention times of these non-polar, non-polarizable molecules increase. When the CD density on the surface of the silica gel is increased, the retention time of the alkanes also increases. The interaction of alkanes with CDs must involve a non-polar region, therefore that interaction must dominantly occur in the cavity.

Unsaturated compounds are heavily retained on silica gel SPs. The mechanism involves the acidic silanol groups and the sorbate's polarizable π-bonds. CD SPs bonded to silica gel reduce or eliminate accessible silanol groups, but, alcohol groups are added. Alcohols are less acidic and do not polarize π-bonds as strongly as silanols do and unsaturated compounds are not retained as strongly on CDs as silica gel. The elution order of alkanes, alkenes and alkynes on CD indicates a polar SP, therefore, the retention mechanism of these unsaturated compounds may involve an inclusion process, but also involves the CD's polar alcohol groups.

Smolkova et al. (1982) reported the measurement of a wide range of sorbates from 50 to 80°C on alpha and beta-CD. Two compounds (n-pentane and n-hexane) are in common. Differences in our experiments need be noted : 1) supports - chromosorb W at 60/80 mesh (250 - 177 μm) versus silica gel at 325 mesh (40 μm), 2) coated versus bonded phase, and 3) isothermal versus temperature programming. Hence for pentane, Smolkova et al. reports elution at an adjusted retention time (t_r') of 496 seconds at 80°C, while in this paper the acetylated beta CD (used for comparison since it had the shortest retention time of all the CD phases), had an t_r' of 1100 seconds and elution occurred at approximately 160°C. Berthod et al. (in press)

TABLE I. COMPARISON OF LIGHT HYDROCARBON CAPACITY FACTORS (K') BY STATIONARY PHASE.

Hydrocarbons	BP(°C)	Silica	Epoxy[a]	CBIII[b]	CBIIIAC[c]	CBI[d]	HIGH[e]	CBIAC[f]
Hydrogen	-252.8	0.00	0.00	0.00	0.00	0.00	0.00	0.00
Methane	-161.4	0.69	0.70	0.85	0.83	0.85	0.92	0.76
Ethane	-88.6	3.87	4.12	5.37	5.13	5.43	6.42	4.67
Propane	-42.1	9.68	10.15	12.35	11.79	12.47	14.29	11.18
Butane	-0.5	15.90	16.46	19.02	18.25	19.23	21.55	17.55
Pentane	36.1	21.23	21.87	24.59	23.76	24.87	27.56	22.98
Hexane	69.0	25.79	26.55	29.40	28.58	29.72	32.94	27.75
Ethene	-103.7	7.03	5.20	5.90	5.33	6.12	8.33	4.68
Propene	-47.7	15.28	12.96	14.27	13.28	14.47	17.25	12.37
1-Butene	-6.3	20.48	18.56	20.29	19.31	20.51	23.47	18.38
1-Pentene	30.1	24.86	23.39	25.45	24.52	25.70	28.93	23.55
1-Hexene	63.5	29.01	27.86	30.13	29.25	30.43	34.80	28.25
Acetylene	-84.0	11.58	8.85	9.20	8.77	9.35	12.01	7.70
Propyne	-23.2	23.26	19.27	19.87	18.77	20.06	23.55	17.29
1-Butyne	8.1	27.45	23.48	24.35	23.47	24.55	28.41	22.06
2-Butyne	27.0	31.78	27.22	27.84	26.63	27.99	32.29	24.97
Isobutane	-11.7	14.99	15.45	17.91	17.37	18.10	20.15	16.56
2,2-Dimethyl propane	9.5	19.29	19.59	22.05	21.60	22.24	24.28	20.69
2-Methyl butane	27.9	20.61	21.18	23.85	23.25	24.10	26.62	22.32
2,2-Dimethyl butane	49.7	24.59	25.04	27.70	27.24	27.93	30.37	26.24
2-Methyl pentane	60.3	25.25	25.93	28.74	28.16	29.02	31.96	27.15
3-Methyl pentane	63.3	25.25	25.93	28.74	28.16	29.02	31.96	27.15
Isobutane	-11.7	14.98	15.44	17.90	17.37	18.10	20.16	16.53
N-butane	-0.5	15.94	16.45	19.04	18.41	19.26	21.56	17.54
Isobutylene	-6.9	21.86	19.11	20.65	19.85	20.86	24.14	18.68
1-Butene	-6.3	20.78	18.47	20.65	19.85	20.86	23.47	18.68
Cis 2-butene	3.7	22.20	19.64	21.32	20.54	21.52	24.56	19.36
Trans 2-butene	0.9	22.20	19.64	21.32	20.54	21.52	24.56	19.36
1,3-Butadiene	-4.4	22.63	19.57	21.40	20.71	21.72	25.32	19.45
1-Butyne	8.1	28.01	23.37	24.32	23.44	24.55	28.38	22.03
Cyclopentane	49.3	21.34	22.15	24.89	24.47	25.07	27.09	23.69
2,3-Dimethyl butane	58.0	25.06	25.65	28.45	27.89	28.73	31.44	27.02
2,3-Dimethyl pentane	89.8	29.20	29.87	33.12	32.50	33.52	38.01	31.45

[a]Epoxy terminated 6-10 atom linkage connecting CD to silica gel. [b]CBIII is native α–CD bonded to silica gel. [c]CBIIIAC is acetylated α–CD bonded to silica gel. [d]CBI is native β–CD bonded to silica gel. [e]HIGH is a high density surface coverage β-CD on silca gel (2-3 times more coverage than CBI). [f]CBIAC is acetylated β–CD bonded to silica gel.

reported a strong mechanistic temperature dependence in derivatized CD liquid SPs; the same compound could have different retention mechanisms at different temperatures, and these mechanisms are determined case by case. Smolkova et al. reports a factor of 50-100 difference for t_r' on alpha (larger t_r') and beta-CD for

TABLE II. COMPARISON OF LIGHT HYDROCARBON CAPACITY FACTORS (K') BY STATIONARY PHASE AND BOILING POINT (°C).

Hydrocarbons	BP(°C)	Silica	Epoxy[a]	CBIII[b]	CBIIIAC[c]	CBI[d]	HIGH[e]	CBIAC[f]
Hydrogen	-252.8	0.00	0.00	0.00	0.00	0.00	0.00	0.00
Methane	-161.4	0.69	0.70	0.85	0.83	0.85	0.92	0.76
Ethene	-103.7	7.03	5.20	5.90	5.33	6.12	8.33	4.68
Ethane	-88.6	3.87	4.12	5.37	5.13	5.43	6.42	4.67
Acetylene	-84.0	11.58	8.85	9.20	8.77	9.35	12.01	7.70
Propene	-47.7	15.28	12.96	14.27	13.28	14.47	17.25	12.37
Propane	-42.1	9.68	10.15	12.35	11.79	12.47	14.29	11.18
Propyne	-23.2	23.26	19.27	19.87	18.77	20.06	23.55	17.29
Isobutane	-11.7	14.99	15.45	17.91	17.37	18.10	20.15	16.56
Isobutylene	-6.9	21.86	19.11	20.65	19.85	20.86	24.14	18.68
Butene	-6.3	20.78	18.47	20.65	19.85	20.86	23.47	18.68
1,3-Butadiene	-4.4	22.63	19.57	21.40	20.71	21.72	25.32	19.45
Butane	-0.5	15.90	16.46	19.02	18.25	19.23	21.55	17.55
Trans 2-butene	0.9	22.20	19.64	21.32	20.54	21.52	24.56	19.36
Cis 2-butene	3.7	22.20	19.64	21.32	20.54	21.52	24.56	19.36
1-Butyne	8.1	27.45	23.48	24.35	23.47	24.55	28.41	22.06
2,2-Dimethyl propane	9.5	19.29	19.59	22.05	21.60	22.24	24.28	20.69
2-Butyne	27.0	31.78	27.22	27.84	26.63	27.99	32.29	24.97
2-Methyl butane	27.9	20.61	21.18	23.85	23.25	24.10	26.62	22.32
1-Pentene	30.1	24.86	23.39	25.45	24.52	25.70	28.93	23.55
Pentane	36.1	21.23	21.87	24.59	23.76	24.87	27.56	22.98
Cyclopentane	49.3	21.34	22.15	24.89	24.47	25.07	27.09	23.69
2,2-Dimethyl butane	49.7	24.59	25.04	27.70	27.24	27.93	30.37	26.24
2,3-Dimethyl butane	58.0	25.06	25.65	28.45	27.89	28.73	31.44	27.02
2-Methyl pentane	60.3	25.25	25.93	28.74	28.16	29.02	31.96	27.15
3-Methyl pentane	63.3	25.25	25.93	28.74	28.16	29.02	31.96	27.15
Hexene	63.5	29.01	27.86	30.13	29.25	30.43	34.80	28.25
Hexane	69.0	25.79	26.55	29.40	28.58	29.72	32.94	27.75
2,3-Dimethyl pentane	89.8	29.20	29.87	33.12	32.50	33.52	38.01	31.45

[a]Epoxy terminated 6-10 atom linkage connecting CD to silica gel. [b]CBIII is native α–CD bonded to silica gel. [c]CBIIIAC is acetylated α–CD bonded to silica gel. [d]CBI is native β–CD bonded to silica gel. [e]HIGH is a high density surface coverage β-CD on silca gel (2-3 times more coverage than CBI). [f]CBIAC is acetylated β–CD bonded to silica gel.

pentane, and attributes this to the tighter inclusion complex formed in alpha-CD rather than beta-CD. With the conditions operative in this study, little difference in retention times was observed for compounds tested on alpha and beta-CD. At the higher elution temperatures of this study, a tight inclusion complexation may play a minimal role in retention. The SP polarity (apolar cavity) may be a more dominant mechanism than the actual inclusion complex mechanism.

Smolkova-Keulemansova et al. (1985) reported large differences in the retention times of isomers (branched versus straight chained) on alpha, but not beta CD. This again was attributed to the cavity size; the branched alkane was prohibited by size from entering the alpha-CD's cavity, and was less retained than the straight chain alkane which could form an inclusion complex. Smolkova-Keulemansova et al. found that branched nonanes eluted before n-heptane, even though the nonanes had a higher boiling point. In our studies, the elution time of branched versus straight chained aliphatic isomers occurred by boiling point (silica gel and none polar SPs have the same trend). Smolkova-Keulemansova et al. partially methylated (66%) CDs, and found that the large differences in retention times between branched and linear hydrocarbons was diminished. Steric effects of the methyl groups, thereby decreasing cavity accessibility, was used to explain this decreased separation.

Acetylating CDs decreases the accessibility of the cavity and decreases the SP polarity. Acetylated CDs have shorter retention times than native CDs. This can be explained by steric effects for alkanes (decreasing accessibility will decrease non-polar/non-polar interactions and result in a decreased retention time. The unsaturated compounds retention times were also decreased. Again, a decreased accessibility to the cavity can be a factor, but also a decrease in the number of alcohol groups (π-interactions) can be important in the overall mechanism.

Bonding the epoxy chain to the CD results in two factors. First, for the alkanes, the epoxy group decreases SP polarity, so, compared with the silica gel column, alkanes are adsorbed stronger. This decrease in SP polarity is still minimal compared with the apolar CD cavity and the retention times on the Epoxy column are considerably shorter than the retention times on the native CD columns. Secondly, the epoxy group decreases the number and accessibility of the silanol groups, which makes the unsaturated compounds elute faster then they would on the silica gel column.

Bonding CD to the polar silica gel support decreases that supports polarity. This modification of the surface polarity changes adsorption strengths and hence column selectivities vary. This phenomena of differing selectivities between CDs and silica gel leads to gas mixtures separable on CDs but not on silica gel. Figures 1 and 2 show this selectivity difference where HIGH (Figure 1) separates C_1-C_6 paraffins from C_2-C_6 1-alkenes but an analogous silica gel (Figure 2) column does not completely resolve all peaks.

CD bonded to silica gel allows for differing selectivities in regards to lower hydrocarbons. A dual retention mechanism is a factor in the separation of these compounds. Alkanes are retained through an interaction with the apolar cavity, while unsaturated molecules can interact with the cavity and/or through the alcohol groups

on the CDs. Separation of geometric isomers is inadequate, which should be a CD strength. New approaches are being tested to improve the generality and selectivity of the CD columns.

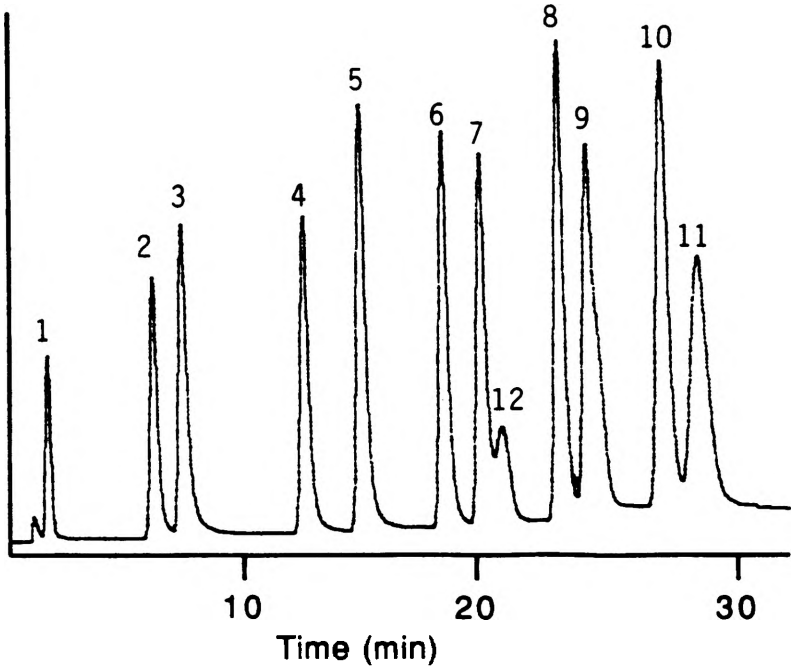

Figure 1. Chromatogram of C_1-C_6 n-alkanes and C_2-C_6 1-alkenes on HIGH. Temperature program : 30°C for 2 minutes, ramp at 7.5°C/minute to 200°C. 1, methane; 2, ethane; 3, ethene; 4, propane; 5, propene; 6, butane; 7, butene; 8, pentane; 9, pentene; 10, hexane; 11, hexene; 12, impurity.

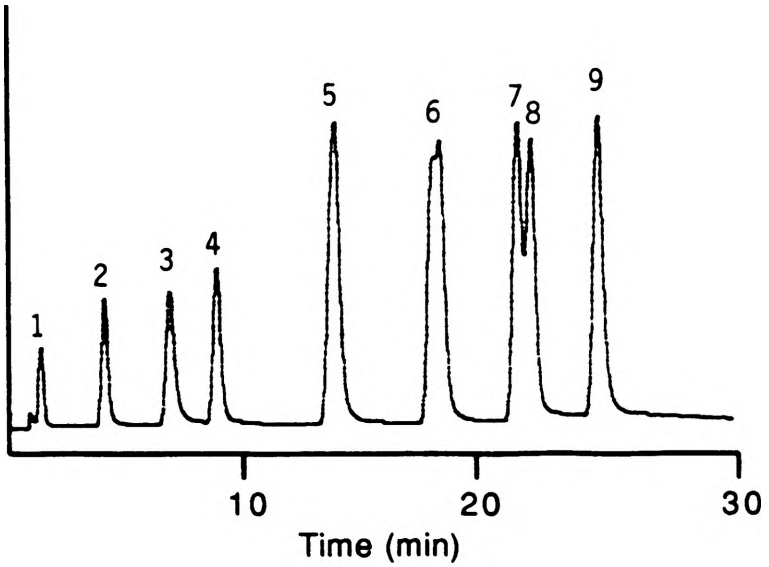

Figure 2. Chromatogram of C_1-C_6 n-alkanes and C_2-C_6 1-alkenes on Silica gel. Temperature program : 30°C for 2 minutes, ramp at 7.5°C/minute to 200°C. 1, methane; 2, ethane; 3, ethene; 4, propane; 5, propene/butane; 6, butene/pentane; 7, pentene; 8 hexane; 9, hexene.

ACKNOWLEDGMENTS

I would like to thank the University of Missouri - Rolla concerning the undergraduate research funding and Dr. Daniel W. Armstrong for allowing my participation in his research group over the past several semesters. A special thanks goes to George Reid for his insight and assistance in the completion of this project.

REFERENCES

1 A.J.P. Martin and R.L. Synge, *Biochem. J.*, 35 (1941) 1358.

2 C.F. Poole and S.A. Schuette, *Contemporary Practice of Chromatography*, Elsevier Science Publishing Co., New York, 1984, p. 72.

3 L.S. Ettre and J.E. Purcell, *Adv. Chromatogr.*, 10 (1974) 1.

4 R.G. Mathews, J. Torres and R.D. Schwartz, *J. Chromatogr.*, 199 (1980) 97.

5 W. Schneider, J.C. Frohne and H. Bruderreck, *J Chromatogr,* 155 (1978) 311.

6 N. Brenner and V.J. Coates, *Nature*, 181 (1958) 1401.

7 B.T. Whitman, *Nature*, 182 (1958) 391.

8 S.A. Greene, M.L. Moberg and E.M. Wilson, *Anal. Chem.,* 28 (1956) 1369.

9 S.A. Greene and H. Pust, *Anal. Chem.,* 29 (1957) 1055.

10 H.N. Morrow and K.B. Buckley, *Petrol. Refiner.,* 36 (1957) 157.

11 O.L. Hollis, *Advances in Gas Chromatography 1965,* A. Zlatkis and L.S. Ettre, eds., Preston Technical Abstracts Co., Evanston, 1966, p. 56.

12 O.L. Hollis, *Anal. Chem.,* 38 (1966) 309.

13 O.L. Hollis and W.V. Hayes, *J. Gas Chromatogr.*, 4 (1966) 235.

14 W.F. Wilhite and O.L. Hollis, *J. Gas Chromatogr.,* 6 (1968) 84.

15 C.N. Jones, *Anal. Chem.,* 39 (1967) 1858.

16 H.W. Patton, J.S. Lewis and W.I. Kaye, *Anal. Chem.*, 27 (1955) 170.

17 S. Ohksoshi, Y. Fujita, and T. Kwan, *Shokubai*,15 (1958) 1.

18 N.H. Ray, *J. Appl. Chem.*,4 (1954) 21.

19 A.B. Littlewood, *Gas Chromatography Principles, Techniques, and Applications*, Academic Press, New York, 1970, p. 431.

20 E. Smolkova-Keulemansova, *J. Chromatogr.*, 251 (1982) 17.

21 W.Y. Li, H.L. Jin and D.W. Armstrong, *J. Chromatogr.*, 509 (1990) 303.

22 D.W. Armstrong, W. Li, A.M. Stalcup, J.I. Seeman, H.V. Secor, R.R. Izac, *Anal. Chim. Acta.*, 234 (1990) 365.

23 D.W. Armstrong, W. Li, C.D. Chang and J. Pitha, *Anal. Chem.*, 62 (1990) 914.

24 W.A. Konig, R. Krebber and P. Mischnick,*J. High Res. Chromatogr.*,12 (1989) 732.

25 E. Smolkova-Keulemansova, L. Feltl and S. Krysl, *J. Inclusion Phenomena*, 3 (1985) 183.

26 E. Smolkova, H. Kralova, S. Krysl and L. Feltl, *J. Chromatogr.*, 241 (1982) 3.

27 A. Berthod, W. Li and D.W. Armstrong, *Anal. Chem.*, In Press.

28 F. Cramer and F.M. Henglein, *Angew. Chem.*, 68 (1956) 649.

29 F. Cramer and F.M. Henglein, *Chem. Ber.*, 90 (1957) 2572.

30 D.W. Armstrong, US Patent No. 4,359,399 (1985).

31 D.W. Armstrong and W. Demond, *J. of Chromatogr. Sci.*, 22 (1984) 411.

THE SYNTHESIS AND CHARACTERIZATION OF METAL BINDING POLYMERS CONTAINING 2, 2'-BIIMIDAZOLE

Proctor, R.A. Department of Chemistry

ABSTRACT

Epoxides are known to form ring-opened polymer products that have demonstrated improved material strength, high heat stability, and chemical resistance as adhesives, coatings, and molding materials. It has been suggested that imidazoles can be used in the catalysis of this polymerization, and that the pyridyl nitrogen of the imidazole ring participates in epoxy ring-opening and is then incorporated in the polymeric structure. This study was conducted to test this theory of the role of pyridyl nitrogen in the reaction of 1,1'-dihydroxyethyl-2,2'-biimidazole (HEB) and metal-HEB complexes with the diglycidyl ether of bisphenol A (DGEBA). Of particular interest in this study is that HEB also exhibits two alcohol functionalities which are known to induce epoxy ring-opening and that HEB also forms an alkoxide ion adduct which promotes chain growth. DSC and IR were used to monitor the reactions of HEB and its metal complexes with DGEBA. These studies support the conjecture that the pyridyl nitrogen participates in epoxide ring-opening. They also suggest that the pyridyl nitrogen ring-opening is the first reaction, followed by the formation of the alkoxide adduct formation and the hydroxyethyl group etherification. NMR and GPC were employed to further characterize the polymer formed. NMR results varified the proposed polymer structure, and molecular weight determination by GPC showed a high molecular weight, highly cross-linked polymer product.

INTRODUCTION

Epoxides are known to form epoxide ring-opened polymer products in the presence of various reactive organic compounds such as acids (anhydrides), amines, alcohols and phenolics. These polymer products have found significant utility as adhesives, polymeric coating materials, and

molding materials and have demonstrated improved material strength, high heat stability, and chemical resistance in these capacities.

Among known catalysts for the ring-opening and subsequent homopolymerization of epoxy compounds are imidazoles. Imidazoles are added to initiate esterification reactions in epoxy-anhydride systems, are used to catalyze specific epoxy-phenolic hydroxyl reactions, and are used as hardeners in a variety of commercial epoxy resin systems.

Previous investigations [1-3] on epoxy/imidazole systems have put forth some general conclusions about the formation of epoxy/imidazole adducts. As can be seen in Figure 1, these conclusions say that for a 1:1 epoxy/imidazole reaction in which the imidazole is a 1-unsubstituted imidazole, both a 1:1 hydroxide (OH) adduct and a 2:1 alkoxide (O-) adduct are formed. In these reactions, the imidazole becomes a part of the polymeric structure. In fact, in the formation of the 2:1 alkoxide (O-) adduct it has been suggested that the pyridyl nitrogen of the imidazole ring participates in epoxy ring-opening and is then incorporated in the polymeric structure.

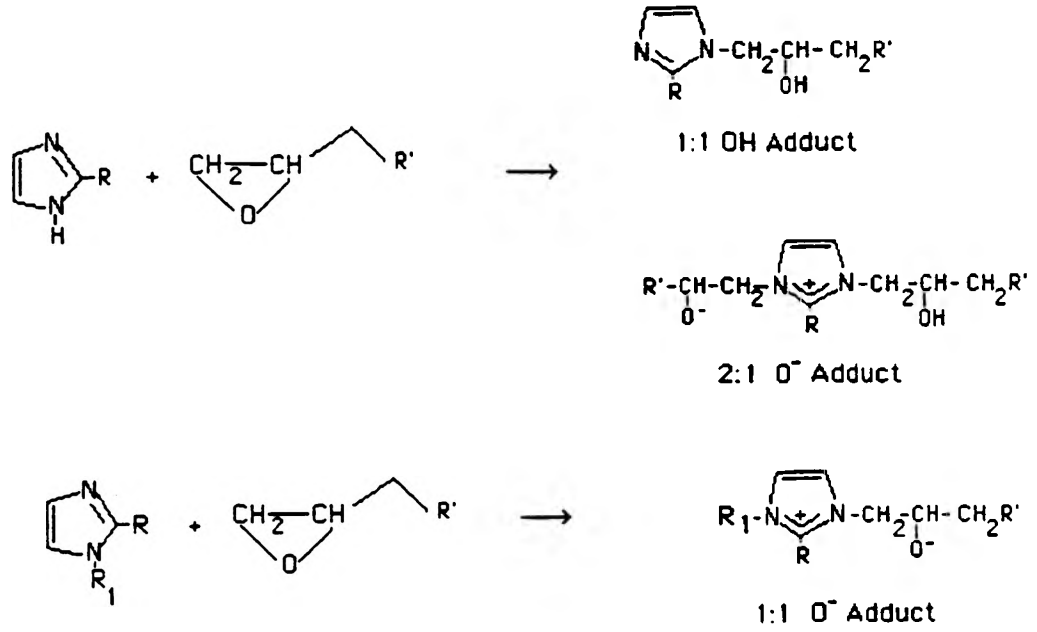

Figure 1. Imidazoles as Epoxy Catalysts.

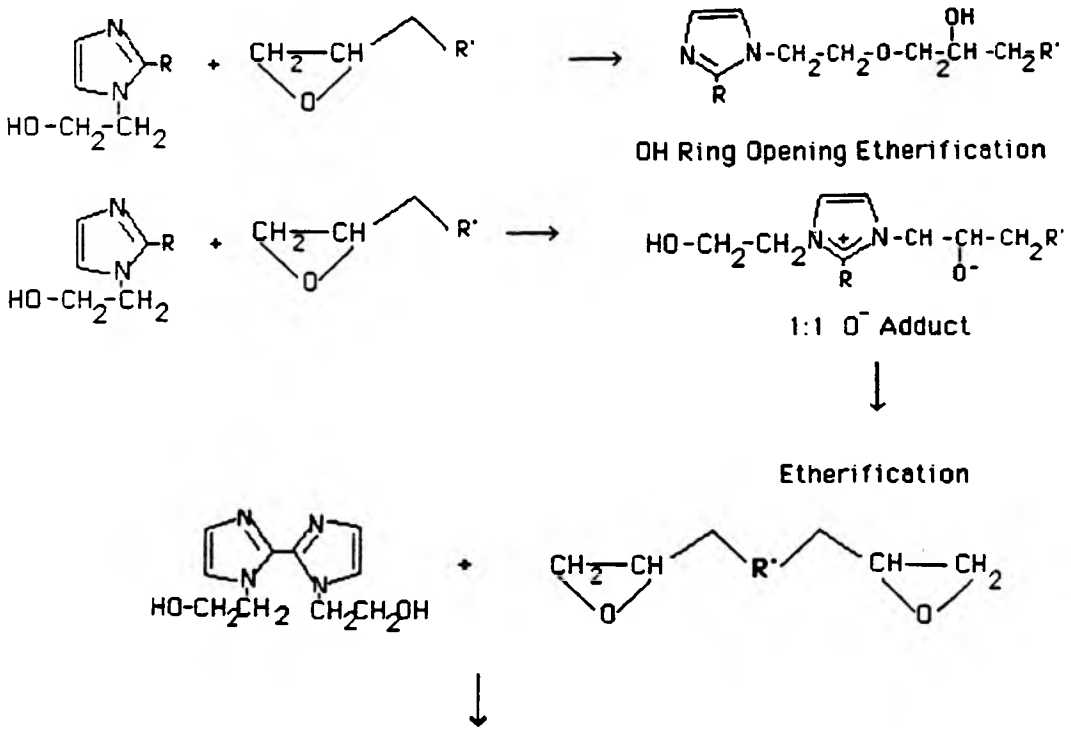

Figure 2. 1-Substituted Imidazole Epoxide Catalyst.

In a similar fashion, the formation of a 1:1 alkoxide (O-) adduct is expected for 1-substituted imidazole/epoxide reactions. In this case the pyridyl nitrogen is again utilized in the adduct formation.

Suppose the 1-substitution on the imidazole is a hydroxyl ethyl group as suggested by Figure 2. Then one must not only consider the previously mentioned 1:1 alkoxide adduct formed by epoxy ring-opening by the pyridyl nitrogen of imidazole, but one must also consider the possibility of the formation of a 1:1 imidazole/hydroxy ether adduct via hydroxyethyl ring-opening.

Subsequent to the formation of these adducts, which have been proposed to occur rapidly and initially, is the etherification reaction, which results in chain growth via OH-etherification and O-etherification reactions.

Another important consideration is that the alkoxide ion is highly reactive, and once placed in such a situation, will promote the O-etherification reaction.

The question posed by this phase of the investigation is: "is it possible to observe some discernment in the reaction of 1,1'-dihydroxyethyl-2,2'-biimidazole (HEB) with diepoxides?" For example, can the formation of the imidazole pyridyl nitrogen-epoxy adduct and the formation of the hydroxyethyl-epoxy adduct be observed? Can the proposed etherification reactions be observed? And what is the metal ion effect when it is used to block the pyridyl nitrogen sites?

I plan to discover the role of HEB, nickel-HEB, and cobalt-HEB (HEB, Ni-HEB, and Co-HEB respectively), complexes in reactions with the diglycidyl ether of bisphenol A, or DGEBA. If it is expected that there is an ordering of reactive groups for this and related reactions, then one might expect that the thermal monitoring of this reaction as a function of temperature may provide insight to what actually occurs.

In this particular case, the reaction order was expected to proceed as follows: the epoxide ring opening with the formation of the imidazole ring pyridyl nitrogen-epoxy alkoxide adduct; and the more rapid reaction of the alkoxide adduct with epoxide groups as well as the hydroxyethyl group ring-opening etherification.

It is proposed that if the pyridyl nitrogen sites are occupied by a transition metal ion, then the principle reaction should be the hydroxyethyl group ring-opening etherification.

EXPERIMENTAL

Materials and Reagents: The epoxide used in this study, the diglycidyl ether of bisphenol A (DGEBA), was obtained from DAJAC Laboratories, Incorporated and was utilized without further purification.

Purification of HEB: The first problem confronted in this experiment was the task of purifying the 1,1'-dihydroxyethyl-2,2'-biimidazole. Testing a sample to determine its purity entailed a simple thin layer chromatographic analysis. First the sample of the crude HEB was dissolved in methanol and was dotted on a 1x6 inch thin layer chromatography silica plate. Once dry, it was placed in a covered graduated cylinder and allowed to develop for approximately 90 minutes to 2 hours in an 8:3:1 hexane : propanol : ethanol solvent mixture. The crude HEB was found to resolve into two basic components: mono-substituted HEB and the desired di-substituted HEB.

It was decided to employ flash chromatography in the purification process. After a lot of procedures were tried and sample purity was tested by the procedure outlined above, a sketchy method of purification was developed that gave consistently pure HEB. First, approximately 0.5 g of the crude HEB was dissolved in methanol. This often required a little heating, and usually, there was some insoluble solid present that was assumed to be impurities and was filtered out of the solution. Second, the flash chromatography column was rinsed with 8:3:1 hexane : propanol : ethanol solvent mix. Next, the dissolved HEB was introduced to the column and pumped down into the silica. Then the HEB mixture was chased through with the 8:3:1 solvent mix until pure white silica became discolored. At this point, the solvent was switched to methanol and the methanol was pumped through the column. A distinct yellow band was observed to form and move slowly down the silica column. This band contained the pure, golden HEB. The methanol wash was continued until the band reached the bottom of the column. Now, in a separate vial, the pure product was able to be collected by continuing the methanol strip until the yellow band was gone, and approximately 30 mL of the liquid was collected beyond that point. Finally, the methanol was allowed to evaporate in a beaker so that only the pure HEB sample remained.

Thermal Analysis: From the purified HEB, Ni-HEB, and Co-HEB samples, 1:1 molar HEB : DGEBA reaction samples were prepared in vials. These samples were weighed out on a Mettler PM460 Tare Scale. They were then mixed with a spatula, and stored under Argon gas in a 6° to 8° Celsius refrigerator. These precautions were taken to ensure a moisture and heat-free atmosphere so that no reactions occurred during storage.

Thermal analysis of the samples involved monitoring by Differential Scanning Calorimetry, or DSC. Five milligrams of the previously prepared reaction mixture were placed in aluminum sample pans and covered with a lid. These samples were placed in the Perkin-Elmer DSC-4 and scanned between 50° and 250° Celsius under a nitrogen atmosphere at a heat rate of 20 degrees per minute. They were then analyzed and sent to the printer. Four samples of each of the three reaction mixtures were ran to ensure reproducibility.

Fourier Transform Infrared Spectroscopy: A thin film of the HEB reaction mixture (prepared as described in the thermal analysis section) was cast with MEK onto each of three NaCl salt plates according to the procedure used by Heise and Martin [3]. One plate was not heated, one was

heated for five minutes and the third was heated for 20 minutes in a 180° oven. They were then all quenched cool in a 6° to 8° C refrigerator, and, once cool, were scanned by a Perkin-Elmer Model 1750 Fourier transform infrared spectrometer, or FTIR, under a dry air purge. Peak assignments and percent transmittances were printed out for each plot. The transmittance peaks were identified according to the previous work by Stevens [4].

This procedure was repeated for the NiHEB and the CoHEB reaction mixtures.

Nuclear Magnetic Resonance Spectroscopy: A well mixed 1:1 molar HEB : DGEBA sample was prepared in an NMR tube. The reaction mixture was cooked in a 180° oven for 20 minutes and allowed to cool. DMSO was added to the NMR tube, partially dissolving a portion of the polymer product. NMR spectra were obtained for the polymer with a JEOL FX-100 Fourier transform nuclear magnetic resonance spectrometer at room temperature, using TMS as an external standard.

This procedure was repeated for the NiHEB and the CoHEB reaction mixtures.

Gel Permeation Chromatography: GPC samples were prepared by mixing a 1:1 molar HEB : DGEBA sample in a sample vial, cooking the sample for 20 minutes in a 180°C oven, and then adding enough DMF to form a .3% solution (given that all the sample had dissolved). The molecular weights of the soluble portions were measured with a modified-component high pressure liquid chromatography (HPLC) system which was calibrated with narrow molecular weight distribution polystyrene samples.

This procedure was repeated for the NiHEB and the CoHEB reaction mixtures.

RESULTS AND DISCUSSION

Thermal Analysis: The monitoring by DSC of HEB, NiHEB, and CoHEB with DGEBA is illustrated in Figure 3. The endotherm for the HEB-DGEBA reaction is presumably due to the heat of reaction required for the pyridyl nitrogen to initiate ring-opening. The wide exotherm thereafter, at about 150°C, is thought to account for the alkoxide and hydroxyethyl reactions with epoxide. Compare this to the DSC scans obtained for the reactions of NiHEB and CoHEB with DGEBA, which clearly show a single exotherm at approximately 200°C and 250°C respectively. Since, in the case of the

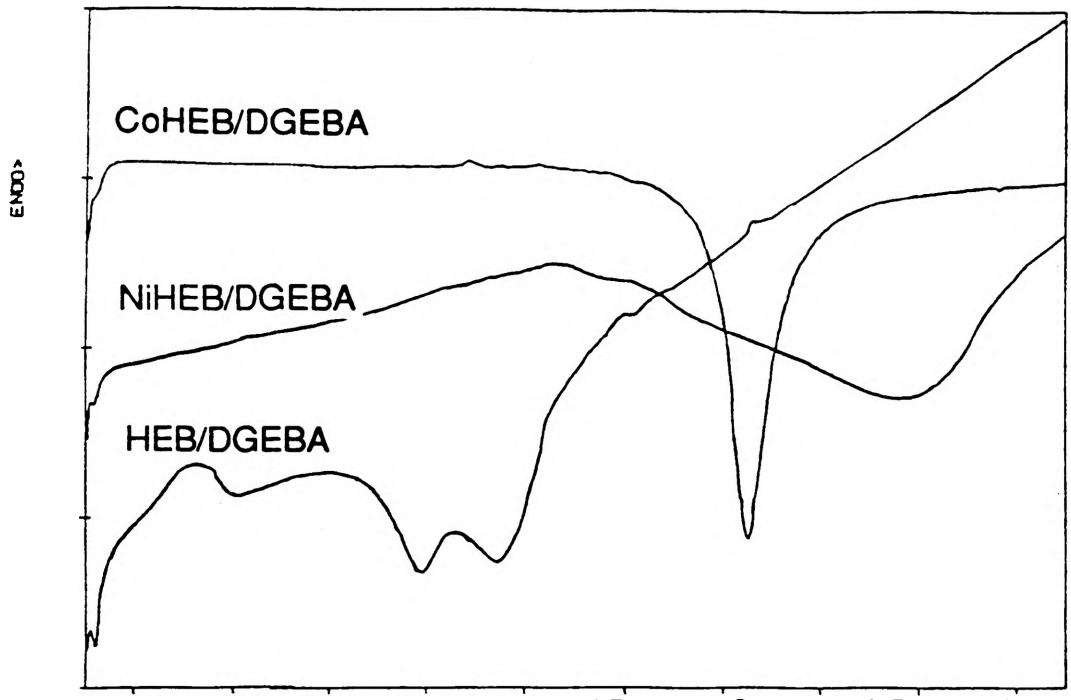

Figure 3. DSC Monitoring of HEB, NiHEB, and CoHEB/DGEBA Reactions

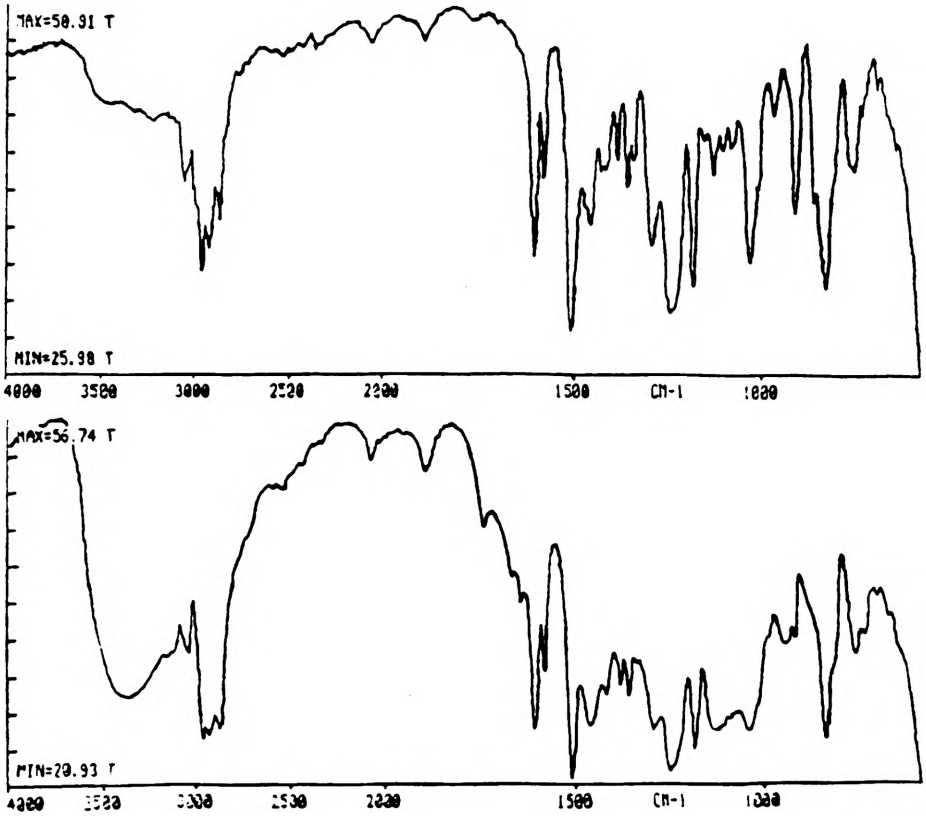

Figure 4. IR Spectra of HEB/DGEBA Before and After Polymerization

metal HEB molecules, the pyridyl nitrogen has been blocked, this single peak is due to the reaction of the hydroxyethyl group with the diepoxide.

Fourier Transform Infrared Spectroscopy: In the next phase of the experiment, the three samples of each reaction mixture were heated at time intervals of 0, 5, and 20 minutes in a 180° C oven and scanned by FTIR after each period. The intention was to catch the reaction in various stages towards completion. The change in the reaction mixture, however, could be seen best when comparing the 0 and 20 minute samples of each reactant/product pair.

The infrared examination of the mixture of HEB and DGEBA before the reaction is shown at the top of Figure 4. The epoxy peak can be seen here at approximately 916 cm^{-1}, and at the end of the 20 minute period, the scan for which is shown at the bottom of this figure, the reaction is completed and the epoxide is gone as expected. Note also the band assignments at 1670, the C=N, and the broad band appearing in the 3200 to

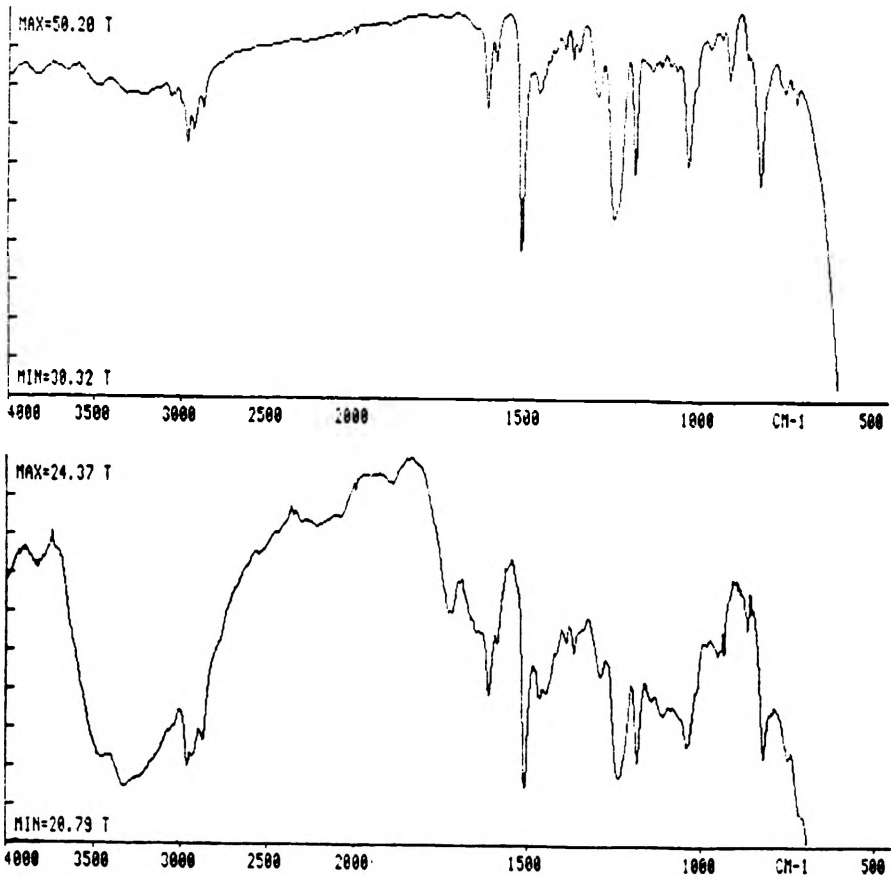

Figure 5. IR Spectra of NiHEB/DGEBA Before and After Polymerization

3400 cm^{-1} region, the N-H stretching region of the 1-substituted imidazole, as proof of the incorporation of HEB into the polymeric network. This band is especially exciting since the substance scanned initially is believed to be only DGEBA since the reaction mixture was rather heterogeneous. The growth of this peak from the initial to the final scans is further proof of the incorporation of the biimidazole in the polymer.

The FTIR scans in Figures 5 and 6 show similar results for the reaction of NiHEB and CoHEB with DGEBA. Before heating for 20 minutes in the 180° C oven, an epoxy peak can be observed at 915 cm^{-1} , but after the heating, the peak is gone and the reaction is complete. These FTIR results help to justify that the expected is occurring, and it is producing an epoxy ring-opened product.

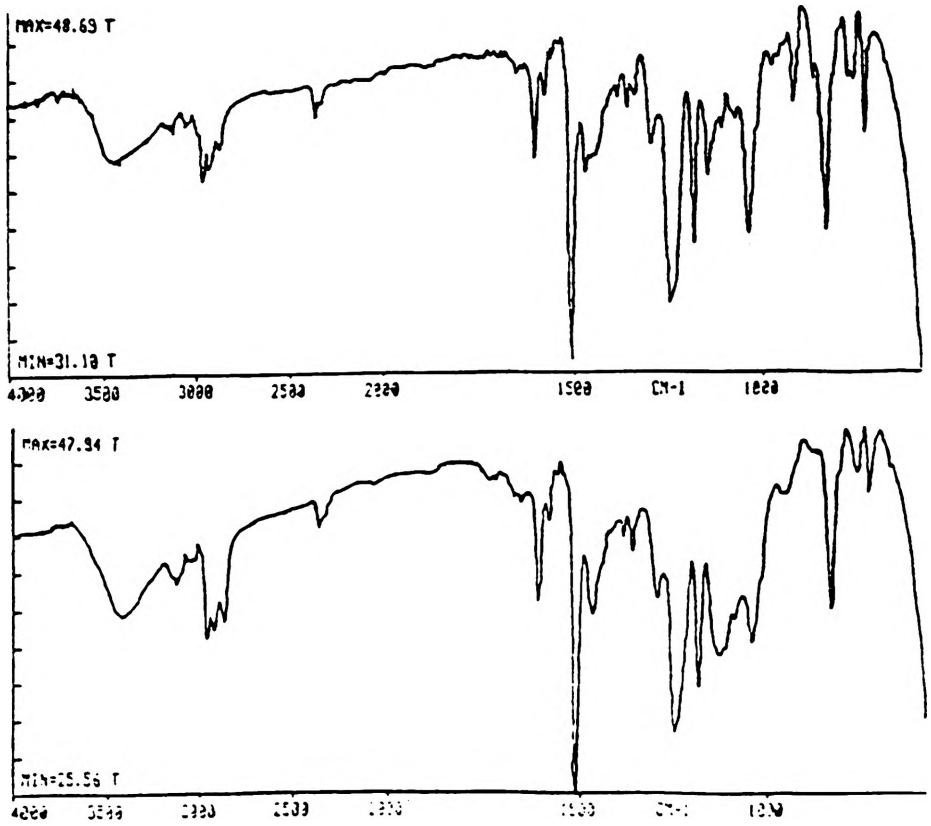

Figure 6. IR Spectra of CoHEB/DGEBA Before and After Polymerization

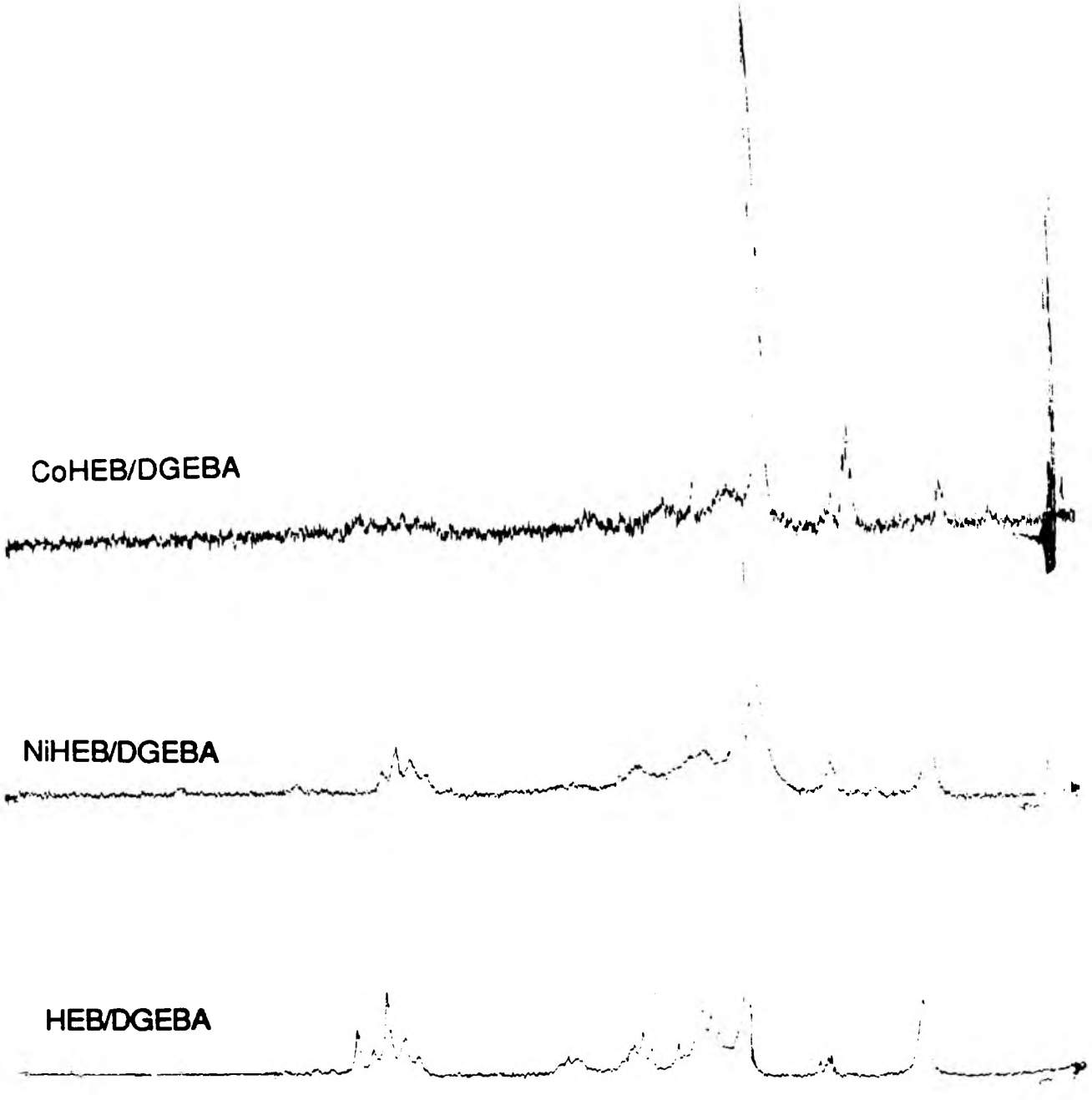

Figure 7. NMR Spectra of HEB, NiHEB, and CoHEB/DGEBA Reactions

Once again the C=N can be observed at 1670 and the broad 1-substituted imidazole band can be observed between 3200 and 3400 cm-1 as the metal HEB is incorporated into the final polymeric structure.

Nuclear Magnetic Resonance Spectroscopy: The proton NMR analysis of the HEB/DGEBA, the NiHEB/DGEBA, and the CoHEB/DGEBA reaction products is illustrated in Figure 7. Chemical shifts due to various functional groups such as those observed at approximately 1.3ppm (epoxy), 3.1ppm (methyl), 3.6ppm (o-methylene), 4.2ppm (N-methylene), and 6.6-7.2ppm (aromatic) proved that the suspected polymer products were being formed.

Gel Permeation Chromatography: The HEB/DGEBA polymer was tested and proved to insoluble in the eluting solvent, DMF. This is proof of a high molecular weight, highly crosslinked polymer.

CONCLUSIONS

So far, by blocking the pyridyl nitrogen sites of HEB with nickel and cobalt, support has been given to the conjecture that the pyridyl nitrogen participates in epoxide ring-opening. An order of reaction for the different functional groups has also been proposed. The product proved to be polymeric in nature, and qualitative nuclear magnetic resonance proved that the expected reactions were occurring by observation of the expected functional group peaks. Finally, the polymer has proven to be minimally soluble in DMF so it is assumed to be a high molecular weight, highly crosslinked species.

Future plans include the expansion of the study to reactions with other diepoxides to witness if the reaction proceeds in a similar manner as described here. Also, this polymer needs to be produced in larger quantities and tested for macromolecular properties such as polymer hardness and adhesion. Such tests may prove this highly crosslinked polymer to be an improvement over currently used epoxy systems in the epoxy paint industry.

ACKNOWLEDGEMENTS

I would like to thank Dr. Harvest Collier, my undergraduate research advisor for all his help and patience. I would also like to thank Mr. Rick Elmer and Mr. Mark Barnett for instructing me on the analytical techniques used during the course of this project.

REFERENCES

[1] Barton, J.M.; Shepard, P.M. Makromol. Chem. 1975, 176, 919.

[2] Dearlove, T.J. Appl. Polym. Sci. 1970, 14,1615.

[3] Heise, M.S.; Martin, G.C. Macromolecules 1989, 22, 99. Syracuse University.

[4] Stevens, G.C. J. of Appl. Polym. Sci. 1981, 26, 426.

HEAD-SPINE FINITE ELEMENT COMPUTER MODEL ON A WORK-STATION

Kay F. Schilli
Department of Mechanical and Aerospace Engineering
and Engineering Mechanics
University of Missouri - Rolla
Rolla, MO 65401

ABSTRACT

In this project, the head-cervical spine finite element computer model has been modified and made portable on the Apollo work-station. The program was developed to aid the researcher in analyzing the simulated behavior of the human spine. The modifications in the computer program have been made in order to utilize the finite element code for continuation of further research.

INTRODUCTION

The spine is the basic structural element that transmits the forces experienced by the upper body and head in daily living. The interaction of the spine with the upper body involves substantial flexure, which in some situations, may lead to injury. This investigation of the spine has attracted much attention.

In recent years, mathematical modelling has been widely used where biological structures had to be investigated to avoid violation of bioethical codes and practice humane treatment of animal and human subjects. The investigation of the human head-spine complex has evolved in stages which are customarily classified into continuous and discrete models. Toth [1] developed an eight degree of freedom model consisting of

rigid masses representing vertebrae and springs and dampers representing inter-vertebral discs. Orne and Liu [2] proposed the first model that included the shear and bending resistance of the intervertebral disc. The first continuum model was proposed by Hess [3], who included only axial response. Subsequently, Moffatt, et al. [4] included both axial and bending response by using a beam type model. However, the analysis was restricted to small displacements. Recently, Liu and Ray [5] developed bar-beam models, including large displacements in the analyses. The stiffness properties of this model were based on that of the isolated, ligamentous spine and the responses they exhibited demonstrated very large deflections.

The model studied and reported here represents the human body by a collection of rigid bodies interconnected by deformable elements. The rigid bodies are used for the modelling of bones, while the deformable elements are used to model ligaments, muscles, and connective tissues. The treatment of bones as rigid bodies is preferable since the stiffness of bones is usually orders of magnitudes greater that of connective tissue.

MATHEMATICAL MODEL

The computer procedure is basically a matrix structural analysis technique, which serves as a framework for constructing the equations of motion. The program enables these equations of motion to be integrated in time by either explicit or implicit techniques, or analyzed by modal procedures, which give the natural frequencies and modes of the model. The formulation is completely three dimensional and treats arbitrarily large rotations and displacements of the rigid bodies. However, the deformation of some of the elements is restricted to be moderately small. Material properties may be linear or nonlinear and linear viscous forces can be included.

Two types of nodes are used:

a) primary nodes, each of which has six degrees of freedom consisting of three translations and three rotations; the centroid of a rigid body must be a primary node;

b) secondary nodes, each of which is connected through a rigid body to a primary node and which thus has no independent

degrees of freedom.

The model consists of the following elements:

1. rigid bodies
2. spring elements
3. beam elements
4. hydrodynamic elements
5. elastic surfaces.

The coordinate system and the element nodes are shown in Figure 1.

The equations are obtained from the principle of virtual work with the inertial forces included in the d'Alembert sense. The principle of virtual work, when applied to the system treated here, states that

$$\dot{\hat{u}}_{iA}^{(e)*}\,\hat{f}_{iA}^{(e)} + \hat{w}_{iA}^{(e)*}\,\hat{m}_{iA}^{(e)}$$

$$= \dot{u}_{il}^{*}\,F_{il}^{ext} + \bar{w}_{il}^{*}\,\bar{M}_{il}^{ext}$$

$$- \mu_l\,\dot{u}_{il}^{*}\,\ddot{u}_{il} - \bar{w}_{il}^{*}\,\dot{L}_{il} \qquad (1)$$

where:

f = element nodal force
m = moment applied to the element
u = displacement of the node
w = angular velocity
F^{ext} = externally applied force
M^{ext} = externally applied moment
L = angular momentum
μ = density of element material.

The superscript e is summed over all elements, subscript A over all nodes of each element, and I over all primary nodes. Superscript dots denote time derivatives, while asterisks denote virtual quantities.

The left hand side of Eqn. (1) represents the rate of work expended on the deformable elements, that is, the internal rate of work, while the first two terms of the right hand side represent the rate of external work. The rate of work of the inertial forces is represented by the last two terms of the right hand side.

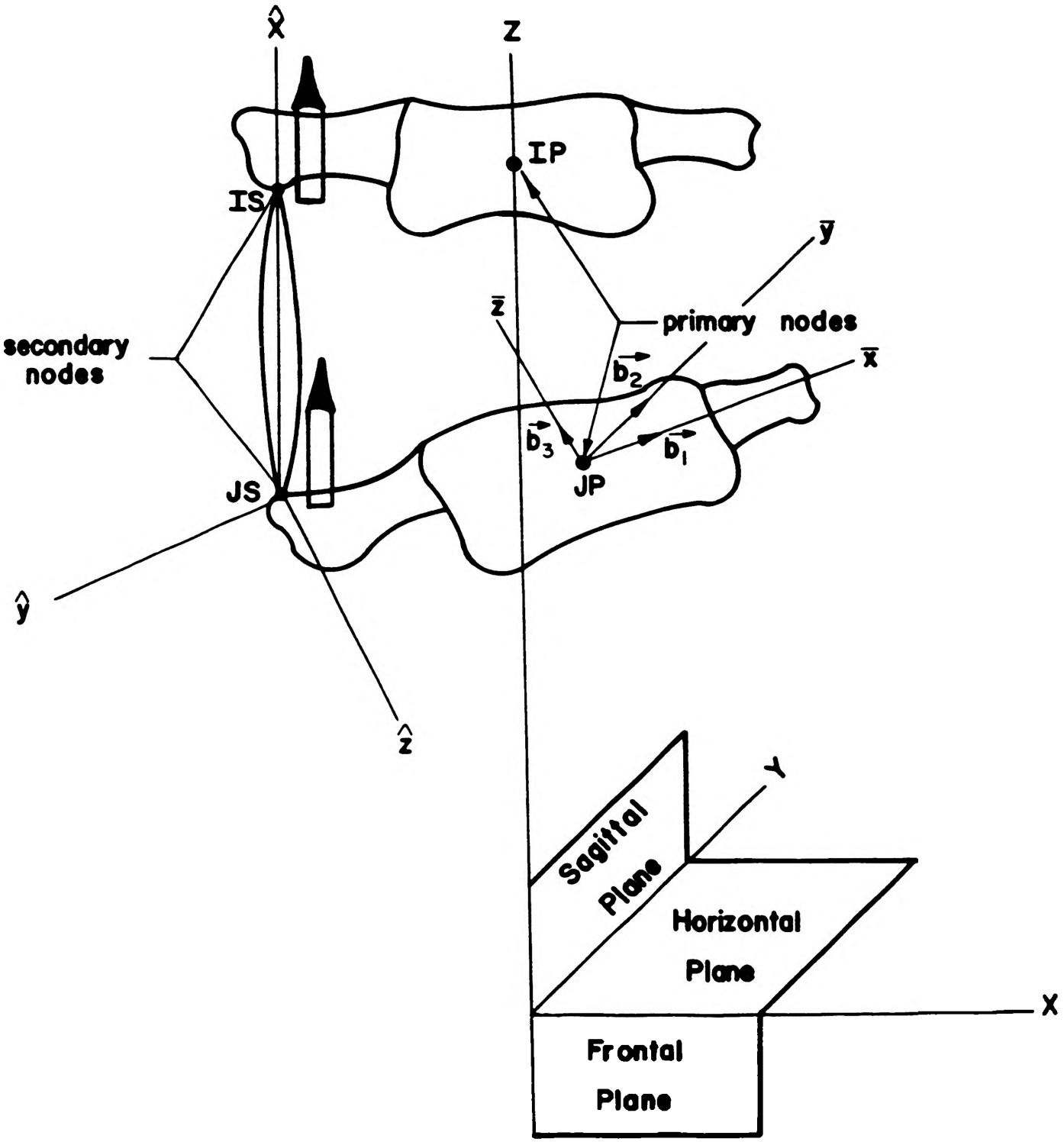

Figure 1 : Rigid body representation and coordinate systems: global coordinates (x, y, z); body coordinates ($\bar{x}$, $\bar{y}$, $\bar{z}$) and element coordinates ($\hat{x}$, $\hat{y}$, $\hat{z}$).

SOLUTION PROCEDURE

One of the methods for solving the equations of motion of this model is the explicit method. This method is by far the most efficient per time step, but the time step must be quite small if the model has a high frequency content, that is, low masses connected by stiff springs.

The explicit integration employs the Newmark-Beta formulas (Newmark [6]) with ß=0, which are almost identical to the central difference formulas (see Belytschko [7]). These formulas predict the velocities and displacements at a time step in terms of the accelerations at the previous step. For the translational components, these formulas may be used directly, so

$$\dot{u}_{ij}^{j+1} = \dot{u}_{ij}^{j} + 1/2\ \Delta t(\ddot{u}_{ij}^{j} + \ddot{u}_{ij}^{j+1}) \qquad (2)$$

$$u_{ij}^{j+1} = u_{ij}^{j} + \Delta t\ \dot{u}_{ij}^{j} + 1/2\ \Delta t^2\ \ddot{u}_{ij}^{j} \qquad (3)$$

where the superscripts denote the time step and Δt the time increment during the step. The flow chart for this procedure follows:

1. Set initial conditions, t=0.
2. Compute $\{u(t+\Delta t)\}$.
3. Update unit vectors and transform to global components.
4. Find deformation displacements.
5. Find the strain in the convected coordinates.
6. Use the stress-strain law.
7. Find local nodal forces $\{f^d\}$.
8. Add $\{f^d\}$ into $\{f^{int}\}$.
9. Compute $\{\ddot{u}(t+\Delta t)\}$.
10. Compute $\{\dot{u}(t+\Delta t)\}$.
11. $t = t + \Delta t$; go to 2.

COMPUTER PROGRAM AND MODIFICATIONS

The original program package developed consists of two distinct programs: an analysis program for predicting the dynamic response of the human body under prescribed loads or accelerations and a graphics package

for depicting deformed and undeformed anatomical configurations. The programs were developed as a research tool.

The data for the program is input by a separate input file. The file consists of fifteen different lines, including nodal parameters, element properties, and plotting data. The data is read into the program through a series of subroutines.

The program provides the capability of modelling various crash environments. An acceleration time history is given by modifying the equations of motion for those primary nodes of the model that are in contact with the surrounding bodies; primary nodes not in contact are not affected.

In addition to standard printer output, the program has provisions for Calcomp and printer plot graphical output of time histories of responses such as displacements, velocities, accelerations, forces, stresses, and strains.

The input for the graphics package can be automatically generated by the analysis program. In addition, the graphics program can be used independently for other studies.

Both programs were developed on an IBM 370/158 computer system. They are completely written in FORTRAN IV. The program originally written for the IBM 370/158 computer, has been adapted to be run on the Apollo 3000 series computer. By this adaptation, the program becomes more versatile and portable. An effort has been made to maintain the modularity of subroutine functions so that additional features may be added.

ACKNOWLEDGEMENTS

The author wishes to acknowledge, with thanks, the immense help and guidance of Professor Xavier J.R. Avula, Department of Mechanical and Aerospace Engineering and Engineering Mechanics, without whom this project would have never come about. Thanks are also due to Gerald K. O'Brennan and Chris Townsend of the UMR Computer Center who tolerated the many questions and problems that arose throughout this study.

REFERENCES

[1] Toth, R., "Multiplying Degree of Freedom, Nonlinear Spinal Model," Proc. of 19th Annual Conference on Engineering in Medicine and Biology 8, 1966.

[2] Orne, D. and Liu, Y., "A Mathematical Model of Spinal Response to Impact," J. of Biomechanics 4, 49-71, 1970.

[3] Hess, J.L. and Lombard, C.F., "Theoretical Investigations of Dynamic Response of Man to High Vertical Accelerations," Aviation Medicine, 66-75, 1958.

[4] Moffatt, C.A., Advani, S.H. and Lin, C., "Analytical and Experimental Investigations of Human Spine Flexure," American Society of Mechanical Engineers, Division of Biomechanical and Human Factors, 71-WA/BHF-7, November 1971.

[5] Liu, Y.K. and Ray, G., "A Finite Element Analysis of Wave Propagation in the Human Spine," Final Report for Contract F33615-72-C-1212, Aerospace Medical Research Laboratory, Wright-Patterson A.F.B., Ohio, 1973.

[6] Newmark, N., "A Method of Computation for Structural Dynamics," J. Eng. Mech. Div., Proc. of ASCE, 67-94, 1959.

[7] Belytschko, T., "Transient Analysis," Structural Mechanics Computer Programs, ed. W. Pilkey, et al., University Press of Virginia, 255-276, 1974.

SOLUTION OF DIVERTOR MAGNETOHYDRODYNAMIC EQUILIBRIA FOR THE STUDY OF ALPHA PARTICLE EDGE TRANSPORT IN FUSION PLASMAS

by J. W. Schumer
Nuclear Engineering

ABSTRACT

Removal of thermalized alpha particles from deuterium-tritium (D-T) fusion plasmas can be accomplished through the use of divertor magnetic fields if the magnetohydrodynamic (MHD) equilibria is well understood [1]. Modifying a MHD variational energy principle for poloidal flux surfaces described by $\chi = \chi(\rho,\theta)$ results in an inverse Fourier representation of the three-dimensional (3-D) equilibria solution. Application of the $\chi(\rho,\theta)$ flux profile allows transformation of the magnetic field into a non-singular coordinate system along the divertor separatrix [2] and therefore, analysis of different divertor schemes. Derivation of the coupled, non-linear differential equations follows [5] except in the contravariant representation of the magnetic field. Theoretical background, formulation of the variational principle, benchmark results, and preliminary computations are presented.

INTRODUCTION

Transport, accumulation, and thermalization of alpha particles in a deuterium-tritium (D-T) plasma are critical phenomena which may preclude sustained ignition in a fusion reactor. Alpha particles are produced by the D-T reaction [1],

$$ {}_1^2D + {}_1^3T \rightarrow {}_0^1n(14.1\ MeV) + {}_2^4He(3.52\ MeV) \qquad (1) $$

releasing 2.818E-12 J/reaction for continued ignition of the plasma. Unfortunately, non-classical transport or containment of thermalized helium ash (low energy population of alphas) could quench the fusion reaction [1,4]. Removal of helium ash may be accomplished using a poloidal divertor (see Figure 1) to scrape the plasma edge if ash distributions are fairly flat and if the resulting perturbation of magnetohydrodynamic (MHD) equilibrium is well understood.

This research involved the enhancement of VMEC (Variational Moments Equilibrium Code [5,6,7,8]), allowing it to solve the high-β MHD equilibria equations associated with a divertor magnetic separatrix. The separatrix is the bounding surface between open and closed field lines [2] (see Figure 2) and equilibrium calculations are simplest when using magnetic coordinates $\alpha(\rho,\theta,\zeta)$ in which the contravariant form of the magnetic field is defined,

$$\vec{B} = \nabla\phi\times\nabla\theta - \nabla\chi(\phi)\times\nabla\zeta \qquad (2)$$

where ϕ is the toroidal flux, ζ is the toroidal angle, χ is the poloidal flux, and θ is the poloidal angle. However, this form is mathematically singular along the separatrix because the helical flux $\chi_h(\psi)$ is a function of toroidal flux alone and the toroidal flux ψ goes to infinity along the separatrix. Recent progress [3] has revealed a transformation to nonmagnetic coordinates which preserves some of the attractive features of magnetic coordinates while removing their discontinuous nature. By retaining the helical flux in the contravariant form of the magnetic field, defined as

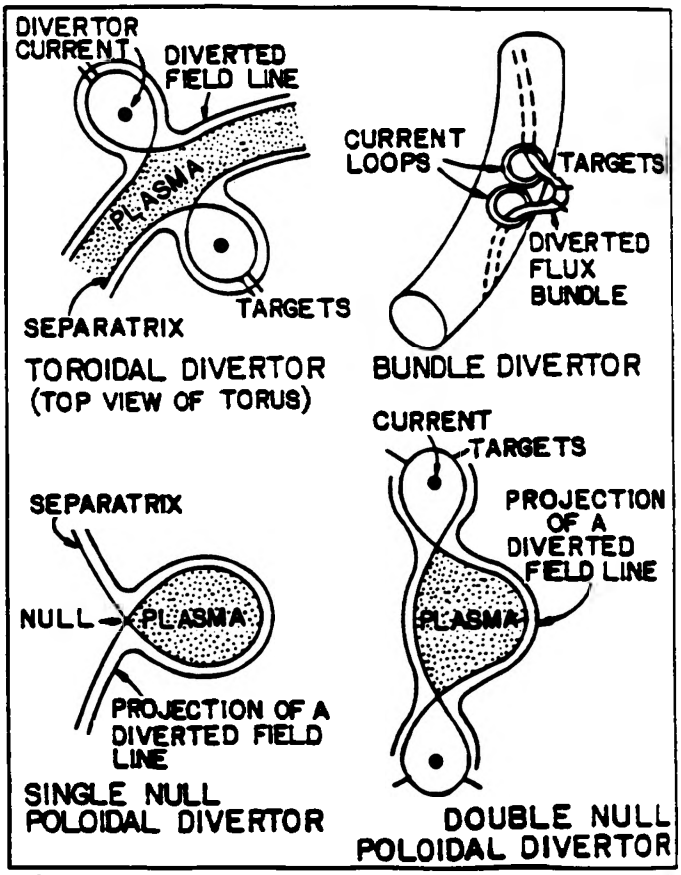

Figure 1. Toroidal, poloidal, and bundle divertors (from Dolan, 729).

$$\vec{B} = \nabla\phi\times\nabla\theta - \nabla\chi(\rho,\theta)\times\nabla\zeta \qquad (3)$$

allows for the modification of the variational moments MHD energy principle in VMEC and the production of an efficient, finite-series representation for the three-dimensional (3-D) plasma boundary with a separatrix.

ANALYTICAL DERIVATIONS

Magnetic field

Generally, Equation (3) is the form of the magnetic field

used for solution of force-balance equation $\vec{F} = -\vec{J}\times\vec{B} + \nabla p = 0$, where F is the residual force vanishing at equilibrium and p is the pressure on the radial flux surface labeled by ρ. However, to aid in the convergence of the inverse Fourier series representation used in VMEC, the renormalization parameter λ is introduced, allowing for distinction between geometric and magnetic angles [6]. The renormalization parameter is a function of the three magnetic coordinates $\alpha(\rho,\theta,\zeta)$ and is used in linear combination with one of the cylindrical coordinates normally visualized with fusion toroidal devices (see Figure 3). Unfortunately, implementation of this parameter with the poloidal angle does not allow for conservation of the magnetic field along flux surfaces. However, using λ with the toroidal angle satisfies $\vec{B}\cdot\nabla\chi(\rho,\theta) = 0$ *when* $\zeta^* = \zeta \pm \lambda$ and results in the following contravariant magnetic representation:

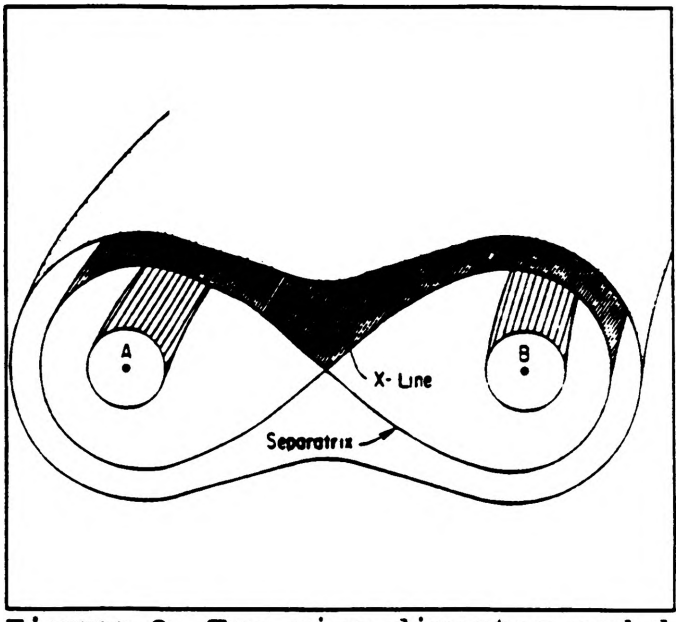

Figure 2. Two-wire divertor model illustrating separatrix and X-line (Boozer, 2398).

$$\vec{B} = \nabla\phi\times\nabla\theta - \nabla\chi\times\nabla\zeta \pm \nabla\chi\times\nabla\lambda \ . \tag{4}$$

Taking the dot product of (4) with its covariant basis vectors $\nabla\alpha_i$ *where* $\alpha = (\rho,\theta,\zeta)$ [10], the contravariant components of $\vec{B}$ are

$$B^{\rho} = -\frac{\chi_\theta}{\sqrt{g}}(1 - \lambda_\rho) \tag{5a}$$

$$B^{\theta} = \frac{\chi_\rho}{\sqrt{g}}(1 - \lambda_\rho) \tag{5b}$$

$$B^{\zeta} = \frac{1}{\sqrt{g}}(\phi_\rho + \chi_\rho\lambda_\theta + \chi_\theta\lambda_\rho) \tag{5c}$$

where $\sqrt{g} = (\nabla\rho\cdot\nabla\theta\times\nabla\zeta)^{-1}$ is the Jacobian. These results will be used in the derivation of energy principle.

Variational Principle

The variational principle used for the solution of the equilibrium is based on the plasma energy

$$W = \int \left(\frac{|B|^2}{2\mu_o} + \frac{p}{(\gamma - 1)} \right) d^3x \quad (6)$$

where $d^3x = x(R,\phi,Z)$ is the Cartesian coordinate system and $\gamma > 0$ is the adiabatic index. By taking the inverse representation, for which $\alpha = \alpha(x) = \alpha(\rho,\theta,\zeta)$, the mass and flux are conserved in the contravariant representation of B. Differentiating (6) and integrating by parts, the spatial differentials are separated into a steepest-descent formulation for the F=0 solution of MHD force equation that preserves finite positive energy, such that

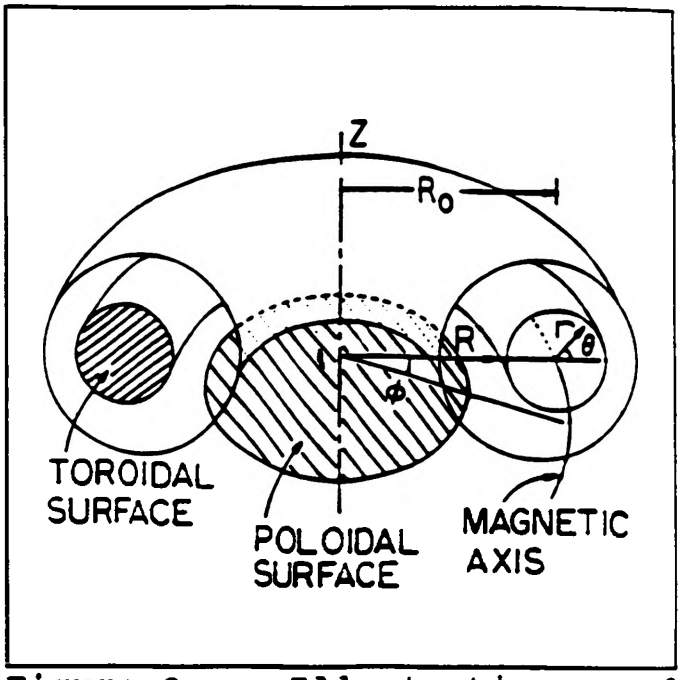

Figure 3. Illustration of toroidal and poloidal surfaces and directions (Dolan, 338).

$$\frac{dW}{dt} = -\int F_i \dot{x}\, d^3\alpha \quad (7)$$

where

$$F_i = \frac{d}{dx_i}\sqrt{g}\left[\frac{|B|^2}{2\mu_o} + \frac{p}{\gamma - 1} \right] \quad (8)$$

and $\dot{x}_i = (\dot{R},\dot{\lambda},\dot{Z})$ *by use of* $\phi = \zeta$ in the geometric system. Since (8) is a 2nd order differential in flux coordinates, a conservative finite-difference representation is found by integrating (8) over a radial mesh. Spectral analysis of (θ,ζ) is then used so that no higher-order derivatives are computed in the solution of the coupled equations. Equating the magnetic and geometric toroidal angles sets $\partial\phi/\partial\zeta = 0$ and the conservative force equations become

$$F_R = -\frac{\sqrt{g}}{\mu_o}\left[\frac{\partial}{\partial\rho}\left((B^\rho)^2 R_\rho + (B^\rho B^\theta) R_\theta + (B^\rho B^\phi) R_\phi \right) \right. \quad (9a)$$

$$+ \frac{\partial}{\partial\theta}\left((B^{\rho}B^{\theta})R_{\rho} + (B^{\theta})^2 R_{\theta} + (B^{\theta}B^{\phi})R_{\phi}\right)$$
$$+ \frac{\partial}{\partial\phi}\left((B^{\rho}B^{\phi})R_{\rho} + (B^{\theta}B^{\phi})R_{\theta} + (B^{\phi})^2 R_{\phi}\right)\Big]$$
$$+ \frac{\partial}{\partial\theta}(PZ_{\rho}) - \frac{\partial}{\partial\rho}(PZ_{\rho}) - \frac{PG}{R} + \frac{G(RB^{\phi})^2}{\mu_o}$$

$$F_{\lambda} = -\frac{1}{\mu_o}\Big[\frac{\partial}{\partial\phi}(\chi_{\theta}B_{\rho} - \chi_{\rho}B_{\theta}) - \frac{\partial}{\partial\rho}(\chi_{\theta}B_{\phi}) + \frac{\partial}{\partial\theta}(\chi_{\rho}B_{\phi})\Big] \qquad (9b)$$

with the F_Z equation being symmetric to (9a) except in lacking the last two energy terms and having the R and Z derivatives switched. Note that subscripts on each coordinate denote the first derivative, $G = \sqrt{g}/R$, and $P = R(p+B^2/2\mu_o)$.

Poloidal Flux Profile

For accurate prescription of the poloidal flux, n-degree polynomials in ρ were used as coefficients in a cosine series, represented mathematically as

$$\chi(\rho,\theta) = \chi_o(\rho) + \chi_2(\rho)\cos(m\theta) \qquad (10)$$

$$\text{where } \chi_i(\rho) = \sum_{j=0}^{N} c_i^j \rho^j$$

The number of separatrix X-points is defined by m in (10) and the coefficients are chosen so that the following condition is satisfied:

$$\frac{\partial\chi}{\partial\rho} = \frac{\partial\chi}{\partial\theta} = 0 \qquad (11)$$

Noting that when $\theta = 0,\pi/2,\pi,3\pi/2 \ldots$, then $\partial\chi/\partial\theta = 0$. Therefore, the only flux condition defining the polynomial coefficients of the poloidal flux cosine series is

$$\frac{\partial\chi_o}{\partial\rho} \pm \frac{\partial\chi_2}{\partial\rho} = 0 \; . \qquad (12)$$

NUMERICAL METHOD

Computational analysis required discretization of the energy principle for numerical integration. Fourier transforms of the

coordinates allow exact interpolation on the half-mesh for more accurate numerical differentiation [9]. Hence, the coordinates are decomposed into even-odd harmonics as

$$\boldsymbol{x}(R,\lambda,Z) = x_{even} + \sqrt{\Delta\rho_{\frac{1}{2}}}\, x_{odd} \tag{13}$$

and averaged onto each nodal point. Following [1] by using central sum and difference formulas on the full-mesh (angular coordinates) and half-mesh (radial coordinate) requires an averaging scheme such that

$$\langle xy \rangle = \left(\frac{x^i y^i + x^{i+1} y^{i+1}}{2} \right) \tag{14}$$

to facilitate higher convergence. However, faster computations could be achieved by averaging the terms separately as $\langle x \rangle \langle y \rangle$. By varying individual nodal amplitudes of the Fourier-transformed force representation, the complete formulation of the steepest-descent algorithm is

$$\frac{\partial X_j^{mn}}{\partial t} = F_j^{mn} \tag{15}$$

Applying (8) as the kernel of the energy integral over all mesh points, averaging onto the full-mesh before differentiation of the energy integral, and decomposing each spatial variable into even and odd components, the Fourier amplitudes may be realized and used to calculate the equilibria solution of minimum plasma energy.

$$R(\rho,\theta,\phi) = \sum_{m,n} R^{mn}(\rho)\cos(m\theta - n\phi) \tag{16a}$$

$$Z(\rho,\theta,\phi) = \sum_{m,n} Z^{mn}(\rho)\sin(m\theta - n\phi) \tag{16b}$$

$$\lambda(\rho,\theta,\phi) = \sum_{m,n} \lambda^{mn}(\rho)\sin(m\theta - n\phi) \tag{16c}$$

NUMERICAL RESULTS

Replication of a standard 3-D MHD equilibria without divertor was easily acquired. Figure 4 illustrates a case in which the modified code successfully solved the MHD equations when the angular dependence was not activated in the poloidal flux (i.e. $\chi(\rho,\theta)=\chi(\rho)$). Shown are the toroidal flux surfaces

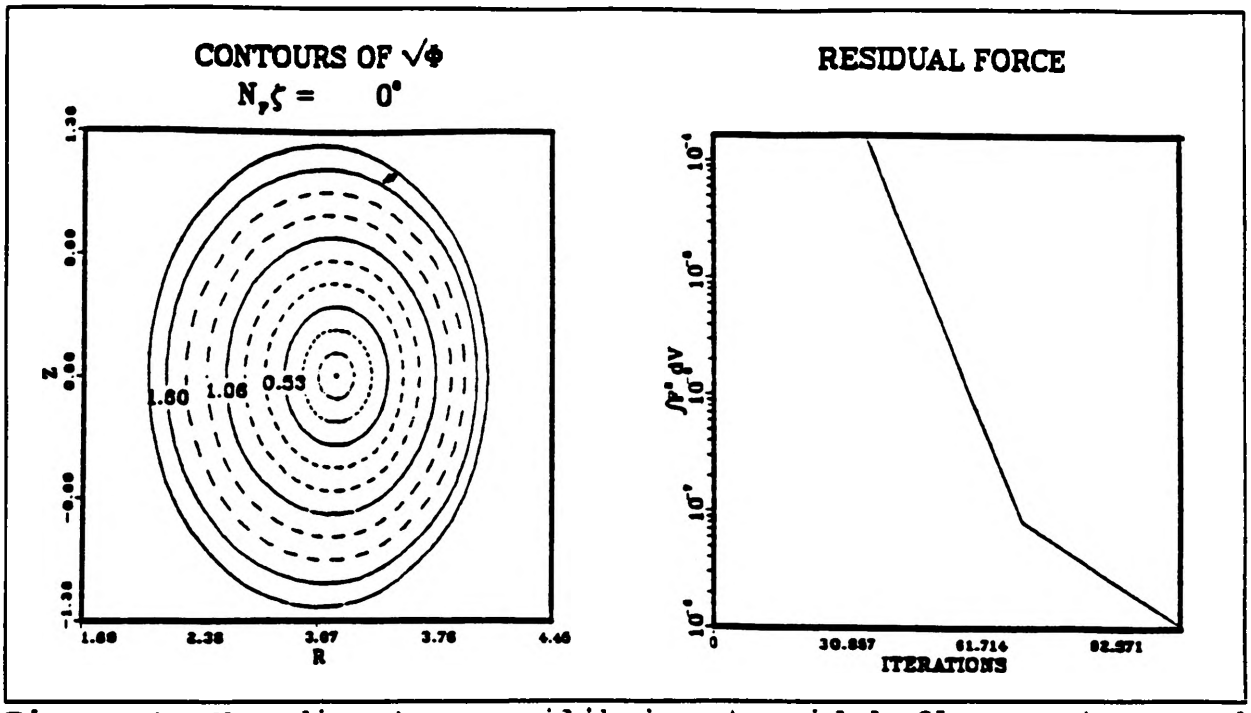

Figure 4. Non-divertor equilibrium toroidal flux contour and residual force decay.

and the residual force going to zero in about 100 iterations. In Figure 5, the angular dependence was "switched" on but the separatrix was not formed within the plasma boundary. The convergence in this case was again adequate.

Two examples of angular-dependent flux profiles in which the X-point is within the plasma boundary are shown in Figures 6 and 7. However, these runs did not converge, even for finer spatial meshes, as is visualized in Figures 8 and 9. The iterative force residual did not smooth out and the magnetic axis (center of ellipsoids) was not resolved.

DISCUSSION

The standard case without divertor was reproducible, as was the case including angular poloidal flux dependence. However, when the separatrix was within the plasma boundary, the residual forces did not decay. This may be due to improper discretization of the energy principle. A finer mesh may improve the convergence properties, but this fact was not seen in any of the cases run here. Analytical derivations are not straightforward and may have led to anomalous errors.

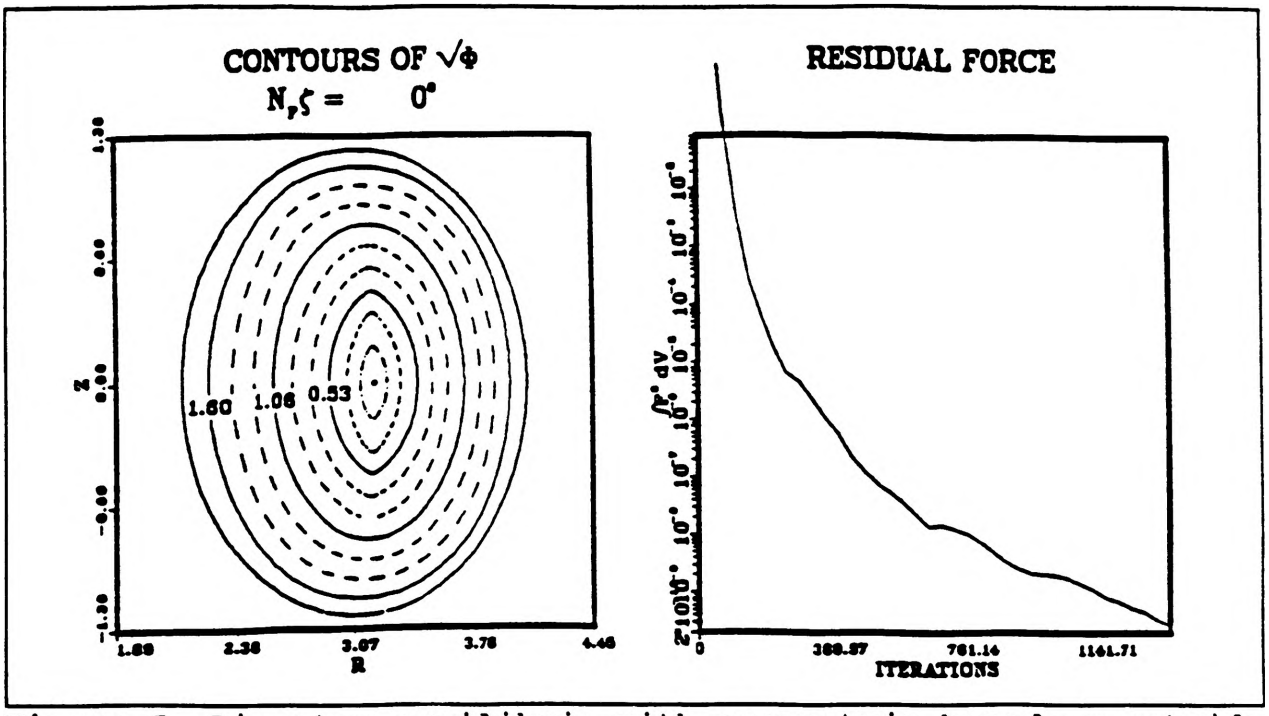

Figure 5. Divertor equilibria with separatrix boundary outside plasma boundary.

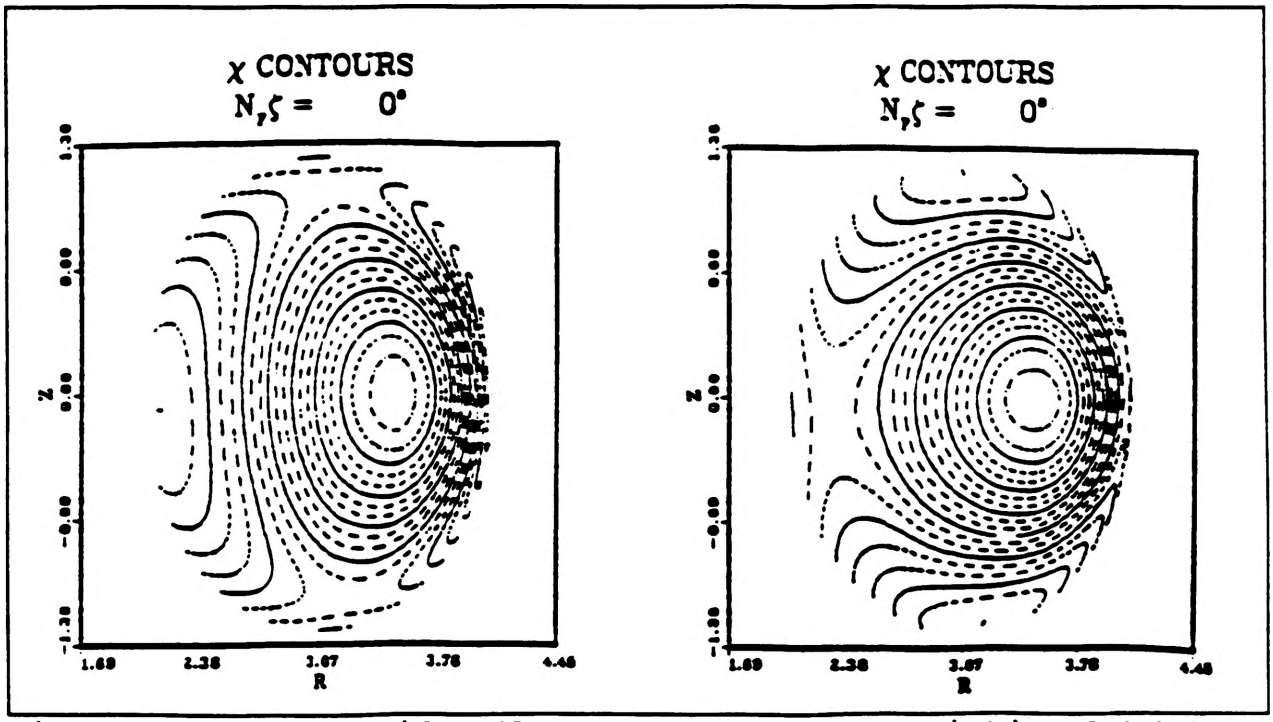

Figure 6(a,b). Poloidal flux surfaces characteristic of (a) top-bottom double-nulled divertor and (b) left (outboard) single-nulled divertor.

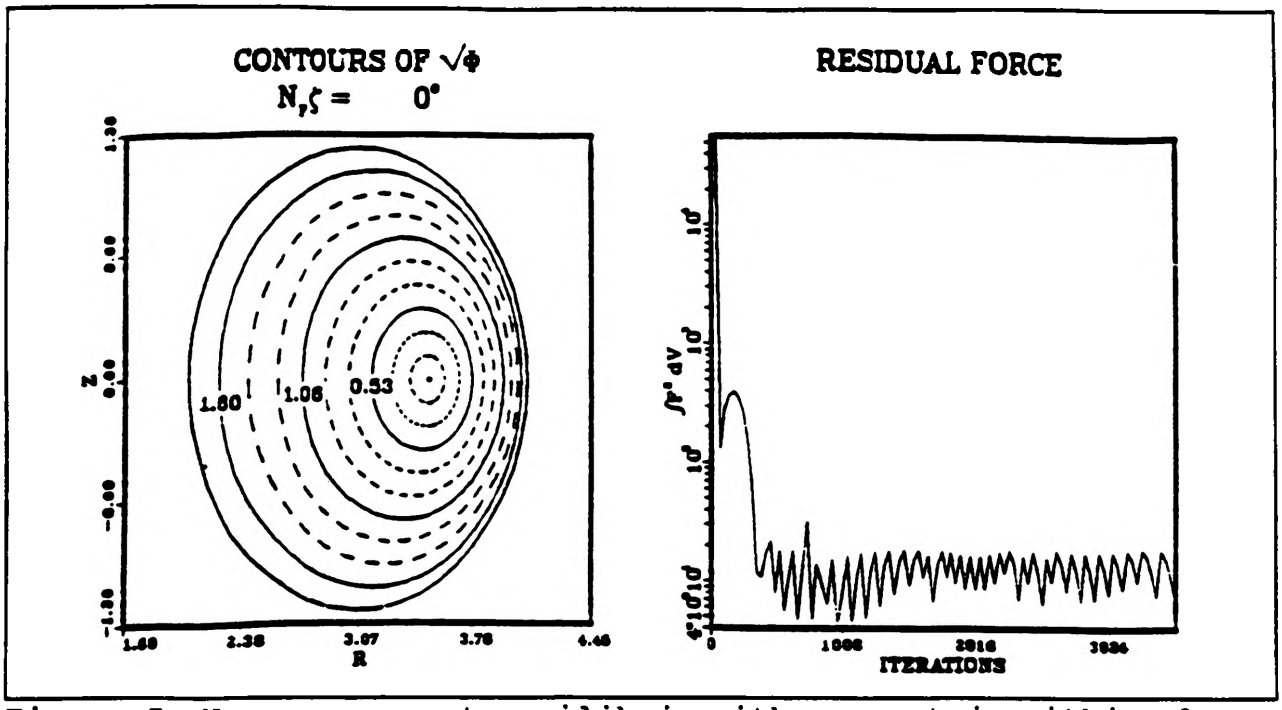

Figure 7. Non-convergent equilibria with separatrix within plasma boundary (number of iterations>1000).

ACKNOWLEDGEMENTS

I would like to thank Dr. Gary Mueller for his helpful guidance and useful conversation. I would also like to thank Steven Hirshman for our insightful discussions. This work was accomplished on a CRAY-2 at the National Magnetic Fusion Energy Computational Center in Lawrence Livermore, California using the Internet and Telnet lines of the Oak Ridge National Laboratory Fusion Energy Division and the UMR Nuclear Engineering AT&T 3B15 mainframe.

REFERENCES

Dolan, T. J. *Fusion Research: Principles, Experiments, & Technology*. Pergamon Press Inc. (1982).

Auerbach, S. P. and Boozer, A. H. "Classical Diffusion in the presence of an X point." Phys. Fluids **23** (1980): 2396-2412.

Boozer, A. H. and Rechester, A. B. "Effect of magnetic perturbations on divertor scrape-off width." Phys. Fluids **21** (1978): 682-689.

Boozer, A. H. "The drift Hamiltonian in a magnetic field with a separatrix." Phys. Fluids B **3** (1991): 875-879.

Hirshman, S. P. and Whitson, J. C. "Steepest-descent moment method for three-dimensional magnetohydrodynamic equilibria." Phys. Fluids **26** (1982): 3552-3568.

Hirshman, S. P., Schwenn, W., and Nuhrenberg, J. "Improved Radial Differencing for Three-Dimensional Magnetohydrodynamic Equilibrium Calculations." J. of Comput. Phys. **87** (1990): 396-407.

Hirshman, S. P. and Betancourt, O. "Preconditioned Descent Algorithm for Rapid Calculations of Magnetohydrodynamic Equilibria." J. of Comput. Phys. **96** (1991): 99-109.

Hirshman, S. P., van Rij, W. I., and Merkel, P. "Three-Dimensional Free Boundary Calculations Using A Spectral Green's Function Method." Computer Physics Communication **43** (1986): 143-155.

Hirshman, S. P. "Curvilinear Coordinates for Magnetic Confinement Geometries." ORNL/TM-8393 Fusion Energy Document (1982).

Kuo-Petravic, G., Boozer, A. H., Rome, J. A., and Fowler, R. H. "Numerical Evaluation of Magnetic Coordinates for Particle Transport Studies in Asymmetric Plasmas." J. of Comput. Phys. **51** (1983): 261-272.

A PESSIMISTIC LOOK AT OPTIMISM

Maureen Sidio Catherine A. Riordan

Department of Psychology

University of Missouri - Rolla

ABSTRACT

The personality construct of optimism has been shown to be related to important outcome measures like depression, physical health and achievement. Several recent studies have questioned the psychometric uniqueness of the concept of optimism and its relationship to neuroticism. This study examined this relationship and found that the measures of optimism were as highly correlated with neuroticism as they were with each other. Results are discussed in the context of optimism being a subordinate construct in the multifaceted construct of neuroticism.

INTRODUCTION

Optimism is defined as a personality construct wherewith individuals have generally positive expectations about the future and are more likely to persist in their effort to achieve their goals (Smith, Pope, Rhodewalt & Poulton, 1989). When faced with stressful situations optimists' perceive them as a challenge and are motivated to investigate every avenue they can in an attempt to solve or actively cope with the problem. Research has established that individuals with a more positive outlook on life are more likely to succeed and are better adjusted than those with a negative outlook (Seligman, 1991). Additionally, it has been suggested that the more effective coping of optimists, the feeling of being in control of ones own destiny is responsible for alleviating the negative effects of stress on an individual's physical and emotional health (Scheier & Carver, 1987).

The personality construct of optimism also has been shown to be related to important outcome measures like depression, physical health and achievement (Seligman, 1991). Recently however, it has been suggested that it is neuroticism rather than optimism that is the predictive personality construct (Smith et. al., 1989), and that findings with respect to optimism merely reflect the more pervasive personality dimension of neuroticism.

Neuroticism is defined as a broad stable dimension of personality consisting of chronic negative emotions including sadness, anxiety, guilt and anger, as well as associated cognitive and behavioral characteristics such as low self-esteem, preoccupation and insecurity (Smith et. al., 1989). Neuroticism often results in depression, decline in physical health and low levels of achievement despite intellectual capability.

Another important construct that correlates with optimism and neuroticism is attributional style or the way we explain events in our lives. The helplessness theory of depression (Abramson, Seligman, & Teasdale, 1978) holds that the way in which people explain events in their lives has an important impact on the extent and duration of depression. Specifically, people who attribute bad events to internal, stable and global causes are believed to be more susceptible to depression. These individuals would also be expected to be less optimistic about the future as a result of having an attributional style where they attribute bad events to internal and enduring causes.

In sum, this study reexamined the possibility suggested by Smith et al. that optimism is merely a special case of neuroticism. Secondly, it examined the relationship of optimism to attributions which should serve as basis for optimism and neuroticism according to the predominant personality theories.

METHOD

One hundred eighty-one students participated in partial fulfillment of an introductory psychology research requirement. In group sessions of 8 to 10, subjects completed the questionnaires.

Optimism was measured using the Life Orientation Test (LOT; Scheier & Carver, 1985) and the Personal Ladder (PL; Cantril, 1963). Neuroticism was measured using the Taylor Manifest Anxiety Scale (TMAS; Taylor, Carver, 1985) and the Beck Depression Inventory (BDI; Beck, 1967). Attributional Style was measured using the Attributional Style Questionnaire (ASQ; Seligman, Abramson, Semmel & VonBaeyer, 1979).

RESULTS

In Table I, the correlations of the two measures of optimism and two measures of neuroticism can been seen. The LOT and PL were as highly correlated with neuroticism as they were with each other providing some support for Smith et al.'s argument that optimism, as measured by the LOT, is not empirically distinct from neuroticism.

TABLE I

CORRELATIONS OF MEASURES OF OPTIMISM AND NEUROTICISM

OPTIMISM	LOT	PL	BDI
Life Orientation Test (LOT)			
Personal Ladder (PL)	.39**		
NEUROTICISM			
Beck Depression Inventory (BDI)	-.38**	-.36**	
Taylor Manifest Anxiety Scale (TMAS)	-.46**	-.35**	.62**

Table II shows the correlations of the optimism measures with attributions which serve as the basis for optimism. Only the LOT was significantly related to a hopeful attributional pattern, and that was only weakly correlated.

TABLE II

CORRELATIONS OF OPTIMISM AND NEUROTICISM WITH HOPEFUL AND HOPELESS ATTRIBUTIONAL STYLES

	Attributional Style	
OPTIMISM	Hopeful	Hopeless
Life Orientation Test	.16*	.04
Personal Ladder	.08	.12
NEUROTICISM		
Beck Depression Inventory	-.09	.05
Taylor Manifest Anxiety Scale	-.06	.12

DISCUSSION

The correlational pattern observed in this study was similar to that obtained by Smith et al.(1989) even though the personality measures used were not the same and correlations not as high: The two optimism measures were more highly correlated with each other than they were with the measures of neuroticism. Thus, these results too call into question the uniqueness of the concept of optimism as measured by the LOT and PL. There was little evidence to refute the argument that measures of optimism are confounded with measures of neuroticism.

Carver (1989) pointed out that in personality research, what looks like confounding could be two concepts, are facets of a larger, multi-faceted construct. Optimism being a subordinate construct in the multi-faceted concept of neuroticism would be consistent with the results of this study and those obtained by Smith et al.

The fact that attributional style was associated with optimism as measured by the LOT, but not with either measure of neuroticism, suggests that optimism may be an important concept, apart from its role in neuroticism, in understanding the attributional style which may precipitate neuroticism and chronic negative affective states. On a theoretical level, the hopeful and hopeless attributional style should lead to both optimism and neuroticism. However, optimism, because of its similarity to those specific attributions may be a more sensitive measure of the cognitions that foster neuroticism.

It is quite possible that optimism, measured independently, might be a better predictor of outcome measures more directly based on expectancies (e.g. motivation) than neuroticism as a global concept. In fact, only looking at neuroticism and ignoring the optimism component could result in a loss of important information. Thus, it would seem justifiable--both empirically and theoretically--to choose to focus on optimism in some instances and neuroticism in others (see Carver, 1989 for a discussion of these issues).

A cautionary note should be offered concerning the convergent validity of the two optimism measures. The Personal Ladder may not provide the strongest test of convergent validity for the Life Orientation Test because the scales are very different. The LOT has a standard Likert-type format. The PL asks subjects to pick a place on the ladder that best reflects how positively they feel about their lives in the past, now, and in the future.[1] Thus, a much more global judgement is made by subjects than the very specific items (e.g., "If something can go wrong, it will") on the

---

[1]All these judgements are significantly correlated with each other ($p's < .25$-$.66$) and with neuroticism ($p's < .19$-$.41$).

LOT. Moreover, it is possible the PL may be less reliable due to greater influence of recent events on these broad judgements. Thus, in future examinations of the convergent validity of the LOT, it would be advisable to use other measures of optimism that should move method variance.

Future research might extend the methodological approach used in this study by looking at the relationship of optimism and neuroticism to the many outcome measures that have been shown to be related to optimism. If treatment interventions are to be effective, knowing the underlying dimension one is trying to affect would be important. Focusing on optimism rather than the broader concept of neuroticism may lead to treatments that are not as effective as they could be. Similarly, using only neuroticism may lead to loss of important information that could be useful in understanding the attributions which lead to neuroticism.

REFERENCES

Abramson, L.Y., Seligman, M.E.P., & Teasdale, J.D. (1978). Learned helplessness in humans: Critique and reformulation. Journal of Abnormal Psychology, 87, 49-74.

Beck, A.T. (1967). Depression: Clinical, experimental and theoretical aspects. New York: Harper & Row.

Cantril, H. (1963). A study of aspirations. Scientific American, 208, 41-45.

Scheier, M.F. & Carver, C.S. (1987). Dispositional optimism and physical well-being: The influence of generalized outcome expectancies on health. Journal of Personality, 55, 169-210.

Seligman M.E.P. (1991). Learned Optimism. New York: Alfred A. Knopf.

Seligman M.E.P., Abramson L.Y., Semmel A., & VonBaeyer C. (1979). Depressional attributional style. Journal of Abnormal Psychology, 88(3), 242-247.

Smith T.W., Pope M.K., Rhodewalt F., & Poulton J.L. (1989). Optimism, neuroticism, coping and symptoms report: An alternative interpretation of the Life Orientation Test. Journal of Personality & Social Psychology. 56, 640-648.

Taylor J.A., (1953). A personality scale of manifest anxiety. Journal of Abnormal & Social Psychology, 48, 285-290.

CALCULATION OF NEUTRON FLUX AND NEUTRON RADIATION DOSE IN A HUMAN PHANTOM

L. Alan Smith
Nuclear Engineering Department

ABSTRACT

At present, the neutron dose received by personnel working in nuclear installations is recorded by body surface dosimeters worn by workers. To estimate the true neutron dose to internal organs, this "surface dose" is multiplied by empirical factors to account for the attenuation of the body itself.

The objective of this work was to obtain better estimates of the internal dose by calculating the attenuation of the neutron flux provided by the body. Using DOT, a 2-D radiation transport code, the neutron flux as a function of energy was calculated at several points in a 2-D model of the human body. These flux values were used to calculate the neutron dose at all points in the human phantom. These neutron doses were then compared to the "surface dose." The ratios thus obtained could be used by practicing health physicists to evaluate internal doses.

INTRODUCTION

In every installation where neutrons may be present, accurate determination of the neutron dose received by personnel is of paramount importance. Currently, the neutron dose to internal organs of the body is calculated by multiplying the dose recorded by a surface dosimeter by an empirical factor. This factor accounts for changes in the neutron field caused by the body itself, which are important since the radiation dose from a neutron beam is very energy-dependent. DOT, a 2-D transport code, was used to calculate these factors in a human phantom.

CALCULATION

In order to preform neutron transport calculations, neutron cross sections are needed. These cross sections are calculated for different materials and energy groups from cross section libraries through the use of computer codes. In most cases, these codes collapse fine group cross sections into smaller broad group cross sections. The cross sections are collapsed because the computer time needed to run the codes is decreased if a smaller number of energy groups is utilized.

Computer Codes

Several computer codes were used for the calculation of the flux at points in the human phantom. The order in which these codes are used is outlined in Figure 1 on page 3. LAVA is used to setup the cross section library of isotopes in the model. The LAVA code reads these values from the BUGLE-80 collection which contains the cross sections of various materials collapsed to 47 neutron groups. Since the BUGLE-80 cross sections are contained in two different files, LAVA must be run twice if isotopes are needed from both files. NITAWL is used to combine the files created by the two LAVA runs. The created NITAWL cross section library is entered into the 1-D transport code, XSDRNPM. In XSDRNPM a 1-D model of the geometry to be studied, in this case the human body, is entered along with the neutron source position and energy spectrum. XSDRNPM calculates the flux as a function of position in the model and collapses the cross sections into a 20 broad group library from the original 47 groups of the BUGLE-80 library.

XSDRNPM creates the cross section library to be used in DOT, a 2-D transport code. In DOT, a 2-D model of the geometry under study is entered. As in XSDRNPM, the neutron source position and energy is set-up as desired. The neutron flux at several points of the model and at each of the 20 energy groups is calculated by DOT. These flux values can be used to calculate the neutron dose at positions inside the model relative to the surface dose.

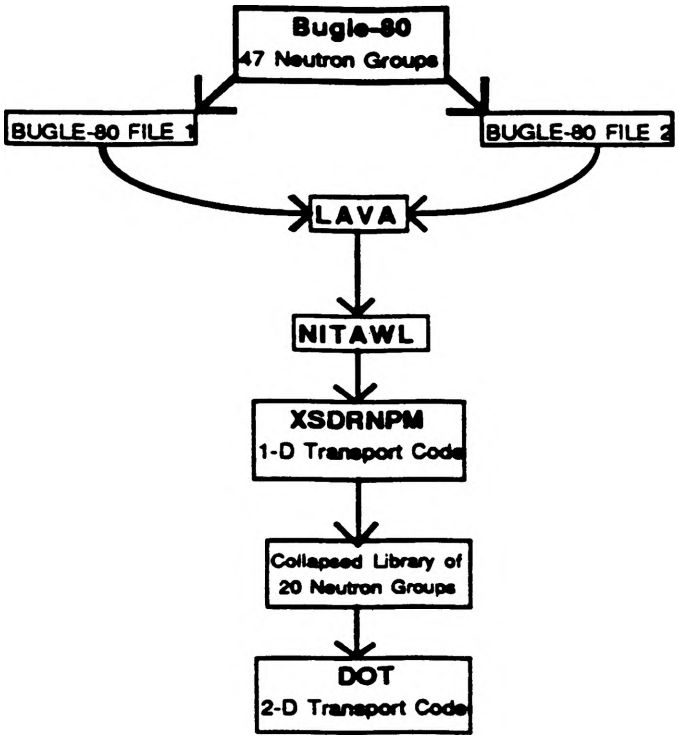

Figure 1. Computer Code Structure.

HUMAN PHANTOM

XSDRNPM

A 1-D model of the human waist line was used in XSDRNPM. The model is shown below in Figure 2. Slab geometry, S_8 angular quadrature, and P_3 scattering order were used for the calculation. Reflective boundaries were assumed on both sides of the model to simulate the containment area of a nuclear reactor. The fission spectrum of Uranium was used as the source on both sides. The 47 group cross sections from BUGLE-80 were collapsed to 20 groups. The energy groups and the resulting collapsed energy groups are shown in Table I on page 5.

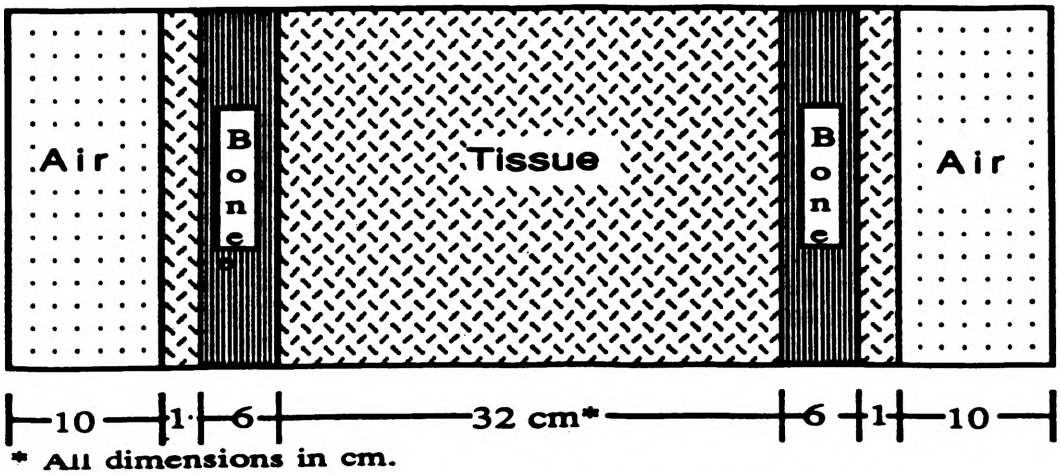

Figure 2. XSDRNPM 1-D Model of Human Waist.

Table I. Broad and Collapsed Energy Groups.

Fine Group Structure		Broad Group Structure	
Group No.	Energy(MeV)	Group No.	Energy(MeV)
1	17.33299	1	17.33299
2	14.19100		
3	12.21400		
4	10.00000		
5	8.60100	2	8.6071
6	7.4682		
7	6.0653	3	6.0653
8	4.9659		
9	3.6788		
10	3.0119	4	3.0119
11	2.7253		
12	2.466		
13	2.3653		
14	2.3457	5	2.3457
15	2.2313		
16	1.9205		
17	1.653		
18	1.3534	6	1.3534
19	1.0026		
20	8.2080E-1		
21	7.4274E-1		
22	6.0810E-1	7	6.0810E-1
23	4.9798E-1		
24	3.6883E-1		
25	2.9720E-1		
26	1.8316E-1	8	1.8316E-1
27	1.1109E-1		
28	6.7379E-2		
29	4.0868E-2		
30	3.1828E-2	9	3.1828E-2
31	2.6058E-2		
32	2.4176E-2		
33	2.1875E-2	10	2.1875E-2
34	1.5034E-2		
35	7.1017E-3		
36	3.3546E-3	11	3.3546E-3
37	1.5846E-3		
38	4.5400E-4	12	4.5400E-4
39	2.1445E-4		
40	1.0130E-4	13	1.0130E-4
41	3.7267E-5	14	3.7267E-5
42	1.0677E-5	15	1.0677E-5
43	5.0435E-6	16	5.0435E-6
44	1.8554E-6	17	1.8554E-6
45	8.7642E-7	18	8.7642E-7
46	4.1399E-7	19	4.1399E-7
47	1.0000E-7	20	1.0000E-7
48	1.0000E-11	21	1.0000E-11

Three different materials were used in the model; general body tissue, bone tissue, and air. The weight percent of each isotope in these materials and the material's density are shown in Table II. The XSDRNPM code was used to produce the collapsed cross section library to be used in DOT and the 2-D model of the human body.

Table II. Weight Percent and Density of Isotopes Used in Model.

Isotope	General Tissue	Bone Tissue	Air
H	10.47%	7.04	0.00
C	23.02	22.80	0.00
N	2.34	3.90	78.94
O	63.21	48.60	21.06
Na	0.13	0.32	0.00
P*	0.84	17.35	0.00
Density (g/cm^3)	0.987	1.486	$1.29*10^{-3}$

* Mg, Al, Si, S, Cl, K, Ca, and Fe isotopes were assumed to be P due to their small weight percent.

DOT

The 2-D model of the human body is shown in Figure 3 on page 6. X-Y geometry was used and reflective boundaries were assumed on the sides and the top of the model while the bottom of the model was assumed to be void. Two different neutron sources were considered; first, the fission spectrum and second, a source of only 0.5 MeV neutrons. The source was placed in the air surrounding the phantom. A XSDRNPM model of a typical containment area was run in XSDRNPM to try to determine a neutron spectrum with an average energy of 0.5 MeV. However, the spectrum calculated by the model did not have the desired average energy and could not be used in DOT. Therefore, the source containing only 0.5 MeV neutrons was used.

A 2-D model of the torso region was examined in R-θ geometry too. The model used is shown in Figure 4. The same neutron sources were used as in the X-Y geometry model.

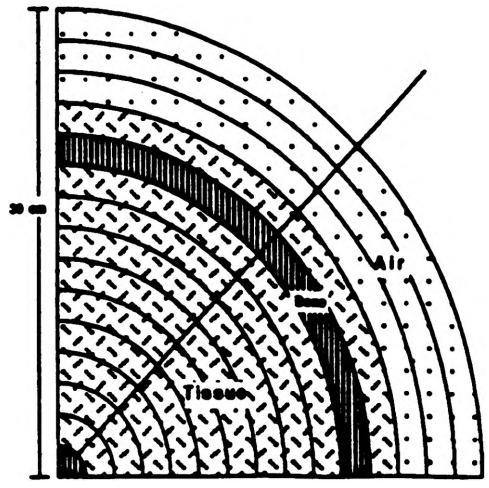

Figure 4. Model of Chest Area in R-θ Geometry.

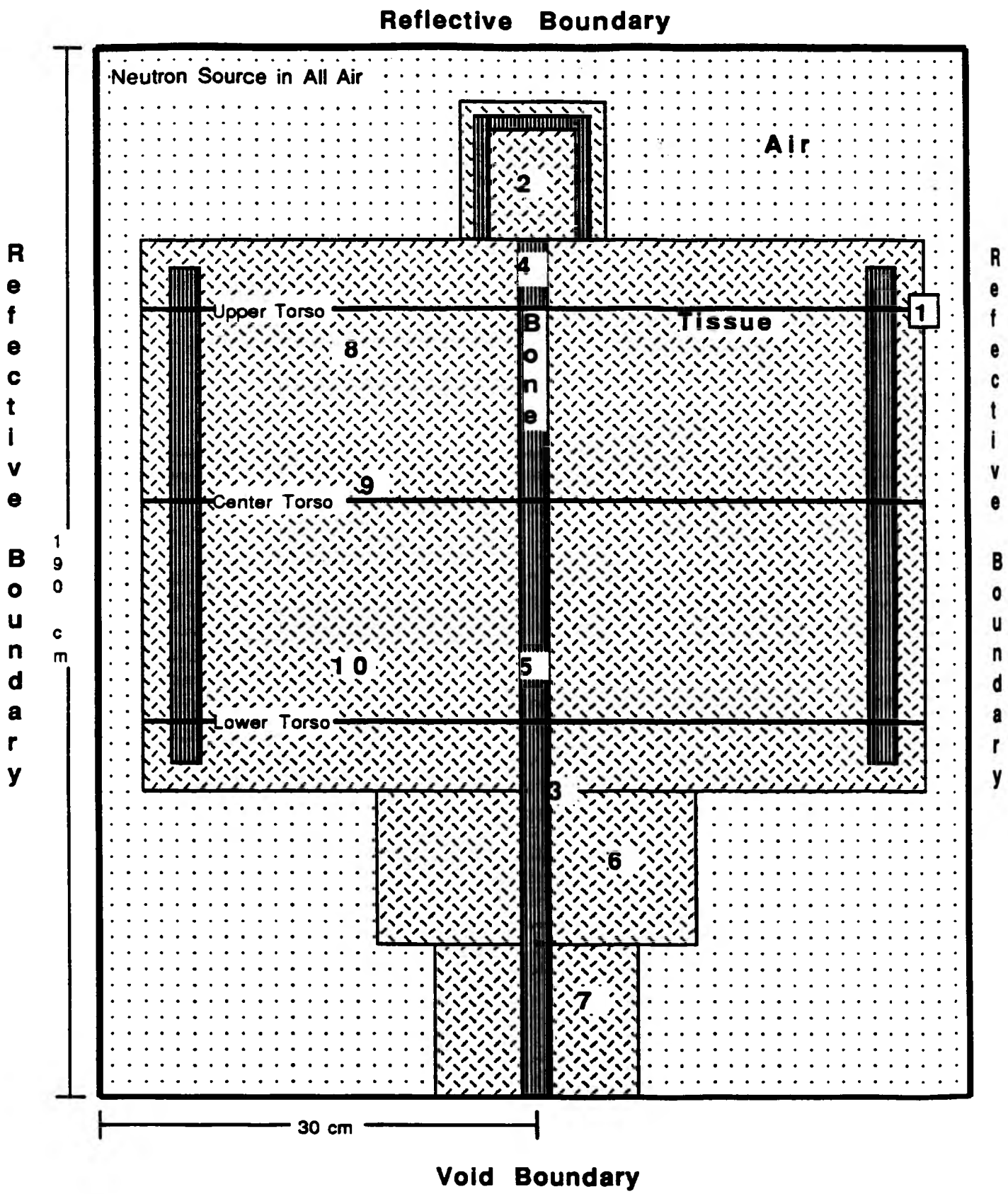

Figure 3. 2-D Model of Human Phantom.

NEUTRON DOSE

After the neutron fluxes were calculated by DOT, these fluxes were utilized in the calculation of the neutron dose at several points in the phantom. The fluxes were converted to radiation doses through the use of two different formulas. The American National Standard is the source of the flux-to-dose-rate conversion factors at different neutron energies. The first dose calculation used the 1990 version of the formula whereas 1977 conversion factors were used in the second calculation. These dose equations and there coefficients are shown in Table III.

Table III. Neutron Flux-To-Dose-Rate Conversion Factors.

Equation 1-1977 Version

Polynomial Coefficients In Analytic Fit-- Ln DF(E) = $A+B*X+C*X^2+D*X^3$.
DF(E) = (rem/hr)/(n/cm^2-s), E=neutron energy in MeV, and X=Ln E.

Neutron Energy (MeV)			A	B	C	D
2.5 -08	to	1.0-07	-1.2514+01			
1.0 -07	to	1.0-02	-1.2210+01	1.7165-01	2.603402	1.0273 -03
0.01	to	0.1	-8.9302	7.8440-01		
0.1	to	0.5	-8.6632	9.0037-01		
0.5	to	1.0	-8.9359	5.0696-01		
1.0	to	2.5	-8.9359	-5.5979-02		
2.5	to	5.0	-9.2822	3.2193-01		
5.0	to	7.0	-8.4741	-1.8018-01		
7.0	to	10.0	-8.8247			
10.0	to	14.0	-1.1208+01	1.0352		
14.0	to	20.0	-9.1202	2.4395-01		

Equation 2-1990 Version

Polynomial Coefficients In Analytic Fit-
$h(E)=10^{-12}*EXP(A+B*X+C*X^2+D*X^3+E*X^4)$ Sv-cm^2, E=Energy (MeV), and X=Ln E.

Neutron Energy Bounds	A	B	C	D	E
E<=0.01 MeV	2.42866	0.65022	0.08819	0.00475	0.00009
E>0.01MeV	4.22421	0.84705	-0.06771	-0.01213	0.00183

These doses were then divided by a reference "surface dose" which would have been read by a dosimeter on the phantom's chest to produce a relative dose. The dose just inside the body was much lower than that of the air just outside the body; therefore, all doses were divided by the average of these two doses to attain the reference "surface dose". The relative doses at several points of the body are shown in Table IV. The 1977 equation consistently gives lower dose rates for both energies. Figure 5 on page 8 shows the difference between the dose rates at the center of the torso for both dose equations. The difference between the two dose equations is greater for the 0.5 MeV spectrum. The dose at the center waist line of the phantom is about 4% of the dose

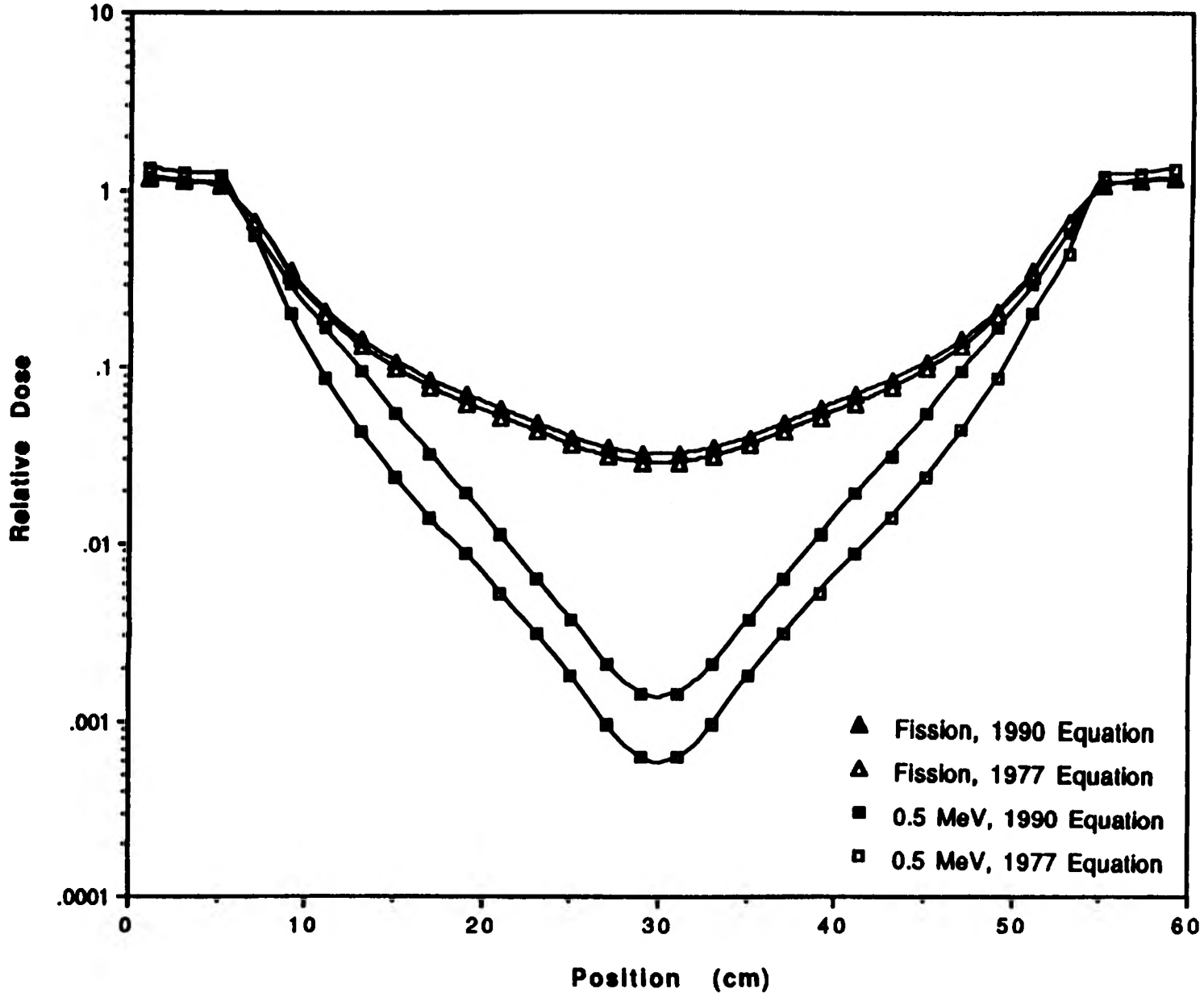

Figure 5. Relative Dose vs. Position at Waist Line Comparing 1990 and 1977 Dose Equations.

Table IV. Relative Dose Percent at Several Points in Phantom.

Position	Uranium Fission Spectrum		0.5 MeV Neutrons	
	1977 Equation	1990 Equation	1977 Equation	1990 Equation
Surface or pocket dosimeter position(1*)	1.00	1.00	1.00	1.00
Head(2)	0.30	0.33	0.13	0.46
Pelvic Region(3)	0.07	0.08	0.002	0.007
Upper Spine(4)	0.07	0.08	0.007	0.002
Lower Spine(5)	0.03	0.032	1.37E-4	4.61E-4
Upper Leg(6)	0.32	0.34	0.08	0.21
Lower Leg(7)	0.51	0.53	0.26	0.42
Mid-Region(8)	0.05	0.06	3.45E-5	7.11E-5
Mid-Region(9)	0.03	0.04	1.52E-4	5.26E-4
Mid-Region(10)	0.02	0.05	0.001	0.005

*Number corresponds to Figure 3 on page 6.

received at the surface for the fission spectrum source and only 0.1% for the 0.5 MeV source. This drop in dose is caused by the decrease in the neutron energy and flux as neutrons pass through the body.

The dose at the middle of the torso was calculated in X-Y and R-Θ geometry. Figures 6 and 7 on pages 10 and 11 show the relationship between the dose rate calculated in the X-Y and R-Θ geometries in DOT. In the X-Y geometry, three cross sections were examined; the upper, center, and lower torso as shown in Figure 3. The center-line of the model was used in the R-Θ geometry. In Figure 6 the source is the fission spectrum, while Figure 7 the 0.5 MeV source is examined. The R-Θ geometry matches X-Y geometry well for the fission spectrum especially at the upper and lower lines of the torso. It does not match as well of the 0.5 MeV source, however. The relationship between the dose at different cross sections for the two sources is shown in Figure 8 on page 12. The dose due to the 0.5 MeV source is lower than that of the fission source at all positions. The difference in the dose at the center of the torso is larger than that of the upper and lower torso.

CONCLUSION

Since, at the present time, it is impossible to measure the dose received by internal organs, empirical factors must be used to estimate the doses received by these organs. Using a computer model of a human body, the dose to these organs can be calculated by somewhat reliable transport codes such as XSDRNPM and DOT. The radiation dose relative to the "surface dose" that would be measured by a dosimeter was found at several places in the human phantom. These factors can be used to estimate the dose to internal organs when the "surface dose" is known.

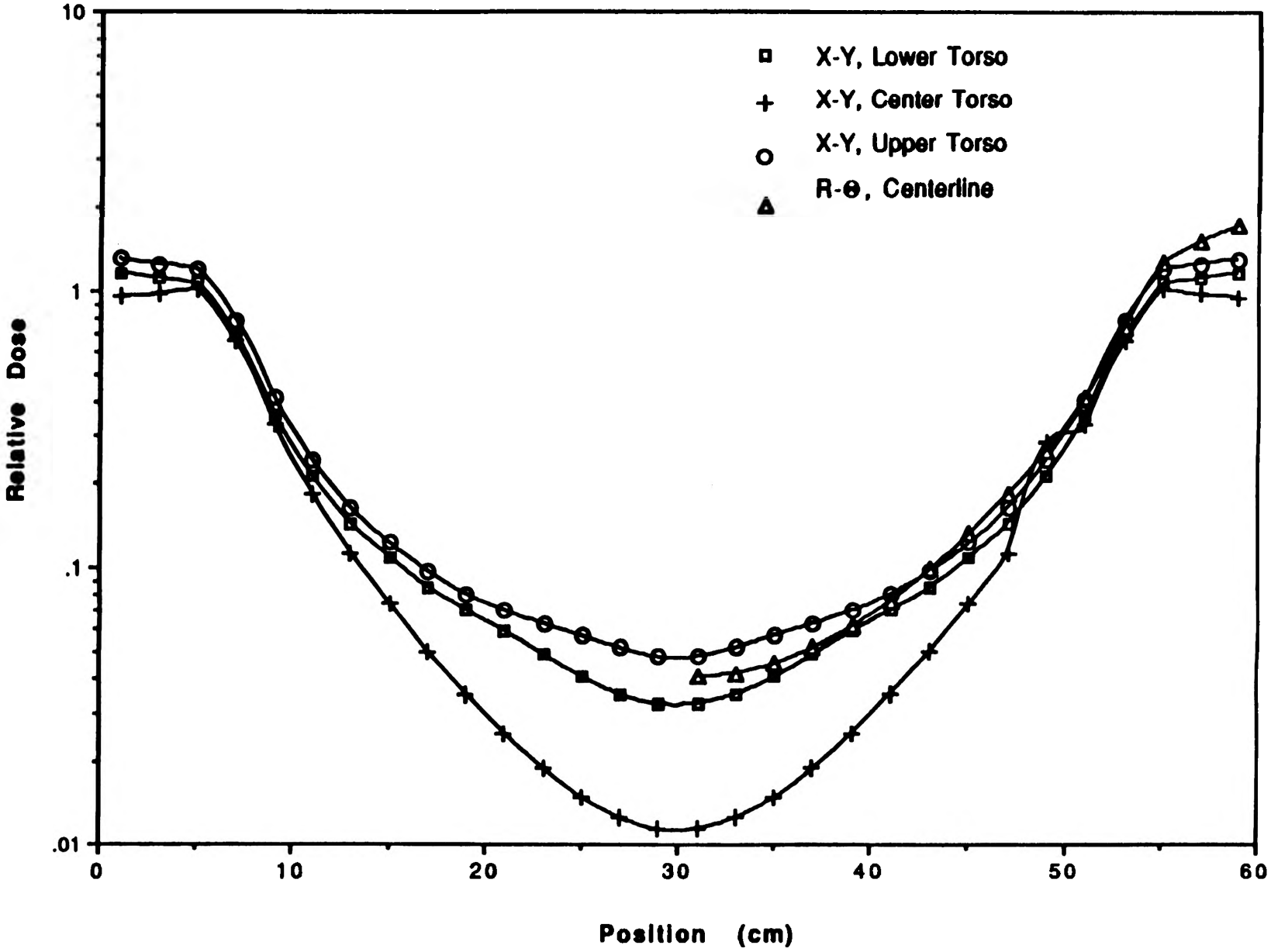

Figure 6. Dose vs. Position for R-O and X-Y Model for Fission Spectrum.

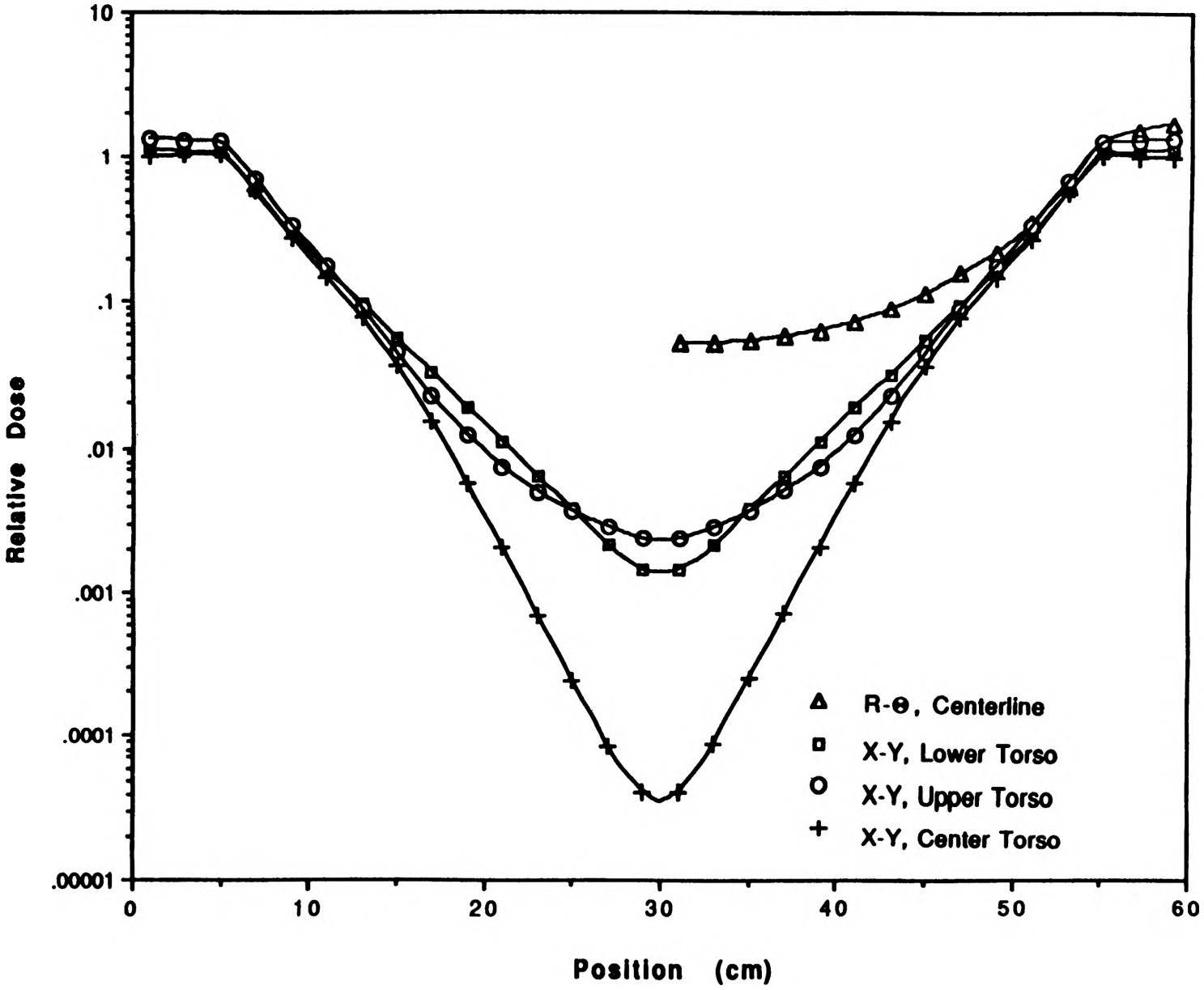

Figure 7. Dose vs. Position for R-O and X-Y Model for 0.5 MeV Spectrum.

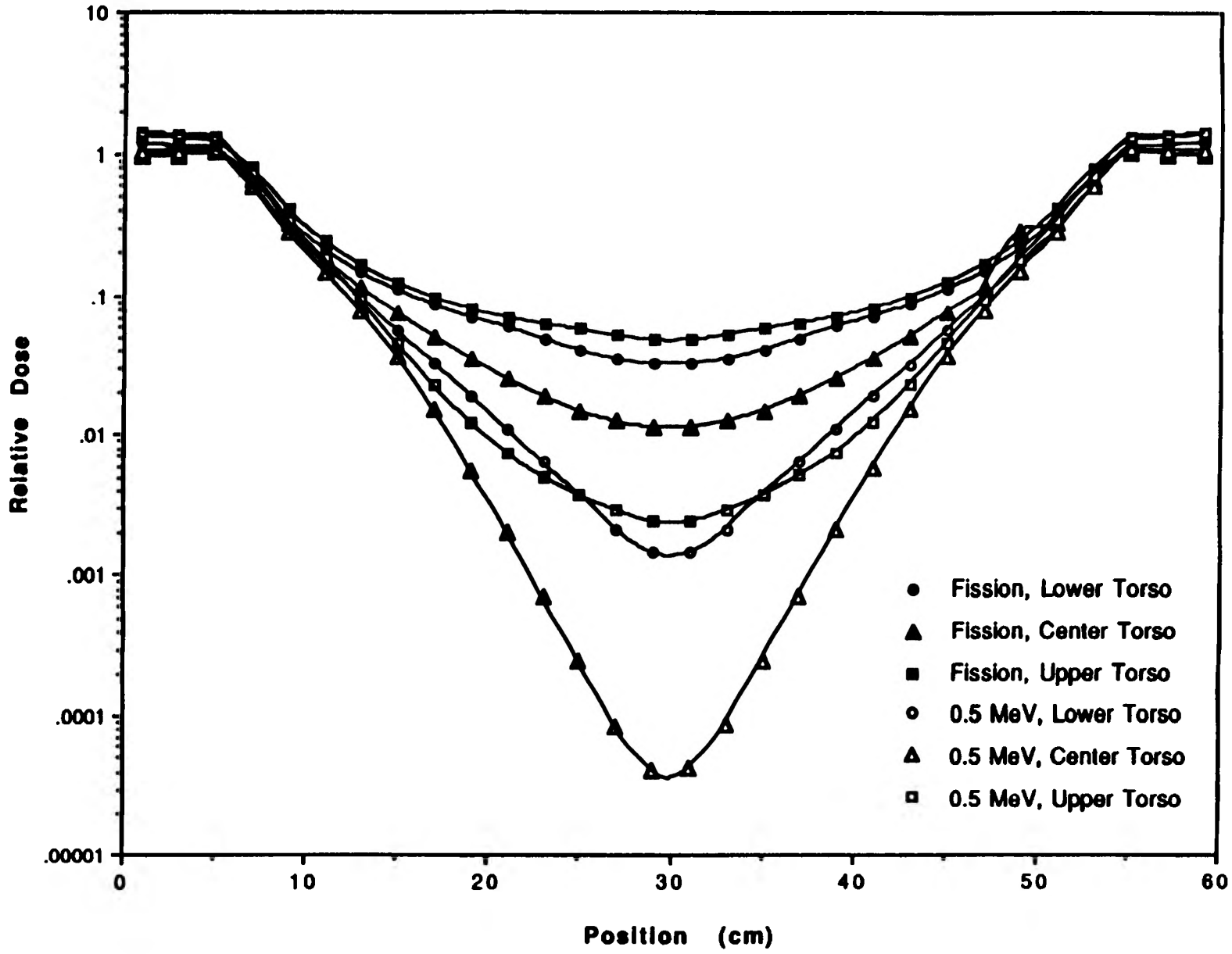

Figure 8. Dose vs. Position for Fission and 0.5 MeV Spectra.

A HEAT BALANCE PROGRAM FOR A NUCLEAR POWER PLANT

Timothy C. Steadham
Dept. of Nuclear Engineering

ABSTRACT

In a coal fired power plant, the steam leaving the boiler can reach 1000 °F and 3000 psia; this state is superheated considerably. On the other hand, a nuclear power plant is not capable of reaching such conditions without compromising reactor safety and integrity. Therefore, the steam leaving the reactor might only be a few degrees superheated, and hence the steam leaving each turbine will be wet. Since wet steam will erode turbine blades very quickly, devices must be placed between turbines to separate the steam into saturated vapor and saturated liquid. The steam is routed through the next turbine and the water is added elsewhere in the system (usually a feedwater heater, FH). This device is called a moisture separator, and my task was to add the FORTRAN code necessary to accurately model a moisture separator into an existing heat balance program.

INTRODUCTION

Background and Theory

Kam W. Li and A. Paul Priddy authored a heat balance program called AHBP [1], Advanced Heat Balance Program. Upon analyzing the program for a couple of weeks, the structure of the program became clear and the scope of the project was evident: there should not be too much code needed to add, in relation to the overall program.

The following figure gives a simplified schematic of a moisture separator (MS):

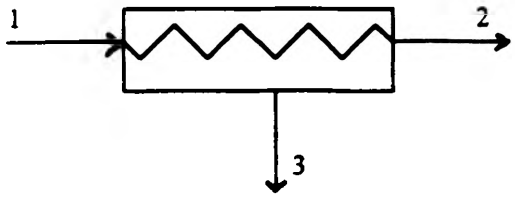

Figure 1. Simplified schematic of a MS.

State 1 is the steam entering the MS, state 2 is the saturated vapor exiting the MS, and state 3 is the saturated liquid leaving the MS. As with any component in a power plant, there is a pressure drop (DP) across the MS, so the temperature should be different leaving the MS. This temperature is the same as the saturation temperature at the decreased pressure. Moreover, since the steam leaving the MS has a quality of around 1.0, the conditions (enthalpy, entropy, and specific volume) at that point are equal to the conditions at point g on figure 2. Likewise, the conditions at point 3 are the same as point f on the same figure. This project required the addition of two Ms's, 1 between the HP and IP turbine, and one between the IP and LP turbine. The water is routed to a FH.

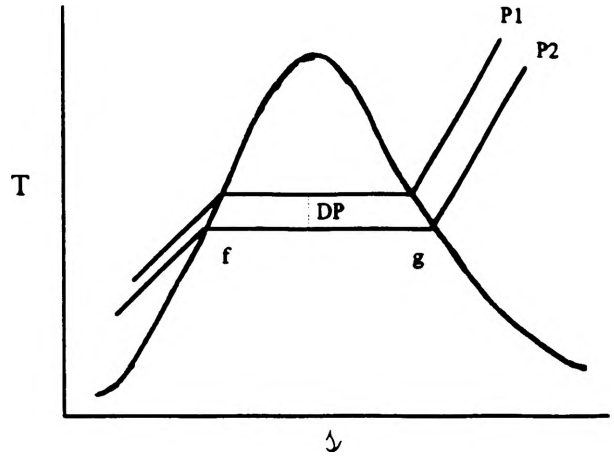

Figure 2. A simplified temperature-entropy diagram with a DP of P1-P2 for the MS.

PROGRAMMING ASSUMPTIONS

As with any generalized heat balance program, there must be some assumptions made which will limit the scope and degrees of freedom given to the user to model a particular solution. The assumptions made in the development of the MS code are:

- In fig. 2, P1 is the inlet pressure, and P2 is the outlet pressure
- The outlet temperature is, of course, the saturation temperature at P2, T2
- Point f has a quality of 0.0, and point g has a quality of 1.0
- There is no heat addition or work done on the MS control volume
- The water leaving the MS (point f) is routed to a FH, not the condenser
- The pressure of the extraction steam going to a FH is less than the pressure of the water leaving the MS going to the same FH
- There are only two MS's and they are found between the HP & IP turbines and the IP & LP turbines

Assumptions 1 and 2 are just simple applications of thermodynamic laws; however the third assumption is not. This assumption is based on the principle of an MS, and how it operates. The purpose of the MS is to separate the steam from the water, and to route the steam back into the turbine system, hence many MS's are coupled with a reheater. Additionally, this program is not concerned with how the separation is occurring but rather, what the final result is (i.e. a "black box" approach). Any heat added to the MS is neglected, and no work is assumed. For the sake of simplicity and without compromising educational value, this is a valid assumption as this code is not intended to be used as an official heat balance program for a commercial power plant.

The assumption that the water is routed only to a FH is a good assumption, also. However, in many nuclear power plants, this water is first sent to a drain cooler pump. Again, simplicity and ease of use demands that this assumption be used. The next assumption is based on the fact that, going into the MS, steam at one pressure and water at another will not mix well. There might be some form of "backwashing" into the line of lower pressure, so the water is assumed to be "flashed" to a lower pressure to match the incoming steam. Doing so changes the thermodynamic properties of the water, but simplicity and ease of use is still conserved. The reason why the water pressure is lowered is that flashing of the steam is physically harder and presents more problems than trying to flash the water. These problems and limitations are not addressed in this paper as they are of little consequence to the overall problem. Again, there must be some limitations in the program, and this was chosen to be one of them.

Finally, the program is assuming that there are only two MS's in the system, and that they fall between the HP and LP turbines and the IP and LP turbines. However, most nuclear power plants have more than two; usually four. Only two were used because educational value is not compromised and that ease of use and simplicity demanded it. If more than two MS's were used, then there would be lines routed to FH's and much more room for

user input data errors. To alleviate any problems like this, only two MS's are needed. A simplified sample schematic of a steam-turbine system is shown below in fig. 3.

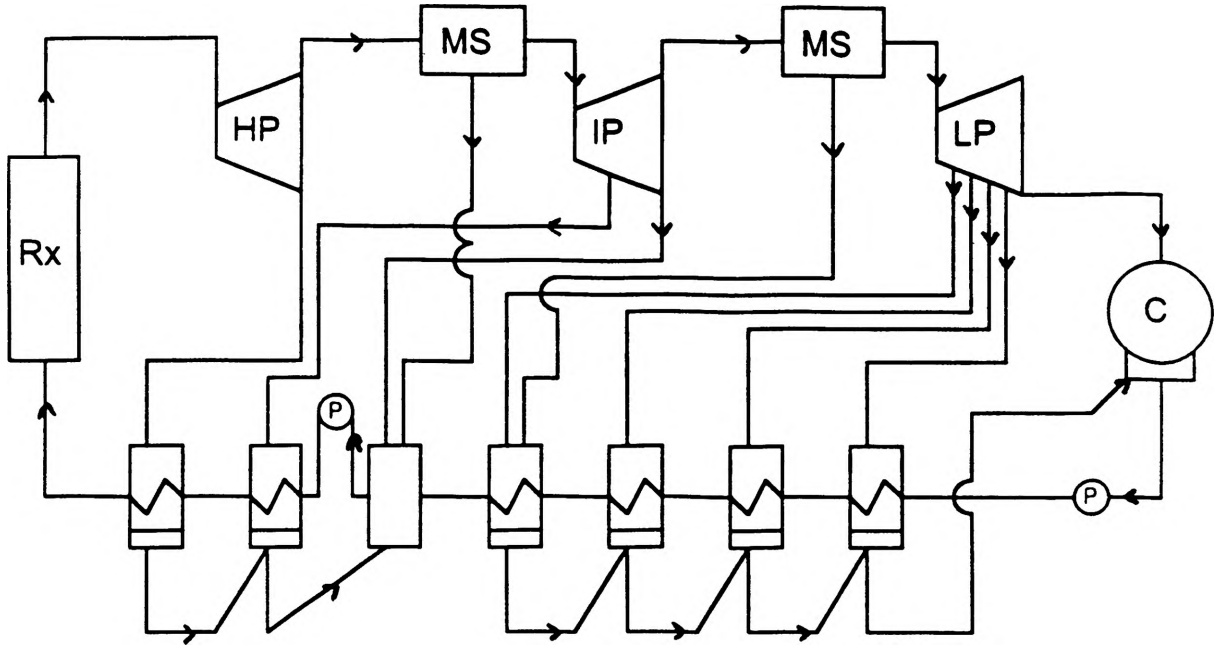

Figure 3. A sample steam-turbine system

FORTRAN CODE ADDITION

Preliminary

Since the general code is much too long, and the added code is more complex than this paper is meant to be, the actual code will not be included here. However, the process by which the code was generated will be explained. The heat balance code is separated into 11 sections. Since the program is so long, it was not feasible to search the entire code line by line for relevant parts. In response to this, all of the variables that were defined in the program were examined. In this list, the variables that looked relevant were highlighted. Using a text editor, a search throughout the entire document was performed on all of the variables. Reading the code around the points that the searches stopped at, and noting any relevant lines, the parts of the code that needed to be changed were quickly found. Upon later checking the entire program, it was concluded that these points were indeed the only places where code needed to be added. In short, the added code encompasses the following ideas:

- Changing of input data to include input for the Ms's
- Changing of read input data line in code to include MS variables
- Changing of turbine steam outlet/inlet conditions
- Changing of mass flow rate calculations
- Changing of the output data

Each of the changes necessary are described below.

The input data was the easiest, by far, to change. There was a small problem with the format specifiers, though, but the changes were:

- Delete the reheater outlet temperature
- Add two more variables detailing where the outlet water from each MS goes (i.e. which heater)
- Add the pressure drop over the MS

Where appropriate, a read line was added to the code to read in the new values for the new variables.

As can be seen from fig. 3, the inlet conditions for the IP and the LP turbines may change. Depending on whether or not the steam is saturated coming out of the HP or LP turbine will determine if a MS is needed. If a MS is not needed, then obviously the outlet conditions of one turbine will be the same as the inlet conditions for the next turbine. However, if the steam is in the saturated state, then the conditions will change making the outlet for one turbine different from the inlet of the next turbine.

First, a pressure drop is encountered in the MS. Assuming that the steam and water is going to leave the MS at the same spot, they should be at the same pressure. Since both the steam and the water is saturated, it follows that they should also be at the same temperature. It can also be concluded that the steam outlet conditions of the MS are the same as the inlet conditions of the next turbine. Additionally, referring back to fig. 2, the steam conditions are evaluated at point g, and the water conditions are evaluated at point f. Also, the conditions are evaluated at the outlet pressure, not the inlet. It is assumed that there is no heating of the steam during the process of separating the moisture from the steam.

Next, from the second law of thermodynamics [2], the energy balance around the MS (referring back to fig. 1) is:

$$W_{rev} = \sum m_i\left(h_i + \frac{V_i}{2} + gZ_i\right) - \sum m_e\left(h_e + \frac{V_e^2}{2} + gZ_e\right) \qquad (1)$$

Assuming $W_{rev} = 0$, $V_i = V_e$, and $Z_i = Z_e$, eq. 1 can be rewritten as

$$m_1h_1 - m_2h_2 - m_3h_3 = 0 \qquad (2)$$

$$m_3 = m_1 - m_2 \qquad (3)$$

$$m_1h_1 - m_2h_2 - (m_1 - m_2)h_3 = 0 \qquad (4)$$

Reducing eq. 4 yields

$$m_2 = m_1\frac{h_3 - h_1}{h_3 - h_2} \qquad (5)$$

Equation four was used in the mass flow rate calculation around the MS. Now knowing m_2,and m_1, m_3 can be found using eq. 3. If a MS is used, then the mass flow rate entering the turbine is the same as m_2. If a MS is not used, then the outlet mass flow rate from one turbine is the same as the inlet mass flow rate for the next turbine. Eq. 5 was entered into the program in the appropriate place, and other minor changes that needed to be made were done so. Additionally, the same methodology was used for the mass flow rates around the FH's.

To change the output, all mentions of a reheater were changed to read the corresponding value for the appropriate MS. For example, the output that originally read "Reheater outlet temp." was changed to read "First MS outlet temp." All output was done for both MS's, and they are distinguished by either "first" or "second," as the previous example shows.

After the output was changed, all of the modifications that were thought to have been needed were made. With the exception of making a few changes to some equations for partial load case, the program was finished.

CONCLUSION

The code for the MS, along with all of the required equations, has been tested, and they seem to be correct. In addition, the installation of the various parts of the code is still being performed. The final program, with the required MS's, should be ready by the time that the next group of students require the program for a design project.

NOMENCLATURE

Throughout this paper, the following abbreviations are used:

- "MS" stands for "moisture separator"
- "FH" stands for "feedwater heater"
- "point f" refers to the point on the steam dome with a pressure, P, and quality 0.0
- "point g" refers to the point on the steam dome with a pressure, P, and quality 1.0
- "water" is the saturated liquid which will be put back into a FH
- "steam" is the saturated vapor which will be put back into the next turbine in the series
- "HP" is the high pressure turbine
- "IP" is the intermediate pressure turbine
- "LP" is the low pressure turbine

ACKNOWLEDGMENTS

I would like to thank the following people for their valued help:

- Dr. Edwards, my advisor on this project, for his help and patience with me
- Dr. Mueller for his valued comments on the subject
- The graduate office for their involvement in promoting undergraduate research

REFERENCES

1. Li, K.W. and Priddy, A.P., "Advanced Heat Balance Program."
2. Van Wylen, G.J., Fundamentals of Classical Thermodynamics, 3rd Edition, SI version, John Wiley and Sons, Inc., 1985, pg. 258.

BEHAVIOR OF COMPOSITES FOR THE NASP PROJECT*

Robert B. Stone
Department of Mechanical and Aerospace Engineering
University of Missouri-Rolla
Rolla, MO 65401-0249

ABSTRACT

It is well known that ceramics are strong, highly heat resistant, refractory materials. Unfortunately, they are brittle and fail catastrophically. However, the strength as well as fracture toughness of ceramics can be greatly improved with the addition of continuous fibers, thus obtaining ceramic matrix composites (CMC). Normally the addition of aligned continuous fibers to a matrix degrades the transverse (the direction 90° to the fiber axes) properties while greatly improving the longitudinal properties. It has been shown that the addition of whiskers to a continuous fiber CMC will improve moduli and strength properties in both the transverse and longitudinal directions. Any improvement in the transverse direction is a tremendous advantage as loads may not always act along the longitudinal fiber direction, thus avoiding the necessity for lamination and angle plies.

Strengthening ceramics by the addition of fibers and whiskers can hopefully produce a reliable refractory material that will offer service on the National Aerospace Plane (NASP) and other related space/hypersonic vehicles. If CMC can be shown to have high strength and toughness, they could fill a spot on the nosecap, leading edge surfaces as well as primary structures of the NASP.

* This work was supported by OURE (UMR Opportunity for the Undergraduate Research Experience Program), NASA Missouri Space Grant Consortium, and L. R. Dharani, faculty advisor.

BEHAVIOR OF COMPOSITES FOR THE NASP PROJECT

Robert B. Stone
Department of Mechanical and Aerospace Engineering
University of Missouri-Rolla
Rolla, MO 65401-0249

INTRODUCTION

Ceramic matrix composites (CMC) are well known to withstand high temperatures (1000°C and higher).1,2 This characteristic immediately made CMC a contender when the materials search was begun for the National Aerospace Plane (NASP).3 CMC were considered for nose cap and leading edge structures of the NASP, areas that must withstand extremely high temperatures. But before this potential use is achieved, CMC must overcome their poor transverse properties.4

Reinforcing the brittle CMC with continuous fibers increases its strength and fracture toughness in the direction of the fibers while degrading the transverse direction strength.5 The addition of randomly oriented fibers is theorized to improve the transverse properties of unidirectional fiber reinforced composites. This paper details the research undertaken to test this theory as part of an undergraduate research opportunity.

MATERIALS

Any material that can be considered for use on a hypersonic or NASP application must meet more demanding requirements than ordinary materials. The inherent properties of ceramic matrices meet these requirements: a high oxidation resistance, a high melting point, low coefficient of thermal expansion and chemical compatibility of fiber and matrix. The matrix used was a 8-10 micron cordierite powder from Ferro. Its properties are given in Table I. Continuous silicon carbide fibers were obtained from UBE Industries. Silicon carbide whiskers from the American Matrix Company were used to form the hybrid matrix. Fiber and whisker properties are given in Table II.

Table I. Properties of the Cordierite Matrix

Melting Point (°C)	Density (g/cm^3)	E (GPa)
1410	2.65	110

Table II. Properties of the Silicon Carbide Fibers and Whiskers

E (GPa)	Density (g/cm^3)	Diameter (μm)
200	3.2	16

CMC FABRICATION PROCESS

The fabrication process of CMC is at best time consuming. Four specimens were prepared: matrix (M), matrix-whisker (MW), matrix reinforced with unidirectional fiber (MF) and matrix-whisker reinforced with unidirectional fiber (MWF). Reviewing the fabrication techniques of Carroll et al[2], essentially the same method was followed. The matrix was cordierite powder and the reinforcing fibers and whiskers were silicon carbide.

Pre-Preg Fabrication

The cordierite specimen was easily fabricated. Powder was measured to produce a 76mm diameter disk approximately 3mm thick. The powder was then hot pressed. To adequately mix the cordierite and silicon carbide whiskers for the matrix and whiskers specimen, the components were ball milled in an isopropyl alcohol mixture for 6 hours. The alcohol was then dried off, the powder finely ground and hot pressed.

One of the major concerns of producing fiber reinforced composites is obtaining a even mixture of matrix and fibers.[6] Continuous fibers are contained in a tow of approximately 10,000 close packed fibers and complete wetting of the fibers by the matrix is difficult. Considerable care was taken to insure that maximum fiber wetting was achieved during the fabrication of the continuous fiber reinforced composites. A slurry of cordierite powder, water and organic binders was ball milled overnight. The mass of cordierite used was 165g, enough to produce one disk. The following day the unidirectional prepregs were wound. As shown in Figure 1., the silicon carbide fibers were passed across a flame to release the fiber bundle and then passed through the continuously agitated slurry via a set of rollers. From there, the slurry coated fiber was passed in front of a compressed air nozzle to remove excess slurry and then wound onto the octagonal drum. Three layers of fiber were wound onto the drum, completely exhausting the slurry supply. It was decided to use three layers so that a specimen could be made from one winding. The prepreg was allowed to dry overnight and then it was cut into 76mm diameter disks. Care was taken to assure that the laminae were unidirectionally aligned. The organic binders were burned off of the prepregs in a small oven and then hot pressed. The organic burn-off schedule is presented in Table III.

Figure 1. Pre-Preg Winding Process for CMC

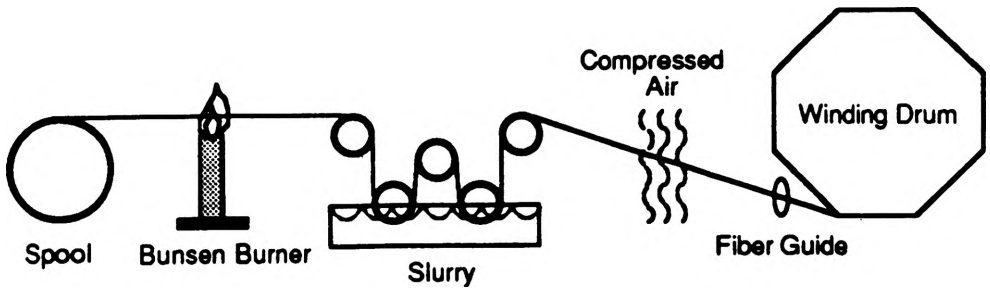

Table III. ORGANIC BURN-OFF SCHEDULE

Temperature (°C)	Burn Duration (hr)
120	1
250	1.5
450	4

The same procedure was followed for the hybrid matrix, whisker and fiber specimen. The slurry contained a 30% V of whiskers. It was prepared as the matrix only slurry with the total mass of cordierite and silicon carbide whiskers totalling 165g. The winding and hot pressing procedures were the same as those of the matrix and fiber specimen.

Hot Pressing

All specimens were hot pressed in a glassy state in a 76.2mm (three inch) graphite mold at 13.8 MPa (2000 psi) and 900°C. The specimens were gradually heated to 900°C and pressure was applied at 500°C. When the specimens reached 900°C, they were held at that temperature and pressure for one hour. All hot pressing was done at McDonnell Douglas Research Laboratory in St. Louis, MO.

Following the hot pressing, a final heat treatment was required to recrystallize the matrix. Table IV. presents the firing schedule that was used.

Table IV. Recrystallization Heat Treatment

Ramp Time (min)	Temp. (°C)	Soak Time (min)
30	275	60
360	815	180
480	950	No Soak
120	1150	120

POROSITY

A good test of the fabrication process is the final density of the composites. Experimental density was calculated by:

$$\rho_a = \frac{m}{\pi (d^2/4)\, t} \qquad (1)$$

where m is the mass of the disk, d is the average diameter and t is the average thickness of the disk. The actual densities were compared with the theoretical densities which were calculated by the following rule of mixture:

$$\rho_t = \rho_f V_f + \rho_m V_m \qquad (2)$$

where ρ_f is the known density of the silicon carbide whiskers and fibers, V_f is the volume fraction of SiC fibers and whiskers, ρ_m is the known density of the cordierite powder and V_m is the volume fraction of matrix. The comparison and subsequent porosity levels are presented in Table V.

Table V. Porosities of Specimens

Composite System	Density (g/cm^3) Theoretical	Actual	% Void
Matrix	2.65	2.59	2.3
Matrix & whiskers	2.82	2.16	33.3
Matrix & fiber	2.87-2.98	1.88	35.0
Matrix,whisker & fiber	2.87-2.98	2.15	26.0

The matrix densified the most, yielding a calculated density of 97.7% of the theoretical density of the cordierite matrix. The continuous fiber reinforced disks were much worse with porosity values of 30-35% of the total disk volume. Possible explanations for these porosity levels have been explored. The most likely problem in the fabrication process is the hot pressing procedure. It is hypothesized that residual organic gases may become entrapped within the pressing die. The three specimens that exhibit the lowest densities all have organic mixers involved in their pre-pressing fabrication. Other work on CMC has produced densities of 99.7% of the theoretical value[6].

TESTING

To test the transverse properties, the four disks were cut into rectangular blocks at least 57.15cm long. Cross section dimensions of the specimens varied: matrix - 5.9mm by 4.3 mm; matrix and whisker - 6.7mm by 4.6mm; matrix and fiber - 5.9mm by 4.2mm; and matrix, whisker and fiber - 5.9mm by 3.2mm. The specimens were cut at a 90° angle to the continuous fiber direction so that the fibers were perpendicular to the length of the specimen as shown in Figure 2.

Figure 2. Fiber Orientation of Transverse CMC Specimen

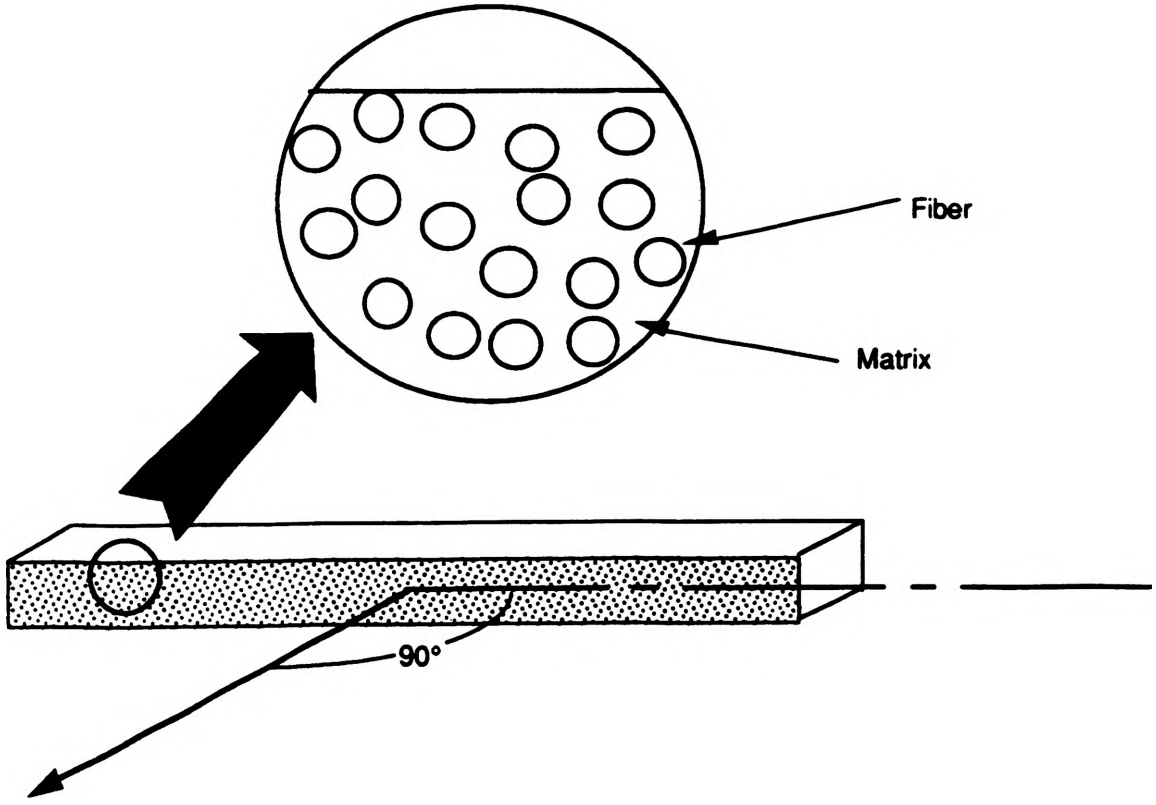

It is well known that in brittle materials the normal tensile test cannot easily be performed due to presence of flaws at the surface.[7] Even though this is a well established fact, a tensile test was attempted. It was proposed that the addition of the fibers might toughen the CMC enough to allow a tensile test. The specimens failed at very low stresses of the order of 600kPa (approximately 100psi). The tensile tests were conducted on a MTS loading frame with hydraulic grips specially designed for composite materials. It was determined that there was a slight misalignment of the grips, thus inducing bending stress as well as axial stress and

possibly explaining the failure at low stresses. This problem will be corrected before future tensile tests are performed.

The standard test for brittle materials is the three-point bend test where the modulus of rupture is measured. A schematic of the three-point bend test is given in Figure 3. The load P is applied at midspan of the specimen which is supported by the two rollers beneath it. At the location of the applied load, the top of the specimen is in compression while the bottom experiences a tensile stress. Failure always initiates from surface that is in tension and thus at failure, the measured stress is the ultimate tensile strength.

Figure 3. Three-Point Bend Test Setup

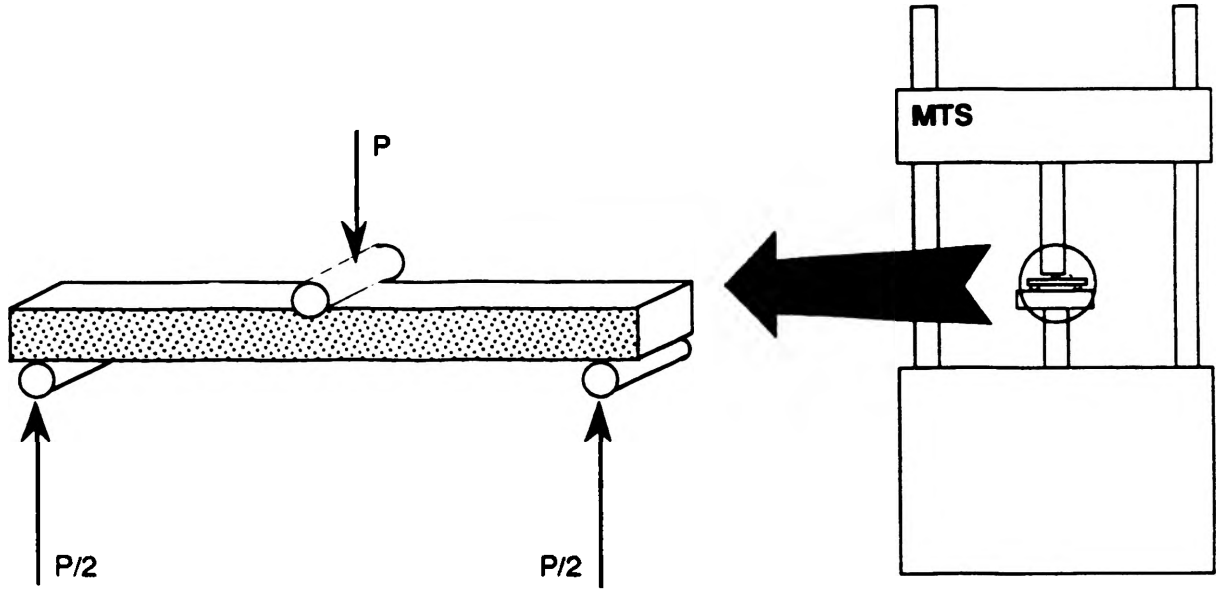

The three-point bend tests were conducted on a MTS loading frame at room temperature. All four types of CMC were tested at a span of 38.1mm (1.5 in) and had a span-to-depth ratio >8.0. The matrix and matrix and whiskers were loaded at a cross-head speed of 0.127mm/sec and the matrix and whisker and matrix, whisker and fiber were loaded at a speed of 0.254 mm/sec. Previous attempts at using an extensometer to measure deflection had not produced significant improvements in deflection reading so the cross head displacement was used for the deflection reading. Testing data (load and displacement) was stored on a PC via a data acquisition program and connection to the MTS Microconsole.

RESULTS

Results of the three-point bend test are given in Table 6. The modulus of rupture or the ultimate tensile strength is given by:

$$\sigma_u = \frac{3\,PL}{2\,bh^2} \qquad (3)$$

where P is the applied load, L is the span and b and h are the width and height of the specimen, respectively.

Table VI. Results of the Three-point Bend Test on 90° Fiber CMC

CMC Type	σ_{tu} (MPa)	L/h
Matrix	112	8.88
Matrix,whisker	145	8.24
Matrix, fiber	25	9.04
Matrix, whisker,fiber	47	11.78

Three specimens of each group of CMC were tested. The values of the ultimate tensile strength given in Table VI represent the average of the three specimens' measured ultimate tensile strength. The test results show that the transverse strength of the CMC can be improved by the addition of whiskers to the matrix. An improvement in ultimate strength of 88% is indicated above. While the failure is still brittle, failure of the matrix, whisker and fiber CMC was less catastrophic as an initial crack was observed momentarily before failure. Failure of the matrix and fiber CMC was quick and catastrophic.

Figure 4. shows the toughening effect of the whiskers on the transverse properties of the matrix, whisker and fiber. The initial change in slope represents the point of matrix cracking and the whiskers provide additional load carrying capability past that point.

Figure 4. Toughening Effect of Whiskers on Transverse Direction

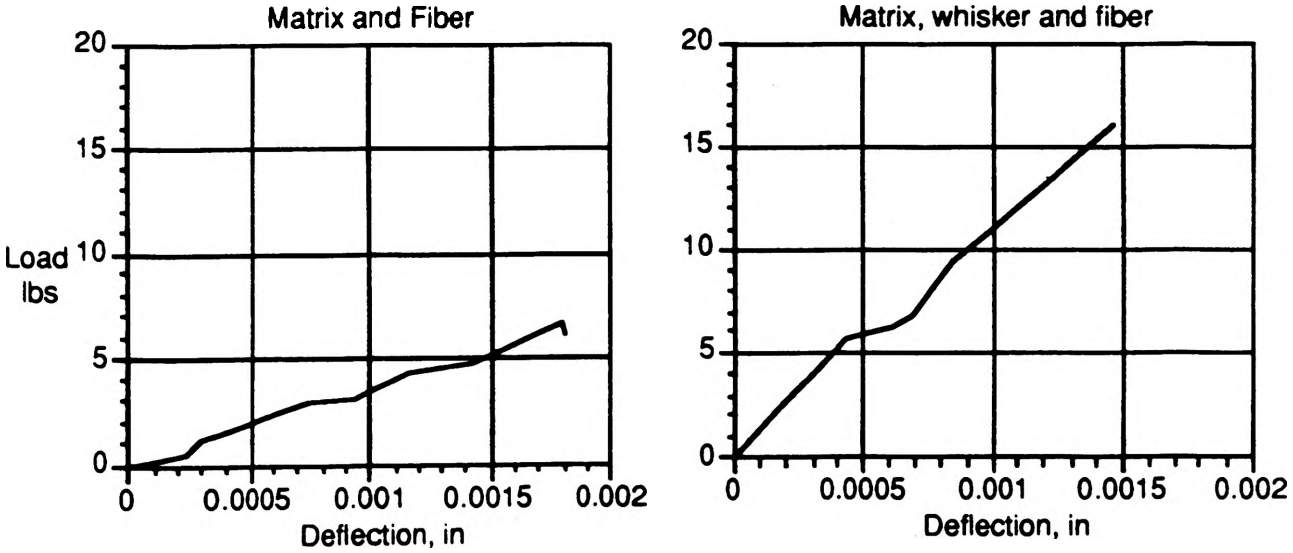

These test results are encouraging. It has been shown that the addition of whiskers to the matrix increase the longitudinal properties of CMC, and it appears that whiskers offer considerable improvement of transverse properties as well.[2,6] Any improvement in the transverse properties is welcome as there are few cases of purely axial loads. Unexpected loads acting in directions other than the fiber direction can now be more confidently carried.

Conducted at room temperature, the conclusion stated above must be qualified. If CMC are to be considered for the NASP and other future hypersonic vehicles, high temperature testing must be performed to complete these findings for the transverse properties. Porosity does affect the strength of the CMC, but the results presented here do serve as a valid comparison of strengths of four classes of CMC.

ACKNOWLEDGEMENTS

The author would like to express his gratitude for the instruction and assistance of Dr. Lowkesh R. Dharani, Ph.D., faculty advisor, Dr. Doug Carroll, Ph.D., and Gopal Padmanabhan on this project.

REFERENCES

1. Hyde, A. R., "Ceramic Matrix Composites," *Materials & Design,* Vol. 11, No. 1, p 30-36, February 1990.

2. Carroll, D. R., L. R. Dharani and D. Y. Yeng, "Hybrid Ceramic Matrix Composites: Mechanical Properties and Failure Modes," Private communication (1991).

3. McConnell, Vicki P., "The National Aerospace Plane: A New Regime in Flight," *Advanced Composites,* p 37-45, November/December 1990.

4. Fukuda, H. and T. W. Chou, "Stiffness and Strength of Short Fiber Composites as Affected by Cracks and Plasticity," *Fibre Science and Technology,* p 243-256, 1981.

5. McDonough, W. J., "Ceramics Composites, A new class of structural materials for utilization in advanced heat engines," *ASTM Standardization News,* p 44-49, October 1987.

6. J. Aveston, "Strength and Toughness in Fibre-Reinforced Ceramics," pp. 68-73.

7. Askeland, Donald R., *The Science and Engineering of Materials,* Boston: PWS-Kent Publishing Company, 1989, pp. 155-156.

AN INVESTIGATION INTO THE ENGINEERING CONSIDERATIONS REQUIRED TO DESIGN AN ULTRA LOW NOISE LOGARITHMIC AMPLIFIER FOR AN ULTRASOUND IMAGING SYSTEM

Michael Wilhelm
Electrical Engineering Dept.

ABSTRACT

Ultrasound imaging instruments and other "radar" type systems frequently employ variable gain amplifiers to effectively process signals of high dynamic range. One such device uniquely suited for this task is the logarithmic amplifier. Presented in this paper are many of the key design issues and solutions concerning the enhancement of one particular company's ultrasound system.

INTRODUCTION

Ever since Lee DeForest created the first true power amplifier, uncountable man hours have been spent developing linear devices and circuits. Occasionally the need arises for a nonlinear amplifier. Logarithmic amplifiers, or log amps for short, are typically employed in systems where it is advantageous to compress a signal of large dynamic range into one of much smaller dynamic range. An ultrasound imaging instrument is one such system. These systems must recover and process signals which have been highly attenuated due to scattering and losses. In many scanners only the relative amplitude of the signal and its time of arrival are important. Log amps may be used compress these signals and allow the inspection of relative changes in the signal's amplitude as opposed to its absolute value.

There are four basic topics which must be tackled in proper order:

1) The requirements of the amplifier must be determined. A successful design requires the marriage of an amplifier to the sensor, the converse will not work.

2) Low noise design concepts must be understood before a circuit can be optimized for low noise.

3) A log amp must be chosen which will best fit the needs of the system. A "drop-in" replacement for the current amplifier is highly desirable.

4) Practical considerations always require some preplanning and compromises.

Due to publishing constraints the length of this article has been limited. The interested reader is welcome to contact the author for a more detailed report.

AMPLIFIER REQUIREMENTS

The Transducer:

The key element of any ultrasound instrument is the transducer; it is the backbone of the system. This cannot be overstressed. For an engineer or product development team engaged in the design of a new ultrasound system, the selection of the piezoelectric element will be one of the first and most important design decisions made. The two primary specifications for the finished product will be its scan depth and its resolution. To achieve high resolution, a sensor must be chosen having a characteristic frequency such that the wavelength of acoustic energy in the media will be approximately the same size as the smallest object to be sought during a scan. To achieve an adequate scan depth, the sensor must be capable of converting any returning ultrasound waves into electrical signals for processing. No amount of creative signal processing can retrieve a signal where there isn't one to be recovered.

In the system under consideration, the sensor was not specifically chosen to meet the acoustic requirements but was instead chosen to meet stringent mechanical requirements which allow the instrument to fulfill unique medical needs. This is not surprising since all designs of reasonable complexity require compromises during their construction. However, in order to meet the ever present demands of competition the manufacturer wishes to increase the scan depth of the instrument without changing transducers. Thus the engineer is faced with the task of optimizing the second most important component in the system - the logarithmic amplifier.

As mentioned above, a transducer must be selected to meet the needs of the designer and in order to meet the scan depth requirement the engineer must insure that the transducer will still provide an output in response to the waves which are highly attenuated upon their return to the probe. All electrical devices whose temperature is above absolute zero will produce thermal noise. It is this noise which represents the fundamental limit of sensor usefulness.

Determining the Transducer's Noise Level:

Noise data was not available from the transducer's manufacturer and thus it was determined experimentally. Thermal noise may be calculated from the equation [1]:

$$V_t^2 = 4\ k\ T\ R(f)\ dF \qquad (1)$$

where: V_t = total RMS noise voltage
k = Boltzman's Constant, 1.38×10^{-23}
T = temperature, °K
$R(f)$ = resistance or real portion of impedance
dF = bandwidth or element of integration

Ultrasound pulses launched by the element into the media consist of about three cycles of a 10MHz sinusoid. An examination of the spectra of this pulse showed a significant amount of energy up to and beyond 25MHz. If the instrument is to have sharp resolution then the log amp must therefore have wide bandwidth, covering the range of about 5MHz to 25MHz. With a reasonable bandwidth in hand, the overall minimal noise voltage may be predicted from equation 1.

To use equation 1, the input impedance of the complete probe assembly needed to be determined over the band of interest. Impedance measurements were made at frequencies from 1MHz to 20MHz in 2MHz intervals (the range of the available equipment). Using these data points the thermal noise was estimated by trapazoidally integrating $Re\{Z_{in}\}$ over the 1MHz to 20MHz band. These calculations showed that the thermal noise mechanism contributes about 3uV of noise voltage over this frequency range. However, the transducer is a resonant device and the resistive portion of the impedance was increasing rapidly above 15MHz. I suspect that a significant amount of noise will be contributed by the sensor in the 20MHz to 25MHz band. A conservative estimate of 6uV of noise will be used to compensate for what could not be measured.

LOW NOISE DESIGN

The Noise Model:

An excellent source of information is the book: Low Noise Electronic Design by Motchenbacher and Fitchen [4]. I can't begin to present all of the pertinent details of noise analysis without simply plagiarizing their work. However, I will point out the significant details as they apply to this project.

Motchenbacher and Fitchen recommend the following model be used for noise analysis:

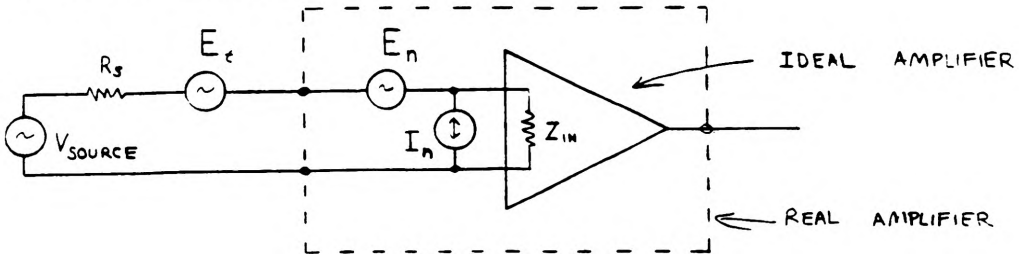

FIGURE 1, The noise model

Both E_n and I_n are required to adequately represent the function of the amplifier.

Since we are dealing with AC sources of different frequencies it is not permissible to simply add the effects of these sources. The resultant noise quantity must be calculated from the square root of the sum of the squares if the sources are uncorrelated. Since the adopted convention is to use power

in all noise calculations, the square noise voltage will be handy to work with. Hence if we want to find the effect of multiple uncorrelated noise sources we may apply superposition to square of each noise source and obtain a resultant square noise voltage.

For the above noise model the expression for equivalent input noise is:

$$E_{ni}^2 = E_t^2 + E_n^2 + I_n^2 R_s^2 \qquad (2)$$

E_n may be determined by setting $R_s = 0$, measuring the amplifier's output, and dividing by its gain. I_n will be producing an input voltage via the amplifier's input resistance and thus may be found by replacing R_s with a large resistance (remove the probe from the log amp input), measuring the amplifier's output, and dividing by its gain. E_n and I_n vary with frequency, Q-point, and type of input device.

For the noise model above, it can be shown that the noise figure may be represented by:

$$NF = 10 \log \frac{E_t^2 + E_n^2 + I_n^2 R_s^2}{E_t^2} \qquad (3)$$

$$\text{where } E_t^2 = 4\ k\ T\ R(f)\ dF$$

It should be pointed out here that if the NF of an existing system is 3dB or lower, then at least half of the noise is emitted from the source. Further reductions in the noise of the amplifier will provide little improvement.

To obtain the smallest contribution of noise from the amplifier we must somehow adjust the input resistance of the amplifier such that the total equivalent input noise reaches a minimum value. So, do we make $R_{in} = R_s$? No! This only maximizes signal flow from sensor to amplifier, it has absolutely nothing to do with minimizing noise. To minimize E_{ni}^2, we must find R_s such that NF is at a minimum, or $dNF/dR_s = 0$. Solving for R_s yields: $R_s = E_n/I_n$. This is very important. If we have the luxury of adjusting the biasing of the amplifier (and hence R_{in}), it may be possible to minimize noise and maximize signal power flow at the same time. Unfortunately it's not that simple when R_s is a function of frequency and it's even worse when the source has resonance points. Perhaps an impedance equalizing network can be placed between the probe and the log amp. An arrangement such as this will make noise reduction much simpler.

Choosing the Best Semiconductor Device:

To achieve good noise characteristics, the signal source must be followed by the proper amplifier. Bipolar transistors are best suited as input devices in amplifiers where a low impedance source must be used (50Ω to 1KΩ). Higher impedance

sources work best when followed by FET input amplifiers (R_g = 100KΩ and up). When the source impedance is very low a transformer may be required to bring the impedance up to a more manageable level.

This application would seem to call for a bipolar input stage since the average value of R_g is around 20Ω, but not just any bipolar device will do. Careful consideration must be employed when selecting a transistor. For instance, PNP devices tend to be quieter than NPN ones. Also, IC designs tend to be noisier than discrete component designs. My recommendation is to use either the MAT-02 (NPN device) or the MAT-03 (PNP device) matched differential pairs marketed by PMI Inc. [5]. The need for a differential pair will be discussed next. One last handy detail to note is that the noise performance of each of the three basic amplifier configurations is about the same (common emitter, common base, and common collector). This gives the designer some extra flexibility.

THE LOGARITHMIC AMPLIFIER

Log amps have been in existence for quite some time and consequently there are numerous versions to choose from. I believe that a log amp based upon the dual gain/lin-limit technique will be ideal for this application. A block diagram of its circuit is shown in figure 2; its operation is compared to an ideal logarithmic compression in figure 3.

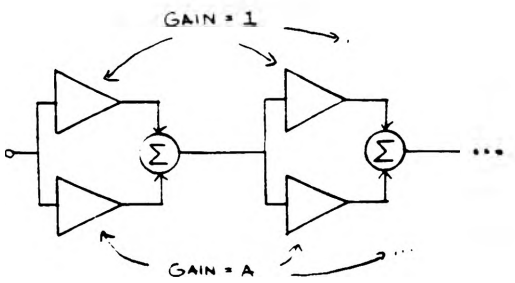

FIGURE 2

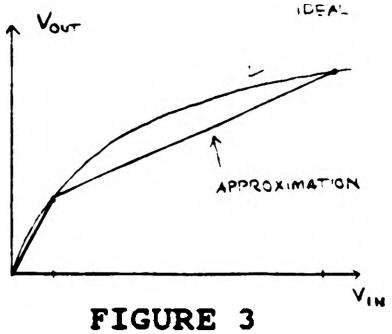

FIGURE 3

Lin-limit is a truncation of the words "linear" and "limit". The lin-limit log amp is composed of several dual gain stages. For small signals, all amplifiers will be active. For input signals of increasing amplitude, successive stages will fall into limit, reducing the overall gain, and compressing the signal. The unity gain amplifiers simply pass the signal on to following stages and must be prevented from falling into limit [1,12].

The log amp's output will eventually be processed through a detector where the amplitude of each echo will be extracted and measured. The lin-limit technique allows the use of only

one detector as opposed to other designs which incorporate multiple detectors. Since the current system also uses only one detector the proposed log amp could therefore serve as a "drop-in" replacement for the current circuit.

Since this particular system does not require precise logging action, a few stages of higher gain will suffice. This is important for two reasons. First, fewer stages allows for a simpler and smaller circuit. Second, a low overall noise figure requires that at least the first stage have high gain. The differential amplifier seems to be the best candidate for the dual gain stage. It is of common emitter design and provides a high power gain. Perhaps most important of all is the fact that differential amplifiers do not saturate. Saturation causes amplifiers to become sluggish. A basic schematic of one dual gain/ lin-limit stage is shown below. Note that the collector resistor provides a convenient summing point:

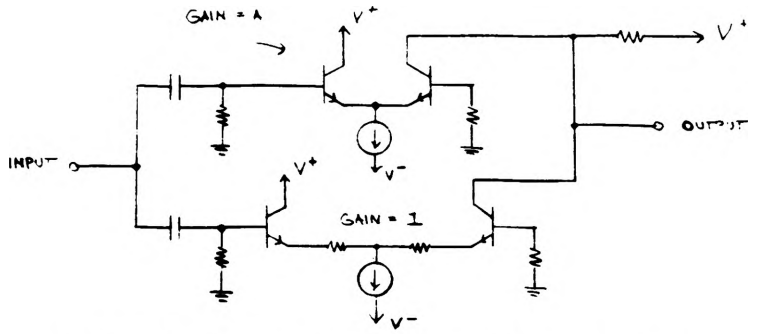

FIGURE 4, The dual-gain stage

The log amp which is currently in use has a theoretical small signal gain of 105dB, or 178,000 V/V. However, only about 80dB of the 105dB is available for use since noise and low level oscillations use up its first 25dB of amplification. This is no simple problem to overcome. For the replacement amplifier, four dual gain stages each with a small signal gain of about 18 will provide an overall gain of 105dB.

PRACTICAL CONSIDERATIONS

Rarely does a circuit behave exactly as we would like it to and so is the case with this log amp. In practice there are hundreds of decisions to be made before the final product emerges, too numerous to discuss here. However, there are a few key points which will be addressed:

1) Limiting the amplifier's bandwidth.
2) Grounding and shielding precautions.
3) Justifications for using linear circuit theory to analyze a non-linear amplifier.

Limiting the Amplifier's Bandwidth:

There are two fundamental problems experienced by the designers of high gain/high bandwidth amplifiers:

1) Bandwidth breeds noise.
2) High gain helps promote the threat of oscillations.

As discussed above, noise voltage increases with bandwidth; however, resolution requires bandwidth. To resolve this conflict more compromises must be made. It is difficult to say exactly where the log amp's cutoff points should be placed. Cutoff frequencies of about 5MHz and 25MHz should be adequate and some experimentation will be required. These figures were chosen after viewing the spectra of the ultrasound signals on a spectrum analyzer, they are not values which must be strictly adhered to.

More threatening is the possibility of rampant oscillations. Oscillations are almost unavoidable in situations such as this and if not minimized they will "use up" the small signal compression capabilities of the log amp and thus limit the system's useful scanning depth. To perform this feat, several sources recommend placing a bandpass filter in the middle of the log amp [1,7].

Filter design is an art in itself. However, after sifting through various texts on the subject there is one filter was found which has some promising features: the Gaussian-Transitional filter [8]. This filter follows a Gaussian frequency response out to a cutoff frequency after which it changes to a Chebyschev response. A relatively high order will be required for the bandpass filter since the log amp will be applying more amplification to the smaller signals.
Perhaps neutralization may be helpful in stubborn cases.

Grounding and Shielding:

Proper grounding and shielding techniques are often over looked in the initial design stages. It has always been my philosophy to install what ever may be necessary in the preliminary stages rather than scramble to squeeze them in later when things go awry. A high gain amplifier such as this will be prone to oscillations if improper or insufficient techniques are applied.

There are three points which require recognition. First, careful attention must be applied to the circuit layout. Often neglected is the return path that each signal must use. It is critically important to follow the physical path from each high frequency source to its load **and back again** to its source. If the returning signal is forced to wander very far from its outgoing path, a larger than necessary loop will be enclosed by this current and an extra inductance will be created in the circuit. Unwanted mutual inductances may easily couple energy from the log amp's output back to its input causing oscillations.

Second, I highly recommend that each half of the log amp be placed in a metal enclosure containing three compartments, two for each half of the log amp and one for the filter which joins the two. Also, be careful to avoid mounting the filter coils in a manner which allows mutual coupling, this can severely alter its frequency response.

Third, don't forget to apply proper grounding and shielding techniques to the rest of the system. One particular source of noise which must be carefully suppressed is the scanning motor which resides in the probe along with the transducer. Currently the positive lead of the motor connects to the system via a small choke while the return lead of the motor does not. A significant improvement in noise suppression may be obtained by feeding power to the motor through a bifilar wound coil. This device will insure that both motor leads are isolated from the system. I have observed a few cases in the past where brush noise was traveling from the commutator, out through the "unchoked" motor lead, and back to the commutator via the motor case. The addition of bifilar chokes completely severed all troublesome loops and eliminated the interference.

Justification for Using Linear Circuit Theory in a Non-Linear Circuit:

By now I'm sure that the attentive reader has wondered why linear circuit theory has been applied to a nonlinear amplifier. The lin-limit design is only an approximation of an ideal logarithmic response. Lin-limit log amps are constructed of linear amplifiers and their transfer functions are piecewise linear. Thermal noise is only troublesome when its level is near that of the smallest signals to be processed. When this occurs, the lin-limit log amp will be operating in its first linear segment. As long as the amplifier operates within the first linear segment, the application of linear circuit theory is permissible.

CONCLUSIONS

This project was initiated by the desire to increase the scan depth of an existing ultrasound scanner. The current system is unshielded and is troubled by noise and low level oscillations. Presented in this paper are guidelines which the manufacturer may follow to upgrade the system. A four stage lin-limit log amp incorporating dual gain stages will be an ideal replacement. The amplifier should be divided into two halves and a high order Gaussian-Transitional bandpass filter placed between them. The entire three module assembly should be placed in a metal shielding enclosure having separate compartments for each module. Once assembled, few modifications will be required of the existing system and this assembly will be a near drop-in replacement for the current log amp. Finally, all sources of interference within the system should be minimized. One such conspicuous source is the scanning mechanism drive motor. The use of a bifilar choke to isolate it from the rest of the system is highly recommended.

ACKNOWLEDGEMENTS

I would like to express my thanks to the following people for their patience and assistance throughout this project:

To Prof. T. Herrick for his guidance in approaching this project and for his many hours of assistance with the details of ultrasound technology.

To Prof. J. Bourquin for his many hours of help with filter design.

To Prof. T. Van Doren for his assistance with grounding and shielding techniques.

To John Carlson for his help in performing FFT's with the MathCad software package.

REFERENCES

1) Logarithmic Amplification With Application to Radar and EW, Richard Smith Hughes, Artech House Inc., 1986.

2) Circuit Simulation of Ultrasonic Transducer Systems, C.G. Hutchens, ISA Transactions, Vol. 27, No4.

3) Effects of Backing and Matching on the Performance of Piezoelectric Ceramic Transducers, G. Kossoff, IEEE Transactions on Sonics and Ultrasonics, Vol. SU-13, No. 1

4) Low Noise Electronic Design, C.D. Motchenbacher, F.C. Fitchen, John Wiley & Sons, 1973.

5) Analog Integrated Circuits, PMI Inc., Volume 10, pgs 9-10 through 9-31.

6) MIC Microwave & IF/RF Products, RHG Electronics Laboratory Inc., Catalog #400, pgs 100-125.

7) Linear Products Data Book, Analog Devices Inc., 1990/1991, pgs 7-3 through 7-22.

8) Handbook of Filter Synthesis, Anatol I Zverev, John Wiley & Sons Inc., 1967.

9) Logarithmic Amplifier Design, SJ Solms, IRE Transactions on Instrumentation, Dec 1959.

10) New Log Amp Cascades to Desired Range, Richard S. Hughes, Electronic Design 22. Oct 25, 1969.

11) Spreadsheet Helps You Evaluate System Noise, Peter Fazekas, EDN, May 26, 1988

12) A True I.F. Logarithmic Amplifier Using Twin Gain Stages, A. Woroncow, J. Croney, The Radio and Electronic Engineer, Sept 1966.

13) Four Pitfalls in Using Log Amplifiers, Ron Hirsch, EEE-Circuit Design Engineering, Aug 1966.

14) Designers Guide to Logarithmic Amplifiers, Alan Risley, EDN, August 5, 1973.

15) A Guide to Specifying and Testing Logarithmic Devices, D. Sheingold, J. Cadogan, EDN Dec 20 1973.

SHOOTING METHOD SOLUTIONS OF EIGENVALUE PROBLEMS

Xi Chen
Mathematics & Statistics Department
University of Missouri-Rolla
Rolla, MO 65401

Abstract. A shooting method was developed to study eigenvalue problems derived from Schrödinger equation. The challenging problem, the two-dimensional hydrogen system with the logarithmic potential function, was successfully solved by the shooting method. But no complete proof was given for its rationale and correctness. This paper not only gives the complete proof for the shooting method, but also generalizes it to solve a large class of eigenvalue problems. In a certain sense, the shooting method proves more effective numerically and more powerful theoretically than the classical functional analysis approach.

I. INTRODUCTION

Recently, a shooting method was developed to study eigenvalue problems in quantum mechanics [1,2,3]. Originally, the method served to solve some specific eigenvalue problems associated with the Schrödinger operator, but as was pointed out [4], the shooting method ought to prove general in nature and be applicable for solving the Schrödinger equation with a wide variety of potential energy functions. In this paper, we will go far beyond even that; we will establish the validity of the shooting method for the following general problem.

Generalized Eigenvalue Problem. Let $Q(v,\lambda)$ be a continuous function of $v \in (-\infty,\infty)$ and $\lambda \in I$, where $I=[a,b]$ is a closed interval. Find all λ and corresponding nontrivial bounded solutions $R_\lambda(v)$ to

$$\frac{d^2R}{dv^2} = Q(v,\lambda)R. \tag{1}$$

It is not rigorous but convenient to call such numbers λ and corresponding solutions $R_\lambda(v)$ eigenvalues and eigenfunctions of (1) under the bounded condition, respectively.

Definitions. A function $R(v)$ defined on the real line is left-bounded if it is bounded when $v \in (-\infty,0]$ and right-bounded if it is bounded when $v \in [0,+\infty)$.

Obviously, $R(v)$ is bounded on the whole real line if and only if it is both left and right- bounded. It leads to the basic idea of the shooting method. The idea is very simple in nature: first to find all the right-bounded solutions of (1) and then to select left-bounded ones among these solutions. To make it more specific, we need to impose some additional assumptions for $Q(v,\lambda)$.

A1. $Q(v,\lambda)$ has a continuous partial derivative with respect to λ and

$$\frac{\partial Q(v,\lambda)}{\partial\lambda} \le 0 \quad \left[\frac{\partial Q(v,\lambda)}{\partial\lambda} \ge 0\right] \text{ for all } v \in (-\infty,\infty) \text{ and } \lambda \in I.$$

A2. The set $\{\lambda \in I : \dfrac{\partial Q(v,\lambda)}{\partial\lambda} = 0 \text{ for all } v \in (-\infty,\infty)\}$ is of measure zero.

A3. $\displaystyle\int_{-\infty}^{+\infty} |v|Q_-(v,\lambda)dv < \infty$ for all $\lambda \in I$, where

$$Q_-(v,\lambda) = \begin{cases} -Q(v,\lambda) & Q(v,\lambda) < 0; \\ 0 & Q(v,\lambda) \ge 0. \end{cases}$$

As will be proved later, *A3* assures that for every λ, there exists a nontrivial right-bounded solution to (1), unique except for a nonzero factor. Let $Z(\lambda)$ be the number of zeros of such a right-bounded solution for every $\lambda \in I$. Several authors [1,2,3] notice that every discontinuity of $Z(\lambda)$ is an eigenvalue of (1) in some special cases. Actually, the discontinuities give all the eigenvalues of $Z(\lambda)$ provided $Q(v,\lambda)$ satisfies *A1*, *A2* and *A3*. We will establish the following four theorems.

Theorem A. If $Q(v,\lambda)$ satisfies *A3*, then for every λ, there exists a nontrivial right-bounded [left-bounded] solution to (1), unique except for a nonzero factor.

Theorem B. If $Q(v,\lambda)$ satisfies *A1* and *A3*, then every discontinuity of $Z(\lambda)$ is an eigenvalue of (1).

Theorem C. If $Q(v,\lambda)$ satisfies *A1*, *A2* and *A3*, every eigenvalue of (1) is a discontinuity of $Z(\lambda)$.

Theorem D. If $Q(v,\lambda)$ satisfies *A1* and *A3*, then $Z(\lambda)$ is a nondecreasing [nonincreasing] function in λ.

II. PROOF OF THEOREMS A-D

The following two lemmas are useful tools in our discussion later and can be easily proved in various ways.

Lemma E. Let ϕ and ψ be nontrivial solutions to $y'' = p(v)y$ and $y'' = q(v)y$ on $[v_0,\infty)$ $[(-\infty,v_0]]$ respectively, satisfying the same initial conditions: $\phi(v_0) = \psi(v_0)$ and $\phi'(v_0) = \psi'(v_0)$. If $p(v) \le q(v)$ and $\phi(v) > 0$ for all $v > v_0$ $[v < v_0]$, then

1° $\dfrac{\psi(v)}{\phi(v)} \ge \dfrac{\psi(v_1)}{\phi(v_1)}$ for all $v > v_1 > v_0$ $[v < v_1 < v_0]$.

2° $\psi(v) \ge \phi(v)$ for all $v > v_0$ $[v < v_0]$.

Lemma F. Let $q(v)$ be a non-positive continuous function defined on $[v_0,\infty)$ $[(-\infty,v_0]]$ which satisfies

$$\int_{v_0}^{\infty} |(v-v_0)q(v)|dv < 1 \quad \left[\int_{-\infty}^{v_0} |(v-v_0)q(v)|dv < 1\right].$$

Let $R(v)$ be the solution to

$$\frac{d^2R}{dv^2} = q(v)R$$

satisfying the initial conditions $R(v_0) = 0$ and $R'(v_0) = 1$ $[R'(v_0) = -1]$. Then

$$k|v-v_0| \le R(v) \le |v-v_0| \text{ for all } v > v_0 \ [v < v_0],$$

where $k = 1 - \displaystyle\int_{v_0}^{\infty} |(v-v_0)q(v)|dv$ $\left[k = 1 - \int_{-\infty}^{v_0} |(v-v_0)q(v)|dv\right]$.

Suppose $Q(v,\lambda)$ satisfies *A1* in our following arguments. For every $\lambda \in I$, there exists a positive number $v_0 = v_0(\lambda)$ such that

$$\int_{v_0}^{\infty} vQ_-(v,\lambda)dv < \frac{1}{2}.$$

Let F_λ and G_λ be the solutions to (1) satisfying the initial conditions $F_\lambda(v_0) = 1$, $F'_\lambda(v_0) = 0$ and $G_\lambda(v_0) = 0$, $G'_\lambda(v_0) = 1$, respectively. Compare G_λ with g_λ, the solution to

$$\frac{d^2R}{dv^2} = -Q_-(v,\lambda)R$$

satisfying the initial conditions $g_\lambda(v_0) = 0$, $g_\lambda(v_0) = 1$.

Since $\displaystyle\int_{v_0}^{\infty} (v-v_0)Q_-(v,\lambda)dv \le \int_{v_0}^{\infty} vQ_-(v,\lambda)dv \le \frac{1}{2}$, according to *Lemma F*,

$$\frac{v-v_0}{2} \le g_\lambda(v) \le v - v_0 \text{ for all } v > v_0,$$

and according to *Lemma E*,

$$\frac{v-v_0}{2} \le g_\lambda(v) \le G_\lambda(v) \text{ for all } v > v_0 \text{ and } \lambda \in I.$$

Thus $\int_v^\infty G_\lambda^{-2}(w)dw < \infty$ for all $v > v_0$. Define

$$R_\lambda(v) = G_\lambda(v) \int_v^\infty G_\lambda^{-2}(w)dw \text{ for } v \in (v_0, \infty).$$

According to *Lemma E*,

$$\frac{G_\lambda(v_2)}{g_\lambda(v_2)} \geq \frac{G_\lambda(v_1)}{g_\lambda(v_1)} \text{ for all } v_2 > v_1 > v_0.$$

Therefore

$$\frac{\int_v^\infty g_\lambda^{-2}(w)dw}{\int_v^\infty G_\lambda^{-2}(w)dw} \geq \frac{G_\lambda^2(v)}{g_\lambda^2(v)} \geq \frac{G_\lambda(v)}{g_\lambda(v)} \geq 1 \text{ for all } v > v_0.$$

Thus

$$R_\lambda(v) = G_\lambda(v) \int_v^\infty G_\lambda^{-2}(w)dw \leq g_\lambda(v) \int_v^\infty g_\lambda^{-2}(w)dw \leq (v - v_0) \int_v^\infty \frac{4}{(t - v_0)^2} dt = 4 \text{ for all } v > v_0,$$

namely, $R_\lambda(v)$ is right-bounded. It is not difficult to check that R_λ is a solution to (1) on (v_0, ∞). Extending it to a solution on the whole real line, we get a right-bounded solution to (1). Consequently, to every $\lambda \in I$, there corresponds a nontrivial right-bounded solution to (1). Obviously, for every λ, such a solution is unique except for a constant factor; in fact, it can be written as

$$c\left[F_\lambda(v) - G_\lambda(v) \lim_{w \to -\infty} \frac{F_\lambda(w)}{G_\lambda(w)}\right].$$

Symmetrically, we can draw the same conclusions regarding left-bounded solutions of (1), and we have *Theorem A*.

The next lemma follows immediately.

Lemma G. If $Q(v, \lambda)$ satisfies *A3*, then a solution of (1) on $(-\infty, \infty)$, say $R_\lambda(v)$, is right-bounded [left-bounded] if and only if

$$\lim_{v \to +\infty} \frac{R_\lambda(v)}{G_\lambda(v)} = 0 \left[\lim_{v \to -\infty} \frac{R_\lambda(v)}{G_\lambda(v)} = 0\right].$$

Although we have introduced the function $Z(\lambda)$, we cannot take it for grant that it is a regular function which is finite everywhere. Namely, it may take ∞ as its value somewhere. But the following theorem eliminates such possibilities.

Theorem H. If $Q(v, \lambda)$ satisfies *A3*, then every nontrivial solution to (1) has only finitely many zeros.

Proof. Let R_λ be a nontrivial solution to (1). If it is not right-bounded, obviously, it must have finitely many zeros in $[0, \infty)$. Otherwise, if it is right-bounded, since

$$\frac{d[F_\lambda(v)/G_\lambda(v)]}{dv} = -\frac{1}{G_\lambda^2(v)} < 0 \text{ for } G_\lambda(v) \neq 0, \tag{2}$$

$$\frac{F_\lambda(v)}{G_\lambda(v)} > \lim_{v \to +\infty} \frac{F_\lambda(v)}{G_\lambda(v)} \text{ for all } v > v_0.$$

Therefore,

$$R_\lambda(v) = c\left[F_\lambda(v) - G_\lambda(v) \lim_{w \to -\infty} \frac{F_\lambda(w)}{G_\lambda(w)}\right] \neq 0 \text{ for all } v > v_0.$$

Thus, R_λ has finitely many zeros in $[0, \infty)$. Similarly, we can show R_λ has finitely many zeros in $(-\infty, 0)$. ∎

Let $T_\lambda(v)$ be the right-bounded solution to (1) satisfying the initial condition $T_\lambda(v_0) = 1$. It is easy to show

$$T_\lambda(v) = F_\lambda(v) - G_\lambda(v) \lim_{w \to -\infty} \frac{F_\lambda(w)}{G_\lambda(w)}.$$

Notice the choice of the number v_0 depends on λ in our arguments. It is hard to obtain properties of F_λ, G_λ and T_λ as functions of λ. However, if $Q(v,\lambda)$ satisfies both *A1* and *A3*, we can choose a constant number $v_0 > 0$ such that

$$\int_{v_0}^{\infty} vQ_-(v,\lambda)dv < \frac{1}{2} \text{ for all } \lambda \in I = [a,b].$$

In fact, we can simply choose $v_0 > 0$ such that

$$\int_{v_0}^{\infty} vQ_-(v,b)dv < \frac{1}{2}.$$

Since $Q(v,\lambda)$ is nonincreasing in $\lambda \in I$, $Q_-(v,\lambda)$ is nondecreasing in λ. Consequently, for all $\lambda \in I$,

$$\int_{v_0}^{\infty} vQ_-(v,\lambda)dv \le \int_{v_0}^{\infty} vQ_-(v,b)dv < \frac{1}{2}.$$

Lemma 1. If $Q(v,\lambda)$ satisfies *A1* and *A3*, then the function $\lim\limits_{v\to+\infty} \dfrac{F_\lambda(v)}{G_\lambda(v)}$ is continuous with respect to $\lambda \in I$.

Proof. According to (2),

$$\left|\frac{F_\lambda(v_2)}{G_\lambda(v_2)} - \frac{F_\lambda(v_1)}{G_\lambda(v_1)}\right| \le \frac{1}{k^2}\left(\frac{1}{v_1 - v_0} - \frac{1}{v_2 - v_0}\right) \text{ for all } \lambda \in I \text{ and } v_2 > v_1 > v_0.$$

Thus $\dfrac{F_\lambda(v)}{G_\lambda(v)}$ converges uniformly with respect to λ. Since it is obvious that $\dfrac{F_\lambda(v)}{G_\lambda(v)}$ is continuous for every fixed $v > v_0$, it then follows that

$$\lim_{v\to+\infty} \frac{F_\lambda(v)}{G_\lambda(v)}$$

is a continuous function of λ. ∎

The following lemma shows a kind of stability for unbounded solutions of (1).

Lemma 2. Let $R_\lambda(v,x,y)$ denote the solution to (1) satisfying the initial conditions $R_\lambda(a) = x$ and $R'_\lambda(a) = y$, where a is a constant, and suppose

$$\lim_{v\to+\infty} R_\lambda(v,x,y) = \infty \quad \left[\lim_{v\to-\infty} R_\lambda(v,x,y) = \infty\right]$$

at a certain point $(\lambda,x,y) = (\lambda_0,x_0,y_0)$. Then there is a neighborhood O of (λ_0,x_0,y_0) in which

1° $\lim\limits_{v\to+\infty} R_\lambda(v,x,y) = \infty \quad \left[\lim\limits_{v\to-\infty} R_\lambda(v,x,y) = \infty\right]$.

2° there exists a number v_1 such that $R_\lambda(v,x,y) \neq 0$ for all $v \ge v_1[v \le v_1]$.

Proof. Without loss of generality, we suppose

$$\lim_{v\to+\infty} R_{\lambda_0}(v,x_0,y_0) = +\infty.$$

Choose $v_1 > v_0$ such that $R_{\lambda_0}(v,x_0,y_0) > 0$ for all $v \ge v_1$. Let $P_\lambda(v)$ and $S_\lambda(v)$ be the solutions to (1) with the initial conditions $P_\lambda(v_1) = 1$, $P'_\lambda(v_1) = 0$ and $S_\lambda(v_1) = 0$, $S'_\lambda(v_1) = 1$, respectively. Obviously, P_λ and S_λ have the same properties as we described before for F_λ and G_λ. Observe that

$$\frac{R_\lambda(v,x,y)}{S_\lambda(v)} = R_\lambda(v_1,x,y)\frac{P_\lambda(v)}{S_\lambda(v)} + R'_\lambda(v_1,x,y),$$

where $R_\lambda(v_1, x, y)$ and $R'_\lambda(v_1, x, y)$ are continuous functions of (λ, x, y). According to *Lemma I*, $\lim_{v\to+\infty} \frac{P_\lambda(v)}{S_\lambda(v)}$ is a continuous function of λ. So $\lim_{v\to+\infty} \frac{R_\lambda(v, x, y)}{S_\lambda(v)}$ is a continuous function of (λ, x, y). By *Lemma G*,

$$\lim_{v\to+\infty} \frac{R_{\lambda_0}(v, x_0, y_0)}{S_{\lambda_0}(v)} > 0.$$

Thus there exists a neighborhood O of (λ_0, x_0, y_0) in which

$$\lim_{v\to+\infty} \frac{R_\lambda(v, x, y)}{S_\lambda(v)} > 0 \text{ and } R_\lambda(v_1, x, y) > 0.$$

Conclusion 1° is valid for $(\lambda, x, y) \in O$ by *Lemma G*, and according to (2),

$$\frac{R_\lambda(v, x, y)}{S_\lambda(v)} \geq \lim_{v\to+\infty} \frac{R_\lambda(v, x, y)}{S_\lambda(v)} > 0 \text{ for all } v \geq v_1.$$

Thus 2° is also satisfied for $(\lambda, x, y) \in O$. ∎

Now we can prove *Theorem B*.

It suffices to prove that any λ for which T_λ is unbounded cannot belong to $D(Z)$. Let T_{λ_0} be unbounded. Since $T_\lambda(v_0) = 1$ and $T'_\lambda(v_0) = -\lim_{v\to+\infty} \frac{F_\lambda(v)}{G_\lambda(v)}$ where the latter is continuous with respect to λ by *Lemma I*, there must be a neighborhood O_1 of λ_0 and a number v_1 such that $T_\lambda(v) \neq 0$ for all $\lambda \in O_1$ and $v \leq v_1$ (see *Lemma E*). Thus all the zeros of such T_λ must lie in $[v_1, v_0]$. According to the continuity of $T_\lambda(v)$ on $I \times [v_1, v_0]$, there is a neighborhood O_2 of λ_0 in which all the T_λ have the same number of zeros on $[v_1, v_2]$ as $\lambda \in O_2$. Therefore, all the T_λ, $\lambda \in O_1 \cap O_2$, have the same number of zeros, so $Z(\lambda)$ is continuous at λ_0. ∎

The shooting method produces all the eigenvalues and eigenfunctions of (1) only if the converse of *Theorem B* holds. The converse, however, is not necessarily true if no additional conditions are imposed on $Q(v, \lambda)$ other than *A1* and *A3*. A counterexample can be simply constructed as

$$Q(v, \lambda) = 4v^2 - 2, \ v \in (-\infty, +\infty) \text{ and } \lambda \in [-1, 1].$$

Obviously, $Q(v, \lambda)$ satisfies *A1* and *A3*, and it is easy to check that $T_\lambda(v) = e^{-v^2}$ are bounded solutions of (1) for all $\lambda \in [-1, 1]$, but $Z(\lambda) = 0$ has no discontinuities. Nevertheless, we can prove the converse if *A2* is added. That is *Theorem C*.

The next lemma follows immediately from the definition of T_λ and *Theorem A*.

Lemma K. T_λ is bounded if and only if

$$\lim_{v\to-\infty} \frac{F_\lambda(v)}{G_\lambda(v)} = \lim_{v\to+\infty} \frac{F_\lambda(v)}{G_\lambda(v)}.$$

The following equality is extremely important, since it reveals some essential properties of the system (1) and (2).

Lemma L. If $Q(v, \lambda)$ has a continuous partial derivative with respect to λ on $(-\infty, \infty) \times I$, then for $G_\lambda(v) \neq 0$,

$$\frac{\partial[F_\lambda(v)/G_\lambda(v)]}{\partial\lambda}$$

exists and has the value

$$\int_{v_0}^{v} \frac{\partial Q(s, \lambda)}{\partial\lambda} \left[F_\lambda(s) - G_\lambda(s)\frac{F_\lambda(v)}{G_\lambda(v)}\right]^2 ds. \tag{3}$$

Proof. Since $Q(v,\lambda)$ is continuously partially differentiable with respect to λ, $z(v) = \partial F_\lambda(v)/\partial\lambda$ exists and is the solution to

$$\frac{d^2z}{dv^2} - Q(v,\lambda)z = \frac{\partial Q(v,\lambda)}{\lambda} F_\lambda(v)$$

satisfying the initial conditions

$$z(v_0) = z'(v_0) = 0;$$

thus

$$\frac{\partial F_\lambda(v)}{\partial\lambda} = \int_{v_0}^{v} \frac{\partial Q(s,\lambda)}{\partial\lambda} F_\lambda(s)[F_\lambda(s)G_\lambda(v) - F_\lambda(v)G_\lambda(s)]ds.$$

Similarly,

$$\frac{\partial G_\lambda(v)}{\partial\lambda} = \int_{v_0}^{v} \frac{\partial Q(s,\lambda)}{\partial\lambda} G_\lambda(s)[F_\lambda(s)G_\lambda(v) - F_\lambda(v)G_\lambda(s)]ds.$$

By a straightforward calculation, we get (3).

Lemma M. If $Q(v,\lambda)$ satisfy *A1* and *A2*, then, at a certain point λ_0,

1° there exists a neighborhood O of λ_0 in which

$$Z(\lambda) = Z(\lambda_0) \text{ if } \lambda < \lambda_0 \ [\lambda > \lambda_0]$$

and

$$Z(\lambda) \geq Z(\lambda_0) \text{ if } \lambda > \lambda_0 \ [\lambda < \lambda_0];$$

2° in addition, if $Q(v,\lambda)$ satisfies *A2*, O can be chosen such that

$$Z(\lambda) = Z(\lambda_0) + 1 \text{ if } \lambda > \lambda_0 \ [\lambda < \lambda_0] \text{ and } \lambda \in O.$$

Proof. *Lemma K* implies that $|G_{\lambda_0}(v)| \to \infty$ as $v \to -\infty$. Without loss of generality, suppose $G_{\lambda_0}(v) \to +\infty$ as $v \to -\infty$. According to *Lemma E*, there exist a number v_1 and a neighborhood O_1 of λ_0 in which $G_\lambda(v) \to +\infty$ as $v \to -\infty$ and $G_\lambda(v) > 0$ for all $v \leq v_1$.

Formula (3) shows that as a function of λ, $F_\lambda(v)/G_\lambda(v)$ is nondecreasing for a fixed $v \leq v_1$ and nonincreasing for a fixed $v > v_0$, so

$$\lim_{v\to-\infty} \frac{F_\lambda(v)}{G_\lambda(v)} - \lim_{v\to+\infty} \frac{F_\lambda(v)}{G_\lambda(v)} \leq 0 \text{ for all } \lambda \leq \lambda_0 \text{ and } \lambda \in O_1.$$

According to (2),

$$\begin{aligned} T_\lambda(v) &= G_\lambda(v)\left[\frac{F_\lambda(v)}{G_\lambda(v)} - \lim_{v\to+\infty}\frac{F_\lambda(v)}{G_\lambda(v)}\right] \\ &< G_\lambda(v)\left[\lim_{v\to-\infty}\frac{F_\lambda(v)}{G_\lambda(v)} - \lim_{v\to+\infty}\frac{F_\lambda(v)}{G_\lambda(v)}\right] \leq 0 \text{ for all } v \leq v_1,\ \lambda \in O_1 \text{ and } \lambda < \lambda_0. \end{aligned}$$

By the continuity of $T_\lambda(v)$ at every $(v,\ \lambda) \in [v_1, v_0] \times I$, there is a neighborhood $O \subset O_1$ of λ_0 in which all $T_\lambda(v)$ have the same number of zeros in $[v_1, v_0]$ and $T_\lambda(v_1) < 0$. Then 1° is obvious.

For $\lambda \in O$ and $\lambda > \lambda_0$, with (3) we have

$$\lim_{v\to-\infty}\frac{F_\lambda(v)}{G_\lambda(v)} - \lim_{v\to-\infty}\frac{F_{\lambda_0}(v)}{G_{\lambda_0}(v)} = \lim_{v\to-\infty}\int_{\lambda_0}^{\lambda}\int_{v_0}^{v}\frac{\partial Q(s,t)}{\partial t}\left[F_t(s) - G_t(s)\frac{F_t(v)}{G_t(v)}\right]^2 dsdt.$$

Since

$$\frac{\partial Q(s,t)}{\partial t}\left[F_t(s) - G_t(s)\frac{F_t(v)}{G_t(v)}\right]^2 \leq 0 \text{ when } v \leq v_1,$$

according to Fatou's Lemma [6],

$$\lim_{v\to-\infty}\frac{F_\lambda(v)}{G_\lambda(v)}-\lim_{v\to-\infty}\frac{F_{\lambda_0}(v)}{G_{\lambda_0}(v)}\geq\int_{\lambda_0}^{\lambda}\left\{\lim_{v\to-\infty}\int_{v_0}^{v}\frac{\partial Q(s,t)}{\partial t}\left[F_t(s)-G_t(s)\frac{F_t(v)}{G_t(v)}\right]^2 ds\right\}dt$$

$$\geq\int_{\lambda_0}^{\lambda}\int_{v_0}^{-\infty}\frac{\partial Q(s,t)}{\partial t}\left[F_t(s)-G_t(s)\lim_{v\to-\infty}\frac{F_t(v)}{G_t(v)}\right]^2 dsdt$$

Similarly, we can prove

$$\lim_{v\to+\infty}\frac{F_\lambda(v)}{G_\lambda(v)}-\lim_{v\to+\infty}\frac{F_{\lambda_0}(v)}{G_{\lambda_0}(v)}\leq\int_{\lambda_0}^{\lambda}\int_{v_0}^{+\infty}\frac{\partial Q(s,t)}{\partial t}\left[F_t(s)-G_t(s)\lim_{v\to+\infty}\frac{F_t(v)}{G_t(v)}\right]^2 dsdt$$

when $\lambda\in O$ and $\lambda>\lambda_0$. Therefore,

$$\lim_{v\to-\infty}\frac{F_\lambda(v)}{G_\lambda(v)}-\lim_{v\to+\infty}\frac{F_\lambda(v)}{G_\lambda(v)}\geq\int_{\lambda_0}^{\lambda}\left\{\int_{v_0}^{-\infty}\frac{\partial Q(s,t)}{\partial t}\left[F_t(s)-G_t(s)\lim_{v\to-\infty}\frac{F_t(v)}{G_t(v)}\right]^2 ds\right.$$

$$\left.-\int_{v_0}^{+\infty}\frac{\partial Q(s,t)}{\partial t}\left[F_t(s)-G_t(s)\lim_{v\to+\infty}\frac{F_t(v)}{G_t(v)}\right]^2 ds\right\}dt\geq 0$$

if $\lambda\in O$ and $\lambda>\lambda_0$. If $Q(v,\lambda)$ satisfies $A2$, the equality can never hold, i.e.,

$$\lim_{v\to-\infty}\frac{F_\lambda(v)}{G_\lambda(v)}-\lim_{v\to+\infty}\frac{F_\lambda(v)}{G_\lambda(v)}>0.$$

Thus $T_\lambda(v)\to+\infty$ as $v\to-\infty$ if $\lambda\in O$ and $\lambda>\lambda_0$. Since $T_\lambda(v_1)<0$ and

$$\frac{F_\lambda(v)}{G_\lambda(v)}-\lim_{v\to+\infty}\frac{F_\lambda(v)}{G_\lambda(v)}$$

is decreasing in v for a fixed $\lambda\in O$. T_λ must have exactly one zero in (∞,v_1) when $\lambda\in O$ and $\lambda>\lambda_0$. 2° follows immediately. ▌

Now *Theorem C* is a direct inference of *Lemma M*, and it is also easy to show *Theorem D* by *Lemma M* and *Theorem H*.

If $Z(\lambda)$ is not a nondecreasing function, there exists λ_0 such that

$$\limsup_{\lambda\to\lambda_0-0}Z(\lambda)>\liminf_{\lambda\to\lambda_0+0}Z(\lambda).$$

Then λ_0 belongs to $D(Z)$, so T_{λ_0} is bounded (see *Theorem E*). This contradicts conclusion 1° of *Lemma J*. ▌

Theorem D reveals the structure of $D(Z)$, or equivalently, the eigenvalues of (1) under the bounded condition, when $Q(v,\lambda)$ satisfies $A1$, $A2$, and $A3$: $D(Z)$ must be composed of

$$\lambda_n=\sup\{\lambda: T_\lambda \text{ has } n-1 \text{ zeros}\}\ [\lambda_n=\inf\{\lambda: T_\lambda \text{ has } n+1 \text{ zeros}\}]$$

where $Z(a)<n\leq Z(b)$ $[Z(a)>n\geq Z(b)]$. Therefore Z has only a finite number of discontinuities in $I=[a,b]$.

III. APPLICATIONS OF THE SHOOTING METHOD TO THE SCHRÖDINGER EQUATION

In this section, we apply the shooting method to the radial equation associated with the n-dimensional Schrödinger equation with a spherically symmetric potential [7]:

$$\frac{d^2R_0}{dr^2}+\left(\frac{n-1}{r}\right)\frac{dR_0}{dr}+\left(c[\lambda-V(r)]+\frac{k_n(l)}{r^2}\right)R_0=0 \tag{4}$$

subject to the condition

$$\int_0^\infty |R_0(r)|^2 r^{n-1} dr < \infty. \tag{5}$$

In these expressions, l is the angular number, $k_n(l)$ denotes the lth eigenvalue of the Laplace-Beltrami operator corresponding to the sphere in n-dimensional space, and c is a positive physical constant. Setting $r = e^{v/n}$ and $R_0(e^{v/n}) = e^{(1/n-1/2)v} R(v)$ in (4) and (5), yields

$$\frac{d^2R}{dv^2} = \left(\frac{c}{n^2}[V(e^{v/n}) - \lambda]e^{2v/n} - \frac{k_n(l)}{n^2} + \left(\frac{1}{2} - \frac{1}{n}\right)^2 \right) R \tag{6}$$

and

$$\int_{-\infty}^\infty |R(v)|^2 e^{2v/n} dv < \infty. \tag{7}$$

If λ is real number for which there exists a nontrivial solution $R_\lambda(v)$ of (6) satisfying (7), then λ and $R_\lambda(v)$ are called an eigenvalue and an eigensolution, respectively, of (6)-(7).

We pause the general discussion to give three typical examples. (Positive physical coefficients in the potential functions are ignored).

Ex1. The two-dimensional hydrogen atom with the logarithmic potential function was discussed in [1, 2]; here, $n = 2$ and $V(r) = \log r$, so

$$\frac{d^2R}{dv^2} = \left[\frac{l^2}{4} + c\left(\frac{v}{2} - \lambda\right)e^v \right] R \tag{8}$$

and

$$\int_{-\infty}^\infty |R(v)|^2 e^v dv < \infty. \tag{9}$$

Substituting $v = u + 2\lambda$ produces the simple form frequently used in standard works [1, 8]:

$$\frac{d^2R}{du^2} - \left(\frac{l^2}{4} + \sigma u e^u \right) R = 0 \tag{10}$$

and

$$\int_{-\infty}^\infty |R(u)|^2 e^u du < \infty, \tag{11}$$

where $\sigma = ce^{2\lambda}/2$.

Ex2. The familiar three-dimensional hydrogen atom with the Coulomb potential, i.e. $n = 3$ and $V(r) = -1/r$, was discussed via the shooting method in [3].

$$\frac{d^2R}{dv^2} = \left(\frac{c}{9}(-e^{-v/3} - \lambda)e^{2v/3} + \frac{l(l+1)}{9} + \frac{1}{36} \right) R \tag{12}$$

and

$$\int_{-\infty}^\infty |R(v)|^2 e^{2v/3} dv < \infty. \tag{13}$$

Ex3. The shooting method was used in [3] to study the three-dimensional Schrödinger equation with the isotropic harmonic oscillator potential. For this case, $n = 3$ and $V(r) = r^2$, so

$$\frac{d^2R}{dv^2} = \left(\frac{c}{9}(e^{2v/3} - \lambda)e^{2v/3} + \frac{l(l+1)}{9} + \frac{1}{36} \right) R \tag{14}$$

and

$$\int_{-\infty}^\infty |R(v)|^2 e^{2v/3} dv < \infty. \tag{15}$$

Returning to the general case, it is clear that if $V(r)$ is continuous for $r \in (0,\infty)$, then

$$Q(v,\lambda) = \frac{c}{n^2}[V(e^{v/n}) - \lambda]e^{2v/n} - \frac{k_n(l)}{n^2} + \left(\frac{1}{2} - \frac{1}{n}\right)^2$$

satisfies both *A1* and *A2*. To ensure that *A3* holds, we will consider continuous potentials satisfying the following conditions.

A4. Let $\lim_{v\to+\infty} V(e^{v/n}) = \sup V(e^{v/n}) = M$, where M may be $+\infty$. For all $\lambda \geq M$, there exists v_0 such that $Q(v,\lambda)$ is negative and has a negative partial derivative with respect to v when $v > v_0$.

A5. $\int_{-\infty}^{0} |vQ_-(v,0)|dv < \infty$.

Obviously, both *A4* and *A5* are satisfied in *Ex1*, *Ex2* and *Ex3*.

The next theorem implies the well-known fact that all eigenvalues in *Ex2* are negative [9].

Theorem N. If $V(r)$ is continuous for $r \in (0,\infty)$ and satisfies *A4*, then all eigenvalues of the system (6) and (7) lie in the interval $(-\infty, M)$.

Proof. If there is an eigenvalue $\lambda \geq M$ of (6) and (7), let $R(v)$ be a corresponding eigensolution. Since $-Q(v,\lambda)$ is positive and increasing when $v > v_0$, by Sturm's Separation Theorem [10], it is easy to see that $R(v)$ has a sequence of zeroes, say $\{v_n\}$, which approach $+\infty$.

If v is large enough, then

$$\frac{d\{-Q(v,\lambda)R^2(v) + [R'(v)]^2\}}{dv} = -\frac{\partial Q(v,\lambda)}{\partial v}R^2(v) \geq 0,$$

and this implies

$$\int_0^{\infty} [R'(v)]^2 dv - \int_0^{\infty} Q(v,\lambda)R^2(v)dv = \infty.$$

On the other hand,

$$\begin{aligned}\int_0^{v_n} Q(v,\lambda)R^2(v)dv &= \int_0^{v_n} R(v)R''(v)dv \\ &= -\int_0^{v_n} [R'(v)]^2 dv - R(0)R'(0).\end{aligned}$$

Since $v_n \to +\infty$ as $n \to \infty$, it is easy to deduce

$$\int_0^{\infty} Q(v,\lambda)R^2(v)dv = \infty.$$

Clearly, there exists a constant $k > 0$ such that $Q(v,\lambda) < ke^{2v/n}$ when v is large enough, and therefore

$$\int_0^{\infty} R^2(v)e^{2v/n}dv = \infty,$$

a contradiction. ∎

It is not difficult to obtain the following theorem.

Theorem O. If $V(r)$ is continuous and satisfies both *A4* and *A5*, then the corresponding $Q(v,\lambda)$ satisfies *A3* on any closed interval $I \subset (-\infty, M)$.

If $V(r)$ satisfies both *A4* and *A5*, then the shooting method can be applied to find all the eigenvalues and eigensolutions of the system consisting of (6) and the bounded condition

$$R_\lambda(v) \text{ is bounded for } v \in (-\infty, +\infty). \tag{16}$$

The next result is obvious but needs to be claimed to show the relation between this eigenvalue problem and the one consisting of (6) and (7).

Theorem P. Let $V(r)$ be continuous for $r \in (0, \infty)$ and satisfy both *A4* and *A5*, then every bounded solution of (6) must satisfy (7).

The shooting method can only be used to find the bounded solutions of (6), and although we have seen in *Theorem P* that bounded solutions must be eigensolutions of (6) and (7), the converse is not always true. In the ground state, that is, when $l = 0$, *Ex1* and *Ex3* have all the real numbers as their eigenvalues of (6) and (7), while *Ex2* has all the negative numbers as its eigenvalues of (6) and (7) [2]. In these cases, the shooting method only produces a part of all the eigenvalues and eigensolutions. In fact, the eigensolutions to (6) largely depend on the domain of Schrödinger operator. It is not surprising at all that we get different eigenvalues and eigensolutions if we change condition (7). But it is also easy to see in our three examples, when $l \neq 0$, the eigensolutions of (6) and (7) must be bounded. Even in the ground state, the bounded solutions are still the most interesting ones in a physical sense [11]. The shooting method is sufficiently general to solve a wide class of Schrödinger equations.

By the shooting method, we can easily get a generalization of a classical theorem regarding *Ex1* [12].

Theorem Q. The eigenvalues of (6) and (16) are isolated and only have finite multiplicities, that is, for every λ, there are only a finite number l's such that λ is an eigenvalue of (6) and (16).

Proof. The isolation follows directly from our previous arguments.

It is known that $k_n(l)$ is a polynomial and non-negative for $l \in Z$. Let σ denote $-k_n(l)/n^2$. For a fixed λ, $P(v, \sigma) = Q(v, \lambda)$ satisfies both *A1*, *A2* and *A3*, so we can apply the shooting method for (6) and (16) with respect to σ. Let T_λ have N zeros when $\sigma = 0$. Since the number of zeros of T_λ is nonincreasing in σ (see *Theorem D*) and $\sigma \geq 0$, the system (6) and (16) has at most N eigenvalues for σ. Thus there are only finitely many l's such that λ is an eigenvalue.

IV. ACKNOWLEDGEMENTS

I owe a lot to my advisor, Dr. David Grow, for his generous help. His instructions and encouragements led me to go further and further on this topics. He not only helped me a lot with my English, but also detected some mathematical errors in my original paper. Especially, he helped me sketch out the proof of *Theorem C.* For these I am greatly indebted.

V. REFERENCES

[1] K. Eveker et al., "The two-dimensional hydrogen atom with a logarithmic potential energy function," Am. J. Phys. **58**, pp. 1183-1192. (1990).

[2] X. Chen and D. Grow, "A shooting method solution of the two dimensional hydrogen atom," J. Math. Phys. (to be published).

[3] D. Grow et al., "Shooting method solutions for the 3-D hydrogen atom and 3-D isotropic harmonic oscillator," (to be published).

[4] Ref. 1, p. 1184.

[5] T. Myint-U, *Ordinary Differential Equations* (North-Holland, New York, 1978), p. 39.

[6] C. D. Aliprantis and O. Burkinshaw, *Principles of Real Analysis* (North Holland, New York, 1981), p. 131.

[7] M. Reed and B. Simon, *Methods of Modern Mathematical Physics* (Academic, New York, 1975), Vol. 2, pp. 160-161.

[8] F. Gesztesy and L.Pittner, "Electrons in logarithmic potentials I. solution of the Schödinger equation," J. Phsy. A: Math. Gen., **11**, pp. 679-686. (1978).

[9] E. Schrödinger, "Quantization as a problem of proper values (Part I)," (in German), Annalen der Physik 79 (1926).

[10] Randal H. Cole, *Theory of Ordinary Differential Equations* (Appleton-Century-Crofts, New York, 1968), p. 223.

[11] L. I. Schiff, *Quantum Mechanics* (McGraw-Hill, New York, 1955), 2nd ed., p. 32.

[12] Ref. 8, p. 683.